Mathematical Modelling of the Fluid Dynamics Involved in Colonic Mixing with Applications to Drug Delivery

by

Allison Bridget Mary Davies

A thesis submitted to
The University of Birmingham
for the degree of
Doctor of Philosophy

School of Mathematics
The University of Birmingham
August 2013

Abstract

Within the pharmaceutical industry there is current interest in the colon as a site for drug delivery: in particular delivery to the proximal colon, which possesses the most favourable characteristics for absorption. The most prevalent type of contraction of the smooth colonic muscle is segmental, rather than propulsive, in nature. This promotes the mixing of material within the lumen, which in turn increases the contact of contents with the epithelial surface, aiding absorption. The colonic epithelium is lined with a thin layer of mucus which acts as a protective barrier and provides lubrication.

Very few physical or theoretical models have been developed to assist with the understanding of dosage form behaviour within the colon. Better understanding of this could help in product development through the prediction of residence time and uptake of a given drug.

We model the colon as a cylindrical pipe, whose boundary represents the circular muscle layer. Under the assumption that the boundary of the pipe is axisymmetric and that the contractions may be modelled by a standing wave of small amplitude, we employ a perturbation expansion to describe the behaviour of both one and two layer fluid flow. Using both Newtonian and non-Newtonian constitutive equations and numerical techniques to solve the ODEs arising from our asymptotic analysis we present the resulting flow fields.

Utilising the results for one layer flow and the method of Lagrangian particle tracking

we create a model of drug delivery which analyses the proportion, by volume, of a drug reaching the colonic epithelium. In doing this we find that the segmental contractions of the colon lead to effective mixing of the fluid. We investigate the results of varying the fluid rheology and contractile properties, finding that the amplitude of contraction has the largest effect of the proportion of particles absorbed. The results prove themselves robust to variation in contractile frequency, fluid viscosity and ratio between radius and wavelength, which is promising in terms of consistent drug delivery across a range of physiological states.

Acknowledgements

Firstly I would like to thank my supervisors, Dr Dave Smith and Dr Rosemary Dyson for their help and support; I would also like to thank Professor Steve Decent, Professor Mark Simmons and Dr Rachel Bridson for the input of their specialist mathematical, experimental fluid dynamics and pharmacological expertise.

A big thank you goes to my husband, Will, for his unwavering support and help in reaching this stage, as well as to my family and friends. A special thank you goes to my son, Ben, for remaining in utero until after this thesis was first submitted.

Finally, I would like to thank EPSRC for their financial support which has allowed me to continue with my studies and the School of Mathematics for allowing me the opportunity to gain paid teaching experience.

Contents

Chapter 1

Introduction

The gastrointestinal (GI) tract forms the main part of the digestive system and the colon is the final organ of this. The large intestine is comprised of the caecum and colon, although the terms colon, large intestine and bowel are generally used interchangeably.

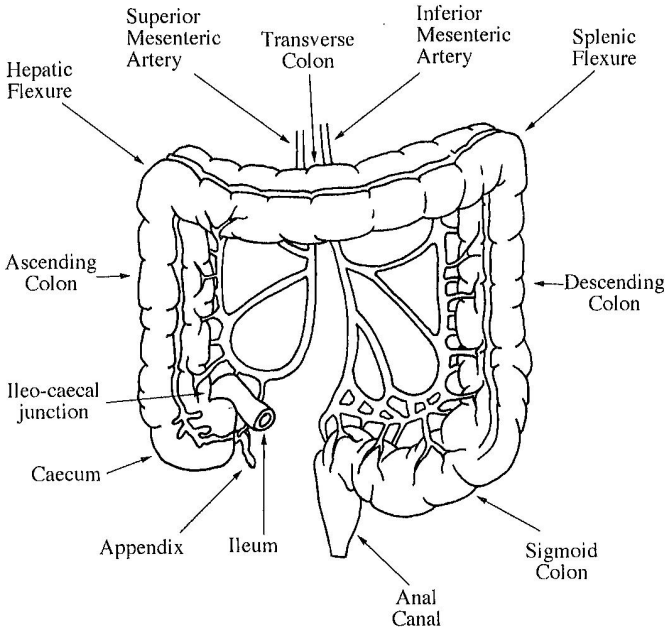

Figure 1.1: Anatomy of the large intestine and rectum [70].

The colon is a continuous tube approximately 1.5 m in length [1], with diameter varying from around 8.5 cm at the caecum to 2.5 cm at the sigmoid colon [70]. The

proximal, or right, colon consists of the ascending and transverse regions and the distal, or left, colon consists of the descending and sigmoid regions. Two sharp bends give the colon its recognisable shape; these bends are known as the right colic, or hepatic, flexure and the left colic, or splenic, flexure and are labelled in figure 1.1.

Material flows into the caecum from the small intestine; this flow is regulated by the ileocaecal valve. The ascending colon is approximately 12 cm in length [1], running between the ileocaecal valve and the hepatic flexure. Here it becomes the transverse colon, which is approximately 45 cm in length [1]. This is the largest part of the colon and also has the most motility. The transverse colon runs along until it reaches the splenic flexure, where it becomes the descending colon. Due to the higher position of the splenic flexure in the body compared to the hepatic, the descending colon is longer than the ascending colon [1]. The sigmoid colon, also known as the 'S-shaped' colon, begins at the pelvic brim, as a continuation of the descending colon. It is approximately 40 cm in length [1].

As will be discussed in more detail later, there is a layer of smooth circular muscle located within the interior of the colonic wall. Perpendicular to this, an outer muscle layer runs longitudinally along the colon and is split into three strips known as the taeniae coli. These three strips fuse together once they reach the rectum. The circular muscle is responsible for segmental contractions which serve to mix the fluid content within the colon whereas contractions of the longitudinal muscle initiate propulsion of the colonic contents distally.

Haustra are created in places along the length of the colon due to the fact that the taeniae are shorter than the true length of the colon [25]. The folds between the haustra are known as interhaustral folds and contain all layers of the colonic wall [25]. Within the proximal colon the haustra are fixed because of the fusion between the taeniae and the underlying circular muscle. In the distal colon, however, the haustra are not fixed and are formed by the contractile activity of the taeniae.

The main functions of the colon are absorption of water and electrolytes as well as the storage of faecal matter [25]. Most absorption takes place in the proximal colon whereas the main role of the distal colon is that of storage.

In this thesis we aim to create a mathematical model of the flow induced by the segmental contractions of the smooth colonic muscle and solve using analytical techniques. In doing so we aim to represent the behaviour and flow of the colonic fluid under such conditions. We do this with the intention of mathematically investigating the pharmacological problem of the behaviour of a drug dosage form once it is exposed to the colonic environment.

1.1 Motivation: Drug Delivery

The oral delivery of a drug to the colonic region of the GI tract is of current interest within the pharmaceutical research industry. Section 1.3.1 describes the colonic environment in more detail.

In order to reach the colon before a drug begins to be released from a dosage form (e.g. a tablet or capsule) some type of modified release is required. Research into modified/controlled release techniques for oral drug delivery has stemmed from a desire to improve the efficacy of medication whilst reducing the side effects, thereby maximising patient compliance [72]. The methods used for targeting the colon are not important to us from a mathematical point of view, i.e. it is not necessary to know these in order to solve the problem; however a brief knowledge of the methods available is useful to create a wider understanding of the overall picture.

Successful targeting of the colon requires the exploitation of some feature unique to the colonic environment [49]. Perhaps the simplest method would be to release the drug after a pre-determined amount of time, possibly around four hours after leaving the stomach [70], due to a relatively consistent small intestinal transit time. However, there is

still an amount of variation between individuals and even within individuals [38]. Alternatively there is a change in pH at the junction between the small intestine and colon which could be utilised for modified release [49, 70]. At this junction contents are exposed to large pressures and break up of dosage forms is often observed [72], suggesting pressure-controlled dosage forms as a method [49], although its reliability has not yet been thoroughly tested [72]. The colonic environment has a higher bacterial concentration than the more proximal regions of the GI tract [38], in addition these bacteria are unique to the colon [49, 70, 72]. The enzymes produced by these bacteria could also be used to achieve site-specific release. For example bacterial degradable polymers have been used to coat a dosage form, shielding the drug from the hostile environments of the stomach and small intestine and allowing it to be released in the colon; this is due to biodegradable enzymes being found only in the colon [57]. Ultimately it is the physical and chemical properties of the drug itself which should determine which delivery system is adopted [49].

The reasons for pharmaceutical interest lie in both topical (localised) and systemic (whole body) delivery [68]. Drugs delivered to the colon may be used for the local treatment of diseases such as ulcerative colitis, bowel cancer and Crohn's disease. Preventing drug release until the dosage arrives at the colon increases the bioavailability of the drug at the site it is to treat [58] and allows a lower dose to be administered, thus reducing the side effects to the rest of the body [57]. Delivery to the colon for treatment of a non-local disease would be chosen if the characteristics of the colon or of the drug made the colon a more attractive site for delivery than other regions.

For systemic treatment a method of delivery known as mucoadhesion is receiving much interest [17, 59, 68]. Bioadhesion occurs when two surfaces, with at least one biological in nature, adhere to one another for a prolonged period of time; mucoadhesion is the term used in pharmaceutical sciences when the biological surface in question is either mucus or a mucous membrane (mucosa) [59]. In particular the colon may prove a good site for

mucoadhesion. A thin layer (of the order of tens of microns) of mucus lines the interior wall of the colon, making this a viable method; section 1.3.1 deals with the physiology and conditions within the interior of the colon.

The original motivation for research into the mucoadhesive process was its potential to manipulate the transit time of a dosage form [68]. Within the GI tract contents are subject to highly variable transit times [68]; this variability has caused problems, particularly with modified release dosage forms [38]. In theory mucoadhesion could reduce this variability thus helping to improve the efficacy and reliability of a given drug. In addition, once a dosage form has attached itself to the mucus or mucosa at a given site, the drug diffusion barrier may be reduced [68], improving the rate of absorption; this attachment could also protect a drug from any degradation which may otherwise occur from any colonic material [68].

There has not been much *in vivo* success with mucoadhesive approaches in either the human stomach or small intestine, despite *in vitro* and small animal studies showing the potential for success [38]. As of yet relatively little research has been conducted into colonic mucoadhesion, but several properties of colonic physiology and motility make success look more promising here than in the upper GI regions [68], these properties will be discussed in sections 1.3.1 and 1.3.2.

Traditionally many protein and peptide based drugs such as insulin have been unable to be delivered via the oral route, due to enzymatic degradation and poor absorption in the stomach and small intestine [57]. The delivery of drugs such as these to the colon shows promise due to its less hostile environment when compared to the more proximal GI regions [27].

Other advantages of targeting the colon for systemic drug treatment relate to general types of delivery approach. Targeting the colon for drug absorption provides an opportunity to increase the time between consecutive doses [72]. In addition a near neutral pH,

relatively long transit time and less digestive enzymatic activity than the stomach and small intestine all provide the colon with advantages as a site for drug targeting [58].

Quantifying and modelling the fluid within the colon presents a challenge. Colonic fluid has some complex properties and is non-Newtonian in nature (refer to section 1.2); in addition to this, its composition alters as it progresses through the colon - from a viscous liquid to a semi-solid state. Research literature into the viscosity and density of fluids within the GI tract is limited and often not comparable due to different rheological measuring techniques. As well as the bulk fluid (also known as chyme or digesta), the properties of colonic mucus need investigating. Again this is a non-Newtonian fluid and is described as viscoelastic [28] - having both viscous and elastic properties. As far as we are aware data on human colonic mucus in its normal state has not been published, potentially due the relative inaccessibility of the colonic region, although there is some information available for mucus from other regions of the human body.

As well as the complex nature of the fluid in the colon, the motility of the circular colonic muscle presents modelling difficulties. The motility patterns of the colon vary between and within individuals and are affected by eating patterns, time of day and disease, amongst other things. Data on the motility of the colon, including both segmental and propulsive contractions, are reviewed in section 1.3.2. We will see that it is the contractions of the circular muscle which cause mixing of the fluid within the colon and that this is key to the absorption of material into the bloodstream.

In the design of dosage forms and methods of drug targeting, often only one or two variables relating to the GI tract are considered [38]. Clearly this cannot be representative of the colonic environment. A mathematical model can be formulated in terms of parameters which will allow far more variables to be taken into account and the relative importance of each variable to be quantified. It is important to be able to do this since gut physiology is not well understood [38] and so being able to test dosage form behaviour

over a wide range of values for each variable is desirable. In particular the effects of disease on the colonic environment and motility has received little attention despite its obvious influence on the efficacy of a given drug [38, 72]. For example, opposite effects on drug absorption can be seen from increased fluid volumes as opposed to increased motility [72]. The use of a mathematical model gives an advantage here as it provides the opportunity to investigate both drug and fluid behaviour at physical extremes.

1.2 An Introduction to Rheology

In this section we investigate the types of constitutive equation for some classes of fluid related to those which may be found within the colonic lumen.

One of the most useful tools in studying the behaviour of a material is the set of general equations of motion (under the assumptions made within a continuum mechanics framework), given in Cartesian vector form by

$$\rho\left(\frac{\partial \boldsymbol{u}}{\partial t} + (\boldsymbol{u}\cdot\nabla)\,\boldsymbol{u}\right) = -\nabla p + \nabla\cdot\boldsymbol{\tau} + \rho\boldsymbol{F}, \tag{1.2.1}$$

where t is time; $\boldsymbol{u}$, ρ, p, $\boldsymbol{\tau}$ are the velocity, density, pressure and shear stress of the fluid respectively; and $\rho\boldsymbol{F}$ is the body force acting on the fluid. This equation is made specific to a material via a constitutive equation for the shear stress $\boldsymbol{\tau}$. To fully describe the flow and behaviour of a given material additional information is required such as the compressibility of the material and possibly various thermodynamic equations.

Generalised Newtonian Fluids

Newtonian fluids obey a linear relationship between shear stress, $\boldsymbol{\tau}$, and shear rate (or rate of strain), $\dot{\boldsymbol{\gamma}}$, with the constant of proportionality, μ, known as the (dynamic) viscosity of the fluid. In terms of the fluid velocity the shear rate is given by $\nabla\boldsymbol{u} + (\nabla\boldsymbol{u})^T$, so that in

Cartesian co-ordinates the components of shear rate are given by

$$\dot{\gamma}_{ij} = \frac{\partial u_i}{\partial x_j} + \frac{\partial u_j}{\partial x_i}. \tag{1.2.2}$$

The Newtonian model describes the behaviour of various fluids, such as water, extremely well. However, many fluids of importance in industry and the sciences (including biological fluids) do not follow this simple relation. In particular many materials exhibit both fluid and solid properties under different conditions. We shall utilise various rheological models in our study of the complex behaviour and flow within the colon.

After Newtonian fluids, the most simple type of model is that of a generalised Newtonian fluid (GNF). For such fluids the viscosity is not constant but a function of shear rate. The constitutive equation of a GNF is of the form [9, p170]

$$\boldsymbol{\tau} = \mu(\dot{\gamma})\dot{\boldsymbol{\gamma}},$$

where $\mu(\dot{\gamma})$ is known as the apparent viscosity of the fluid and

$$\dot{\gamma} = \sqrt{\frac{\mathrm{tr}(\dot{\boldsymbol{\gamma}}^T\dot{\boldsymbol{\gamma}})}{2}},$$

with $\mathrm{tr}(A)$ denoting the trace of the matrix A and the sign of the square root chosen such that $\dot{\gamma} \geq 0$. The GNF model is particularly useful in industrial flow problems where the effects of shear-dependent viscosity are of primary importance [9, p169].

One of the first proposed GNF models was the power law model of Ostwald (1925)-de Waele (1923) [15]. The constitutive equation for a power law fluid is given by [5, p19]

$$\boldsymbol{\tau} = k\dot{\gamma}^{n-1}\dot{\boldsymbol{\gamma}},$$

where k is known as the consistency index (with units $\mathrm{Pa} \cdot \mathrm{s}^n$) and n is a nondimensional parameter known as the power law exponent. The response of the fluid viscosity as the shear rate increases or decreases is described by n. If $n = 1$ then the equation reduces to that of a Newtonian fluid (with viscosity k). If $n < 1$ then the fluid is described as shear thinning, i.e. the viscosity decreases as the shear rate increases, for example modern paints. If $n > 1$ then the fluid is described as shear thickening, i.e. the viscosity increases as the shear rate increases, for example custard.

This model has been used extensively for industrial problems due to its simplicity and the fact that often the most important region of the $\log \mu$ vs $\log \dot{\gamma}$ plot (determined experimentally) is the linear region, also termed the 'power law region', see figure 1.3. It is in this region that the power law holds; however care should be taken as the model breaks down at very high or very low shear rates when compared to experimental results (due to the prediction of infinite viscosity) and should be avoided for flows which may be subject to either of these conditions.

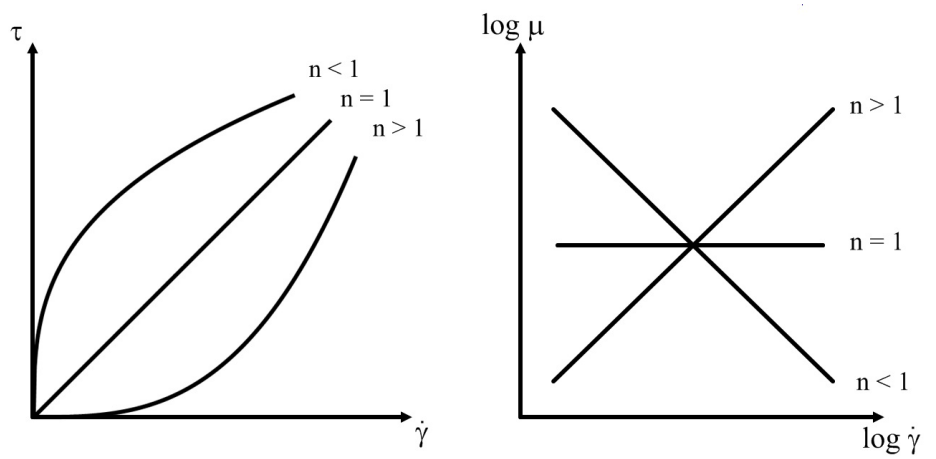

(a) Shear stress vs shear rate

(b) Viscosity vs shear rate (logarithmic scale)

Figure 1.2: Constitutive relationships for a power law fluid.

A GNF model which avoids the problem of infinite and zero viscosity at very high or

very low shear rates is that of Carreau (1972). The apparent viscosity for a Carreau fluid is given by [5, p18]

$$\frac{\mu - \mu_\infty}{\mu_0 - \mu_\infty} = [1 + (m\dot{\gamma})^2]^{\frac{n-1}{2}}, \tag{1.2.3}$$

where μ_0 is the limit of viscosity as $\dot{\gamma} \to 0$ (zero-shear viscosity), μ_∞ is the limit of viscosity as $\dot{\gamma} \to \infty$, (infinite-shear viscosity), m is a constant parameter with dimension time and n is a dimensionless parameter which has the same meaning as in the power law model. Using (1.2.3) we may write the constitutive equation for a Carreau fluid as

$$\boldsymbol{\tau} = \mu_0[(1 - \mu_c)(1 + (m\dot{\gamma})^2)^{\frac{n-1}{2}} + \mu_c]\dot{\boldsymbol{\gamma}}, \tag{1.2.4}$$

where $\mu_c = \mu_\infty/\mu_0$ is the ratio between the infinite-shear and zero-shear viscosities. The main difference between this and the power law model can be seen by the predicted behaviour of the viscosity at very high and very low shear rates. For a shear thinning power law fluid:

$$\mu \to \begin{cases} \infty, & \text{as } \dot{\gamma} \to 0 \\ 0, & \text{as } \dot{\gamma} \to \infty, \end{cases}$$

whereas for a Carreau fluid:

$$\mu \to \begin{cases} \mu_0, & \text{as } \dot{\gamma} \to 0 \\ \mu_\infty, & \text{as } \dot{\gamma} \to \infty. \end{cases}$$

The Carreau model was later extended by Yasuda by the addition of a dimensionless parameter a, to give the Carreau-Yasuda model [45, p231]

$$\boldsymbol{\tau} = \mu_0[(1 - \mu_c)(1 + (m\dot{\gamma})^a)^{\frac{n-1}{a}} + \mu_c]\dot{\boldsymbol{\gamma}}.$$

In this model a describes the transition between the zero-shear region and the power law

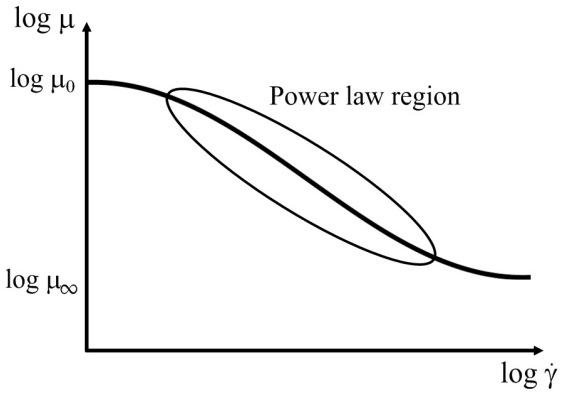

Figure 1.3: Viscosity vs shear rate for a Carreau fluid with logarithmic scale.

region [9, p171]. Note that setting $a = 2$ returns the Carreau equation.

An example of a constitutive equation which has been used to model food data is the De Kee model [10, p40]. In this model the apparent viscosity given by

$$\mu(\dot{\gamma}) = \mu_1 \mathrm{e}^{-t_1\dot{\gamma}} + \mu_2 \mathrm{e}^{-0.1t_1\dot{\gamma}} + \mu_\infty,$$

where the parameters μ_1, μ_2 and μ_∞ are all viscosities and the parameter t_1 has dimension time. This model describes the behaviour of a shear thinning fluid, with $\mu \to \mu_1 + \mu_2 + \mu_\infty = \mu_0$ as $\dot{\gamma} \to 0$ and $\mu \to \mu_\infty$ as $\dot{\gamma} \to \infty$.

There are several shortcomings of GNF models, in particular with the power law model due to its simplicity (only two parameters); however it is this very simplicity which makes its use so attractive within industry. As has already been mentioned, the power law model cannot describe viscosity for shear thinning fluids at low shear rates, although this problem can be overcome by using a Carreau model; it should be noted that the Carreau model does not lend itself to analytical solutions. In addition, according to Bird et al. [9, p175], it is not possible to relate the power law parameters k and n with the molecular weight and concentration within the fluid. It may be especially desirable to be able to do this in fields such as polymer science. More generally questions arise as to the limits

of validity for GNF models due to the empirical nature of their development [9, p233], with such models arising via curve-fitting existing data on viscosity - shear rate - shear stress relationships. Ultimately choosing which GNF model to use, or whether to use a more complicated model altogether, comes down to a balancing act between realism and actually being able to formulate a mathematical model which can be solved to provide (useful) results.

Viscoelastic Fluids

Analogous to Newtonian fluids we have Hookean solids. In the same way that shear stress is related to shear rate via constant viscosity for a Newtonian fluid, for a Hookean solid the shear stress is related to the strain, $\boldsymbol{\gamma}$, via a constant elastic modulus, G, i.e. $\boldsymbol{\tau} = G\boldsymbol{\gamma}$. If we consider small displacements and let l_i represent the displacement in the i-direction from the reference configuration at t_0 to time t, then the linear theory for small deformations gives us the infinitesimal strain tensor (in Cartesian co-ordinates) [9, p257]

$$\gamma_{ij}(t_0, t) = \frac{\partial l_i}{\partial x_j} + \frac{\partial l_j}{\partial x_i}. \tag{1.2.5}$$

Since $\boldsymbol{\gamma}$ depends on two times, t_0 and t, Hookean solids may be described as having 'memory', whereas Newtonian fluids, where $\dot{\boldsymbol{\gamma}}$ depends only on time t, do not have a memory of past events.

Materials may be considered as lying on a continuum between Hookean behaviour and Newtonian behaviour; this is where the Deborah number, De, proves useful. The Deborah number was introduced by Reiner and is defined as

'The ratio of a characteristic (relaxation) time of a material to a characteristic time of the relevant deformation process.' [5, p161]

In the limit $\mathrm{De} \to 0$, Newtonian behaviour may be observed. This corresponds to a short characteristic time or a long deformation process, for example if we consider a glass

window of uniform thickness over a long enough period of time, there will appear to have been a flow of glass from the top of the window to the bottom. In the limit $\mathrm{De} \to \infty$, material behaves as a Hookean solid. This may be due to either a long relaxation time or a fast deformation process, for example it is sometimes the case that lubricating oils passing through gears appears solid-like [5, p6].

The earliest in depth work into materials which are neither Hookean nor Newtonian was undertaken by Weber in 1935, studying silk threads [15]. He identified the phenonomen of stress relaxation, which he termed the 'after effect' [15].

Maxwell appears to have been the first to attempt to obtain a constitutive equation for a viscoelastic fluid. He postulated that fluids with both elastic and viscous properties could be described by [9, p258]

$$\tau_{xy} + \frac{\mu}{G}\frac{\partial \tau_{xy}}{\partial t} = \mu \dot{\gamma}_{xy}. \tag{1.2.6}$$

For steady-state motions, $\partial \tau_{xy}/\partial t = 0$ and (1.2.6) simplifies to the equation for a Newtonian fluid with viscosity μ. At the other extreme, for sudden changes in stress, $\partial \tau_{xy}/\partial t$ dominates the left hand side (LHS) of (1.2.6) and, after integration with respect to t, we arrive at the equation for a Hookean solid with elastic modulus G [9, p258].

More generally, Maxwell's equation is given by [9, p259]

$$\boldsymbol{\tau} + \lambda_1 \frac{\partial \boldsymbol{\tau}}{\partial t} = \mu \dot{\boldsymbol{\gamma}}, \tag{1.2.7}$$

where λ_1 is the relaxation time of the fluid, defined as the time taken for the shear stress in the material to reduce to e^{-1} of its initial value [40]. This first order differential equation may be written in integral form as [9, p260]

$$\boldsymbol{\tau}(t) = \int_{-\infty}^{t} \left(\frac{\mu}{\lambda_1} \mathrm{e}^{-(t-t')\lambda_1} \right) \dot{\boldsymbol{\gamma}}(t') \, \mathrm{d}t',$$

where $(\mu e^{-(t-t')\lambda_1})/\lambda_1$ is known as the relaxation modulus, which decays exponentially as we go backwards in time, i.e. as $t' \to -\infty$ [9, p260]. In its integral form Maxwell's equation relates the stress at the present time t to the shear rate at all past times t', via a weighting factor (the relaxation modulus) which gives more weight to those events in the recent past rather than the distant past. This has been described as a notion of 'fading memory' [9, p260].

Hooke's constitutive equation uses the assumption of small displacements and since Maxwell's linear equation is based on Hooke's equation it follows that Maxwell's equation must only be valid under the same restriction. In addition Maxwell's model has been found to be too simple, with only two constants, to describe linear viscoelastic data. Despite this, Maxwell played a key role in the development of linear viscoelasticity and his equation provided a major starting point for research into nonlinear viscoelastic models [9, p260].

Another linear viscoelastic constitutive equation is the Jeffreys model, given by [9, p261]

$$\boldsymbol{\tau} + \lambda_1 \frac{\partial \boldsymbol{\tau}}{\partial t} = \mu \left(\dot{\boldsymbol{\gamma}} + \lambda_2 \frac{\partial \dot{\boldsymbol{\gamma}}}{\partial t} \right). \tag{1.2.8}$$

This model extends that of Maxwell by the inclusion of the time derivative of $\dot{\boldsymbol{\gamma}}$ and the addition of a second time constant λ_2, the retardation time. The retardation time of a material is defined as the time taken for the strain to reach $1 - e^{-1}$ of its final value after the imposition of a constant shear stress [40]. In integral form the Jeffreys model is given by [9, p261]

$$\boldsymbol{\tau}(t) = \int_{-\infty}^{t} \left(\frac{\mu}{\lambda_1} \left(1 - \frac{\lambda_2}{\lambda_1} \right) e^{-(t-t')\lambda_1} + 2\frac{\mu\lambda_2}{\lambda_1} \delta(t-t') \right) \dot{\boldsymbol{\gamma}}(t') \, dt',$$

which makes use of the Dirac delta function, δ. Both the Maxwell and Jeffreys models may also be written in terms of the strain rather than the shear rate.

The general linear viscoelastic model (GLVM) encompasses both the Maxwell and Jeffreys models as well as many others. The GLVM may be written as [5, p45]

$$\boldsymbol{\tau}(t) = \int_{-\infty}^{t} G(t-t')\dot{\boldsymbol{\gamma}}(t')\,\mathrm{d}t', \tag{1.2.9}$$

where $G(t-t')$ is the relaxation modulus of the material [9, p263].

As already discussed, the GLVM is only valid for materials subjected to small deformations; as a consequence of this the model cannot describe any shear rate dependence of viscosity. Although the GLVM works reasonably well as a starting point for the study of viscoelastic behaviour, more complex mathematical descriptions are required for the majority of materials [9, p264].

In 1903 Zaremba, and later Jaumann in 1905, extended the developed theory of linear viscoelasticity to a nonlinear framework by introducing a 'corotational derivative' (referred to as Jaumann derivatives) [15]. These derivatives allow for a frame of reference which translates and rotates with the material. A major breakthrough in the study of nonlinear viscoelastic models came with the work of J. G. Oldroyd in 1950, in which he introduced to constitutive equations the idea of convected derivatives [15].

Oldroyd proposed necessary criteria for a constitutive equation to be admissible. He states that any such equation should be independent of

1. the frame of reference;

2. the position in space and the motion of the fluid element; and

3. the stress and strain in any neighbouring elements [9, p480].

Since the behaviour of a viscoelastic fluid depends on its past shear rates as well as the present, the third principle tells us that the idea of 'fluid memory' must be associated with material elements rather than points in space [5, p143]. At the very least time derivatives

in the linear models considered thus far should be replaced by the material time derivative, $\mathrm{D}/\mathrm{D}t$; however it turns out that time derivatives of a more complex nature are required in order to satisfy the second principle [5, p144]. This is where Oldroyd's convected time derivatives make an appearance.

Oldroyd introduced the idea of a convected co-ordinate system in relation to constitutive equations in his paper of 1950 [46]. In this system co-ordinate surfaces $\hat{x}^i = \text{constant}$ are embedded in the material and deform with it. Thus any material element has the same co-ordinates $\hat{x}^1, \hat{x}^2, \hat{x}^3$ for all times t [5, p145][9, p480]. In a similar way to how the material time derivative

$$\frac{D}{Dt} : \boldsymbol{v} \mapsto \frac{\partial \boldsymbol{v}}{\partial t} + (\boldsymbol{u} \cdot \nabla)\boldsymbol{v}$$

allows us to move from a Lagrangian system to an Eulerian one, the upper convected (contravariant) time derivative

$$^{\triangledown} : \boldsymbol{A} \mapsto \frac{D\boldsymbol{A}}{Dt} - (\nabla \boldsymbol{u})^T \cdot \boldsymbol{A} - \boldsymbol{A} \cdot (\nabla \boldsymbol{u})$$

allows us to move to a convected system. For a more thorough treatment of the theory behind convected co-ordinates refer to Oldroyd [46], Bird [9] or Barnes [5].

Using his new system, Oldroyd was able to extend the models of Maxwell and Jeffreys by replacing the time derivatives in (1.2.7) and (1.2.8) with upper convected time derivatives. The Oldroyd B, or upper convected Jeffreys, model is given by [5, p147]

$$\boldsymbol{\tau} + \lambda_1 \boldsymbol{\tau}^{\triangledown} = \mu(\dot{\boldsymbol{\gamma}} + \lambda_2 \dot{\boldsymbol{\gamma}}^{\triangledown}). \tag{1.2.10}$$

In the next section we study the interior and motility of the colon, in particular we investigate the role and values of the rheological parameters required for use within the relevant rheological models of this section.

1.3 Modelling the Colon

In this section we introduce the features and properties of the colon and its environment that we will require in order to create a representative model.

We investigate the properties of chyme and mucus, taking particular interest in the rheological and physical parameters necessary for the creation of a mathematical model. We also consider the motility patterns of the colon - the frequency, causes and effects of the different types of muscular contraction. Altogether this information will allow us to combine both the fluid properties and the geometrical features of the colon into a mathematical model.

1.3.1 The Interior of the Colon and the Biorheology of Chyme and Mucus

In this section the structure of the internal colonic wall is discussed and the properties of fluids within the colonic lumen are investigated. These properties will provide an important basis for the mathematical modelling of the fluid flow within the colon, allowing us to link the theory of the previous section with the physiological reality.

The mucosa, also known as the mucous membrane, is the moist tissue which lines many organs and body cavities such as the intestines, nose and lungs [17]; the mucosal surface of the colon is described as being relatively smooth [25]. Lying beneath and supporting the mucosa there is a deeper connective tissue known as the submucosa. Between the mucosa and the submucosa is a thin layer of smooth muscle known as the muscularis mucosa [17, 25]. There are a further two layers of smooth muscle - each of which controls various motility patterns (see section 1.3.2).

The colonic mucosa contains enterocytes, as well as goblet and enteroendocrine cells [68]; enterocytes are responsible for absorption, goblet cells secrete mucus and enteroen-

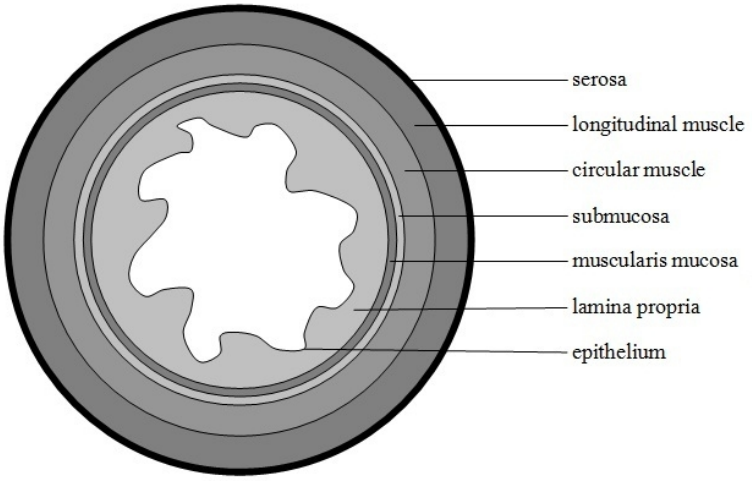

Figure 1.4: The interior of the colon.

docrine cells produce hormones. The mucosa of the GI tract is composed of two main layers: the lamina propria and the luminal epithelium [68].

The lamina propria lies immediately beneath the epithelium, supporting it, and is comprised of loose connective tissue [17]. This tissue contains a combination of fibroblasts, lymphocytes, plasma cells and macrophages [25].

The intestinal epithelium is single-layered [17] and columnar [25]. Single-layered epithelia contain goblet cells which secrete mucin, which then hydrates to create a mucus layer on the surface of the epithelium; making the epithelial layer moist [59]. This mucus layer is viscoelastic in nature [17] and we shall use this type of rheological equation when modelling it. The crypts of Lieberkühn are glands found in the epithelium of the colon (as well as the small intestine) which extend almost as far as the muscularis mucosa. The lining of the base of these crypts is composed of undifferentiated epithelial cells, which show progressive maturation into both goblet cells and columnar epithelium as they climb the walls of the glands [25].

The general concensus is that the main functions of this mucus layer are protection and lubrication; mucus is described by Edsman and Hägerström [17] as *'mediating the*

interactions between the epithelial cells and their environment.' This mediation is achieved by the provision of lubrication between the epithelium and passing fluids and waste, maintaining the water balance at a site and binding particles, bacteria and viruses. The lubricant effect is particularly important in the distal colon, protecting the epithelium from abrasion due to solid matter [70]. Varum et al. [68] also give the mucus layer's role as a diffusion barrier between the epithelium and the lumen, as well as the provision of a hospitable environment for the microflora of the colon. The mucus layer also plays a role in the defence against infection and disease [17, 68]. It may be worth noting that both the adhesive and cohesive properties of the mucus gel are increased as the water content is decreased [17].

It is generally accepted that the mucus of the colon consists of two distinct layers; although most literature on the properties of colonic mucus consider it as just the one layer. The first of these layers is a firmly adherent mucus gel layer which acts as a stable protective barrier between the lumen and the epithelium [62, 68]. It also provides a habitat for the microflora of the gut [62]. Above this firmly adherent layer there lies a loose layer of mucus which provides the lubricative properties [68]. This loose layer is described by Strugala et al. [62] as *'an extensive sloppy mucus layer'* and they hypothesise that its purpose is to act as a lubricant in order to protect the epithelium from shear stress. The thickness of these two layers, both together and relative to each other, differs along the gastrointestinal tract and between species of mammals [68].

The mucus gel is composed predominately of water, approximately 95% [17, 68]. The rest of the mucus gel is made up of glycoproteins, lipids, free proteins and mineral salts [17]. However, it is impossible to know the exact composition in any location in any one person as this will vary depending on factors such as the role of the mucus and the health of the individual [17]. The location of the mucus also affects its composition (for example, the colon versus the small intestine), as do genetics, age, gender and gastrointestinal

activity [68].

Mucus turnover is affected by the sensitivity of the goblet cells to mucus secretory stimuli and also the rate at which mucus is 'lost' due to stresses in the lumen. Although there is little information regarding the rate of mucus renewal in the human gastrointestinal tract [68], Rubenstein and Tirosh [54] showed that mucus turnover and sensitivity to mucus secretory stimuli were lower in the rat caecum and colon than in the stomach and small intestine. It is considered likely that this may also be the case in humans [68].

Both the dynamic viscosity and relaxation time of a fluid are essential in the formulation of a viscoelastic model. Unfortunately these have not been widely investigated, if at all measured, for human colonic mucus; thus numerical data from other regions of the human body must be relied on. Qualitatively the mucus layer viscosity increases progressively from the proximal to the distal colon [63]. The viscosity also varies radially with a low viscosity near the intestinal lumen and a high viscosity adjacent to the epithelium [63].

Lai et al. [28] claim that the macrorheological behaviour of mucus produced at various sites within the body is similar - due to the similar total mucin content. They quote an upper limit for mucus viscosity at low shear rates as $10^4 - 10^6$ times higher than water, i.e. $10 - 1000$ Pa $\cdot$ s. In particular, Lai et al. reference several studies involving pig gastrointestinal mucus which show secretions from different regions displaying overall structural similarities, suggesting similar rheological properties between gastric, duodenal and colonic mucus.

Table 1.1: Mean viscosities of gastric mucus [12].

Shear rate (s^{-1})	1.15	2.30	5.75	11.50	23.0	46.0	115.0	230.0
Viscosity ($\times 10^{-2}$ Pa $\cdot$ s)	8.46	4.69	2.85	1.95	1.48	1.23	0.84	0.61

Table 1.1 displays the results of Curt and Pringle [12], giving the mean viscosity of the gastric mucus of twelve control subjects. The viscoelastic models considered in section

1.2, e.g. Oldroyd B, do not take into account the shear rate dependent nature of a fluid, instead they make use of the zero-shear viscosity. Therefore the viscosities at low shear rates are considered of most importance. The remaining data could be used to attempt to fit the parameters in a power law or Carreau model for example.

Other sites of the human body have had the rheological behaviour of their mucus studied more extensively, for example the lungs, nose and cervix. Mucus displays a spectrum of relaxation times covering several orders of magnitude depending on the frequency of motion it is subjected to. For example Smith et al. [60] found a relaxation time for mucus of approximately 0.03 s by taking data from oscillatory rheometry experiments at a frequency of $5 - 10$ Hz and fitting them to a Maxwell model. For our system the mucus is exposed to much lower frequencies and the review article values that we give are likely to be more indicative of the physical situation.

Within the respiratory system a viscosity of $12 - 15$ Pa $\cdot$ s [28, 51] for bronchial mucus has been reported as optimal for mucociliary clearance [28]. In addition Quraishi et al. [51] quote a general estimate of the relaxation time of mucus of 30 s. For respiratory mucus Lauga [29] reviews studies suggesting a range of viscosities of $10 - 1000$ Pa $\cdot$ s and a relaxation time again of approximately 30 s.

Rheological data available for cervical mucus also shows a relatively wide range of accepted values. Lauga's review reports on agreement in various literature of viscosities in the range $0.1 - 10$ Pa $\cdot$ s and relaxation times of $1 - 10$ s.

The thickness and continuity of the colonic mucus layer is another area which presents difficulties in finding human measurements. Where human data exists it tends to be contradictory, or at the very least not in agreement with other data (see table 1.2). This may be down to the methods used for collection and measurement as some staining techniques cause dehydration, and therefore shrinkage, of the mucus layer [68]. The colon possesses a thicker mucus layer than other regions of the GI tract, which is one reason

why the colon may prove a more successful site for mucoadhesion than the stomach or small intestine [68].

Disease in particular may have a marked effect on mucosal thickness, which is important since one reason for investigating colonic drug delivery is that of localised, or topical, delivery to treat colonic disease; in such conditions, the thickness of mucus may be markedly different. It has been reported, see for example [50, 68], that, in comparison with healthy control subjects, there is a tendency for patients with ulcerative colitis to have a thinner and more discontinuous than usual mucus layer and possibly for those with Crohn's disease to have a thicker than usual layer, although this has not yet proved to have statistical significance.

Pullan et al. [50] conducted a study into the thickness of colonic mucus in patients suffering from either ulcerative colitis or Crohn's disease. They aimed to relate inflammatory activity, age and drug treatment to mucus thickness and found mean values for thickness in the control group ranged from 107 μm in the right colon to 155 μm in the rectum. Matsuo et al. [37] aimed to improve the understanding of the histochemical composition of the surface mucus layer within the human colon. As part of this they measured the mean thickness as ranging from 39.1 μm in the ascending colon to 101.5 μm in the rectum. Finally Strugala et al. [62] published a study which focused mainly on the thickness and continuity of the mucus layer in the rectum of patients suffering from various degrees of ulcerative colitis and Crohn's disease. However, as part of this study they also measured the mucus thickness and percentage of mucus discontinuity throughout the colon of their control subjects; finding a range of mean values of $20 - 52.5$ μm from the caecum to the rectum.

None of these studies found any significant relation between mucus thickness and either age or drug treatment and a summary of their results is given in tables 1.2 and 1.3.

Finally we investigate the main fluid content of the colon. There are various factors

Table 1.2: Summary of Results (Thicknesses given in μm).

	Caecum	Ascending	Transverse	Descending	Sigmoid	Rectum
Pullan Controls	107	107		134	134	155
Matsuo Total	36.7	39.1	57.5		69.6	101.5
Strugala Controls	20		25	35	50	52.5
Pullan UC	90	90		43	43	60
Pullan CD	190	190		232	232	294
Matsuo Loosely Adherent	31.1	34.4	50.5		62.0	88.8
Matsuo Firmly Adherent	5.6	4.7	7.0		7.6	12.7

Table 1.3: Results of Strugala et al. for Rectal Mucus.

Group	Sample Size	Mean Thickness (μm)	% Discontinuity
Normal	10	32.5	1.0
Quiescent UC	18	28.1	1.6
Mild Active UC	12	26.7	13.5
Moderate Active UC	8	25.9	16.6
Severe UC	5	15.0	25.7
Crohn's Disease	6	19.6	6.1

which need to be looked at when considering the digestive fluid within the colonic lumen. From a drug delivery perspective, fluid is essential for the dispersion and absorption of a dosage form; hence the presence, or not, of fluid and the volume available is of high importance. McConnell et al. [38] take values from a study by Cummings et al. which found a mean total fluid volume in the colon of 187 ml, compared to mean post mortem total fluid volumes of 118 ml and 212 ml for the stomach and small intestine respectively, found by Gotch et al. The total fluid volume present does not give a full picture however. Schiller et al. [55] used magnetic resonance imaging (MRI) to determine the free fluid content in the small and large intestine. It was observed that free intestinal water represents only a fraction of the total intestinal water and is inhomogeneously distributed throughout the lumen, forming fluid pockets of different volumes. A pharmaceutical dosage form may be exposed to anything from 1 to 100 ml of free fluid [38] but the behaviour of the dosage may be very different at these two extremes [68]. In this thesis we consider the fluid to be homogeneously distributed, however future modelling work could consider the inhomogeneous distribution of fluid.

Although the colon has a much smaller surface area than the small intestine it is still very efficient at absorbing fluid - for every two litres of water entering the caecum there

is less than 200 ml of residual water in the stools and up to four litres of water a day may be absorbed [70]. In a healthy human adult the flow rate of chyme from the ileum to the colon is $1 - 2$ litres per hour [70].

Chyme is a shear thinning fluid whose rheological behaviour and composition changes as it progresses through the different regions of the colon. The fluid has changed from liquid to a more viscous semi-solid material by the time it has reached the latter stages of the colon, due to water absorption. However, this is not the only cause of change; from about halfway through the ascending colon consolidation of the luminal contents begins to occur, creating a single mass which gradually becomes more homogeneous and viscous [72].

The viscosity of colonic contents has not been well studied, if at all, in humans. Most information pertains to research conducted into the effect of diet on the viscosity of the small intestine digesta of pigs and chickens for example. Since our interest lies in the ascending colon it is worth considering the viscosities in the small intestine because the fluid in the ascending colon is rheologically similar to that in the ileum and there is a lack of data regarding the large intestine. Comparing viscosity measurements across different studies can prove very difficult. The non-Newtonian nature of chyme means that the shear rate at which viscosity is measured is extremely important, ideally a variety of shear rates would be used for measurement or at least the same shear rate used for all measurements to allow comparison, depending on the exact purpose of the study. Due to this dependence on shear rate, values for viscosities found in different studies often cannot be compared nor can the consistency of results be evaluated. In addition the region sampled and whether viscosity is measured with or without the removal of large particles (centrifugation) may affect the viscosity significantly. After the process of centrifugation the material, with large particles removed, is referred to as supernatant.

Lund et al. [34] considered the effect of diet on the viscosity of the small intestinal

content in rats. The rats were fed a diet of cellulose, oat gum or ground oats and measurements were made both before and after centrifugation at a shear rate of 50 s^{-1} using a rotary viscometer with cone and plate attachment. They were unable to measure the viscosity of the control group (fed cellulose) before centrifugation, however after this process the viscosity of the material was described as being not measurably different from water. The mean viscosities for those fed a diet of oat gum were measured as 1.877 $Pa \cdot s$ and 0.111 $Pa \cdot s$ before and after centrifugation respectively. For those fed a diet of ground oats the resulting viscosities were 1.868 $Pa \cdot s$ before centrifugation and 0.82 $Pa \cdot s$ after.

Lee et al. [30] investigated the effect of the concentration of guar meal (because of its use as a high protein, relatively inexpensive feed) in the diet of chickens on the viscosity of small intestinal digesta. Measurements were taken from the duodenum, jejunum and ileum using a cone and plate viscometer. Chyme from the ileum is the most viscous from these three regions and also the closest in nature to that in the caecum and ascending colon. The mean viscosity for ileal material was given as 0.00325 $Pa \cdot s$, with viscosity increasing as the concentration of guar meal increased. At 10% concentration viscosity was measured as 0.0581 $Pa \cdot s$.

Takahashi et al. [64] also used chickens in their research. In contrast to Lund et al. and Lee et al., Takahashi et al. were concerned with the shear-dependant properties of digesta, rather than the influences of diet. The viscosity of small intestinal and caecal contents were measured at a shear rate of 1 s^{-1} using a tube-flow viscometer, producing results of 3.8 $Pa \cdot s$ and 82 $Pa \cdot s$ respectively. The density of the caecal contents with particles was measured as 1030 kg/m^3. In addition, Takahashi and Sakata have published several papers examining the viscous properties of pig caecal contents in relation to the proportion of large particles remaining. They measured the coefficient of viscosity of caecal contents with particles removed to be 0.0013 $Pa \cdot s$ [66] and found this to be independent of shear rate, i.e. the caecal contents without particles were Newtonian in nature. In the

same study the material containing particles displayed shear thinning behaviour with a viscosity of 3.7 $\text{Pa} \cdot \text{s}$ at 1 s^{-1}. They also found density to be independent of the large particle content, with a value given of 1010 kg/m^3 [65].

Other measurements for pig intestinal viscosities include those of Roberts et al. [53] and McDonald et al. [39]. Roberts et al. give a maximum zero shear rate viscosity of 0.057 $\text{Pa} \cdot \text{s}$ for the jejunal digesta of their control group. For McDonald et al. values of viscosity (with particles removed) for the caecum at a shear rate of 60 s^{-1} range between 0.00167 and 0.00618 $\text{Pa} \cdot \text{s}$ depending on diet. Similarly values for the proximal colon are given between 0.00248 and 0.0052 $\text{Pa} \cdot \text{s}$.

Here we have seen a wide range of viscosity values, and not all for the relevant regions. At the very least though they give us an idea of the viscosity of the colonic chyme and the values for the small intestine can give an appropriate lower bound for viscosity. The most appropriate data for our purposes come from the measurements made at low shear rate (e.g. 1 s^{-1}) and without any removal of large particles.

1.3.2 The Motility of the Colon

Understanding the motility of the colon is important in establishing appropriate boundary conditions for a mathematical model. In this section we consider the types of colonic motility and their prevalence as well as factors which affect these.

Transit of contents through the colon is not continuous [38] and is controlled through the motor activity of the colonic smooth muscle. It is widely accepted that there are two main types of contractile activity within the colon - propulsive contractions (mass movements) and non-propulsive contractions (segmental activity) [4, 8, 25, 43, 72].

In the colon the majority of contractions are segmental in nature [37, 47], particularly within the caecum and ascending colon. These are non-propulsive, rapid contractions of the circular muscle layer [25, 70] and they occur independently at adjacent sites within

the colon [71]. The frequency of these contractions is given by Misiewicz [43] as $2.5-3$ per minute, corresponding to an individual duration of $20-24$ s and a duration of $10-60$ s per contraction is given by Weisbrodt [71], which corresponds to a frequency of $1-6$ per minute. Gill et al. [22] investigated the contractile activity of colonic muscle *in vitro* and found a contractile frequency of 6.3 ± 0.6 per minute for the circular muscle in the right colon, significantly higher than that in the left colon of 3.4 ± 0.3 per minute. Segmental contractions serve to mix the luminal contents with colonic enzymes [72] and increase contact of material with the mucosa [70, 43], allowing absorption of water and electrolytes into the bloodstream. In addition contraction of the circular muscle slows transit through the colon [8, 43]. This delay should prove beneficial in terms of drug delivery, increasing the amount of time available for drug absorption; in particular it may mitigate against the lower surface area of the colon in comparison to the small intestine [70, 72]. Raised pressure within the lumen provides a measure of the forces exerted by the colonic muscle on the intraluminal contents [43] and provides a means of identifying segmental contractions [72]. Information on the pressure amplitudes of segmental contractions is generally consistent in the literature, with Misiewicz [43] quoting $10-60$ mmHg ($\sim 1.333-8$ kPa), Bassotti et al. [8] $5-50$ mmHg ($\sim 0.667-6.667$ kPa) and Weisbrodt [71] $10-50$ mmHg ($\sim 1.333-6.667$ kPa).

Mass movements are described as 'rare events', occurring approximately $1-4$ times per day in healthy subjects [70, 71]. The contraction of the longitudinal muscle is responsible for these propulsive mass movements [71] and from the transverse colon to the sigmoid colon these contractions predominate [25]. This type of motion has not been observed elsewhere in the GI tract and may be characterised as an intense and prolonged peristaltic wave [70]. During a propulsive contraction segmental contractions stop and a loss of haustrations may be observed; the colon is then subjected to a contraction of the longitudinal muscle that propels the contents of the lumen distally [71], by creating

a left-right pressure gradient [8]. After a mass movement has taken place, haustrations and contractions of the circular muscle return.

A second type of propulsive activity has been observed in the colon, termed peristaltic or antiperistaltic contractions depending on the direction of propulsion [70]. These type of contractions occur more frequently than mass movements and are also known as propagating sequences, of either 'high' or 'low' amplitude [4, 7, 8]. This classification by amplitude is not absolute and values as to what constitutes a high or low amplitude differ between authors and studies. Additionally high amplitude propagating contractions are sometimes used to mean the same as mass movements in the literature [8].

The lack of clear differentiation between types of activity need not be of concern in this project. Firstly, propagating contractions occur much less frequently than segmental ones and secondly, the segmental contractions of the ascending colon are the ones of interest in terms of successful drug delivery. This is because they serve to both mix the luminal material and delay its transit, thereby optimising the amount of fluid absorbed. Occasional propagating contractions may alter the situation significantly, this is something that could be investigated in future work. Overall, colonic motility is lower and less disruptive than that of the stomach and small intestine [38]. This reduces the stresses in the lumen which in turn helps to lower the rate of mucus removal. This, together with the likely lower sensitivity to mucus secretory stimuli, make colonic mucoadhesive residence time less rate-limited by mucus turnover than the upper regions of the gastrointestinal tract.

The response of colonic motor activity to various stimuli and variations in situation has been experimentally investigated. The main factors which seem to have been considered are response to meals and the sleep-wake cycle. Other considerations have included age, sex and disease.

It is generally accepted that colonic motor activity is increased after meals [4, 8, 43, 70,

63]; however, the type of activity affected is not completely clear. Mass movements may be stimulated by the ingestion of food [43], resulting in the distal transport of contents which allows the potential for further emptying from the small intestine [7]. Contrary to this though, Washington et al. [70] report that despite an almost immediate response to eating of the smooth colonic muscle, there was no emptying of the right colon. This is explained by an increase in non-propagating, rather than propagating, activity immediately after eating [70]. Indeed Bassotti et al. [8] describe the activation of the motor reflexes of both the proximal and distal colon within $1-3$ minutes of eating and report that this response, lasting $2-3$ hours, mainly increases the segmental activity. However, in a later study [7], Bassotti et al. found that the average number of low amplitude propagating contractions increased significantly in the two hours after a meal. In contrast to this Bampton et al. [4] found no overall increase in the frequency of low amplitude propagating sequences between two hours before and two hours after eating, instead they found an increase in the amplitude of these contractions. They also found a significant increase in the number of high amplitude propagating sequences after a meal, with numbers returning to base values three hours afterward.

The type of food consumed is also reported to affect colonic motility, with fat having a greater stimulant effect than either protein or carbohydrates [70]. A meal consisting purely of fat produces both an early ($10-40$ minutes) and a late ($70-90$ minutes) response; with simultaneous ingestion of protein the late response is lost whereas both responses are curtailed by the ingestion of amino acids [70].

The effect of the sleep-wake cycle on colonic motility is clearer than that of eating. It is well documented that sleep has a profound inhibitory effect on both propagating and non-propagating colonic motor activity [7, 43]. In addition to a decrease in activity during sleep there is a specific increase in activity upon waking [70], particularly that of a propagating nature [7].

Segmental activity is reportedly decreased in those suffering from diarrhoea and increased in those with constipation, whereas the opposite is the case with the frequency of mass movements [43]. Those suffering from chronic constipation also have a severely limited or absent motor response to eating, in both the proximal and distal colon [8] as well as a significantly lower response to wakening in comparison with controls [38].

Colonic motor activity is also thought to be affected by age, with the suggestion that segmental activity increases and propulsive activity decreases with age [8]. Both hormones and drugs can affect colonic motility, for example adrenaline and noradrenaline decrease the activity of smooth muscle and morphine delays transit through the caecum and ascending colon [70]. Studies involving women at different stages of the menstrual cycle and during pregnancy have also shown that progesterone may depress colonic motility [70].

Other factors may affect the actual transit of material, for example patients with ulcerative colitis have been found to have a significantly faster transit time than controls [38]. It is unclear as to what role, if any, gender plays in transit time with some studies showing no difference and others reporting a significantly faster transit time in women [70].

Gastric emptying and colonic transit are the major variables involved in the length of time it takes a drug to travel through the GI tract [72]. Whole bowel transit in healthy humans has been placed at $24-36$ hours, with a wide range of variation being shown and times being highly influenced by an individual's pattern of daily activity [70]. McConnell et al. [38], however, place colonic transit time at $6-48$ hours, with values greater than 70 hours reported. These results show that there is a wide range of variation in colonic transit within individuals; in fact there may be large variations even within one individual. As previously mentioned, the mucoadhesive approach can manipulate the transit time of a dosage form, thereby reducing this variability [68]. Wilson [72] breaks the colon down into regions in order to study the transit times of dosage forms. He reports times of $3-5$

hours for the ascending colon; $0.2 - 4$ hours for the transverse colon; and $5 - 72$ hours for the descending colon and sigmoid colon combined.

For the models we present in this thesis we do not consider the effects of factors such as eating or sleep. This may be taken into account in future work, for example by specifying the time of day that a dosage is taken or whether it is taken with food or without. The most important variable relating to colonic motility for our models is the frequency of the contractions. In addition the qualitative information gathered about segmental contractions allows us to choose a suitable mathematical function for the colonic wall and appropriate boundary conditions.

1.4 Existing Models of the Gastrointestinal Tract

The literature on existing models of the GI tract can be divided into roughly three types (with some overlap). These are:

1. artificial physical models;
2. mathematics based computational and theoretical models; and
3. imaging based computational models.

Relatively few of these models consider the colon but we should be able to gain some insight through other regions. The models have different investigative focus, depending on their type, the methods used and the interests of their creators.

Artificial Physical Models

In 1998, Macfarlane et al. [36] developed a three-stage compound continuous culture system to study the responses of human colonic bacteria to the transit time of fluid through the system, in particular the effect on bacterial concentration. The system was designed to mimic the main environmental and nutritional conditions affecting fermentation by

bacteria within the proximal and distal colons. Vessel 1 represents the proximal colon and vessels 2 and 3 represent the distal colon. They concluded that they had produced a useful model for the study, under different environmental and nutritional conditions, of large intestinal microorganisms. The purpose of this model was very different from our own and it did not attempt to take into account the geometry, motility or fluid dynamics within the colon.

A similar model of this kind, for studying the colonic bacterial environment, is that of Spratt et al. [61] from 2005; a three-stage tubular model. This model may be considered an extension of the previous one. The three stages represent the ascending, transverse and descending colons. According to Spratt et al., one key disadvantage of Macfarlane et al.'s model is the oversimplification of the fluid mixing processes due to the use of stirred reactors. This is improved on by the development of a membrane fermenter, with an aqueous solution on the outside used to control the removal of water and metabolites from the interior flow. They also aimed for a system where inlet flow rate and concentration, Reynolds number and total water flux were comparable with the true situation, with some success. Thus Spratt et al. not only considered the reproduction of the fermentation conditions but also some of the fluid dynamic aspects within the colon. Their model proved more representative than that of Macfarlane et al., although neither attempted to consider the effects of colonic motility.

Henry et al. [23] created what they described as an *'ex vivo'* gastric model, constructed using silicone, based on computed tomography (CT) scans of the human stomach. 3D computer models of the stomach were developed from these images and data such as wall thickness, surface area and volume measured. Silicone was identified as a suitable polymer, with similarly distensibility to that of the human stomach, to be used to create the model. The hollow gastric model was created using the computer model and then pressure-volume measurements were taken and compared to experimental values in the

literature, with reasonable results. The main aim of this study was to demonstrate the possibility of manipulating CT scans to obtain realistic models of the stomach, in terms of geometry, compliance and pressure-volume relationship, comparison with human data showed success in this aim.

The physical models reviewed have included two which considered fluid insofar as its bacterial content, but not its dynamics. These models both considered the colon, and considered it as three separate regions with different properties as opposed to just one. The other physical model investigated the solid properties of an organ, namely the stomach, with concerns similar to those we will encounter with the imaging based models.

Mathematics Based Models

Mathematics based models come in two forms: specific and general. General ones look at a mathematical problem that could have applications to the GI tract (and/or other areas of the body). For example Rao and Mishra [52] investigate the peristaltic transport of a power law fluid in a porous tube and Woollard et al. [73] develop a model for solute transport in a wavy walled channel. Both of these have potential applications to small intestinal fluid flow, with the 'wavy walls' representing the villi. Misra and Pandey [44] investigate the peristaltic flow of two layers of power law fluid through a cylindrical tube with the express purpose of providing a model for the study of the flow of chyme through the small intestine. A further study into the flow of chyme through the small intestine using a non-Newtonian fluid is that of Tripathi et al. [67], using a fractional generalised Burgers' fluid[1] with long wavelength and small Reynolds number assumptions. This type of analysis had already been performed using a non-fractional generalised Burgers' model

[1]The fractional generalised Burgers' model is given by

$$\left(1+\lambda_1^{\alpha}\frac{\partial^{\alpha}}{\partial t^{\alpha}}+\lambda_2^{\alpha}\frac{\partial^{2\alpha}}{\partial t^{2\alpha}}\right)\boldsymbol{\tau}=\left(1+\lambda_3^{\beta}\frac{\partial^{\beta}}{\partial t^{\beta}}+\lambda_4^{\beta}\frac{\partial^{2\beta}}{\partial t^{2\beta}}\right)\dot{\boldsymbol{\gamma}},$$

where $0<\alpha\leq\beta<1$ [67].

and Tripathi et al. found the results to be favourable, in terms of the transport of chyme, with the non-fractional model. GI specific papers are presented by Eastwood [16] and Macagno and Christensen [35]. Eastwood develops mathematical equations to describe the effects in the intestinal lumen of dietary fibre and Macagno and Christensen investigate the fluid mechanics, including the transport and mixing, of the duodenum.

In terms of specific models the oesophagus has received a reasonable amount of attention. Until Liao et al. [33] in 2004, most studies into oesophageal mechanics had considered it as a homogeneous one-layered structure. However the outer muscular layer and inner mucosal layer are significantly different [75] making this approach limited in understanding stress and strain distributions. Using images of snap-frozen rats' oesophagus, Liao et al. produced a two-layered finite element model of the solid mechanics. Adding the material constants for each layer allowed them to simulate deformations and calculate stress-strain distributions. A two-layered finite element model was also developed by Yang et al. [75] and published in 2006. This model additionally considers the effects of mucosal buckling, a phenomenon caused by the instability under active contraction of the inner mucosal layer [74]. The purpose of this study was to demonstrate the feasibility of using finite element analysis to simulate the peristaltic nature of transport through the oesophagus and the potential benefits of the relationship between the structures, functions and mechanical properties of the tissue. Both of these models consider only the material tissue properties and none of the properties of fluid within the lumen, the dynamics of flow or the coupling between the solid and fluid mechanics.

Also investigating the oesophagus is a study by Yassi et al. [76] from 2004. The focus of this research however, lies with the lower oesophagus sphincter (LOS) rather than the oesophageal tissue. The LOS regulates flow between the oesophagus and stomach; it allows contents to flow into the stomach and acts as a barrier to prevent flow from the high pressure environment of the stomach to the lower pressure environment of the oesoph-

agus. An ineffective LOS may cause gastroesophageal reflux or, at the other extreme, dysphagia (difficulty in swallowing) - both of which are serious disorders. In this study photographic images were used to obtain geometric information for the oesophagus and gastroesophageal junction. A volume mesh was then fitted to this data using an iterative finite element linear fitting process and the muscle fibre directions of each muscle layer were embedded into the finite element geometry. This study provides a model which can act as a framework for future research into the functional behaviour during swallowing of the oesophagus and LOS.

Dillard et al. [14] concern themselves with a different GI junction - the antroduodenal junction between the stomach and the duodenum of the small intestine. This junction is thought to play a role in the effectiveness of the mixing of gastric content and duodenal secretions, which in turn affects the absorption of the material once it reaches the small intestine. Computational models were designed to allow a variety of physical situations and mathematical parameters to be studied. These models were based on 2D channel flows which allow the inclusion of a prescribed moving boundary and the Navier-Stokes equations were used for flow, with the Reynolds number lying between 1 and 333. The fluid mixing was then quantified in each case using a scalar variance, where the variance of the scalar species concentration, ϕ, is calculated (see [14] for details). The main considerations of this study were the effects on transport and mixing of the pulsatile nature of gastric outflow, the geometric features of the junction and the interaction of these with the wall motion at the junction.

After developing a computational model of the stomach, Pal et al. [48] used it to present evidence for their discovery of a new phenomenon of gastric contractile activity, one which differs from the classical description of gastric emptying and has implications for drug delivery. In the classical description the proximal stomach (the fundus) stores chyme and supplies it the distal stomach (the antrum), with fundic contractions maintaining the

gastro-duodenal pressure difference. Chyme is then ground and mixed by the action of antral contractions before passing into the duodenum at a rate controlled by the pyloric sphincter. Pal et al. used MRI data from a healthy human stomach to create a geometrical model and quantified the fluid motion via the lattice Boltzmann method (see [48] for details), extended to incorporate moving boundary conditions. From here they used particle tracking to validate their idea of the existence of a 'Magenstrasse' or stomach road. This is a narrow path from the fundus, through the centre of the antrum, to the duodenum, allowing content to pass from the most proximal regions of the stomach to the intestines within 10 minutes. Their next step was to demonstrate that this path is created by antral contraction waves by 'turning off' this activity in their computer simulation. The implications for drug delivery are in terms of transit time, with those released on the Magenstrasse able to reach the small intestine within minutes as opposed to hours for those released off it.

All of the theoretical models mentioned are based on the fluid dynamics created by the wall motion and geometry, whereas the papers of Dillard et al. and Pal et al. are the only computational ones which consider any of the fluid dynamics within the GI tract. In addition there does appear to be a significant gap in fluid dynamics based models for the ileum and colon. Both of the studies by Dillard et al. and Pal et al. also indicate one of the main advantages of computer simulation and mathematical models over physical models: the ability to adjust parameters. This enables us to investigate different observable events and their causes as well as what the effects of changes caused by, for example disease, may be. The other studies of this type reviewed appear to mainly concentrate on the material tissue properties and geometry of an organ and their relation to functional behaviour.

Imaging Based Models

The most widely used method for studying the biomechanics of the GI tract is bag distension [19, 31]. In brief this method involves the insertion of an inflatable 'bag' into the relevant area using a specially designed probe containing a channel for the infusion and withdrawal of water. Data obtained via distension are traditionally based on pressure-volume measurements [31], however these cannot provide the information necessary for studying the mechanical properties of the organ tissue [19]. Several studies have indicated that the mechanoreceptors of the GI wall are not directly sensitive to pressure or volume [20], but instead are tension receptors [31]. In addition, symptoms associated with the GI tract are often related to disturbances in mechanical function and motility [19]. These factors, together with the complex GI geometry, have led researchers to develop techniques based on cross-sectional imaging in order to assess geometric variables [21].

One method of imaging, which has been shown to produce reliable measurements for pressure changes and the geometry of the gastroesophageal junction, is a device known as a functional lumen imaging probe (FLIP). McMahon et al. [41] used data gathered from this device to investigate the flow through the gastroesophageal junction using computational fluid dynamics (CFD). They created a 2D model using cross-sectional images from FLIP scans and used CFD to predict the flow during reflux, as well as obtaining information on shear stresses at the wall. The main purpose of this study was to illustrate the potential of numerical methods in developing a better understanding of the gastroesophageal junction.

The rest of the studies that we mention in this section follow a similar pattern to one another, with a significant overlap in contributors. They each follow the same general structure, although there are some slight variations. Their main interest in developing computer modelling techniques appears to have been the potential to predict regional stresses and strains in inaccessible locations [31]. First an imaging technique was used to produce cross-sectional images of a given region; a form of bag distension was used to

create distension of the organ under consideration. Various computer programmes were used for the processing of scanned images, with reslicing and surface smoothing used to reconstruct a 3D model. From here various geometric and biomechanical parameters were calculated and although these vary between studies, the main considerations were curvature, wall thickness, tension, stress and strain.

The human stomach was modelled using images acquired from real-time ultrasonography and a Fourier transform method for surface smoothing and curvature calculations [32]. The human rectum was modelled with assistance from MRI scans and a modified non-shrinking Gaussian smoothing method was used to reduce irregularities (see [20] for details). Ultrasound scans were used to create a model of the human duodenum, whose segments were then assessed for circularity [19]. The sigmoid colon was modelled using human MRI scans and again using the modified non-shrinking Gaussian smoothing method to reduce irregularities [21]. In summary, the regions for which computational models have been developed using the general method outlined in the previous paragraph are the stomach, duodenum, sigmoid colon and rectum.

An acknowledged weakness in each of these studies is the method used for calculating the wall stress. Wall tension, T, was calculated using Laplace's law [31]

$$P = T(\kappa_1 + \kappa_2), \tag{1.4.1}$$

where P is the transmural pressure and κ_1, κ_2 are the principal curvatures. From this the stress, σ, could be calculated via [31]

$$\sigma = \frac{T}{h}, \tag{1.4.2}$$

where h is the wall thickness. The authors note that Laplace's law is only valid for thin-walled structures and is based on an assumption of circularity [20] and therefore its use

is not ideal in this situation. However, Laplace's law as given in these papers is more generally used for calculating fluid surface tension and may be too simplistic to generalise this to solid mechanics.

Problems were also encountered when it came to measuring wall thickness and with edge detection. For example, the wall thickness at the thinnest part of the rectum was measured as less than 1mm, yet the pixel size in that study [20] was 0.39mm. This made detecting the exact edge in that region difficult, potentially leading to added inaccuracy in the calculations for wall thickness and stress. The general technique used in these studies requires a large amount of time for image post-processing and computer simulation, as well as some radiological expertise [19]. It is hoped that these problems may be overcome, or limited, in future by the improvement of scanners with better image resolution and increased speed of image acquisition as well as improved software for edge detection and 3D computation [20, 21, 19]. However, these studies have shown the potential benefits of this type of image based modelling and provided a framework and the motivation for further research and refinement of technique and equipment.

In the next section we discuss the type of model we intend to create and the ways in which we will go about this.

1.5 Considerations for Drug Delivery and the Mathematical Modelling of Colonic Motility

In the next three chapters we work towards the presentation of a preliminary analytical model of flow in the human ascending colon under segmental ('mixing') contractions. We attempt to replicate, where possible, the physical and rheological characteristics of the biological situation in our choice of parameter regimes. A model is necessarily an idealisation of the real system, based on our existing knowledge of the colon, digestive system and the fluids within it. Further assumptions will then be made to ensure that

mathematical solutions can be found, in particular the assumption of small amplitude wall movement.

We study the ascending colon due to its relevance in the absorption of drugs and nutrients. We consider only the activity of segmental contractions of the colonic muscle as these contractions are the most prevalent type of motor activity in this region and also the ones responsible for the mixing of luminal content. The efficiency of mixing affects how much material is exposed to the epithelial surface and hence how much is absorbed and the rate at which absorption occurs; this is of paramount importance when considering drug delivery. We do not directly consider the effects of absorption of fluid through the colonic epithelium on the flow, mixing or composition of the luminal fluid.

To simplify the problem we consider the fluid to be homogeneously distributed and the contractions driving the flow to be continuous. We also assume that the pipe modelling the colon and the flow within are axisymmetric, an assumption which is justified by the axisymmetric nature of the muscular contractions. We model the contractions of the circular muscle by prescribing the motion of the pipe boundary; we choose a standing wave of small amplitude in order to allow the use of perturbation techniques. A standing wave is chosen as this mimics the effects of mixing within the lumen created by the contraction of colonic muscle. Figure 1.5 provides a general depiction of the geometries we consider. In our models flow is induced only by the motion of the boundary; there is no underlying pressure gradient.

In chapter 2 we develop the analytical techniques to be used in this thesis by considering a one layer model of Newtonian fluid flow. We build on this model in chapter 3 by adding a second layer of fluid to our model; that is we have an inner core of Newtonian fluid surrounded by an outer layer of Oldroyd B fluid with a solid boundary. This represents the physical situation of chyme filling the intraluminal space, with a layer of viscoelastic mucus lining the intestinal epithelium. We also investigate the relative impor-

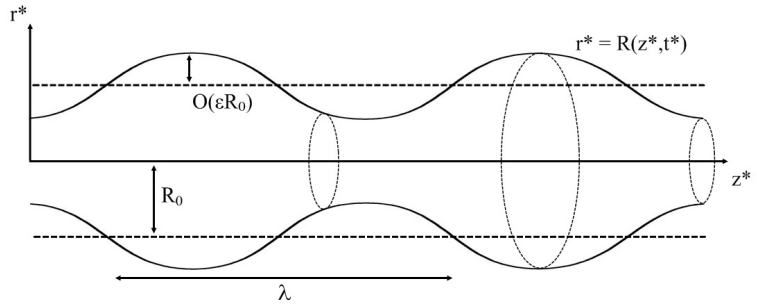

(a) One Fluid Layer.

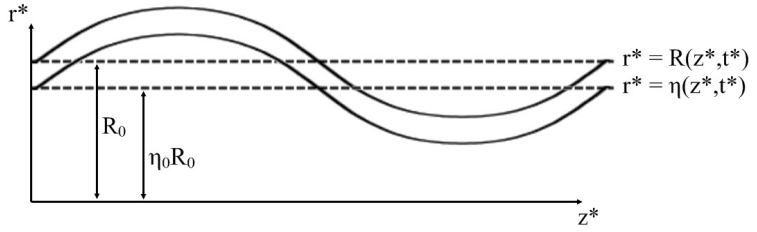

(b) Two Fluid Layers.

Figure 1.5: Two small amplitude models with (a) describing the one layer model and (b) describing the two layer model. In both (a) and (b) R_0 is the mean radius of the pipe, λ is the wavelength, $\varepsilon \ll 1$ is a nondimensional parameter describing the amplitude of the wave and the function $R(z^*, t^*)$ is the boundary function of the pipe, where t^* is time. Additionally in (b) η_0 is the mean position of the interface as a proportion of R_0 and $\eta(z^*, t^*)$ is the function for the free surface at the interface.

tance and influence of the parameters specific to the two layer model; for each parameter we choose a range of values and vary the given parameter within this range whilst leaving the other parameter values fixed.

In chapter 4 we consider a one layer model in which chyme is represented by a shear thinning Carreau rheological model. It is well established that intestinal chyme is a non-Newtonian fluid which displays shear thinning behaviour [13, 39, 64, 66]. Although a power law model would prove the simplest to handle we use the more general Carreau model due to the inadequacies of the power law model at low shear rates. We may expect low shear rates with our model because the flow is governed by the wall motion which is of small amplitude.

Finally, in chapter 5 we consider the delivery of a drug within the colon. To do this we utilise the method of Lagrangian particle tracking to determine the proportion of drug particles which will reach the colon wall over the length of one contraction. Then in section 5.2 we estimate values for the parameters in the fluid model and vary the value of these in order to ascertain the relative influence and importance of each parameter on delivery to the colonic epithelium. This level of analysis involving parameter variation is not possible with physical models and it is the ability to allow parameter variation which gives us the potential to be able to take the effects of disease into account.

Chapter 2

Modelling the Colon as a Pipe subject to Small Amplitude Wall Motion

In this chapter we create a model of mixing within the colon under the assumption of small amplitude boundary oscillations. We model the colon as an axisymmetric cylindrical pipe of arbitrary radius and length, with the single Newtonian fluid flow inside the pipe being driven by the motion of the pipe boundary. Due to the small amplitude of the oscillation we use perturbation theory to analyse the flow and mixing of chyme up to second order.

We are presently concerned with the mixing aspect of colonic motion and as such we choose to consider a standing wave representation of the boundary, rather than a travelling wave which would cause net transport. We set the equation of the pipe boundary as

$$R^*(z^*,t^*) = \mathcal{R}\left(R_0\sqrt{1+2\varepsilon\left(\mathrm{e}^{i\left(\frac{2\pi}{\lambda}z^*-\omega t^*\right)}+\mathrm{e}^{-i\left(\frac{2\pi}{\lambda}z^*+\omega t^*\right)}\right)}\right), \tag{2.0.1}$$

where $\mathcal{R}(z)$ represents the real part of z; R_0 is the mean radius of the pipe; the wavelength and angular frequency of the oscillation are given by λ and ω respectively; $\varepsilon \ll 1$ is a dimensionless parameter; z^* is axial distance along the pipe; and t^* is time. Typical values

for these parameters are given by $R_0 = 0.025$ m; $\omega = \pi/10$ rad/s; and $\lambda = 0.06$ m.

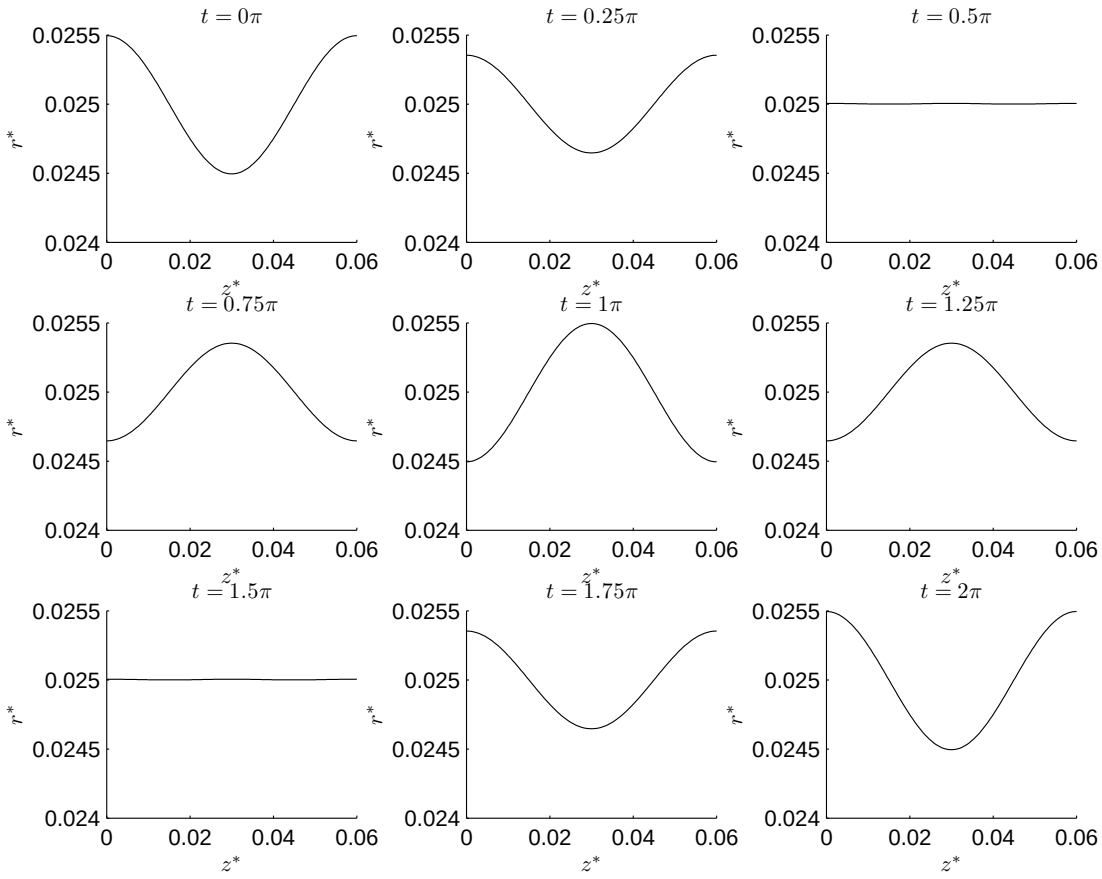

Figure 2.1: Plots of the shape of the boundary, equation (2.0.1) with the typical parameters above and $\varepsilon = 0.01$, for increasing t, where $t = \omega t^*$ represents the proportion of time through one contractile period of length $t = 2\pi$.

The (dimensional) equations for the velocity field of an incompressible Newtonian fluid in axisymmetric cylindrical polar co-ordinates are given by

$$\begin{aligned}
0 &= \frac{1}{r^*}\frac{\partial}{\partial r^*}(r^* u_r^*) + \frac{\partial u_z^*}{\partial z^*} \\
\rho\left(\frac{\partial u_r^*}{\partial t^*} + u_r^*\frac{\partial u_r^*}{\partial r^*} + u_z^*\frac{\partial u_r^*}{\partial z^*}\right) &= -\frac{\partial p^*}{\partial r^*} + \mu\left(\frac{1}{r^*}\frac{\partial}{\partial r^*}\left(r^*\frac{\partial u_r^*}{\partial r^*}\right) + \frac{\partial^2 u_r^*}{\partial z^{*2}} - \frac{u_r^*}{r^{*2}}\right) \\
\rho\left(\frac{\partial u_z^*}{\partial t^*} + u_r^*\frac{\partial u_z^*}{\partial r^*} + u_z^*\frac{\partial u_z^*}{\partial z^*}\right) &= -\frac{\partial p^*}{\partial z^*}\mu\left(\frac{1}{r^*}\frac{\partial}{\partial r^*}\left(r^*\frac{\partial u_z^*}{\partial r^*}\right) + \frac{\partial^2 u_z^*}{\partial z^{*2}}\right),
\end{aligned}$$

where $\boldsymbol{u^*} = (u_r^*(r^*, z^*, t^*), 0, u_z^*(r^*, z^*, t^*))$ is the velocity field, ρ is the density and μ is the dynamic viscosity of the fluid. In addition we have the boundary conditions

$$\begin{aligned} u_r^*(R^*, z^*, t^*) &= \dot{R}^*(z^*, t^*) \\ u_z^*(R^*, z^*, t^*) &= 0 \\ u_r^*(0, z^*, t^*) &= 0 \\ \frac{\partial u_z^*}{\partial r^*}(0, z^*, t^*) &= 0, \end{aligned}$$

where $\dot{R}^*$ is the first derivative of R^* with respect to time. These arise due to no slip at the boundary and symmetry about the z^*-axis.

We must now nondimensionalise our equations, for this we use the scalings

$$\boldsymbol{u^*} = \omega R_0 \boldsymbol{u};\ \boldsymbol{x^*} = R_0 \boldsymbol{x};\ \text{and } t^* = \frac{1}{\omega} t,$$

where ω is the angular frequency of the wall contractions and R_0 is the pipe radius. Additionally we scale pressure by

$$\begin{aligned} p^* &= \mu \omega p \\ &= \frac{\rho(\omega R_0)^2}{\mathrm{Re}} p \end{aligned}$$

where the Reynolds number is given by

$$\mathrm{Re} = \frac{\rho \omega R_0^2}{\mu}.$$

Taking an estimate for the viscosity and density of chyme of $\mu = 5$ Pa·s and $\rho = 1000$ kg/m^3 respectively, we calculate the Reynolds number as approximately 0.03927. We note that the reduced Reynolds number, given by $\varepsilon\mathrm{Re}$, is the one which gives the

physical balance between inertial and viscous forces. Tables 2.1 and 2.2 display the standard parameter values that we use in this chapter.

Table 2.1: Standard Dimensional Parameter Values.

Parameter	Description	Value	Units
R_0	Radius	0.025	m
ω	Contractile frequency	$\pi/10$	rad/s
λ	Wavelength	0.06	m
μ	Zero shear viscosity	5	Pa·s
ρ	Fluid density	1000	kg/m^3

Table 2.2: Standard Nondimensional Parameter Values.

Parameter	Value
Re	0.039
k	$5\pi/6$
ε	0.01

The nondimensional equations of motion are given by

$$\begin{aligned} 0 &= \frac{1}{r}\frac{\partial}{\partial r}(ru_r) + \frac{\partial u_z}{\partial z} \\ \mathrm{Re}\left(\frac{\partial u_r}{\partial t} + u_r\frac{\partial u_r}{\partial r} + u_z\frac{\partial u_r}{\partial z}\right) &= -\frac{\partial p}{\partial r} + \frac{1}{r}\frac{\partial}{\partial r}\left(r\frac{\partial u_r}{\partial r}\right) + \frac{\partial^2 u_r}{\partial z^2} - \frac{u_r}{r^2} \\ \mathrm{Re}\left(\frac{\partial u_z}{\partial t} + u_r\frac{\partial u_z}{\partial r} + u_z\frac{\partial u_z}{\partial z}\right) &= -\frac{\partial p}{\partial z} + \frac{1}{r}\frac{\partial}{\partial r}\left(r\frac{\partial u_z}{\partial r}\right) + \frac{\partial^2 u_z}{\partial z^2} \end{aligned}$$

with the nondimensional boundary conditions given by

$$\begin{aligned} u_r(R,z,t) &= \dot{R}(z,t) \\ u_z(R,z,t) &= 0 \\ u_r(0,z,t) &= 0 \\ \frac{\partial u_z}{\partial r}(0,z,t) &= 0, \end{aligned}$$

where

$$R(z,t) = \mathcal{R}\left(\sqrt{1 + 2\varepsilon\left(\mathrm{e}^{i(kz-t)} + \mathrm{e}^{-i(kz+t)}\right)}\right) \tag{2.0.2}$$

and $k = 2\pi R_0/\lambda$. Since $\varepsilon \ll 1$ we may expand (2.0.2) as follows

$$R(z,t) = \mathcal{R}\left(1 + \varepsilon\left(\mathrm{e}^{i(kz-t)} + \mathrm{e}^{-i(kz+t)}\right) - \frac{\varepsilon^2}{2}\left(\mathrm{e}^{2i(kz-t)} + \mathrm{e}^{-2i(kz+t)} + \mathrm{e}^{-2it}\right) + \mathrm{o}(\varepsilon^3)\right). \tag{2.0.3}$$

We expand the boundary and equation variables about $\varepsilon \ll 1$ so that

$$R(z,t) = 1 + \varepsilon R_1(z,t) + \varepsilon^2 R_2(z,t) + \mathrm{o}(\varepsilon^3) \tag{2.0.4}$$

$$p(r,z,t) = p_0 + \varepsilon p_1(r,z,t) + \varepsilon^2 p_2(r,z,t) + \mathrm{o}(\varepsilon^3), \tag{2.0.5}$$

note that p_0^* is the pressure at leading order, so that

$$p_0 = \frac{\mathrm{Re}}{\rho(\omega R_0)^2} p_0^*.$$

There is no flow at leading order since at O(1), $R = R_0$ and $p = p_0$, both of which are constant, since we assume there is no underlying pressure gradient at O(1). Therefore

$$u_r(r,z,t) = \varepsilon u_{r1}(r,z,t) + \varepsilon^2 u_{r2}(r,z,t) + \mathrm{o}(\varepsilon^3) \tag{2.0.6}$$

$$u_z(r,z,t) = \varepsilon u_{z1}(r,z,t) + \varepsilon^2 u_{z2}(r,z,t) + \mathrm{o}(\varepsilon^3). \tag{2.0.7}$$

In order to work out the boundary conditions we must expand u_r and u_z using Taylor

series. Firstly,

$$\begin{aligned} u_r(R,z,t) &= u_r(1+\varepsilon R_1+\varepsilon^2 R_2+\ldots,z,t) \\ &= u_r(1,z,t)+(\varepsilon R_1+\varepsilon^2 R_2+\ldots)\frac{\partial u_r}{\partial r}(1,z,t)+(\varepsilon R_1+\ldots)^2\frac{\partial^2 u_r}{\partial r^2}(1,z,t)+\ldots \\ &= \varepsilon u_{r1}(1,z,t)+\varepsilon^2\left(u_{r2}(1,z,t)+R_1(z,t)\frac{\partial u_{r1}}{\partial r}(1,z,t)\right)+\mathrm{o}(\varepsilon^3). \end{aligned}$$

Similarly,

$$\begin{aligned} u_z(R,z,t) &= \varepsilon u_{z1}(1,z,t)+\varepsilon^2\left(u_{z2}(1,z,t)+R_1(z,t)\frac{\partial u_{z1}}{\partial r}(1,z,t)\right)+\mathrm{o}(\varepsilon^3) \\ u_r(0,z,t) &= \varepsilon u_{r1}(0,z,t)+\varepsilon^2 u_{r2}(0,z,t)+\mathrm{o}(\varepsilon^3) \\ u_z(0,z,t) &= \varepsilon u_{z1}(0,z,t)+\varepsilon^2 u_{z2}(0,z,t)+\mathrm{o}(\varepsilon^3). \end{aligned}$$

Thus the boundary conditions are given by

$$\begin{aligned} \varepsilon u_{r1}(1,z,t)+\varepsilon^2\left(u_{r2}(1,z,t)+R_1(z,t)\frac{\partial u_{r1}}{\partial r}(1,z,t)\right) &= \varepsilon\dot{R}_1(z,t)+\varepsilon^2\dot{R}_2(z,t) \\ \varepsilon u_{z1}(1,z,t)+\varepsilon^2\left(u_{z2}(1,z,t)+R_1(z,t)\frac{\partial u_{z1}}{\partial r}(1,z,t)\right) &= 0 \\ \varepsilon u_{r1}(0,z,t)+\varepsilon^2 u_{r2}(0,z,t) &= 0 \\ \varepsilon\frac{\partial u_{z1}}{\partial r}(0,z,t)+\varepsilon^2\frac{\partial u_{z2}}{\partial r}(0,z,t) &= 0. \end{aligned}$$

In the next two sections we look at the equations at $\mathrm{O}(\varepsilon)$ and $\mathrm{O}(\varepsilon^2)$ respectively and determine solutions based on the boundary equation.

2.1 Flow at $\mathrm{O}(\varepsilon)$

We consider the flow at $\mathrm{O}(\varepsilon)$ using the results from the previous section. The equations of motion at $\mathrm{O}(\varepsilon)$ are given by

$$\begin{aligned} 0 &= \frac{1}{r}\frac{\partial}{\partial r}(ru_{r1}) + \frac{\partial u_{z1}}{\partial z} && (2.1.1)\\ \mathrm{Re}\frac{\partial u_{r1}}{\partial t} &= -\frac{\partial p_1}{\partial r} + \frac{1}{r}\frac{\partial}{\partial r}\left(r\frac{\partial u_{r1}}{\partial r}\right) + \frac{\partial^2 u_{r1}}{\partial z^2} - \frac{u_{r1}}{r^2} && (2.1.2)\\ \mathrm{Re}\frac{\partial u_{z1}}{\partial t} &= -\frac{\partial p_1}{\partial z} + \frac{1}{r}\frac{\partial}{\partial r}\left(r\frac{\partial u_{z1}}{\partial r}\right) + \frac{\partial^2 u_{z1}}{\partial z^2}. && (2.1.3) \end{aligned}$$

Using the Taylor series for u_r and u_z about both $R(z,t)$ and 0 we see that the boundary conditions at $\mathrm{O}(\varepsilon)$ are given by

$$\begin{aligned} u_{r1}(1,z,t) &= \dot{R}_1(z,t)\\ u_{z1}(1,z,t) &= 0\\ u_{r1}(0,z,t) &= 0\\ \frac{\partial u_{z1}}{\partial r}(0,z,t) &= 0. \end{aligned}$$

Using the equations for the boundary (2.0.3) and (2.0.4) we see that

$$R_1(z,t) = \mathcal{R}\left(\mathrm{e}^{i(kz-t)} + \mathrm{e}^{-i(kz+t)}\right).$$

For this type of boundary we assume that solutions are of the form

$$\begin{aligned} u_{r1}(r,z,t) &= \mathcal{R}\left(f_1(r)\mathrm{e}^{i(kz-t)} + f_2(r)\mathrm{e}^{-i(kz+t)}\right)\\ u_{z1}(r,z,t) &= \mathcal{R}\left(g_1(r)\mathrm{e}^{i(kz-t)} + g_2(r)\mathrm{e}^{-i(kz+t)}\right)\\ p_1(r,z,t) &= \mathcal{R}\left(h_1(r)\mathrm{e}^{i(kz-t)} + h_2(r)\mathrm{e}^{-i(kz+t)}\right). \end{aligned}$$

Substituting these into the O(ε) equations (2.1.1) - (2.1.3) and equating coefficients of $\mathrm{e}^{i(kz-t)}$ and $\mathrm{e}^{-i(kz+t)}$ we obtain the six equations

$$\begin{aligned}
0 &= \frac{\mathrm{d}f_1}{\mathrm{d}r} + \frac{1}{r}f_1(r) + ikg_1(r) && (2.1.4)\\
0 &= \frac{\mathrm{d}f_2}{\mathrm{d}r} + \frac{1}{r}f_2(r) - ikg_2(r) && (2.1.5)\\
0 &= -\frac{\mathrm{d}h_1}{\mathrm{d}r} + \frac{\mathrm{d}^2f_1}{\mathrm{d}r^2} + \frac{1}{r}\frac{\mathrm{d}f_1}{\mathrm{d}r} + \left(i\mathrm{Re} - k^2 - \frac{1}{r^2}\right)f_1(r) && (2.1.6)\\
0 &= -\frac{\mathrm{d}h_2}{\mathrm{d}r} + \frac{\mathrm{d}^2f_2}{\mathrm{d}r^2} + \frac{1}{r}\frac{\mathrm{d}f_2}{\mathrm{d}r} + \left(i\mathrm{Re} - k^2 - \frac{1}{r^2}\right)f_2(r) && (2.1.7)\\
0 &= -ikh_1(r) + \frac{\mathrm{d}^2g_1}{\mathrm{d}r^2} + \frac{1}{r}\frac{\mathrm{d}g_1}{\mathrm{d}r} + \left(i\mathrm{Re} - k^2\right)g_1(r) && (2.1.8)\\
0 &= ikh_2(r) + \frac{\mathrm{d}^2g_2}{\mathrm{d}r^2} + \frac{1}{r}\frac{\mathrm{d}g_2}{\mathrm{d}r} + \left(i\mathrm{Re} - k^2\right)g_2(r). && (2.1.9)
\end{aligned}$$

These equations suggest that we have $f = f_1 = f_2$, $g = g_1 = -g_2$ and $h = h_1 = h_2$. Rearranging (2.1.4) we find that

$$g(r) = \frac{i}{k}\left(\frac{\mathrm{d}f}{\mathrm{d}r} + \frac{f(r)}{r}\right) \tag{2.1.10}$$

and substituting this into (2.1.8) we obtain an expression for h,

$$h(r) = \frac{1}{k^2}\frac{\mathrm{d}^3f}{\mathrm{d}r^3} + \frac{2}{rk^2}\frac{\mathrm{d}^2f}{\mathrm{d}r^2} + \left(\frac{i\mathrm{Re}}{k^2} - \frac{1}{r^2k^2} - 1\right)\frac{\mathrm{d}f}{\mathrm{d}r} + \left(\frac{1}{r^3k^2} + \frac{i\mathrm{Re}}{rk^2} - \frac{1}{r}\right)f(r). \tag{2.1.11}$$

From this and (2.1.6) we obtain an ODE for f, given by

$$\begin{aligned}
0 = \frac{1}{k^2}\frac{\mathrm{d}^4f}{\mathrm{d}r^4} + \frac{2}{rk^2}\frac{\mathrm{d}^3f}{\mathrm{d}r^3} + \left(\frac{i\mathrm{Re}}{k^2} - \frac{3}{r^2k^2} - 2\right)\frac{\mathrm{d}^2f}{\mathrm{d}r^2} + \left(\frac{3}{r^3k^2} + \frac{i\mathrm{Re}}{rk^2} - \frac{2}{r}\right)\frac{\mathrm{d}f}{\mathrm{d}r}\\
+ \left(\frac{2}{r^2} - i\mathrm{Re}\left(1 + \frac{1}{r^2k^2}\right) + k^2 - \frac{3}{r^4k^2}\right)f(r).
\end{aligned} \tag{2.1.12}$$

Taking $A = i\mathrm{Re} - k^2$ for simplicity, the general solution of (2.1.12) is given by

$$f(r) = c_1 I_1(rk) + c_2 K_1(rk) + c_3 J_1(\sqrt{A}r) + c_4 K_1(-i\sqrt{A}r)$$

where J_α, I_α and K_α are Bessel functions of the first kind and modified Bessel functions of the first and second kind respectively.

We must now formulate our boundary conditions in terms of the function f. First we have $u_{r1}(1, z, t) = \dot{R}_1(z, t)$, now

$$\begin{aligned} \dot{R}_1(z,t) &= -i\left(\mathrm{e}^{i(kz-t)} + \mathrm{e}^{-i(kz+t)}\right) \\ u_{r1}(1,z,t) &= f(1)\left(\mathrm{e}^{i(kz-t)} + \mathrm{e}^{-i(kz+t)}\right), \end{aligned}$$

therefore we have

$$f(1) = -i.$$

Next we consider $u_{z1}(1, z, t) = 0$, which implies that we must have $g(1) = 0$. But this is the same as

$$g(1) = \frac{i}{k}\left(\frac{\mathrm{d}f}{\mathrm{d}r}(1) + f(1)\right) = 0,$$

i.e.

$$\frac{\mathrm{d}f}{\mathrm{d}r}(1) = i.$$

The condition $u_{r1}(0, z, t) = 0$ tells us that

$$f(0) = 0.$$

Finally we consider $\partial u_{z1}(0, z, t)/\partial r = 0$, so that $\mathrm{d}g(0)/\mathrm{d}r = 0$, but

$$\frac{\mathrm{d}g}{\mathrm{d}r} = \frac{i}{k}\left(\frac{\mathrm{d}^2 f}{\mathrm{d}r^2} + \frac{1}{r}\frac{\mathrm{d}f}{\mathrm{d}r} - \frac{1}{r^2}f(r)\right)$$

so that we have

$$\frac{\mathrm{d}^2 f}{\mathrm{d}r^2} + \frac{1}{r}\frac{\mathrm{d}f}{\mathrm{d}r} - \frac{1}{r^2} f(r) \to 0 \text{ as } r \to 0.$$

Thus, to summarise, the boundary conditions are given by

$$\begin{aligned} f(1) &= -i \\ \frac{\mathrm{d}f}{\mathrm{d}r}(1) &= i \\ f(0) &= 0 \\ \frac{\mathrm{d}^2 f}{\mathrm{d}r^2} + \frac{1}{r}\frac{\mathrm{d}f}{\mathrm{d}r} - \frac{1}{r^2} f(r) &\to 0 \text{ as } r \to 0. \end{aligned}$$

In order to determine the constants c_2 and c_4 we consider the behaviour of f and its derivatives as $r \to 0$, using the small argument expansions given for Bessel functions [2, p360,375]. Now

$$\begin{aligned} f(r) &\sim c_1 \frac{rk}{2} + c_2 \frac{1}{rk} + c_3 \frac{\sqrt{A}r}{2} + c_4 \frac{i}{\sqrt{A}r} \text{ as } r \to 0 \\ &\to c_2 \frac{1}{rk} + c_4 \frac{i}{\sqrt{A}r} \text{ as } r \to 0. \end{aligned}$$

In order to satisfy the condition $f(0) = 0$ we require

$$c_2 \frac{1}{k} + c_4 \frac{i}{\sqrt{A}} = 0, \text{ i.e. } c_2 = -\frac{ikc_4}{\sqrt{A}}.$$

We now consider the second condition at $r = 0$; differentiating $f(r)$ we have

$$\begin{aligned} \frac{\mathrm{d}f}{\mathrm{d}r} = c_1 k \left(I_0(rk) - \frac{I_1(rk)}{rk} \right) + c_2 k \left(-K_0(rk) - \frac{K_1(rk)}{rk} \right) \\ + c_3 \sqrt{A} \left(J_0(\sqrt{A}r) - \frac{J_1(\sqrt{A}r)}{\sqrt{A}r} \right) - i c_4 \sqrt{A} \\ \left(-K_0(-i\sqrt{A}r) - \frac{iK_1(-i\sqrt{A}r)}{\sqrt{A}r} \right), \end{aligned}$$

which leaves us with

$$\frac{\mathrm{d}f}{\mathrm{d}r} \sim c_1\frac{k}{2} + c_2 k\left(\ln(rk) - \frac{1}{(rk)^2}\right) + c_3\frac{\sqrt{A}}{2} - ic_4\sqrt{A}\left(\ln(-i\sqrt{A}r) + \frac{1}{Ar^2}\right)$$
$$\text{as } r \to 0.$$

Differentiating again we have

$$\frac{\mathrm{d}^2 f}{\mathrm{d}r^2} = c_1 k^2\left(-\frac{I_0(rk)}{rk} + I_1(rk) + \frac{2I_1(rk)}{(rk)^2}\right) + c_2 k^2\left(\frac{K_0(rk)}{rk} + K_1(rk) + \frac{2K_1(rk)}{(rk)^2}\right)$$
$$+c_3 A\left(-\frac{J_0(\sqrt{A}r)}{\sqrt{A}r} - J_1(\sqrt{A}r) + \frac{2J_1(\sqrt{A}r)}{Ar^2}\right) - c_4 A$$
$$\left(\frac{iK_0(-i\sqrt{A}r)}{\sqrt{A}r} + K_1(-i\sqrt{A}r) - \frac{2K_1(-i\sqrt{A}r)}{Ar^2}\right),$$

so that

$$\frac{\mathrm{d}^2 f}{\mathrm{d}r^2} \sim c_1\frac{k^3 r}{2} + c_2 k^2\left(-\frac{\ln(rk)}{rk} + \frac{1}{rk} + \frac{2}{(rk)^3}\right) - c_3\frac{\sqrt{A}^3 r}{2}$$
$$+c_4 A\left(\frac{i\ln(-i\sqrt{A}r)}{\sqrt{A}r} - \frac{i}{\sqrt{A}r} + \frac{2i}{(\sqrt{A}r)^3}\right)$$
$$\text{as } r \to 0.$$

Therefore as $r \to 0$,

$$\begin{aligned}\frac{\mathrm{d}^2 f}{\mathrm{d}r^2} + \frac{1}{r}\frac{\mathrm{d}f}{\mathrm{d}r} - \frac{1}{r^2}f(r) \sim c_1\frac{k^3 r}{2} + c_2 k^2\left(-\frac{\ln(rk)}{rk} + \frac{1}{rk} + \frac{2}{(rk)^3}\right) - c_3\frac{\sqrt{A}^3 r}{2} \\ + c_4 A\left(\frac{i\ln(-i\sqrt{A}r)}{\sqrt{A}r} - \frac{i}{\sqrt{A}r} + \frac{2i}{(\sqrt{A}r)^3}\right) + c_1\frac{k}{2r} \\ + c_2\frac{k}{r}\left(\ln(rk) - \frac{1}{(rk)^2}\right) + c_3\frac{\sqrt{A}}{2r} \\ - ic_4\frac{\sqrt{A}}{r}\left(\ln(-i\sqrt{A}r) + \frac{1}{Ar^2}\right) \\ - c_1\frac{k}{2r} - c_2\frac{1}{r^3 k} - c_3\frac{\sqrt{A}}{2r} - c_4\frac{i}{\sqrt{A}r^3},\end{aligned}$$

that is, as $r \to 0$,

$$\begin{aligned}\frac{\mathrm{d}^2 f}{\mathrm{d}r^2} + \frac{1}{r}\frac{\mathrm{d}f}{\mathrm{d}r} - \frac{1}{r^2}f(r) \;\to\; & \frac{1}{r}\Big(c_2 k - ic_4\sqrt{A} - c_2 k\ln(rk) + ic_4\sqrt{A}\ln(-i\sqrt{A}r) \\ & + c_2 k\ln(rk) - ic_4\sqrt{A}\ln(-i\sqrt{A}r)\Big) + \frac{1}{r^3} \\ & \left(\frac{2c_2}{k} + \frac{2ic_4}{\sqrt{A}} - \frac{c_2}{k} - \frac{ic_4}{\sqrt{A}} - \frac{c_2}{k} - \frac{ic_4}{\sqrt{A}}\right) \\ = \;& \frac{1}{r}\left(c_2 k - ic_4\sqrt{A}\right).\end{aligned}$$

In order to satisfy the condition $\mathrm{d}^2 f/\mathrm{d}r^2 + 1/r(\mathrm{d}f/\mathrm{d}r) - f(r)/r^2 \to 0$ as $r \to 0$, we require $c_2 k - ic_4\sqrt{A} = 0$, i.e.

$$c_2 = \frac{ic_4\sqrt{A}}{k}.$$

But in order to satisfy $f(0) = 0$ we require

$$c_2 = -\frac{ikc_4}{\sqrt{A}}.$$

Suppose that $c_4 \neq 0$, then

$$\begin{aligned} \frac{ic_4\sqrt{A}}{k} = -\frac{ikc_4}{\sqrt{A}} \quad &\Leftrightarrow \quad k^2 = -A = -i\mathrm{Re} + k^2 \\ &\Leftrightarrow \quad 0 = i\mathrm{Re}, \end{aligned}$$

in which case we require $\mathrm{Re} = 0$, but we wish this to remain arbitrary. Hence we set $c_4 = 0$ which means that $c_2 = 0$ and

$$f(r) = c_1 I_1(rk) + c_3 J_1(\sqrt{A}r). \tag{2.1.13}$$

Using (2.1.13) and its differentials together with (2.1.10) and (2.1.11) we find that

$$\begin{aligned} g(r) &= \frac{i\left(c_1 k I_0(rk) + c_3\sqrt{A}J_0(\sqrt{A}r)\right)}{k} \\ h(r) &= \frac{i\mathrm{Re}\ c_1 I_0(rk)}{k}. \end{aligned}$$

We now use the remaining two boundary conditions to determine the following matrix equation for c_1 and c_3,

$$\begin{pmatrix} I_1(k) & J_1(\sqrt{A}) \\ kI_0(k) - I_1(k) & \sqrt{A}J_0(\sqrt{A}) - J_1(\sqrt{A}) \end{pmatrix} \begin{pmatrix} c_1 \\ c_3 \end{pmatrix} = \begin{pmatrix} -i \\ i \end{pmatrix}. \tag{2.1.14}$$

Note that (2.1.14) may be solved analytically, however since this will not necessarily be the case in later problems we use MATLAB to determine c_1 and c_3 and plot solutions.

In this section we have considered the geometry of a pipe with arbitrary radius and length and small amplitude wave motion of the wall. The motion of the wall drives the flow of a Newtonian fluid contained within the pipe.

Figures 2.2 - 2.6 display a series of velocity and vorticity plots for various t with

fixed parameters. Recall $R_0 = 0.025$ m, $\omega = \pi/10$ rad/s, $\lambda = 0.06$ m, $\mu_0 = 5$ Pa·s, $\rho = 1000$ kg/m^3, and $\varepsilon = 0.01$. The flow of the interior fluid is slower at $t = 0$ and $t = \pi$ than at $t = \pi/2$ and $t = 3\pi/2$, this is because the wall is at rest for $t = k\pi$. Overall magnitude at the former times is of the order of tenths of microns per second (or tenths of millimetres per hour), whereas at the latter times it is of the order of tenths of millimetres per second (or tens of centimetres per hour).

Flow in the axial direction is antisymmetric about $z^* = 0.03$ m (i.e. half the wavelength) at each time step, due to the nature of the boundary. Radial flow is symmetric about $z^* = 0.03$ m, and for $t = 0, \pi$ (i.e. when the boundary is at rest) it is also symmetric about $r^* = R_0/2 = 0.0125$ m, with velocity magnitude symmetric about $z^* = 0.03$ m. In this sense flow in the negative and positive directions can be considered to 'balance' out over one wavelength at each time step.

In addition to the symmetries at each time step, the figures in this section display anti-symmetry in time over one cycle for u_r^*, u_z^* and the vorticity. For example, at $t = 0$ the plots for u_r^*, u_z^* and the vorticity all have equal magnitude but opposite direction to their respective plots at $t = \pi$ and similarly for $t = \pi/2$ compared with $t = 3\pi/2$. Together these points suggest that there is no overall transport through the pipe - this is a consequence of the boundary function, supporting our choice for R_1.

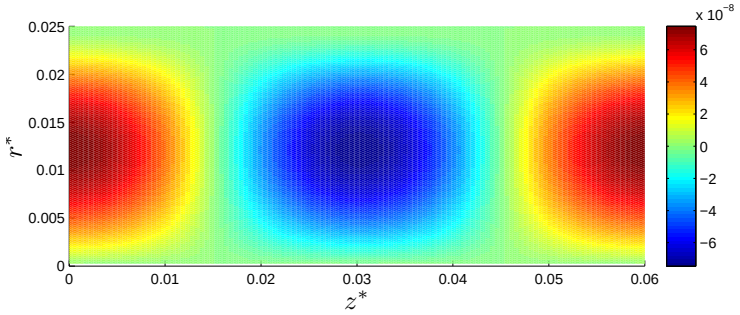

(a) $t = 0$ ($t^* = 0$ s)

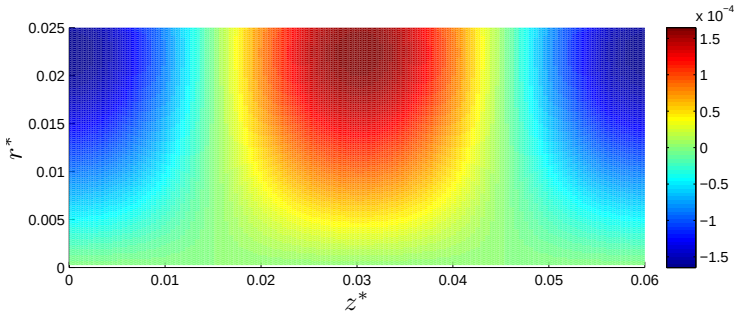

(b) $t = \pi/2$ ($t^* = 5$ s)

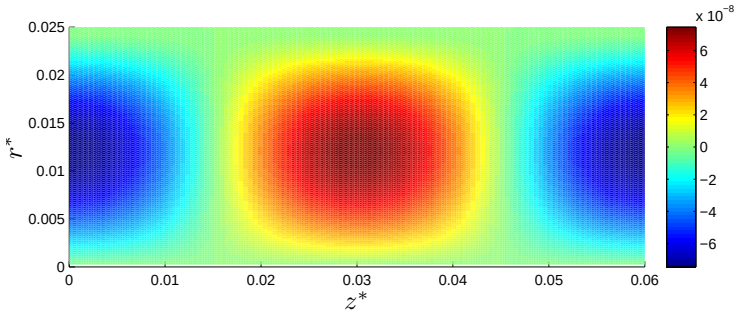

(c) $t = \pi$ ($t^* = 10$ s)

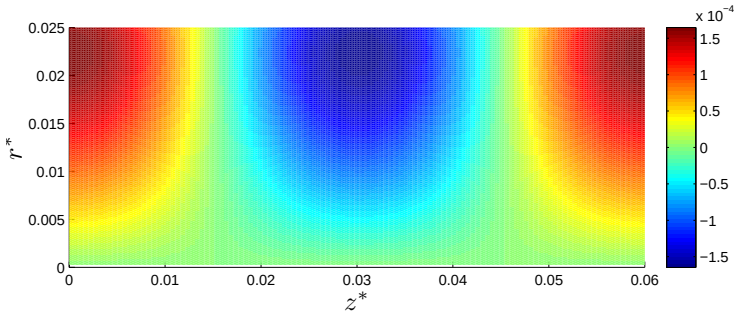

(d) $t = 3\pi/2$ ($t^* = 15$ s)

Figure 2.2: Colour plots of u_r^* (m/s) at O(ε) for the standard parameters, where r^* and z^* have units m. The colour scales differ between subplots in order to prevent detail being lost at the times with slower flow velocity.

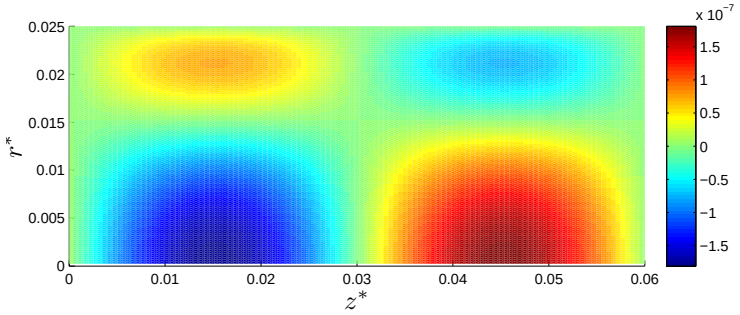

(a) $t = 0$ ($t^* = 0$ s)

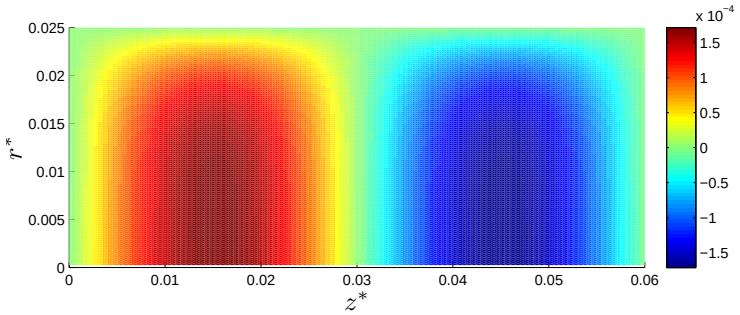

(b) $t = \pi/2$ ($t^* = 5$ s)

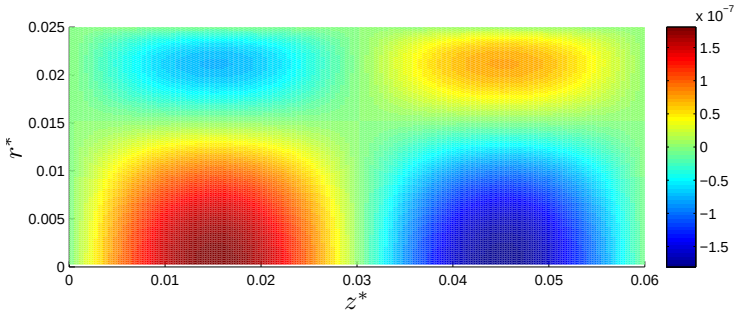

(c) $t = \pi$ ($t^* = 10$ s)

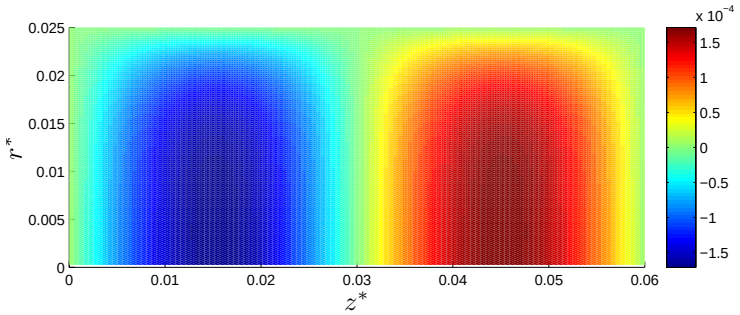

(d) $t = 3\pi/2$ ($t^* = 15$ s)

Figure 2.3: Colour plots of u_z^* (m/s) at O(ε) for the standard parameters, where r^* and z^* have units m. The colour scales differ between subplots in order to prevent detail being lost at the times with slower flow velocity.

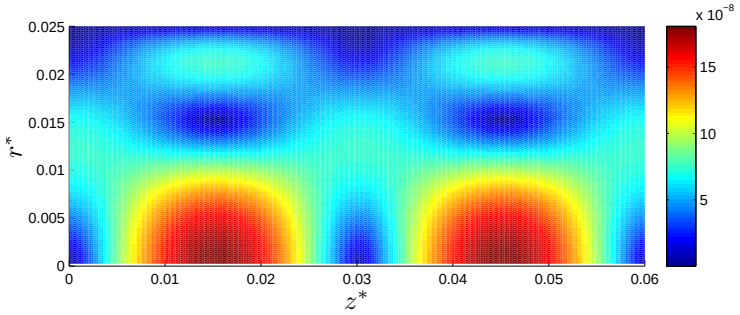

(a) $t = 0$ ($t^* = 0$ s)

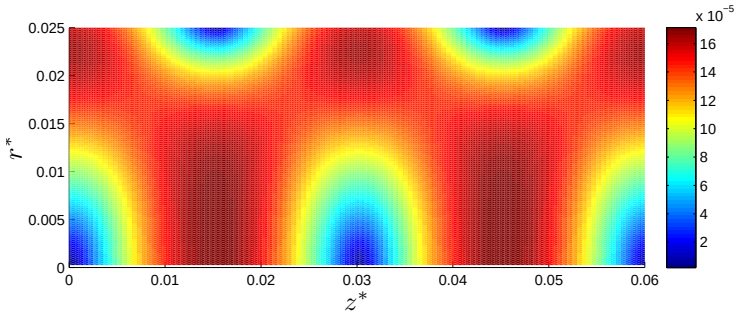

(b) $t = \pi/2$ ($t^* = 5$ s)

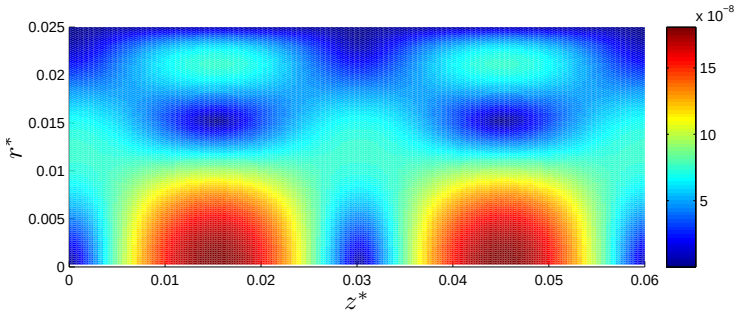

(c) $t = \pi$ ($t^* = 10$ s)

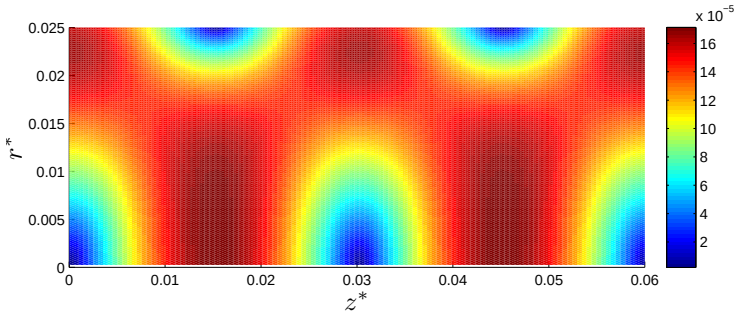

(d) $t = 3\pi/2$ ($t^* = 15$ s)

Figure 2.4: Magnitude of velocity (m/s) at O(ε) for the standard parameters, where r^* and z^* have units m. The colour scales differ between subplots in order to prevent detail being lost at the times with slower flow velocity.

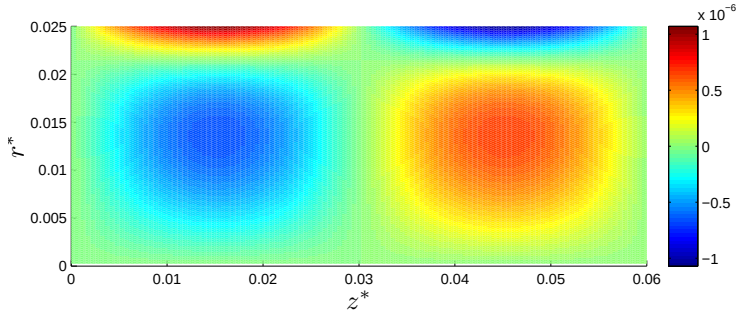

(a) $t = 0$ ($t^* = 0$ s)

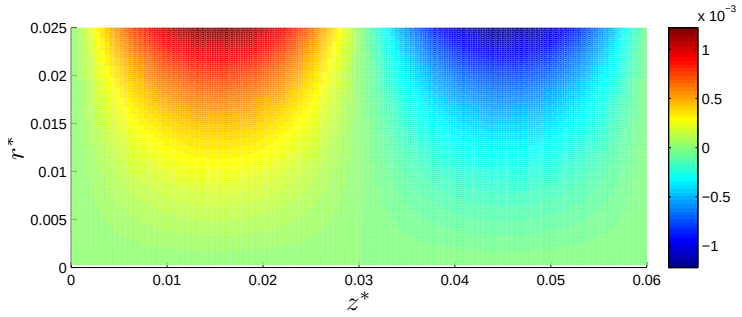

(b) $t = \pi/2$ ($t^* = 5$ s)

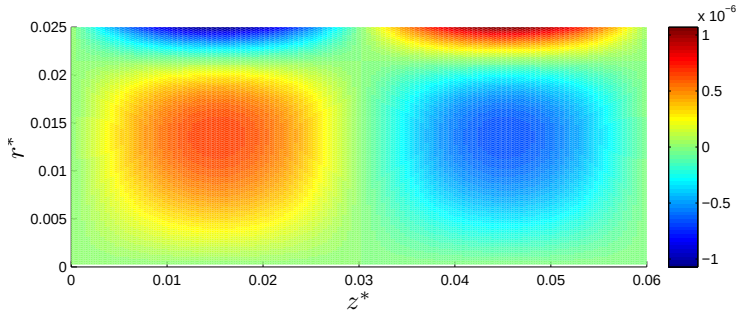

(c) $t = \pi$ ($t^* = 10$ s)

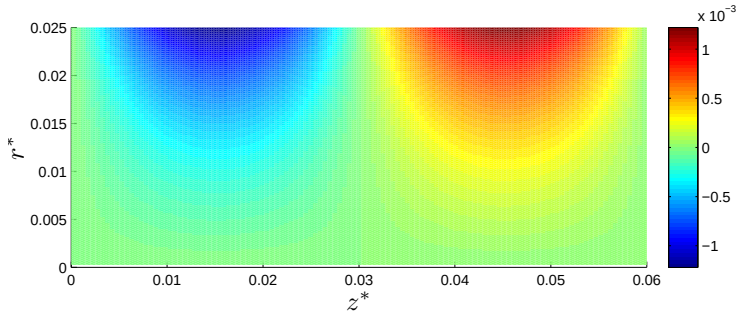

(d) $t = 3\pi/2$ ($t^* = 15$ s)

Figure 2.5: Vorticity of flow (s^{-1}) at $O(\varepsilon)$ for the standard parameters, where r^* and z^* have units m. The colour scales differ between subplots in order to prevent detail being lost at the times with lower vorticity.

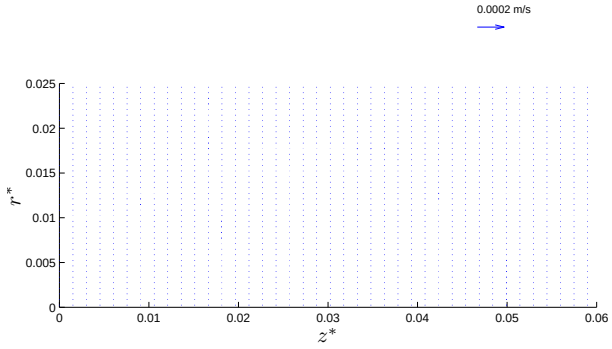

(a) $t = 0$ ($t^* = 0$ s)

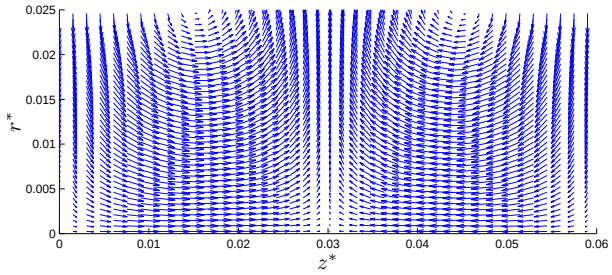

(b) $t = \pi/2$ ($t^* = 5$ s)

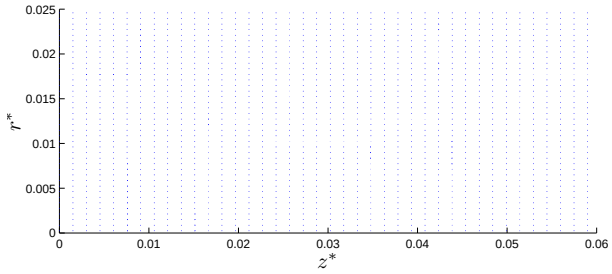

(c) $t = \pi$ ($t^* = 10$ s)

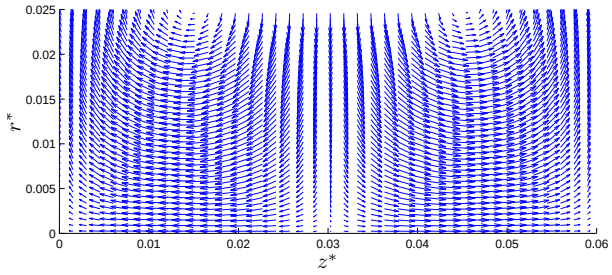

(d) $t = 3\pi/2$ ($t^* = 15$ s)

Figure 2.6: Velocity fields at O(ε) for the standard parameters at four time instants, where r^* and z^* have units m.

2.2 Flow up to $\mathrm{O}(\varepsilon^2)$

We now consider the flow at $\mathrm{O}(\varepsilon^2)$ using the results from earlier in this chapter. The equations of motion at $\mathrm{O}(\varepsilon^2)$ are given by

$$\begin{aligned}
0 &= \frac{1}{r}\frac{\partial}{\partial r}(ru_{r2}) + \frac{\partial u_{z2}}{\partial z} && (2.2.1)\\
\mathrm{Re}\left(\frac{\partial u_{r2}}{\partial t} + u_{r1}\frac{\partial u_{r1}}{\partial r} + u_{z1}\frac{\partial u_{r1}}{\partial z}\right) &= -\frac{\partial p_2}{\partial r} + \frac{1}{r}\frac{\partial u_{r2}}{\partial r} - \frac{u_{r2}}{r^2} + \frac{\partial^2 u_{r2}}{\partial r^2} + \frac{\partial^2 u_{r2}}{\partial z^2} && (2.2.2)\\
\mathrm{Re}\left(\frac{\partial u_{z2}}{\partial t} + u_{r1}\frac{\partial u_{z1}}{\partial r} + u_{z1}\frac{\partial u_{z1}}{\partial z}\right) &= -\frac{\partial p_2}{\partial z} + \frac{1}{r}\frac{\partial u_{z2}}{\partial r} + \frac{\partial^2 u_{z2}}{\partial r^2} + \frac{\partial^2 u_{z2}}{\partial z^2}, && (2.2.3)
\end{aligned}$$

where u_{r1}, u_{z1} are known from the previous section. The above equations differ from the ones at $\mathrm{O}(\varepsilon)$ in that they include some inertial effects.

Using the Taylor series for u_r and u_z about both $R(z,t)$ and 0 we see that the boundary conditions at $\mathrm{O}(\varepsilon^2)$ are given by

$$\begin{aligned}
u_{r2}(1,z,t) &= \dot{R}_2(z,t) - R_1(z,t)\frac{\partial u_{r1}}{\partial r}(1,z,t)\\
u_{z2}(1,z,t) &= -R_1(z,t)\frac{\partial u_{z1}}{\partial r}(1,z,t)\\
u_{r2}(0,z,t) &= 0\\
\frac{\partial u_{z2}}{\partial r}(0,z,t) &= 0.
\end{aligned}$$

Using the equations for the boundary (2.0.3) and (2.0.4) we see that

$$R_2 = \mathcal{R}\left(-\frac{1}{2}\left(\mathrm{e}^{2i(kz-t)} + \mathrm{e}^{-2i(kz+t)} + 2\mathrm{e}^{-2it}\right)\right).$$

For this type of boundary we assume solutions of the form

$$\begin{aligned} u_{r2}(r,z,t) &= \mathcal{R}\left(\alpha_1(r)\mathrm{e}^{2i(kz-t)} + \alpha_2(r)\mathrm{e}^{-2i(kz+t)} + \alpha_3(r)\mathrm{e}^{-2it}\right) \\ u_{z2}(r,z,t) &= \mathcal{R}\left(\beta_1(r)\mathrm{e}^{2i(kz-t)} + \beta_2(r)\mathrm{e}^{-2i(kz+t)} + \beta_3(r)\mathrm{e}^{-2it}\right) \\ p_2(r,z,t) &= \mathcal{R}\left(\delta_1(r)\mathrm{e}^{2i(kz-t)} + \delta_2(r)\mathrm{e}^{-2i(kz+t)} + \delta_3(r)\mathrm{e}^{-2it}\right). \end{aligned}$$

Substituting these, along with those for u_{r1} and u_{z1}, into the $\mathrm{O}(\varepsilon^2)$ equations (2.2.1) - (2.2.3) and equating coefficients of $\mathrm{e}^{2i(kz-t)}$, $\mathrm{e}^{-2i(kz+t)}$ and e^{-2it} we obtain the nine equations

$$\frac{\mathrm{d}\alpha_1}{\mathrm{d}r} + \frac{\alpha_1}{r} + 2ik\beta_1 = 0 \tag{2.2.4}$$

$$\frac{\mathrm{d}\alpha_2}{\mathrm{d}r} + \frac{\alpha_2}{r} - 2ik\beta_2 = 0 \tag{2.2.5}$$

$$\frac{\mathrm{d}\alpha_3}{\mathrm{d}r} + \frac{\alpha_3}{r} = 0 \tag{2.2.6}$$

$$-2i\alpha_1 + f\frac{\mathrm{d}f}{\mathrm{d}r} + ikfg = \frac{1}{\mathrm{Re}}\left(-\frac{\mathrm{d}\delta_1}{\mathrm{d}r} + \frac{1}{r}\frac{\mathrm{d}\alpha_1}{\mathrm{d}r} - \frac{\alpha_1}{r^2} + \frac{\mathrm{d}^2\alpha_1}{\mathrm{d}r^2} - 4k^2\alpha_1\right) \tag{2.2.7}$$

$$-2i\alpha_2 + f\frac{\mathrm{d}f}{\mathrm{d}r} + ikfg = \frac{1}{\mathrm{Re}}\left(-\frac{\mathrm{d}\delta_2}{\mathrm{d}r} + \frac{1}{r}\frac{\mathrm{d}\alpha_2}{\mathrm{d}r} - \frac{\alpha_2}{r^2} + \frac{\mathrm{d}^2\alpha_2}{\mathrm{d}r^2} - 4k^2\alpha_2\right) \tag{2.2.8}$$

$$-2i\alpha_3 + 2f\frac{\mathrm{d}f}{\mathrm{d}r} - 2ikfg = \frac{1}{\mathrm{Re}}\left(-\frac{\mathrm{d}\delta_3}{\mathrm{d}r} + \frac{1}{r}\frac{\mathrm{d}\alpha_3}{\mathrm{d}r} - \frac{\alpha_3}{r^2} + \frac{\mathrm{d}^2\alpha_3}{\mathrm{d}r^2}\right) \tag{2.2.9}$$

$$-2i\beta_1 + f\frac{\mathrm{d}g}{\mathrm{d}r} + ikg^2 = \frac{1}{\mathrm{Re}}\left(-2ik\delta_1 + \frac{1}{r}\frac{\mathrm{d}\beta_1}{\mathrm{d}r} + \frac{\mathrm{d}^2\beta_1}{\mathrm{d}r^2} - 4k^2\beta_1\right) \tag{2.2.10}$$

$$-2i\beta_2 - f\frac{\mathrm{d}g}{\mathrm{d}r} - ikg^2 = \frac{1}{\mathrm{Re}}\left(2ik\delta_2 + \frac{1}{r}\frac{\mathrm{d}\beta_2}{\mathrm{d}r} + \frac{\mathrm{d}^2\beta_2}{\mathrm{d}r^2} - 4k^2\beta_2\right) \tag{2.2.11}$$

$$-2i\beta_3 = \frac{1}{\mathrm{Re}}\left(\frac{1}{r}\frac{\mathrm{d}\beta_3}{\mathrm{d}r} + \frac{\mathrm{d}^2\beta_3}{\mathrm{d}r^2}\right). \tag{2.2.12}$$

These equations suggest that we have $\alpha = \alpha_1 = \alpha_2$, $\beta = \beta_1 = -\beta_2$, $\delta = \delta_1 = \delta_2$ and three ODEs to find α_3, β_3 and δ_3.

Now, solving (2.2.6) gives us

$$\alpha_3 = \frac{a}{r}, \tag{2.2.13}$$

solving (2.2.12) gives us

$$\beta_3 = b_1 J_0(r\sqrt{2i\mathrm{Re}}) + b_2 K_0(r\sqrt{2i\mathrm{Re}}),$$

and solving (2.2.9), together with (2.2.13), gives us

$$\delta_3 = c + \mathrm{Re}\left(2ia\ln r - 2\int_0^r f\frac{\mathrm{d}f}{\mathrm{d}r'}\,\mathrm{d}r' + 2ik\int_0^r fg\,\mathrm{d}r'\right), \tag{2.2.14}$$

where a, b_1, b_2 and c are constants to be determined. Thus our solutions may now be written as

$$\begin{aligned}
u_{r2}(r,z,t) &= \mathcal{R}\left(\alpha(r)\left(\mathrm{e}^{2i(kz-t)} + \mathrm{e}^{-2i(kz+t)}\right) + \frac{a}{r}\mathrm{e}^{-2it}\right)\\
u_{r2}(r,z,t) &= \mathcal{R}\left(\beta(r)\left(\mathrm{e}^{2i(kz-t)} - \mathrm{e}^{-2i(kz+t)}\right) + \left(b_1 J_0(r\sqrt{2i\mathrm{Re}}) + b_2 K_0(r\sqrt{2i\mathrm{Re}})\right)\mathrm{e}^{-2it}\right)\\
p_2(r,z,t) &= \mathcal{R}\left(\delta(r)\left(\mathrm{e}^{2i(kz-t)} + \mathrm{e}^{-2i(kz+t)}\right) + \delta_3(r)\mathrm{e}^{-2it}\right),
\end{aligned}$$

where $\delta_3(r)$ is given by equation (2.2.14).

Rearranging (2.2.4) we find that

$$\beta(r) = \frac{i}{2k}\left(\frac{\mathrm{d}\alpha}{\mathrm{d}r} + \frac{\alpha(r)}{r}\right) \tag{2.2.15}$$

and substituting this into (2.2.10) we obtain an expression for δ,

$$\begin{aligned}
\delta(r) = \frac{1}{4k^2}\frac{\mathrm{d}^3\alpha}{\mathrm{d}r^3} + \frac{1}{2rk^2}\frac{\mathrm{d}^2\alpha}{\mathrm{d}r^2} + \left(\frac{i\mathrm{Re}}{2k^2} - \frac{1}{4r^2k^2} - 1\right)\frac{\mathrm{d}\alpha}{\mathrm{d}r} + \left(\frac{1}{4r^3k^2} + \frac{i\mathrm{Re}}{2rk^2} - \frac{1}{r}\right)\alpha(r)\\
+\frac{\mathrm{Re}}{2}\left(\frac{i}{k}f\frac{\mathrm{d}g}{\mathrm{d}r} - g^2\right).
\end{aligned}$$

Using this and (2.2.7) we obtain an ODE for α, given by

$$\begin{aligned}\frac{1}{4k^2}\frac{\mathrm{d}^4\alpha}{\mathrm{d}r^4}+\frac{1}{2k^2r}\frac{\mathrm{d}^3\alpha}{\mathrm{d}r^3}+\left(\frac{i\mathrm{Re}}{2k^2}-\frac{3}{4k^2r^2}-2\right)\frac{\mathrm{d}^2\alpha}{\mathrm{d}r^2}+\left(\frac{3}{4k^2r^3}+\frac{i\mathrm{Re}}{2k^2r}-\frac{2}{r}\right)\frac{\mathrm{d}\alpha}{\mathrm{d}r}\\ +\left(4k^2+\frac{2}{r^2}-i\mathrm{Re}\left(\frac{1}{2k^2r^2}+2\right)-\frac{3}{4k^2r^4}\right)\alpha\\ +\mathrm{Re}\left(\frac{i}{2k}\left(f\frac{\mathrm{d}^2g}{\mathrm{d}r^2}+\frac{\mathrm{d}f}{\mathrm{d}r}\frac{\mathrm{d}g}{\mathrm{d}r}\right)-g\frac{\mathrm{d}g}{\mathrm{d}r}+f\frac{\mathrm{d}f}{\mathrm{d}r}+ikgf\right)=0.\end{aligned}\tag{2.2.16}$$

In order to solve this we will utilise a Lobatto IIIa finite difference formula implemented via MATLAB's bvp4c algorithm; given a system of ODEs of the form $\boldsymbol{y}' = \boldsymbol{F}(x, \boldsymbol{y})$ on the interval $[a, b]$, bvp4c finds a solution subject to appropriate boundary conditions of the form $\boldsymbol{G}(\boldsymbol{y}(a), \boldsymbol{y}(b)) = \boldsymbol{0}$. First however we must determine appropriate boundary conditions in terms of α.

We begin with the conditions on u_{r2}. We recall that

$$u_{r2}(r,z,t)=\mathcal{R}\left(\alpha(r)\left(\mathrm{e}^{2i(kz-t)}+\mathrm{e}^{-2i(kz+t)}\right)+\frac{a}{r}\mathrm{e}^{-2it}\right);$$

now $u_{r2}|_{r=0} = 0$, hence we must set $a = 0$, leaving

$$\alpha(0)\left(\mathrm{e}^{2i(kz-t)}+\mathrm{e}^{-2i(kz+t)}\right)=0$$

from which we deduce $\alpha(0) = 0$. The second condition is given by

$$u_{r2}(1,z,t)=\dot{R}_2(z,t)-R_1(z,t)\frac{\partial u_{r1}}{\partial r}(1,z,t),$$

now

$$\begin{aligned}R_1\left.\frac{\partial u_{r1}}{\partial r}\right|_{r=1} &= \frac{\mathrm{d}f}{\mathrm{d}r}(1)\left(\mathrm{e}^{2i(kz-t)}+\mathrm{e}^{-2i(kz+t)}+2\mathrm{e}^{-2it}\right)\\ &= i\left(\mathrm{e}^{2i(kz-t)}+\mathrm{e}^{-2i(kz+t)}+2\mathrm{e}^{-2it}\right)\end{aligned}$$

and

$$\dot{R}_2 = i\left(\mathrm{e}^{2i(kz-t)} + \mathrm{e}^{-2i(kz+t)} + 2\mathrm{e}^{-2it}\right),$$

thus

$$\dot{R}_2 - R_1 \left.\frac{\partial u_{r1}}{\partial r}\right|_{r=1} = 0,$$

i.e. $u_{r2}|_{r=1} = 0$. This leaves us with $\alpha(1) = 0$.

Next we look at the conditions on u_{z2}. At $r = 0$, $\partial u_{z2}/\partial r = 0$, but

$$\frac{\partial u_{z2}}{\partial r} = \left(-b_1\sqrt{2i\mathrm{Re}}J_1(r\sqrt{2i\mathrm{Re}}) + ib_2\sqrt{2i\mathrm{Re}}K_1(-ir\sqrt{2i\mathrm{Re}})\right)\mathrm{e}^{-2it} + \frac{\mathrm{d}\beta}{\mathrm{d}r}\left(\mathrm{e}^{2i(kz-t)} - \mathrm{e}^{-2i(kz+t)}\right)$$

therefore we must consider the small argument expansions for Bessel functions [2, p360,375]. As $r \to 0$

$$\begin{aligned} J_1(r\sqrt{2i\mathrm{Re}}) &\sim \frac{\sqrt{2i\mathrm{Re}}}{2}r \\ K_1(-ir\sqrt{2i\mathrm{Re}}) &\sim \frac{i}{r\sqrt{2i\mathrm{Re}}}. \end{aligned}$$

This suggests that we must take $b_2 = 0$ and that $b_1 J_1(0) = 0$, leaving

$$\frac{\mathrm{d}\beta}{\mathrm{d}r}(0)\left(\mathrm{e}^{2i(kz-t)} - \mathrm{e}^{-2i(kz+t)}\right) = 0,$$

i.e.

$$\frac{\mathrm{d}\beta}{\mathrm{d}r}(0) = 0.$$

Now

$$\frac{\mathrm{d}\beta}{\mathrm{d}r} = \frac{i}{2k}\left(\frac{\mathrm{d}^2\alpha}{\mathrm{d}r^2} + \frac{1}{r}\frac{\mathrm{d}\alpha}{\mathrm{d}r} - \frac{\alpha}{r}\right)$$

thus we have

$$\frac{\mathrm{d}^2\alpha}{\mathrm{d}r^2} + \frac{1}{r}\frac{\mathrm{d}\alpha}{\mathrm{d}r} - \frac{\alpha}{r} \to 0 \text{ as } r \to 0.$$

Finally we have

$$\begin{aligned} u_{z2}|_{r=1} &= -R_1 \left.\frac{\partial u_{z1}}{\partial r}\right|_{r=1} \\ &= -\frac{\mathrm{d}g}{\mathrm{d}r}(1)\left(\mathrm{e}^{2i(kz-t)} - \mathrm{e}^{-2i(kz+t)}\right), \end{aligned}$$

but

$$\begin{aligned} \frac{\mathrm{d}g}{\mathrm{d}r}(1) &= \frac{i}{k}\left(\frac{\mathrm{d}^2 f}{\mathrm{d}r^2}(1) + \frac{\mathrm{d}f}{\mathrm{d}r}(1) - f(1)\right) \\ &= \frac{i}{k}\frac{\mathrm{d}^2 f}{\mathrm{d}r^2}(1) - \frac{2}{k}, \end{aligned}$$

where f is known, therefore

$$\beta(1)\left(\mathrm{e}^{2i(kz-t)} - \mathrm{e}^{-2i(kz+t)}\right) - \left(b_1\sqrt{2i\mathrm{Re}}J_1(\sqrt{2i\mathrm{Re}})\right)\mathrm{e}^{-2it} = \left(-\frac{i}{k}\frac{\mathrm{d}^2 f}{\mathrm{d}r^2}(1) + \frac{2}{k}\right)\left(\mathrm{e}^{2i(kz-t)} - \mathrm{e}^{-2i(kz+t)}\right).$$

Equating coefficients of $\mathrm{e}^{2i(kz-t)} - \mathrm{e}^{-2i(kz+t)}$ and e^{-2it} we have

$$\begin{aligned} b_1 &= 0 \\ \beta(1) &= -\frac{i}{k}\frac{\mathrm{d}^2 f}{\mathrm{d}r^2}(1) + \frac{2}{k}. \end{aligned}$$

Using equation (2.2.15), together with $\alpha(0) = 0$, we see that the latter of these conditions is equivalent to

$$\frac{\mathrm{d}\alpha}{\mathrm{d}r}(1) = -2\frac{\mathrm{d}^2 f}{\mathrm{d}r^2}(1) - 4i.$$

In summary, the four boundary conditions are given by

$$\begin{aligned}
\alpha(1) &= 0 \\
\frac{\mathrm{d}\alpha}{\mathrm{d}r}(1) &= -2\frac{\mathrm{d}^2 f}{\mathrm{d}r^2}(1) - 4i \\
\alpha(0) &= 0 \\
\frac{\mathrm{d}^2\alpha}{\mathrm{d}r^2} + \frac{1}{r}\frac{\mathrm{d}\alpha}{\mathrm{d}r} - \frac{1}{r^2}\alpha(r) &\to 0 \text{ as } r \to 0.
\end{aligned}$$

The first three of these conditions are compatible with using bvp4c, however we must simplify the fourth. To this end we consider the behaviour of $\mathrm{d}^2\alpha/\mathrm{d}r^2 + 1/r(\mathrm{d}\alpha/\mathrm{d}r) - \alpha(r)/r^2$ for small values of r. Now, as $r \to 0$

$$\begin{aligned}
\alpha(r) &\sim \alpha(0) + r\frac{\mathrm{d}\alpha}{\mathrm{d}r}(0) + \frac{r^2}{2}\frac{\mathrm{d}^2\alpha}{\mathrm{d}r^2}(0) + \dots \\
\frac{\mathrm{d}\alpha}{\mathrm{d}r}(r) &\sim \frac{\mathrm{d}\alpha}{\mathrm{d}r}(0) + r\frac{\mathrm{d}^2\alpha}{\mathrm{d}r^2}(0) + \dots \\
\frac{\mathrm{d}^2\alpha}{\mathrm{d}r^2}(r) &\sim \frac{\mathrm{d}^2\alpha}{\mathrm{d}r^2}(0) + \dots,
\end{aligned}$$

then (since $\alpha(0) = 0$)

$$\begin{aligned}
\frac{\mathrm{d}^2\alpha}{\mathrm{d}r^2} + \frac{1}{r}\frac{\mathrm{d}\alpha}{\mathrm{d}r} - \frac{1}{r^2}\alpha(r) &= \frac{\mathrm{d}^2\alpha}{\mathrm{d}r^2}(0) + \frac{1}{r}\frac{\mathrm{d}\alpha}{\mathrm{d}r}(0) + \frac{\mathrm{d}^2\alpha}{\mathrm{d}r^2}(0) - \frac{1}{r}\frac{\mathrm{d}\alpha}{\mathrm{d}r}(0) + \frac{1}{2}\frac{\mathrm{d}^2\alpha}{\mathrm{d}r^2}(0) + \mathrm{o}(r) \\
&= \frac{3}{2}\frac{\mathrm{d}^2\alpha}{\mathrm{d}r^2}(0) + \mathrm{o}(r),
\end{aligned}$$

Thus we have $(3/2)(\mathrm{d}^2\alpha/\mathrm{d}r^2) \to 0$ as $r \to 0$ and since α is continuous we have the condition

$$\frac{\mathrm{d}^2\alpha}{\mathrm{d}r^2}(0) = 0.$$

In order to use bvp4c we rewrite the fourth order ODE (2.2.16) as a system of equations

of the form $\boldsymbol{\alpha}' = \boldsymbol{y}(r, \boldsymbol{\alpha})$, with $\alpha_1 = \alpha$, $\alpha_2 = \alpha'$, $\alpha_3 = \alpha''$ and $\alpha_4 = \alpha'''$, so that

$$\begin{aligned}
\alpha_1' &= \alpha_2 \\
\alpha_2' &= \alpha_3 \\
\alpha_3' &= \alpha_4 \\
\alpha_4' &= y(r, \alpha_1, \alpha_2, \alpha_3, \alpha_4),
\end{aligned}$$

where

$$\begin{aligned}
y = 4k^2 \left(-\frac{1}{2k^2 r}\alpha_4 - \left(\frac{i\mathrm{Re}}{2k^2} - \frac{3}{4k^2 r^2} - 2 \right) \alpha_3 - \left(\frac{3}{4k^2 r^3} + \frac{i\mathrm{Re}}{2k^2 r} - \frac{2}{r} \right) \alpha_2 \right. \\
- \left(4k^2 + \frac{2}{r^2} - i\mathrm{Re}\left(\frac{1}{2k^2 r^2} \right) - \frac{3}{4k^2 r^4} \right) \alpha_1 \\
\left. -\mathrm{Re}\left(\frac{i}{2k} \left(f\frac{\mathrm{d}^2 g}{\mathrm{d}r^2} + \frac{\mathrm{d}f}{\mathrm{d}r}\frac{\mathrm{d}g}{\mathrm{d}r} \right) - g\frac{\mathrm{d}g}{\mathrm{d}r} + f\frac{\mathrm{d}f}{\mathrm{d}r} + ikgf \right) \right).
\end{aligned}$$

In order to avoid singularities when solving the problem numerically we set a lower limit of $r = 0.01$ instead of $r = 0$. Thus bvp4c solves the above system of equations subject to $\alpha_1(1) = 0$, $\alpha_1(0.01) = 0$, $\alpha_2(1) = -2\mathrm{d}^2 f(1)/\mathrm{d}r^2 - 4i$ and $\alpha_3(0.01) = 0$.

Recall the parameter values that we use are $R_0 = 0.025$ m, $\omega = \pi/10$ rad/s, $\lambda = 0.06$ m, $\mu_0 = 5$ Pa·s, $\rho = 1000$ kg/m^3, and $\varepsilon = 0.01$.

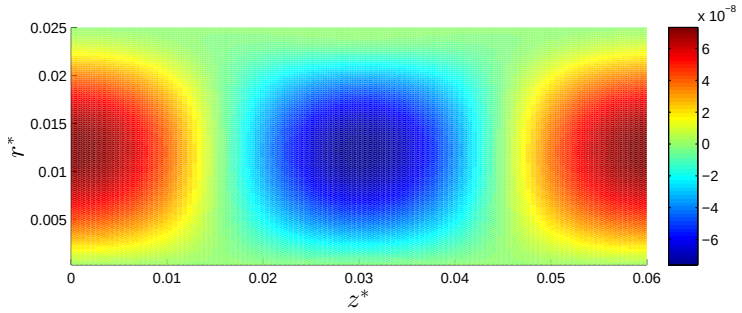

(a) $t = 0$ ($t^* = 0$ s)

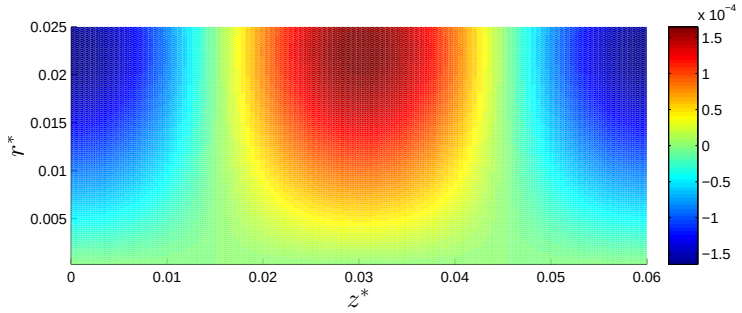

(b) $t = \pi/2$ ($t^* = 5$ s)

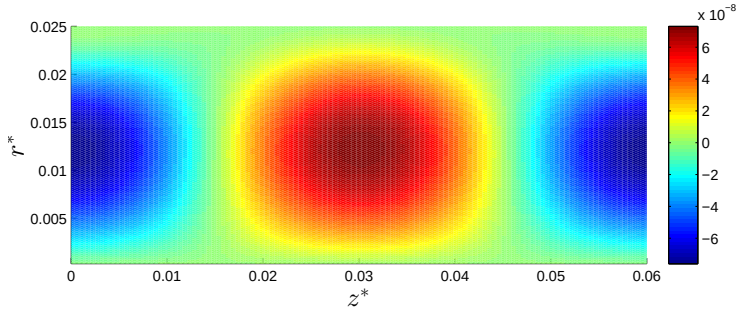

(c) $t = \pi$ ($t^* = 10$ s)

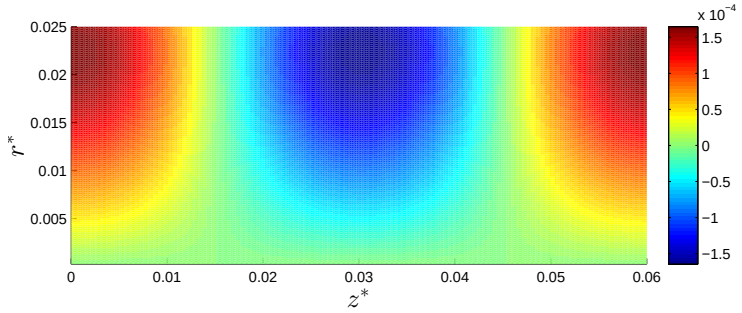

(d) $t = 3\pi/2$ ($t^* = 15$ s)

Figure 2.7: Colour plots of u_r^* (m/s) up to $\mathrm{O}(\varepsilon^2)$ for the standard parameters, where r^* and z^* have units m. The colour scales differ between subplots in order to prevent detail being lost at the times with slower flow velocity.

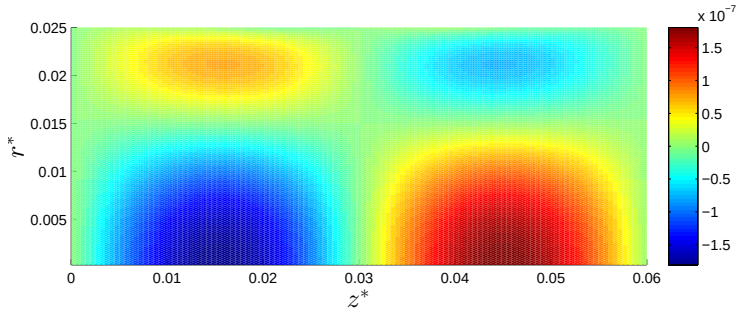

(a) $t = 0$ ($t^* = 0$ s)

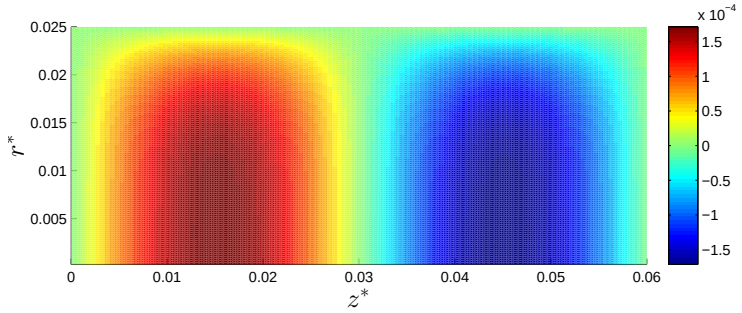

(b) $t = \pi/2$ ($t^* = 5$ s)

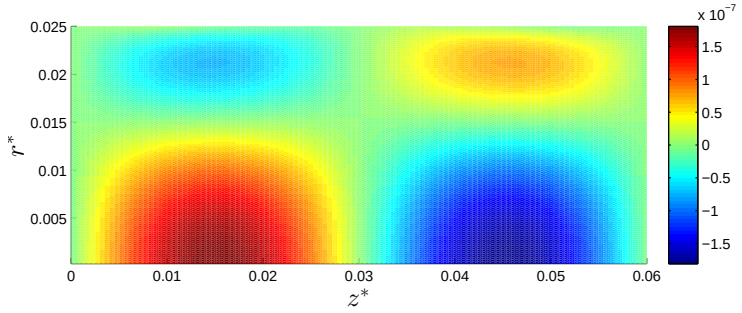

(c) $t = \pi$ ($t^* = 10$ s)

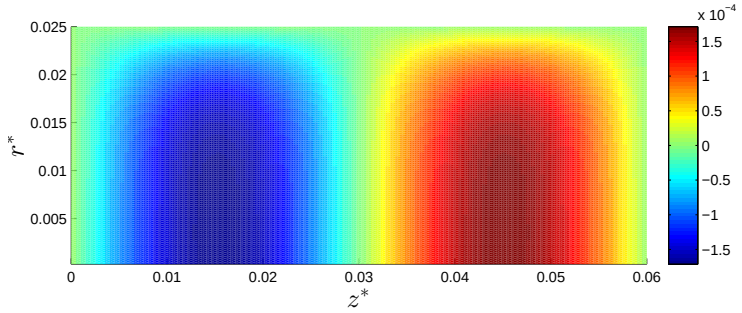

(d) $t = 3\pi/2$ ($t^* = 15$ s)

Figure 2.8: Colour plots of u_z^* (m/s) up to $\mathrm{O}(\varepsilon^2)$ for the standard parameters, where r^* and z^* have units m. The colour scales differ between subplots in order to prevent detail being lost at the times with slower flow velocity.

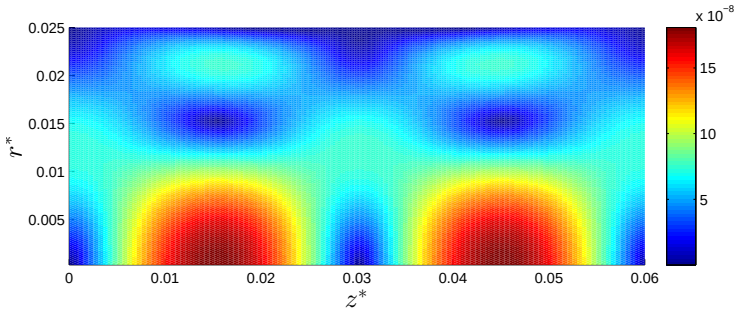

(a) $t = 0$ ($t^* = 0$ s)

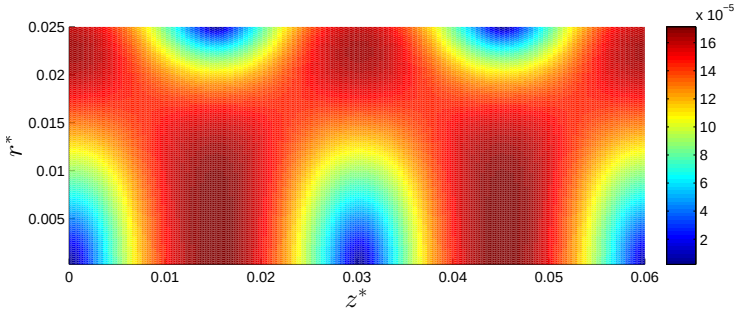

(b) $t = \pi/2$ ($t^* = 5$ s)

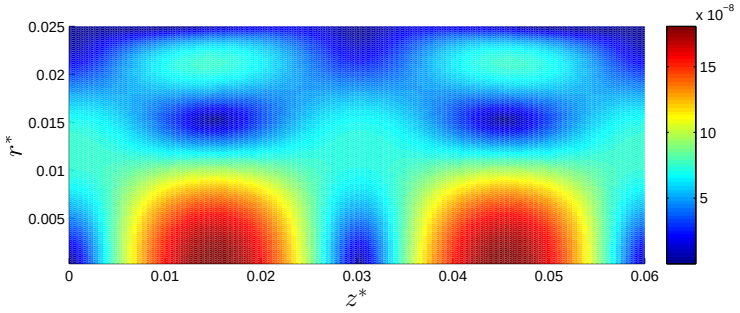

(c) $t = \pi$ ($t^* = 10$ s)

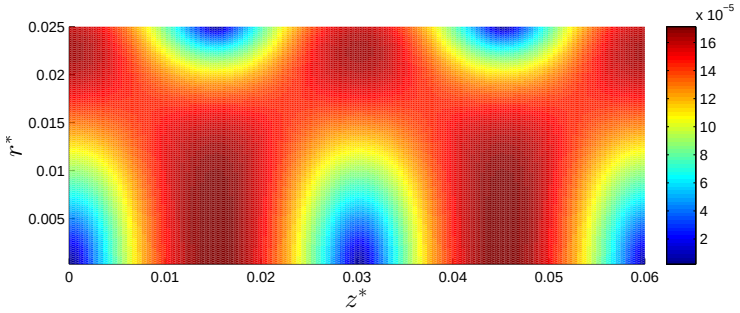

(d) $t = 3\pi/2$ ($t^* = 15$ s)

Figure 2.9: Magnitude of velocity (m/s) up to $O(\varepsilon^2)$ for the standard parameters, where r^* and z^* have units m. The colour scales differ between subplots in order to prevent detail being lost at the times with slower flow velocity.

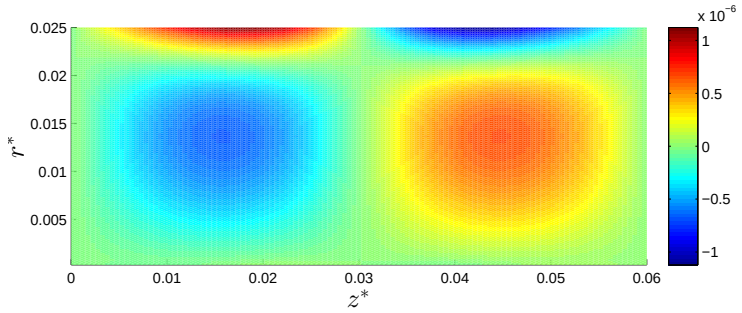

(a) $t = 0$ ($t^* = 0$ s)

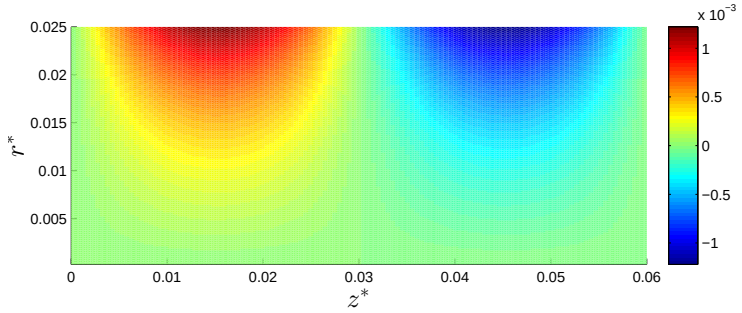

(b) $t = \pi/2$ ($t^* = 5$ s)

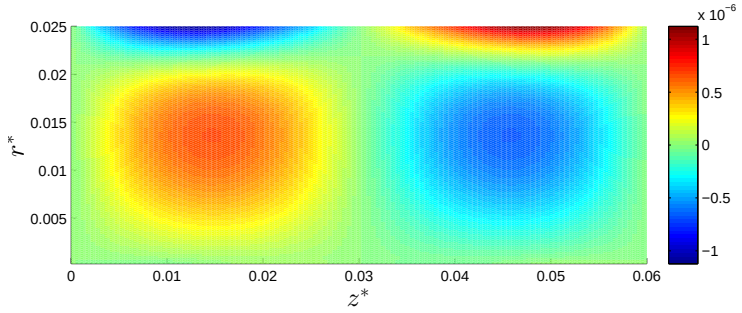

(c) $t = \pi$ ($t^* = 10$ s)

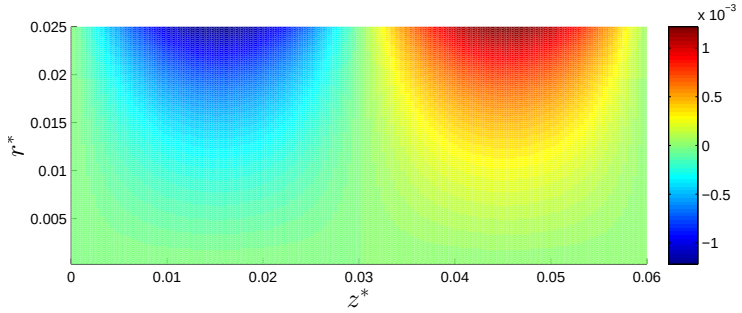

(d) $t = 3\pi/2$ ($t^* = 15$ s)

Figure 2.10: Vorticity of flow (s^{-1}) up to $O(\varepsilon^2)$ for the standard parameters, where r^* and z^* have units m. The colour scales differ between subplots in order to prevent detail being lost at the times with lower vorticity.

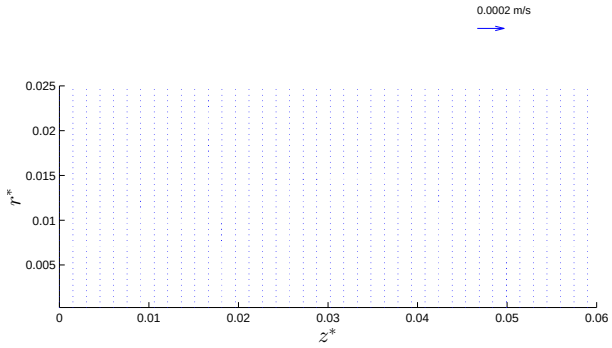

(a) $t = 0$ ($t^* = 0$ s)

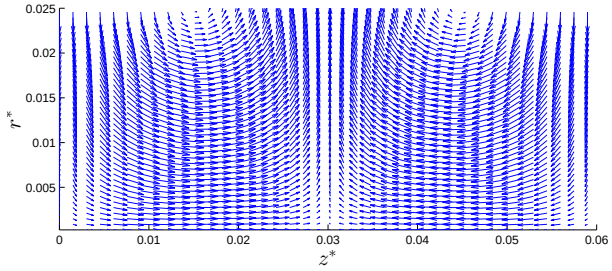

(b) $t = \pi/2$ ($t^* = 5$ s)

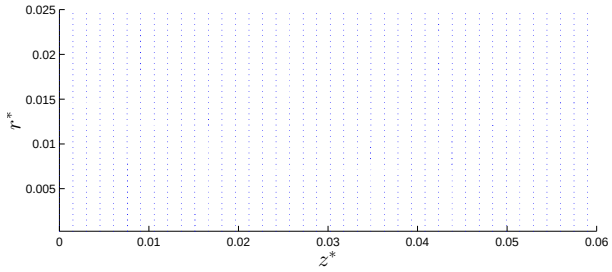

(c) $t = \pi$ ($t^* = 10$ s)

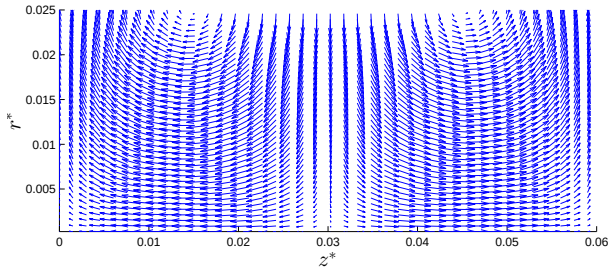

(d) $t = 3\pi/2$ ($t^* = 15$ s)

Figure 2.11: Velocity fields up to $O(\varepsilon^2)$ for the standard parameters at four time instants, where r^* and z^* have units m.

Figures 2.7 - 2.11 represent the combined $O(\varepsilon)$ and $O(\varepsilon^2)$ flow. Comparing figures 2.2 - 2.6 of the previous section to the equivalent figures 2.7 - 2.11 in this section there are no obvious differences in the flow to different orders of ε.

In order to check that this lack of difference is not simply down to taking $\mathrm{Re} \ll 1$ and therefore rendering the additional terms at $O(\varepsilon^2)$ negligible, figures 2.12 and 2.13 compare the flow at both orders for $\mathrm{Re} = 200$. As we see from these figures increasing Re has an effect on the actual flow, however there are still no obvious differences in the flow to different orders of ε.

Thus the main points from section 2.1 hold. At each time step flow in the axial direction is antisymmetric, whilst radial flow is symmetric, about $z^* = 0.03$ m; velocity magnitude is also symmetric about $z^* = 0.03$ m. In this sense flow in the negative and positive directions can be considered to 'balance' out over one wavelength at each time step. In addition to the symmetries at each time step, the plots display antisymmetry in time over one cycle for u_r^*, u_z^* and the vorticity.

In this chapter we have calculated the flow fields of a Newtonian fluid, within a pipe of arbitrary radius and length with a small amplitude standing wave for the pipe wall. We considered flow to both $O(\varepsilon)$ and $O(\varepsilon^2)$, with $\varepsilon = 0.01$, and found that there appears to be no advantage in going to higher order in this case. We shall use these results when we investigate particle transport in chapter 5. In the next chapter we consider a similar geometry but with a thin layer of a second fluid lining the pipe wall to represent the mucus layer in the colon.

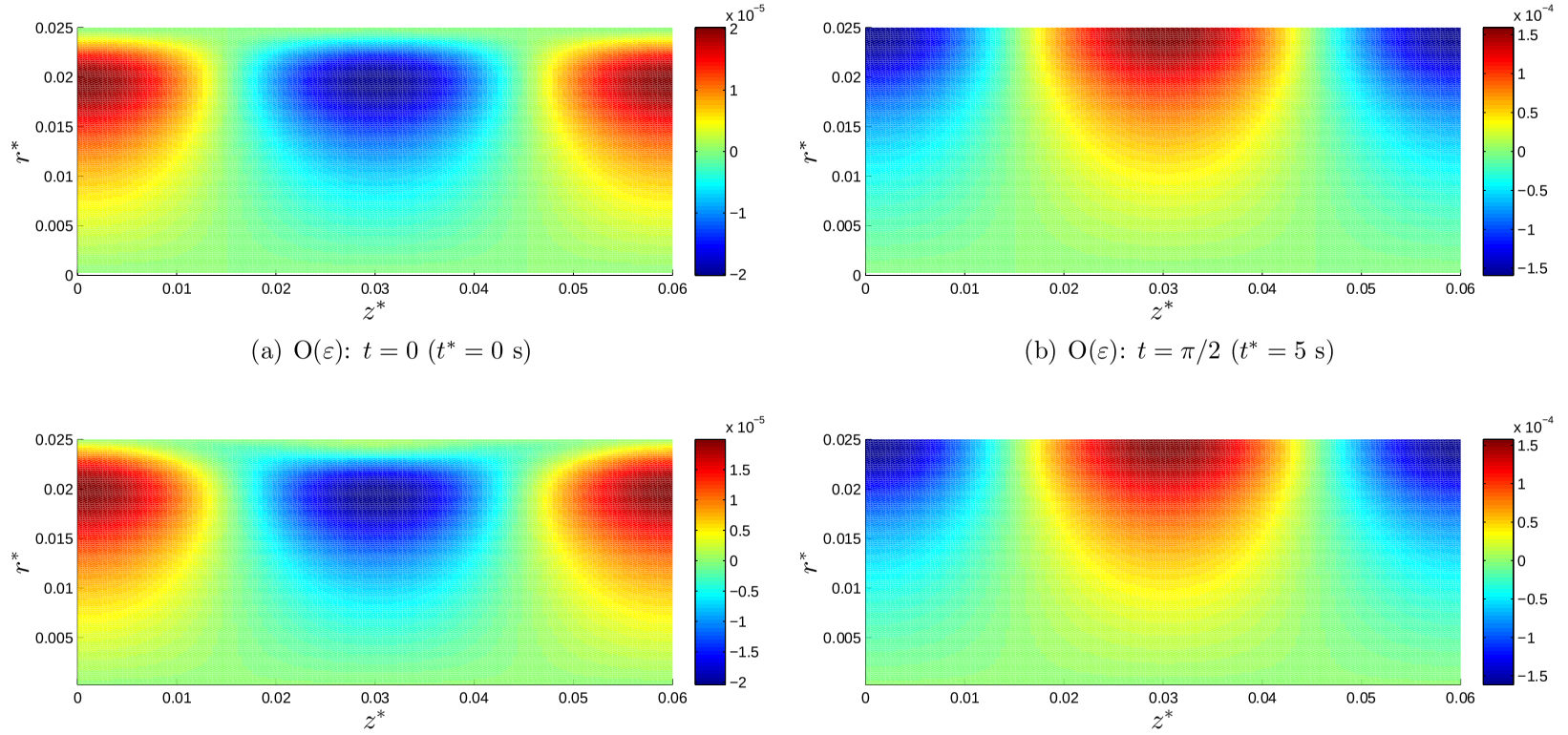

(a) O(ε): $t = 0$ ($t^* = 0$ s)

(b) O(ε): $t = \pi/2$ ($t^* = 5$ s)

(c) O(ε^2): $t = 0$ ($t^* = 10$ s)

(d) O(ε^2): $t = \pi/2$ ($t^* = 15$ s)

Figure 2.12: Colour plots of u_r^* (m/s) comparing flow up to O(ε) with flow up to O(ε^2) for Re = 200, where r^* and z^* have units m. (a) and (b) represent the flow at O(ε) at $t = 0$ and $t = \pi/2$ respectively. (c) and (d) represent the flow at O(ε^2) at $t = 0$ and $t = \pi/2$ respectively.

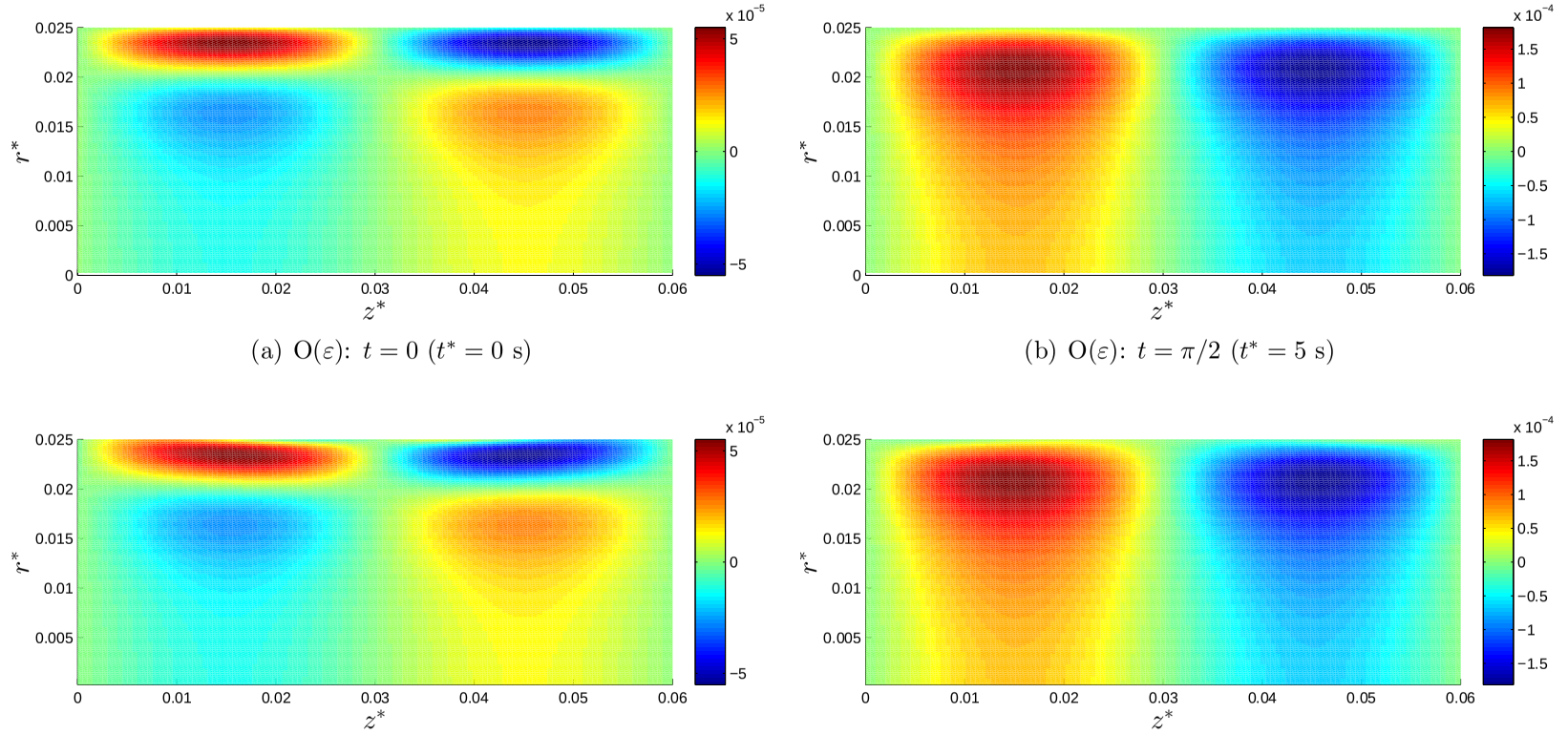

(a) O(ε): $t = 0$ ($t^* = 0$ s)

(b) O(ε): $t = \pi/2$ ($t^* = 5$ s)

(c) O(ε^2): $t = 0$ ($t^* = 10$ s)

(d) O(ε^2): $t = \pi/2$ ($t^* = 15$ s)

Figure 2.13: Colour plots of u_z^* (m/s) comparing flow up to O(ε) with flow up to O(ε^2) for Re = 200, where r^* and z^* have units m. (a) and (b) represent the flow at O(ε) at $t = 0$ and $t = \pi/2$ respectively. (c) and (d) represent the flow at O(ε^2) at $t = 0$ and $t = \pi/2$ respectively.

Chapter 3

Modelling the Colon as a Pipe with Two Layers of Fluid under Small Amplitude Wall Motion

In this chapter we add a mucus layer to the flow to create a two layer model of pipe flow with a standing wave outer wall $R^* = R^*(z^*, t^*)$ and a free surface $\eta^* = \eta^*(z^*, t^*)$ between the two different fluids. Physiologically we are considering the inner fluid to be the bulk digestive fluid, represented by a Newtonian model, and the outer fluid to be a thin mucus layer, represented by the viscoelastic Oldroyd B model. The inner fluid, which is such that $0 \leq r^* < \eta^*(z^*, t^*)$, has velocity $\boldsymbol{u}^{*[1]}$, density $\rho^{[1]}$ and pressure $p^{*[1]}$, whilst the outer fluid, which is such that $\eta^*(z^*, t^*) < r^* < R^*(z^*, t^*)$, has velocity $\boldsymbol{u}^{*[2]}$, density $\rho^{[2]}$ and pressure $p^{*[2]}$. Where the superscript $[i]$ (or subscript i) is used, we take i to range over the values 1 and 2.

3.1 Developing the Equations of Motion with Appropriate Boundary and Interfacial Conditions

The constitutive equation for a Newtonian fluid is given by

$$\boldsymbol{\tau}^{*[1]} = \mu^{[1]}\dot{\boldsymbol{\gamma}}^{*[1]}, \tag{3.1.1}$$

and the constitutive equation for an Oldroyd B fluid is given by

$$\boldsymbol{\tau}^{*[2]} + \lambda_1\boldsymbol{\tau}^{*[2]\triangledown} = \mu^{[2]}(\dot{\boldsymbol{\gamma}}^{*[2]} + \lambda_2\dot{\boldsymbol{\gamma}}^{*[2]\triangledown}), \tag{3.1.2}$$

where $\boldsymbol{A}^{\triangledown}$ is the upper convected derivative of $\boldsymbol{A}$, given by

$$\begin{aligned}\boldsymbol{A}^{\triangledown} &= \frac{D\boldsymbol{A}}{Dt} - (\nabla\boldsymbol{u}^*)^T\cdot\boldsymbol{A} - \boldsymbol{A}\cdot(\nabla\boldsymbol{u}^*)\\ &= \frac{\partial\boldsymbol{A}}{\partial t} + (\boldsymbol{u}^*\cdot\nabla)\boldsymbol{A} - (\nabla\boldsymbol{u}^*)^T\cdot\boldsymbol{A} - \boldsymbol{A}\cdot(\nabla\boldsymbol{u}^*).\end{aligned}$$

In addition, λ_1 is the relaxation time, λ_2 is the retardation time and $\mu^{[2]}$ is the total viscosity of the fluid, given by $\mu^{[2]} = \mu_s + \mu_p$, where μ_s is the solvent viscosity and μ_p is the polymeric viscosity. The equations of motion are given by

$$\begin{aligned}0 &= \frac{1}{r^*}\frac{\partial}{\partial r^*}(r^*u_r^{*[i]}) + \frac{\partial u_z^{*[i]}}{\partial z^*}\\ \frac{\partial u_r^{*[i]}}{\partial t^*} + u_r^{*[i]}\frac{\partial u_r^{*[i]}}{\partial r^*} + u_z^{*[i]}\frac{\partial u_r^{*[i]}}{\partial z^{*[i]}} &= \frac{1}{\rho^{[i]}}\left(-\frac{\partial p^{*[i]}}{\partial r^*} + \frac{\tau_{rr}^{*[i]}}{r^*} - \frac{\tau_{\theta\theta}^{*[i]}}{r^*} + \frac{\partial\tau_{rr}^{*[i]}}{\partial r^*} + \frac{\partial\tau_{rz}^{*[i]}}{\partial z^*}\right)\\ \frac{\partial u_z^{*[i]}}{\partial t^*} + u_r^{*[i]}\frac{\partial u_z^{*[i]}}{\partial r^*} + u_z^{*[i]}\frac{\partial u_z^{*[i]}}{\partial z^*} &= \frac{1}{\rho^{[i]}}\left(-\frac{\partial p^{*[i]}}{\partial z^*} + \frac{\tau_{rz}^{*[i]}}{r^*} + \frac{\partial\tau_{rz}^{*[i]}}{\partial r^*} + \frac{\partial\tau_{zz}^{*[i]}}{\partial z^*}\right).\end{aligned}$$

Using (3.1.1) the relevant components of shear stress for a Newtonian fluid are given

by

$$\begin{aligned}
\tau_{rr}^{*[1]} &= 2\mu^{[1]}\frac{\partial u_r^{*[1]}}{\partial r^*} \\
\tau_{rz}^{*[1]} &= \mu^{[1]}\left(\frac{\partial u_r^{*[1]}}{\partial z^*}+\frac{\partial u_z^{*[1]}}{\partial r^*}\right) \\
\tau_{\theta\theta}^{*[1]} &= 2\mu^{[1]}\frac{u_r^{*[1]}}{r^*} \\
\tau_{zz}^{*[1]} &= 2\mu^{[1]}\frac{\partial u_z^{*[1]}}{\partial z^*},
\end{aligned}$$

with the components of shear stress for an Oldroyd B fluid, using (3.1.2) and Appendix B, given by

$$\begin{aligned}
\tau_{rr}^{*[2]}+\lambda_1\left(\frac{\partial \tau_{rr}^{*[2]}}{\partial t^*}+u_r^{*[2]}\frac{\partial \tau_{rr}^{*[2]}}{\partial r^*}+u_z^{*[2]}\frac{\partial \tau_{rr}^{*[2]}}{\partial z^*}-2\tau_{rr}^{*[2]}\frac{\partial u_r^{*[2]}}{\partial r^*}-2\tau_{rz}^{*[2]}\frac{\partial u_z^{*[2]}}{\partial r^*}\right) \\
=2\mu^{[2]}\left(\frac{\partial u_r^{*[2]}}{\partial r^*}+\lambda_2\left(\frac{\partial^2 u_r^{*[2]}}{\partial t^*\partial r^*}+u_r^{*[2]}\frac{\partial^2 u_r^{*[2]}}{\partial r^{*2}}+u_z^{*[2]}\frac{\partial^2 u_r^{*[2]}}{\partial z^*\partial r^*}\right.\right. \\
\left.\left.-2\left(\frac{\partial u_r^{*[2]}}{\partial r^*}\right)^2-\frac{\partial u_z^{*[2]}}{\partial r^*}\left(\frac{\partial u_r^{*[2]}}{\partial z^*}+\frac{\partial u_z^{*[2]}}{\partial r^*}\right)\right)\right);
\end{aligned}$$

$$\begin{aligned}
\tau_{rz}^{*[2]}+\lambda_1\left(\frac{\partial \tau_{rz}^{*[2]}}{\partial t^*}+u_r^{*[2]}\frac{\partial \tau_{rz}^{*[2]}}{\partial r^*}+u_z^{*[2]}\frac{\partial \tau_{rz}^{*[2]}}{\partial z^*}-\tau_{rr}^{*[2]}\frac{\partial u_r^{*[2]}}{\partial z^*}-\tau_{zz}^{*[2]}\frac{\partial u_z^{*[2]}}{\partial r^*}-\tau_{rz}^{*[2]}\right. \\
\left.\left(\frac{\partial u_r^{*[2]}}{\partial r^*}+\frac{\partial u_z^{*[2]}}{\partial z^*}\right)\right)=\mu^{[2]}\left(\frac{\partial u_r^{*[2]}}{\partial z^*}+\frac{\partial u_z^{*[2]}}{\partial r^*}+\lambda_2\left(\frac{\partial^2 u_r^{*[2]}}{\partial t^*\partial z^*}+\frac{\partial^2 u_z^{*[2]}}{\partial t^*\partial r^*}\right.\right. \\
+u_r^{*[2]}\left(\frac{\partial^2 u_r^{*[2]}}{\partial r^*\partial z^*}+\frac{\partial^2 u_z^{*[2]}}{\partial r^{*2}}\right)+u_z^{*[2]} \\
\left(\frac{\partial^2 u_z^{*[2]}}{\partial z^*\partial r^*}+\frac{\partial^2 u_r^{*[2]}}{\partial z^{*2}}\right)-2\left(\frac{\partial u_r^{*[2]}}{\partial r^*}\frac{\partial u_r^{*[2]}}{\partial z^*}+\frac{\partial u_z^{*[2]}}{\partial r^*}\frac{\partial u_z^{*[2]}}{\partial z^*}\right) \\
\left.\left.-\left(\frac{\partial u_r^{*[2]}}{\partial z^*}+\frac{\partial u_z^{*[2]}}{\partial r^*}\right)\left(\frac{\partial u_r^{*[2]}}{\partial r^*}+\frac{\partial u_z^{*[2]}}{\partial z^*}\right)\right)\right);
\end{aligned}$$

$$\tau_{\theta\theta}^{*[2]} + \lambda_1 \left(\frac{\partial \tau_{\theta\theta}^{*[2]}}{\partial t^*} + u_r^{*[2]} \frac{\partial \tau_{\theta\theta}^{*[2]}}{\partial r^*} + u_z^{*[2]} \frac{\partial \tau_{\theta\theta}^{*[2]}}{\partial z^*} - 2\tau_{\theta\theta}^{*[2]} \frac{u_r^{*[2]}}{r^*} \right) = 2\frac{\mu^{[2]}}{r^*} \left(u_r^{*[2]} + \lambda_2 \left(\frac{\partial u_r^{*[2]}}{\partial t^*} + u_r^{*[2]} \frac{\partial u_r^{*[2]}}{\partial r^*} + u_z^{*[2]} \frac{\partial u_r^{*[2]}}{\partial z^*} - 3\frac{u_r^{*[2]2}}{r^*} \right) \right);$$

and finally

$$\tau_{zz}^{*[2]} + \lambda_1 \left(\frac{\partial \tau_{zz}^{*[2]}}{\partial t^*} + u_r^{*[2]} \frac{\partial \tau_{zz}^{*[2]}}{\partial r^*} + u_z^{*[2]} \frac{\partial \tau_{zz}^{*[2]}}{\partial z^*} - 2\tau_{zz}^{*[2]} \frac{\partial u_z^{*[2]}}{\partial z^*} - 2\tau_{rz}^{*[2]} \frac{\partial u_r^{*[2]}}{\partial z^*} \right) = 2\mu^{[2]} \left(\frac{\partial u_z^{*[2]}}{\partial z^*} + \lambda_2 \left(\frac{\partial^2 u_z^{*[2]}}{\partial t^* \partial z^*} + u_r^{*[2]} \frac{\partial^2 u_z^{*[2]}}{\partial r^* \partial z^*} + u_z^{*[2]} \frac{\partial^2 u_z^{*[2]}}{\partial z^2} - 2 \left(\frac{\partial u_z^{*[2]}}{\partial z^*} \right)^2 - \frac{\partial u_r^{*[2]}}{\partial z^*} \left(\frac{\partial u_r^{*[2]}}{\partial z^*} + \frac{\partial u_z^{*[2]}}{\partial r^*} \right) \right) \right).$$

We take one Reynolds number, valid throughout the pipe, defined as

$$\mathrm{Re} = \frac{\rho^{[1]} \omega R_0^2}{\mu^{[1]}}.$$

Through taking the same parameter values as in the one layer case, i.e. $R_0 = 0.025$ m, $\omega = \pi/10$ rad/s, $\rho^{[1]} = 1000$ kg/m^3 and $\mu^{[1]} = 5$ Pa·s, we have $\mathrm{Re} \approx 0.039$. For the inner fluid we nondimensionalise according to

$$\boldsymbol{u}^{*[1]} = \omega R_0 \boldsymbol{u}^{[1]};\ \boldsymbol{x}^* = R_0 \boldsymbol{x};\ t^* = \frac{1}{\omega} t;\ p^{*[1]} = \frac{\rho^{[1]} (\omega R_0)^2}{\mathrm{Re}} p^{[1]};$$

$$\text{and } \boldsymbol{\tau}^{*[1]} = \mu^{[1]} \omega \boldsymbol{\tau}^{[1]}.$$

The nondimensional equations pertaining to the inner fluid are then given by

$$\begin{aligned}
0 &= \frac{1}{r}\frac{\partial}{\partial r}(r u_r^{[1]}) + \frac{\partial u_z^{[1]}}{\partial z} \\
\frac{\partial u_r^{[1]}}{\partial t} + u_r^{[1]}\frac{\partial u_r^{[1]}}{\partial r} + u_z^{[1]}\frac{\partial u_r^{[1]}}{\partial z} &= \frac{1}{\mathrm{Re}}\left(-\frac{\partial p^{[1]}}{\partial r} + \frac{1}{r}\left(\tau_{rr}^{[1]} - \tau_{\theta\theta}^{[1]} + r\frac{\partial \tau_{rr}^{[1]}}{\partial r} + r\frac{\partial \tau_{rz}^{[1]}}{\partial z}\right)\right) \\
\frac{\partial u_z^{[1]}}{\partial t} + u_r^{[1]}\frac{\partial u_z^{[1]}}{\partial r} + u_z^{[1]}\frac{\partial u_z^{[1]}}{\partial z} &= \frac{1}{\mathrm{Re}}\left(-\frac{\partial p^{[1]}}{\partial z} + \frac{1}{r}\left(\tau_{rz}^{[1]} + r\frac{\partial \tau_{rz}^{[1]}}{\partial r} + r\frac{\partial \tau_{zz}^{[1]}}{\partial z}\right)\right) \\
\tau_{rr}^{[1]} &= 2\frac{\partial u_r^{[1]}}{\partial r} \\
\tau_{rz}^{[1]} &= \left(\frac{\partial u_r^{[1]}}{\partial z} + \frac{\partial u_z^{[1]}}{\partial r}\right) \\
\tau_{\theta\theta}^{[1]} &= 2\frac{u_r^{[1]}}{r} \\
\tau_{zz}^{[1]} &= 2\frac{\partial u_z^{[1]}}{\partial z}.
\end{aligned}$$

For the outer fluid we nondimensionalise using

$$\boldsymbol{u}^{*[2]} = \omega R_0 \boldsymbol{u}^{[2]};\ \boldsymbol{x}^* = R_0\boldsymbol{x};\ t^* = \frac{1}{\omega}t;\ p^{*[2]} = \frac{\rho^{[2]}(\omega R_0)^2}{\mathrm{Re}}p^{[2]};$$

$$\boldsymbol{\tau}^{*[2]} = \mu^{[2]}\omega\boldsymbol{\tau}^{[2]};\ \text{and}\ M^{[2]} = \lambda_1\omega.$$

We also introduce the nondimensional parameters

$$\bar{\mu} = \frac{\mu^{[2]}}{\mu^{[1]}};\ \bar{\rho} = \frac{\rho^{[2]}}{\rho^{[1]}}\ \text{and}\ \bar{\lambda} = \frac{\lambda_2}{\lambda_1}.$$

We take estimates of $\rho^{[2]} = 1000$ kg/m^3, $\mu^{[2]} = 10$ Pa·s and $\lambda_1 = 30$ s for the mucus density, zero shear viscosity and relaxation time respectively. In addition we note that the retardation time in the Oldroyd B model is given by $\lambda_2 = \mu_s\lambda_1/(\mu_p + \mu_s)$ [40]; thus we take $\lambda_2 = 6.5 \times 10^{-4}\lambda_1/\mu^{[2]}$ s, where 6.5×10^{-4} Pa·s is an estimate for the dynamic viscosity of water at body temperature. The equations of motion for the outer fluid are

then given by

$$
\begin{aligned}
0 &= \frac{1}{r}\frac{\partial}{\partial r}(ru_r^{[2]}) + \frac{\partial u_z^{[2]}}{\partial z} \\
\mathrm{Re}\left(\frac{\partial u_r^{[2]}}{\partial t} + u_r^{[2]}\frac{\partial u_r^{[2]}}{\partial r} + u_z^{[2]}\frac{\partial u_r^{[2]}}{\partial z}\right) &= -\frac{\partial p^{[2]}}{\partial r} + \frac{\bar{\mu}}{\bar{\rho}}\left(\frac{1}{r}\left(\tau_{rr}^{[2]} - \tau_{\theta\theta}^{[2]} + r\frac{\partial \tau_{rr}^{[2]}}{\partial r} + r\frac{\partial \tau_{rz}^{[2]}}{\partial z}\right)\right) \\
\mathrm{Re}\left(\frac{\partial u_z^{[2]}}{\partial t} + u_r^{[2]}\frac{\partial u_z^{[2]}}{\partial r} + u_z^{[2]}\frac{\partial u_z^{[2]}}{\partial z}\right) &= -\frac{\partial p^{[2]}}{\partial z} + \frac{\bar{\mu}}{\bar{\rho}}\left(\frac{1}{r}\left(\tau_{rz}^{[2]} + r\frac{\partial \tau_{rz}^{[2]}}{\partial r} + r\frac{\partial \tau_{zz}^{[2]}}{\partial z}\right)\right),
\end{aligned}
$$

whilst the shear stress equations are given by

$$
\begin{aligned}
\tau_{rr}^{[2]} + M^{[2]}\left(\frac{\partial \tau_{rr}^{[2]}}{\partial t} + u_r^{[2]}\frac{\partial \tau_{rr}^{[2]}}{\partial r} + u_z^{[2]}\frac{\partial \tau_{rr}^{[2]}}{\partial z} - 2\tau_{rr}^{[2]}\frac{\partial u_r^{[2]}}{\partial r} - 2\tau_{rz}^{[2]}\frac{\partial u_z^{[2]}}{\partial r}\right) = 2\left(\frac{\partial u_r^{[2]}}{\partial r} + \bar{\lambda}M^{[2]}\right. \\
\left.\left(\frac{\partial^2 u_r^{[2]}}{\partial t \partial r} + u_r^{[2]}\frac{\partial^2 u_r^{[2]}}{\partial r^2} + u_z^{[2]}\frac{\partial^2 u_r^{[2]}}{\partial z \partial r} - 2\left(\frac{\partial u_r^{[2]}}{\partial r}\right)^2 - \frac{\partial u_z^{[2]}}{\partial r}\left(\frac{\partial u_r^{[2]}}{\partial z} + \frac{\partial u_z^{[2]}}{\partial r}\right)\right)\right);
\end{aligned}
$$

$$
\begin{aligned}
\tau_{rz}^{[2]} + M^{[2]}\left(\frac{\partial \tau_{rz}^{[2]}}{\partial t} + u_r^{[2]}\frac{\partial \tau_{rz}^{[2]}}{\partial r} + u_z^{[2]}\frac{\partial \tau_{rz}^{[2]}}{\partial z} - \tau_{rr}^{[2]}\frac{\partial u_r^{[2]}}{\partial z} - \tau_{zz}^{[2]}\frac{\partial u_z^{[2]}}{\partial r} - \tau_{rz}^{[2]}\left(\frac{\partial u_r^{[2]}}{\partial r} + \frac{\partial u_z^{[2]}}{\partial z}\right)\right) \\
= \left(\frac{\partial u_r^{[2]}}{\partial z} + \frac{\partial u_z^{[2]}}{\partial r} + \bar{\lambda}M^{[2]}\left(\frac{\partial^2 u_r^{[2]}}{\partial t \partial z} + \frac{\partial^2 u_z^{[2]}}{\partial t \partial r} + u_r^{[1]}\left(\frac{\partial^2 u_r^{[2]}}{\partial r \partial z} + \frac{\partial^2 u_z^{[2]}}{\partial r^2}\right) + u_z^{[2]}\left(\frac{\partial^2 u_z^{[2]}}{\partial z \partial r}\right.\right.\right. \\
\left.\left.\left. + \frac{\partial^2 u_r^{[2]}}{\partial z^2}\right) - 2\left(\frac{\partial u_r^{[2]}}{\partial r}\frac{\partial u_r^{[2]}}{\partial z} + \frac{\partial u_z^{[2]}}{\partial r}\frac{\partial u_z^{[2]}}{\partial z}\right) - \left(\frac{\partial u_r^{[2]}}{\partial z} + \frac{\partial u_z^{[2]}}{\partial r}\right)\left(\frac{\partial u_r^{[2]}}{\partial r} + \frac{\partial u_z^{[2]}}{\partial z}\right)\right)\right);
\end{aligned}
$$

$$
\begin{aligned}
\tau_{\theta\theta}^{[2]} + M^{[2]}\left(\frac{\partial \tau_{\theta\theta}^{[2]}}{\partial t} + u_r^{[2]}\frac{\partial \tau_{\theta\theta}^{[2]}}{\partial r} + u_z^{[2]}\frac{\partial \tau_{\theta\theta}^{[2]}}{\partial z} - 2\tau_{\theta\theta}^{[2]}\frac{u_r^{[2]}}{r}\right) = \frac{2}{r}\left(u_r^{[2]} + \bar{\lambda}M^{[2]}\right. \\
\left.\left(\frac{\partial u_r^{[2]}}{\partial t} + u_r^{[2]}\frac{\partial u_r^{[2]}}{\partial r} + u_z^{[2]}\frac{\partial u_r^{[2]}}{\partial z} - 3\frac{u_r^{[2]2}}{r}\right)\right);
\end{aligned}
$$

and

$$\tau_{zz}^{[2]} + M^{[2]}\left(\frac{\partial \tau_{zz}^{[2]}}{\partial t} + u_r^{[2]}\frac{\partial \tau_{zz}^{[2]}}{\partial r} + u_z^{[2]}\frac{\partial \tau_{zz}^{[2]}}{\partial z} - 2\tau_{zz}^{[2]}\frac{\partial u_z^{[2]}}{\partial z} - 2\tau_{rz}^{[2]}\frac{\partial u_r^{[2]}}{\partial z}\right) = 2\left(\frac{\partial u_z^{[2]}}{\partial z} + \bar{\lambda}M^{[2]}\right.$$
$$\left.\left(\frac{\partial^2 u_z^{[2]}}{\partial t \partial z} + u_r^{[2]}\frac{\partial^2 u_z^{[2]}}{\partial r \partial z} + u_z^{[2]}\frac{\partial^2 u_z^{[2]}}{\partial z^2} - 2\left(\frac{\partial u_z^{[2]}}{\partial z}\right)^2 - \frac{\partial u_r^{[2]}}{\partial z}\left(\frac{\partial u_r^{[2]}}{\partial z} + \frac{\partial u_z^{[2]}}{\partial r}\right)\right)\right).$$

The boundary conditions are the same as in chapter 2, i.e.

$$\begin{aligned} u_r^{[2]}(R(z,t),z,t) &= \dot{R}(z,t) \\ u_z^{[2]}(R(z,t),z,t) &= 0 \\ u_r^{[1]}(0,z,t) &= 0 \\ \frac{\partial u_z^{[1]}}{\partial r}(0,z,t) &= 0. \end{aligned}$$

In addition to these we must also formulate the interfacial conditions at the free surface between our two fluids.

The kinematic condition (C.1) is given by

$$\frac{\partial \eta}{\partial t} + u_z^{[i]}(\eta(z,t),z,t)\frac{\partial \eta}{\partial z} = u_r^{[i]}(\eta(z,t),z,t)$$

and continuity of velocity is expressed as

$$\boldsymbol{u}^{[1]}(\eta(z,t),z,t) = \boldsymbol{u}^{[2]}(\eta(z,t),z,t).$$

Note that the boundary conditions and the two interfacial conditions above are nondimensional.

The (dimensional) normal and tangential stress conditions are given by

$$\begin{aligned}(\boldsymbol{t}^{*[1]} - \boldsymbol{t}^{*[2]}) \cdot \hat{\boldsymbol{n}}^* &= -\sigma\kappa^* \\ \boldsymbol{t}^{*[1]} \cdot \boldsymbol{l}^* &= \boldsymbol{t}^{*[2]} \cdot \boldsymbol{l}^*,\end{aligned}$$

at $r^* = \eta^*$, where $\boldsymbol{t}^{*[i]}$ are the stress vectors, $\hat{\boldsymbol{n}}^*$ and $\boldsymbol{l}^*$ are the unit normal and a tangential vector to the interface, σ is the interfacial tension and κ^* is the curvature of the interface.

Now $t_j^{*[i]} = \sigma_{jk}^{*[i]} \hat{n}_k^*$, with $\sigma_{jk}^{*[i]} = -p^{*[i]}\delta_{jk} + \tau^{*[i]}$. Using the scalings for $p^{*[i]}$ and $\boldsymbol{\tau}^{*[i]}$ we have $\sigma_{jk}^{*[i]} = \mu\omega\sigma_{jk}^{[i]}$, with

$$\begin{aligned}\sigma_{jk}^{[1]} &= -p^{[1]}\delta_{jk} + \tau^{[1]} \\ \sigma_{jk}^{[2]} &= -\bar{\rho}p^{[2]}\delta_{jk} + \bar{\mu}\tau^{[2]}.\end{aligned}$$

We note that $\hat{\boldsymbol{n}}^* = \hat{\boldsymbol{n}}$ and $\boldsymbol{l}^* = \boldsymbol{l}$, in addition $\kappa^* = \kappa/R_0$, with $\kappa = \nabla \cdot \hat{\boldsymbol{n}}$. Thus the normal stress condition is given by

$$(\boldsymbol{t}^{[1]} - \boldsymbol{t}^{[2]}) \cdot \hat{\boldsymbol{n}} = -\frac{\kappa}{\mathrm{Ca}},$$

where Ca is the capillary number, defined as

$$\mathrm{Ca} = \frac{\mu^{[1]}\omega R_0}{\sigma}$$

and the tangential stress condition is given by

$$\boldsymbol{t}^{[1]} \cdot \boldsymbol{l} = \boldsymbol{t}^{[2]} \cdot \boldsymbol{l}.$$

Taking an estimate for the interfacial tension of $\sigma = 0.072$ N/m we have $\mathrm{Ca} \approx 0.5454$.

In this problem we have

$$\hat{\boldsymbol{n}} = \left(1 + \left(\frac{\partial \eta}{\partial z}\right)^2\right)^{-\frac{1}{2}} \left(1, 0, -\frac{\partial \eta}{\partial z}\right)$$

which gives

$$\kappa = \frac{1}{\eta}\left(1 + \left(\frac{\partial \eta}{\partial z}\right)^2\right)^{-\frac{1}{2}} - \frac{\partial^2 \eta}{\partial z^2}\left(1 + \left(\frac{\partial \eta}{\partial z}\right)^2\right)^{-\frac{3}{2}}.$$

In order for the vector $\boldsymbol{l}$ to be tangential to the interface we require

$$\begin{aligned} \boldsymbol{l} \cdot \hat{\boldsymbol{n}} &= \left(1 + \left(\frac{\partial \eta}{\partial z}\right)^2\right)^{-\frac{1}{2}} \left(l_r - l_z \frac{\partial \eta}{\partial z}\right) \\ &= 0. \end{aligned}$$

Taking $l_r = \partial \eta / \partial z$ and $l_z = 1$ we have

$$\boldsymbol{l} = \left(\frac{\partial \eta}{\partial z}, 0, 1\right).$$

3.2 Developing the Solutions to the Problem

As in the previous chapter we take a boundary of the form

$$R(z,t) \sim 1 + \varepsilon R_1(z,t) + \varepsilon^2 R_2(z,t) + \ldots$$

as $\varepsilon \to 0$. Again we assume that the pressure is constant at leading order, then we have

$$\begin{aligned}
\eta(z,t) &\sim \eta_0 + \varepsilon\eta_1(z,t) + \varepsilon^2\eta_2(z,t) + \dots \\
p^{[i]}(r,z,t) &\sim p_0^{[i]} + \varepsilon p_1^{[i]}(r,z,t) + \varepsilon^2 p_2^{[i]}(r,z,t) + \dots \\
\boldsymbol{u}^{[i]}(r,z,t) &\sim \varepsilon\boldsymbol{u}^{[i]}(r,z,t) + \varepsilon^2\boldsymbol{u}^{[i]}(r,z,t) + \dots \\
\boldsymbol{\tau}^{[i]}(r,z,t) &\sim \varepsilon\boldsymbol{\tau}^{[i]}(r,z,t) + \varepsilon^2\boldsymbol{\tau}^{[i]}(r,z,t) + \dots
\end{aligned}$$

as $\varepsilon \to 0$, where η_0 and $p_0^{[i]}$ are constant. Now $\eta_0 = 1 -$ mucus layer thickness$/R_0$, so taking $\eta_0 = 0.995$ corresponds to a mucus layer thickness of 125 μm.

At leading order there is no flow, so we consider only the behaviour of the fluids at higher order. The equations of motion and shear stress at O(ε) for the inner fluid are given by

$$\begin{aligned}
0 &= \frac{1}{r}\frac{\partial}{\partial r}(r u_{r1}^{[1]}) + \frac{\partial u_{z1}^{[1]}}{\partial z} && (3.2.1)\\
\mathrm{Re}\frac{\partial u_{r1}^{[1]}}{\partial t} &= -\frac{\partial p_1^{[1]}}{\partial r} + \frac{\tau_{rr1}^{[1]}}{r} - \frac{\tau_{\theta\theta1}^{[1]}}{r} + \frac{\partial \tau_{rr1}^{[1]}}{\partial r} + \frac{\partial \tau_{rz1}^{[1]}}{\partial z} && (3.2.2)\\
\mathrm{Re}\frac{\partial u_{z1}^{[1]}}{\partial t} &= -\frac{\partial p_1^{[1]}}{\partial z} + \frac{\tau_{rz1}^{[1]}}{r} + \frac{\partial \tau_{rz1}^{[1]}}{\partial r} + \frac{\partial \tau_{zz1}^{[1]}}{\partial z} && (3.2.3)\\
\tau_{rr1}^{[1]} &= 2\frac{\partial u_{r1}^{[1]}}{\partial r} && (3.2.4)\\
\tau_{rz1}^{[1]} &= \frac{\partial u_{r1}^{[1]}}{\partial z} + \frac{\partial u_{z1}^{[1]}}{\partial r} && (3.2.5)\\
\tau_{\theta\theta1}^{[1]} &= 2\frac{u_{r1}^{[1]}}{r} && (3.2.6)\\
\tau_{zz1}^{[1]} &= 2\frac{\partial u_{z1}^{[1]}}{\partial z}. && (3.2.7)
\end{aligned}$$

The equations of motion and shear stress at O(ε) for the outer fluid are given by

$$
\begin{aligned}
0 &= \frac{1}{r}\frac{\partial}{\partial r}(r u_{r1}^{[2]}) + \frac{\partial u_{z1}^{[2]}}{\partial z} && (3.2.8)\\
\mathrm{Re}\frac{\partial u_{r1}^{[2]}}{\partial t} &= -\frac{\partial p_1^{[2]}}{\partial r} + \frac{\bar{\mu}}{\bar{\rho}}\left(\frac{\tau_{rr1}^{[2]}}{r} - \frac{\tau_{\theta\theta 1}^{[2]}}{r} + \frac{\partial \tau_{rr1}^{[2]}}{\partial r} + \frac{\partial \tau_{rz1}^{[2]}}{\partial z}\right) && (3.2.9)\\
\mathrm{Re}\frac{\partial u_{z1}^{[2]}}{\partial t} &= -\frac{\partial p_1^{[2]}}{\partial z} + \frac{\bar{\mu}}{\bar{\rho}}\left(\frac{\tau_{rz1}^{[2]}}{r} + \frac{\partial \tau_{rz1}^{[2]}}{\partial r} + \frac{\partial \tau_{zz1}^{[2]}}{\partial z}\right) && (3.2.10)\\
\tau_{rr1}^{[2]} + M^{[2]}\frac{\partial \tau_{rr1}^{[2]}}{\partial t} &= 2\left(\frac{\partial u_{r1}^{[2]}}{\partial r} + \bar{\lambda}M^{[2]}\frac{\partial^2 u_{r1}^{[2]}}{\partial t \partial r}\right) && (3.2.11)\\
\tau_{rz1}^{[2]} + M^{[2]}\frac{\partial \tau_{rz1}^{[2]}}{\partial t} &= \frac{\partial u_{r1}^{[2]}}{\partial z} + \frac{\partial u_{z1}^{[2]}}{\partial r} + \bar{\lambda}M^{[2]}\left(\frac{\partial^2 u_{r1}^{[2]}}{\partial t \partial z} + \frac{\partial^2 u_{z1}}{\partial t \partial r}\right) && (3.2.12)\\
\tau_{\theta\theta 1}^{[2]} + M^{[2]}\frac{\partial \tau_{\theta\theta 1}^{[2]}}{\partial t} &= \frac{2}{r}\left(u_{r1}^{[2]} + \bar{\lambda}M^{[2]}\frac{\partial u_{r1}^{[2]}}{\partial t}\right) && (3.2.13)\\
\tau_{zz1}^{[2]} + M^{[2]}\frac{\partial \tau_{zz1}^{[2]}}{\partial t} &= 2\left(\frac{\partial u_{z1}^{[2]}}{\partial z} + \bar{\lambda}M^{[2]}\frac{\partial^2 u_{z1}^{[2]}}{\partial t \partial z}\right). && (3.2.14)
\end{aligned}
$$

We will only be considering flow up to O(ε) in this chapter. This is because the added complexity in going to higher order does not add corresponding detail to the results, as seen in section 2.2.

The boundary conditions at O(ε) are as in section 2.1, i.e.

$$
\begin{aligned}
u_{r1}(1,z,t) &= \dot{R}_1(z,t)\\
u_{z1}(1,z,t) &= 0\\
u_{r1}(0,z,t) &= 0\\
\frac{\partial u_{z1}}{\partial r}(0,z,t) &= 0.
\end{aligned}
$$

Using a Taylor expansion,

$$\begin{aligned}\boldsymbol{u}(\eta(z,t),z,t) &= u_r(\eta_0+\varepsilon\eta_1(z,t)+\ldots,z,t)\\ &= \boldsymbol{u}(\eta_0,z,t)+\varepsilon\eta_1(z,t)\frac{\partial \boldsymbol{u}}{\partial r}(\eta_0,z,t)+\ldots\\ &= \varepsilon\boldsymbol{u}(\eta_0,z,t)+\mathrm{o}(\varepsilon^2),\end{aligned}$$

therefore continuity of velocity is given by

$$\boldsymbol{u}^{[1]}(\eta_0,z,t)=\boldsymbol{u}^{[2]}(\eta_0,z,t).$$

In addition the kinematic condition (3.1) at $\mathrm{O}(\varepsilon)$ is given by

$$u_{r1}^{[i]}(\eta_0,z,t)=\dot{\eta}_1(z,t).$$

Recall that the normal and tangential stress conditions are given by

$$\begin{aligned}(\boldsymbol{t}^{[1]}-\boldsymbol{t}^{[2]})\cdot\hat{\boldsymbol{n}} &= -\frac{\kappa}{\mathrm{Ca}}\\ \boldsymbol{t}^{[1]}\cdot\boldsymbol{l} &= \boldsymbol{t}^{[2]}\cdot\boldsymbol{l}.\end{aligned}$$

Using the binomial expansion on $1/(\eta_0+\varepsilon\eta_1+\ldots)$ and powers of $1+(\partial\eta/\partial z)^2$ we have

$$\begin{aligned}\hat{\boldsymbol{n}} &= \left(1+\mathrm{o}(\varepsilon^2),0,-\varepsilon\frac{\partial\eta_1}{\partial z}+\mathrm{o}(\varepsilon^2)\right)\\ \boldsymbol{l} &= \left(\varepsilon\frac{\partial\eta_1}{\partial z}+\mathrm{o}(\varepsilon^2),0,1+\mathrm{o}(\varepsilon^2)\right)\\ \kappa &= \frac{1}{\eta_0}-\varepsilon\left(\frac{\eta_1}{\eta_0}+\frac{\partial^2\eta_1}{\partial z^2}\right)+\mathrm{o}(\varepsilon^2)\end{aligned}$$

and using Taylor expansions about η_0 we have

$$\begin{aligned} p^{[i]}(\eta(z,t),z,t) &= p_0^{[i]} + \varepsilon p_1^{[i]}(\eta_0,z,t) + \mathrm{o}(\varepsilon^2) \\ \boldsymbol{\tau}^{[i]}(\eta(z,t),z,t) &= \varepsilon \boldsymbol{\tau}_1^{[i]}(\eta_0,z,t) + \mathrm{o}(\varepsilon^2). \end{aligned}$$

From here we may work out the individual components of shear stress at $r = \eta_0$ for each fluid,

$$\begin{aligned} t_r^{[1]} &= \sigma_{rr}^{[1]}\hat{n}_r + \sigma_{rz}^{[1]}\hat{n}_z \\ &= \left(-p^{[1]} + \tau_{rr}^{[1]}\right)\hat{n}_r + \tau_{rz}^{[1]}\hat{n}_z \\ &= -p_0^{[1]} + \varepsilon(-p_1^{[1]} + \tau_{rr1}^{[1]}) + \mathrm{o}(\varepsilon^2) \end{aligned}$$

and

$$\begin{aligned} t_z^{[1]} &= \sigma_{rz}^{[1]}\hat{n}_r + \sigma_{zz}^{[1]}\hat{n}_z \\ &= \tau_{rz}^{[1]}\hat{n}_r + \left(-p^{[1]} + \tau_{zz}^{[1]}\right)\hat{n}_z \\ &= \varepsilon\left(\tau_{rz1}^{[1]} + p_0^{[1]}\frac{\partial \eta_1}{\partial z}\right) + \mathrm{o}(\varepsilon^2), \end{aligned}$$

so that

$$\boldsymbol{t}^{[1]} \sim \begin{pmatrix} -p_0^{[1]} + \varepsilon(-p_1^{[1]} + \tau_{rr1}^{[1]}) \\ 0 \\ \varepsilon\left(\tau_{rz1}^{[1]} + p_0^{[1]}\frac{\partial \eta_1}{\partial z}\right) \end{pmatrix}$$

as $\varepsilon \to 0$. We also have

$$\begin{aligned} t_r^{[2]} &= \sigma_{rr}^{[2]}\hat{n}_r + \sigma_{rz}^{[2]}\hat{n}_z \\ &= \left(-\bar{\rho}p^{[2]} + \bar{\mu}\tau_{rr}^{[2]}\right)\hat{n}_r + \bar{\mu}\tau_{rz}^{[2]}\hat{n}_z \\ &= -\bar{\rho}p_0^{[2]} + \varepsilon\left(-\bar{\rho}p_1^{[2]} + \bar{\mu}\tau_{rr1}^{[2]}\right) + \mathrm{o}(\varepsilon^2) \end{aligned}$$

and

$$\begin{aligned} t_z^{[2]} &= \sigma_{rz}^{[2]}\hat{n}_r + \sigma_{zz}^{[2]}\hat{n}_z \\ &= \bar{\mu}\tau_{rz}^{[2]}\hat{n}_r + \left(-\bar{\rho}p^{[2]} + \bar{\mu}\tau_{zz}^{[2]}\right)\hat{n}_z \\ &= \varepsilon\left(\bar{\mu}\tau_{rz1}^{[2]} + \bar{\rho}p_0^{[2]}\frac{\partial\eta_1}{\partial z}\right) + \mathrm{o}(\varepsilon^2), \end{aligned}$$

so that

$$\boldsymbol{t}^{[2]} \sim \begin{pmatrix} -\bar{\rho}p_0^{[2]} + \varepsilon\left(-\bar{\rho}p_1^{[2]} + \bar{\mu}\tau_{rr1}^{[2]}\right) \\ 0 \\ \varepsilon\left(\bar{\mu}\tau_{rz1}^{[2]} + \bar{\rho}p_0^{[2]}\frac{\partial\eta_1}{\partial z}\right) \end{pmatrix}$$

as $\varepsilon \to 0$.

Using these results for $\boldsymbol{t}^{[i]}$, we have

$$\boldsymbol{t}^{[i]} \cdot \boldsymbol{l} = 0$$

at O(1). At O(ε) we have

$$\begin{aligned} \boldsymbol{t}^{[1]} \cdot \boldsymbol{l} &= \tau_{rz1}^{[1]}(\eta_0, z, t) \\ \boldsymbol{t}^{[2]} \cdot \boldsymbol{l} &= \bar{\mu}\tau_{rz1}^{[2]}(\eta_0, z, t), \end{aligned}$$

therefore the tangential stress condition at $\mathrm{O}(\varepsilon)$ is given by

$$\tau_{rz1}^{[1]}(\eta_0, z, t) = \bar{\mu}\tau_{rz1}^{[2]}(\eta_0, z, t).$$

The jump in stress at the interface is

$$\boldsymbol{t}^{[1]} - \boldsymbol{t}^{[2]} = \begin{pmatrix} -p_0^{[1]} + \bar{\rho}p_0^{[2]} + \varepsilon\left(-p_1^{[1]} + \bar{\rho}p_1^{[2]} + \tau_{rr1}^{[1]} - \bar{\mu}\tau_{rr1}^{[2]}\right) \\ 0 \\ \varepsilon\left(\tau_{rz1}^{[1]} - \bar{\mu}\tau_{rz1}^{[2]} + \frac{\partial\eta_1}{\partial z}\left(p_0^{[1]} - \bar{\rho}p_0^{[2]}\right)\right) \end{pmatrix},$$

thus we have

$$\left(\boldsymbol{t}^{[1]} - \boldsymbol{t}^{[2]}\right) \cdot \hat{\boldsymbol{n}} = -p_0^{[1]} + \bar{\rho}p_0^{[2]} + \varepsilon\left(-p_1^{[1]} + \bar{\rho}p_1^{[2]} + \tau_{rr1}^{[1]} - \bar{\mu}\tau_{rr1}^{[2]}\right) + \mathrm{o}(\varepsilon^2).$$

Therefore the normal stress condition at leading order is given by

$$-p_0^{[1]} + \bar{\rho}p_0^{[2]} = -\frac{1}{\mathrm{Ca}\eta_0}$$

and at $\mathrm{O}(\varepsilon)$ takes the form

$$-p_1^{[1]}(\eta_0, z, t) + \bar{\rho}p_1^{[2]}(\eta_0, z, t) + \tau_{rr1}^{[1]}(\eta_0, z, t) - \bar{\mu}\tau_{rr1}^{[2]}(\eta_0, z, t) = \frac{1}{\mathrm{Ca}}\left(\frac{\eta_1}{\eta_0^2} + \frac{\partial^2\eta_1}{\partial z^2}\right).$$

In summary, at $\mathrm{O}(\varepsilon)$ we have the following conditions

$$\begin{aligned}
u_{r1}(1,z,t) &= \dot{R}_1(z,t) \\
u_{z1}(1,z,t) &= 0 \\
u_{r1}(0,z,t) &= 0 \\
\frac{\partial u_{z1}}{\partial r}(0,z,t) &= 0 \\
\boldsymbol{u}^{[1]}(\eta_0,z,t) &= \boldsymbol{u}^{[2]}(\eta_0,z,t) \\
u_{r1}^{[i]}(\eta_0,z,t) &= \dot{\eta}_1(z,t) \\
\tau_{rz1}^{[1]}(\eta_0,z,t) &= \bar{\mu}\tau_{rz1}^{[2]}(\eta_0,z,t) \\
-p_1^{[1]}(\eta_0,z,t) + \tau_{rr1}^{[1]}(\eta_0,z,t) &= -\bar{\rho}p_1^{[2]}(\eta_0,z,t) + \bar{\mu}\tau_{rr1}^{[2]}(\eta_0,z,t) + \frac{1}{\mathrm{Ca}}\left(\frac{\eta_1}{\eta_0^2} + \frac{\partial^2\eta_1}{\partial z^2}\right).
\end{aligned}$$

As in the one layer case we take

$$R(z,t) = \mathcal{R}\left(\sqrt{1 + 2\varepsilon\left(\mathrm{e}^{i(kz-t)} + \mathrm{e}^{-i(kz+t)}\right)}\right),$$

where $k = 2\pi R_0/\lambda$, thus

$$R_1(z,t) = \mathcal{R}\left(\mathrm{e}^{i(kz-t)} + \mathrm{e}^{-i(kz+t)}\right).$$

We assume that the position of the interface follows the motion of the boundary, therefore we take the free surface at $\mathrm{O}(\varepsilon)$ to be of the form

$$\eta_1(z,t) = \mathcal{R}\left(\tilde{\eta}_1\mathrm{e}^{i(kz-t)} + \tilde{\eta}_2\mathrm{e}^{-i(kz+t)}\right),$$

where $\tilde{\eta}_1$, $\tilde{\eta}_2$ are constant. We then take solutions of the form

$$\begin{aligned}
u_{r1}^{[i]}(r,z,t) &= \mathcal{R}\left(f_1^{[i]}(r)\mathrm{e}^{i(kz-t)} + f_2^{[i]}(r)\mathrm{e}^{-i(kz+t)}\right) \\
u_{z1}^{[i]}(r,z,t) &= \mathcal{R}\left(g_1^{[i]}(r)\mathrm{e}^{i(kz-t)} + g_2^{[i]}(r)\mathrm{e}^{-i(kz+t)}\right) \\
p_1^{[i]}(r,z,t) &= \mathcal{R}\left(h_1^{[i]}(r)\mathrm{e}^{i(kz-t)} + h_2^{[i]}(r)\mathrm{e}^{-i(kz+t)}\right) \\
\tau_{rr1}^{[i]}(r,z,t) &= \mathcal{R}\left(\alpha_1^{[i]}(r)\mathrm{e}^{i(kz-t)} + \alpha_2^{[i]}(r)\mathrm{e}^{-i(kz+t)}\right) \\
\tau_{rz1}^{[i]}(r,z,t) &= \mathcal{R}\left(\beta_1^{[i]}(r)\mathrm{e}^{i(kz-t)} + \beta_2^{[i]}(r)\mathrm{e}^{-i(kz+t)}\right) \\
\tau_{\theta\theta 1}^{[i]}(r,z,t) &= \mathcal{R}\left(\gamma_1^{[i]}(r)\mathrm{e}^{i(kz-t)} + \gamma_2^{[i]}(r)\mathrm{e}^{-i(kz+t)}\right) \\
\tau_{zz1}^{[i]}(r,z,t) &= \mathcal{R}\left(\delta_1^{[i]}(r)\mathrm{e}^{i(kz-t)} + \delta_2^{[i]}(r)\mathrm{e}^{-i(kz+t)}\right).
\end{aligned}$$

We begin by considering the inner fluid, substituting these solutions into the equations (3.2.1) - (3.2.7), we see

$$f_1^{[1]}(r) = f_2^{[1]}(r) = f^{[1]}(r);\ g_1^{[1]}(r) = -g_2^{[1]}(r) = g^{[1]}(r);\ h_1^{[1]}(r) = h_2^{[1]}(r) = h^{[1]}(r);$$

$$\alpha_1^{[1]}(r) = \alpha_2^{[1]}(r) = \alpha^{[1]}(r);\ \beta_1^{[1]}(r) = -\beta_2^{[1]}(r) = \beta^{[1]}(r);$$

$$\gamma_1^{[1]}(r) = \gamma_2^{[1]}(r) = \gamma^{[1]}(r);\ \text{and}\ \delta_1^{[1]}(r) = \delta_2^{[1]}(r) = \delta^{[1]}(r),$$

from which we obtain the seven equations

$$
\begin{aligned}
0 &= \frac{\mathrm{d}f^{[1]}}{\mathrm{d}r} + \frac{f^{[1]}(r)}{r} + ikg^{[1]}(r) && (3.2.15)\\
-i\mathrm{Re}f^{[1]}(r) &= -\frac{\mathrm{d}h^{[1]}}{\mathrm{d}r} + \frac{\alpha^{[1]}(r)}{r} - \frac{\gamma^{[1]}(r)}{r} + \frac{\mathrm{d}\alpha^{[1]}}{\mathrm{d}r} + ik\beta^{[1]}(r) && (3.2.16)\\
-i\mathrm{Re}g^{[1]}(r) &= -ikh^{[1]}(r) + \frac{\beta^{[1]}(r)}{r} + \frac{\mathrm{d}\beta^{[1]}}{\mathrm{d}r} + ik\delta^{[1]}(r) && (3.2.17)\\
\alpha^{[1]}(r) &= 2\frac{\mathrm{d}f^{[1]}}{\mathrm{d}r} && (3.2.18)\\
\beta^{[1]}(r) &= ikf^{[1]}(r) + \frac{\mathrm{d}g^{[1]}}{\mathrm{d}r} && (3.2.19)\\
\gamma^{[1]}(r) &= \frac{2}{r}f^{[1]}(r) && (3.2.20)\\
\delta^{[1]}(r) &= 2ikg^{[1]}(r). && (3.2.21)
\end{aligned}
$$

Upon substitution of (3.2.18) - (3.2.21) into (3.2.15) - (3.2.17) we have

$$
\begin{aligned}
0 &= \frac{\mathrm{d}f^{[1]}}{\mathrm{d}r} + \frac{f^{[1]}(r)}{r} + ikg^{[1]}(r) && (3.2.22)\\
0 &= -\frac{\mathrm{d}h^{[1]}}{\mathrm{d}r} + \frac{\mathrm{d}^2f^{[1]}}{\mathrm{d}r^2} + \frac{1}{r}\frac{\mathrm{d}f^{[1]}}{\mathrm{d}r} + \left(i\mathrm{Re} - \frac{1}{r^2} - k^2\right)f^{[1]}(r) && (3.2.23)\\
0 &= -ikh^{[1]}(r) + \frac{\mathrm{d}^2g^{[1]}}{\mathrm{d}r^2} + \frac{1}{r}\frac{\mathrm{d}g^{[1]}}{\mathrm{d}r} + \left(i\mathrm{Re} - k^2\right)g^{[1]}(r). && (3.2.24)
\end{aligned}
$$

Rearranging (3.2.22) we obtain

$$
g^{[1]}(r) = \frac{i}{k}\left(\frac{\mathrm{d}f^{[1]}}{\mathrm{d}r} + \frac{1}{r}f^{[1]}(r)\right), \tag{3.2.25}
$$

which upon differentiating twice and substituting into (3.2.24) yields

$$
\begin{aligned}
h^{[1]}(r) = \frac{1}{k^2}\frac{\mathrm{d}^3f^{[1]}}{\mathrm{d}r^3} + \frac{2}{rk^2}\frac{\mathrm{d}^2f^{[1]}}{\mathrm{d}r^2} + \left(\frac{i\mathrm{Re}}{k^2} - \frac{1}{r^2k^2} - 1\right)\frac{\mathrm{d}f^{[1]}}{\mathrm{d}r}\\
+ \left(\frac{i\mathrm{Re}}{rk^2} - \frac{1}{r} + \frac{1}{r^3k^2}\right)f^{[1]}(r).
\end{aligned} \tag{3.2.26}
$$

From this and (3.2.23) we obtain a fourth-order ODE for $f^{[1]}(r)$, given by

$$\frac{1}{k^2}\frac{\mathrm{d}^4 f^{[1]}}{\mathrm{d}r^4}+\frac{2}{rk^2}\frac{\mathrm{d}^3 f^{[1]}}{\mathrm{d}r^3}+\left(\frac{i\mathrm{Re}}{k^2}-\frac{3}{r^2k^2}-2\right)\frac{\mathrm{d}^2 f^{[1]}}{\mathrm{d}r^2}+\left(\frac{i\mathrm{Re}}{rk^2}+\frac{3}{r^3k^2}-\frac{2}{r}\right)\frac{\mathrm{d}f^{[1]}}{\mathrm{d}r} + \left(\frac{2}{r^2}-i\mathrm{Re}\left(1+\frac{1}{r^2k^2}\right)+k^2-\frac{3}{r^4k^2}\right)f^{[1]}=0. \tag{3.2.27}$$

In the same way that we have done before, substituting our expressions for $u_{r1}^{[2]}, u_{z1}^{[2]}$ etc. into (3.2.8) - (3.2.14) shows us that

$$f_1^{[2]}(r)=f_2^{[2]}(r)=f^{[2]}(r);\ g_1^{[2]}(r)=-g_2^{[2]}(r)=g^{[2]}(r);\ h_1^{[2]}(r)=h_2^{[2]}(r)=h^{[2]}(r);$$

$$\alpha_1^{[2]}(r)=\alpha_2^{[2]}(r)=\alpha^{[2]}(r);\ \beta_1^{[2]}(r)=-\beta_2^{[2]}(r)=\beta^{[2]}(r);$$

$$\gamma_1^{[2]}(r)=\gamma_2^{[2]}(r)=\gamma^{[2]}(r);\ \text{and}\ \delta_1^{[2]}(r)=\delta_2^{[2]}(r)=\delta^{[2]}(r).$$

Using this we are left with the seven equations relating to the outer Oldroyd B fluid,

$$\begin{aligned}
0 &= \frac{\mathrm{d}f^{[2]}}{\mathrm{d}r}+\frac{f^{[2]}(r)}{r}+ikg^{[2]}(r) && (3.2.28)\\
-i\mathrm{Re}f^{[2]}(r) &= -\frac{\mathrm{d}h^{[2]}}{\mathrm{d}r}+\frac{\bar{\mu}}{\bar{\rho}}\left(\frac{\alpha^{[2]}(r)}{r}-\frac{\gamma^{[2]}(r)}{r}+\frac{\mathrm{d}\alpha^{[2]}}{\mathrm{d}r}+ik\beta^{[2]}(r)\right) && (3.2.29)\\
-i\mathrm{Re}g^{[2]}(r) &= -ikh^{[2]}(r)+\frac{\bar{\mu}}{\bar{\rho}}\left(\frac{\beta^{[2]}(r)}{r}+\frac{\mathrm{d}\beta^{[2]}}{\mathrm{d}r}+ik\delta^{[2]}(r)\right) && (3.2.30)\\
\alpha^{[2]}(r) &= 2\Lambda\frac{\mathrm{d}f^{[1]}}{\mathrm{d}r} && (3.2.31)\\
\beta^{[2]}(r) &= \Lambda\left(ikf^{[2]}(r)+\frac{\mathrm{d}g^{[2]}}{\mathrm{d}r}\right) && (3.2.32)\\
\gamma^{[2]}(r) &= \frac{2}{r}\Lambda f^{[1]}(r) && (3.2.33)\\
\delta^{[2]}(r) &= 2ik\Lambda g^{[1]}(r), && (3.2.34)
\end{aligned}$$

where

$$\Lambda=\frac{1-i\bar{\lambda}M^{[2]}}{1-iM^{[2]}}.$$

Upon substitution of (3.2.31) - (3.2.34) into (3.2.28) - (3.2.30), we obtain

$$0 = \frac{\mathrm{d}f^{[2]}}{\mathrm{d}r} + \frac{f^{[2]}(r)}{r} + ikg^{[2]}(r) \tag{3.2.35}$$

$$0 = -\frac{\mathrm{d}h^{[2]}}{\mathrm{d}r} + \frac{\bar{\mu}\Lambda}{\bar{\rho}}\frac{\mathrm{d}^2 f^{[2]}}{\mathrm{d}r^2} + \frac{\bar{\mu}\Lambda}{r\bar{\rho}}\frac{\mathrm{d}f^{[2]}}{\mathrm{d}r} + \left(i\mathrm{Re} - \frac{\bar{\mu}\Lambda}{r^2\bar{\rho}} - \frac{k^2\bar{\mu}\Lambda}{\bar{\rho}}\right) f^{[2]}(r) \tag{3.2.36}$$

$$0 = -ikh^{[2]}(r) + \frac{\bar{\mu}\Lambda}{\bar{\rho}}\frac{\mathrm{d}^2 g^{[2]}}{\mathrm{d}r^2} + \frac{\bar{\mu}\Lambda}{r\bar{\rho}}\frac{\mathrm{d}g^{[2]}}{\mathrm{d}r} + \left(i\mathrm{Re} - \frac{k^2\bar{\mu}\Lambda}{\bar{\rho}}\right) g^{[2]}(r). \tag{3.2.37}$$

Rearranging (3.2.35) we obtain

$$g^{[2]}(r) = \frac{i}{k}\left(\frac{\mathrm{d}f^{[2]}}{\mathrm{d}r} + \frac{1}{r}f^{[2]}(r)\right), \tag{3.2.38}$$

which upon differentiating twice and substituting into (3.2.37) yields

$$\begin{aligned} h^{[2]}(r) = \frac{\bar{\mu}\Lambda}{k^2\bar{\rho}}\frac{\mathrm{d}^3 f^{[2]}}{\mathrm{d}r^3} + \frac{2\bar{\mu}\Lambda}{rk^2\bar{\rho}}\frac{\mathrm{d}^2 f^{[2]}}{\mathrm{d}r^2} + \left(\frac{i\mathrm{Re}}{k^2} - \frac{\bar{\mu}\Lambda}{r^2k^2\bar{\rho}} - \frac{\bar{\mu}\Lambda}{\bar{\rho}}\right)\frac{\mathrm{d}f^{[2]}}{\mathrm{d}r} \\ + \left(\frac{i\mathrm{Re}}{rk^2} - \frac{\bar{\mu}\Lambda}{r\bar{\rho}} + \frac{\bar{\mu}\Lambda}{r^3k^2\bar{\rho}}\right) f^{[2]}(r). \end{aligned} \tag{3.2.39}$$

From this and (3.2.36) we obtain a fourth-order ODE for $f^{[2]}(r)$, given by

$$\begin{aligned} \frac{\bar{\mu}\Lambda}{k^2\bar{\rho}}\frac{\mathrm{d}^4 f^{[2]}}{\mathrm{d}r^4} + \frac{2\bar{\mu}\Lambda}{rk^2\bar{\rho}}\frac{\mathrm{d}^3 f^{[2]}}{\mathrm{d}r^3} + \left(\frac{i\mathrm{Re}}{k^2} - \frac{3\bar{\mu}\Lambda}{r^2k^2\bar{\rho}} - 2\frac{\bar{\mu}\Lambda}{\bar{\rho}}\right)\frac{\mathrm{d}^2 f^{[2]}}{\mathrm{d}r^2} + \left(\frac{i\mathrm{Re}}{rk^2} + \frac{3\bar{\mu}\Lambda}{r^3k^2\bar{\rho}} - \frac{2\bar{\mu}\Lambda}{r\bar{\rho}}\right) \\ \frac{\mathrm{d}f^{[2]}}{\mathrm{d}r} + \left(\frac{2\bar{\mu}\Lambda}{r^2\bar{\rho}} - i\mathrm{Re}\left(1 + \frac{1}{r^2k^2}\right) + \frac{k^2\bar{\mu}\Lambda}{\bar{\rho}} - \frac{3\bar{\mu}\Lambda}{r^4k^2\bar{\rho}}\right) f^{[2]} = 0. \end{aligned} \tag{3.2.40}$$

We must now formulate our boundary and interfacial conditions in terms of $f^{[i]}(r)$.

As in the one layer fluid case the boundary conditions are given by

$$\begin{aligned} f^{[2]}(1) &= -i \\ \frac{\mathrm{d}f^{[2]}}{\mathrm{d}r}(1) &= i \\ f^{[1]}(0) &= 0 \\ \frac{\mathrm{d}^2 f^{[1]}}{\mathrm{d}r^2} + \frac{1}{r}\frac{\mathrm{d}f^{[1]}}{\mathrm{d}r} - \frac{1}{r^2}f^{[1]} &\to 0 \text{ as } r \to 0. \end{aligned}$$

At $r = \eta_0$ the radial velocity is given by

$$u_{r1}^{[i]}(\eta_0, z, t) = f^{[i]}(\eta_0) R_1(z, t),$$

thus the r-component of the continuity of velocity condition is given by

$$f^{[1]}(\eta_0) = f^{[2]}(\eta_0).$$

Similarly, using the definition for $g^{[i]}(r)$ and the fact that

$$u_{z1}^{[i]}(\eta_0, z, t) = g^{[i]}(\eta_0) \left(\mathrm{e}^{i(kz-t)} - \mathrm{e}^{-i(kz-t)} \right),$$

the z-component of the continuity of velocity condition becomes

$$\frac{\mathrm{d}f^{[1]}}{\mathrm{d}r}(\eta_0) = \frac{\mathrm{d}f^{[2]}}{\mathrm{d}r}(\eta_0).$$

We have the expression for $u_{r1}^{[i]}$ above and

$$\dot{\eta}_1(z, t) = -i\tilde{\eta}_1 \mathrm{e}^{i(kz-t)} - i\tilde{\eta}_2 \mathrm{e}^{-i(kz+t)},$$

therefore

$$f^{[i]}(\eta_0) = -i\tilde{\eta}_1 = -i\tilde{\eta}_2.$$

Since $\tilde{\eta}_1$ and $\tilde{\eta}_2$ are non-zero constants it follows that $\tilde{\eta}_1 = \tilde{\eta}_2 = \tilde{\eta}$. Therefore the kinematic condition is given by

$$f^{[i]}(\eta_0) = -i\tilde{\eta}. \tag{3.2.41}$$

Recall the tangential stress condition is given by $\tau_{rz1}^{[1]} = \bar{\mu}\tau_{rz1}^{[2]}$, using the definitions for $\beta^{[i]}$, (3.2.19) and (3.2.32), this becomes

$$ikf^{[1]} + \frac{\mathrm{d}g^{[1]}}{\mathrm{d}r} = \bar{\mu}\Lambda\left(ikf^{[2]} + \frac{\mathrm{d}g^{[2]}}{\mathrm{d}r}\right).$$

Upon substitution of $g^{[i]}(r)$, i.e. equations (3.2.25) and (3.2.38), into the above equation and using the kinematic condition and continuity of velocity, we obtain the tangential stress condition in terms of $f^{[i]}$,

$$\frac{\mathrm{d}^2 f^{[2]}}{\mathrm{d}r^2} = \frac{1}{\bar{\mu}\Lambda}\frac{\mathrm{d}^2 f^{[1]}}{\mathrm{d}r^2} + \left(\frac{1}{\bar{\mu}\Lambda} - 1\right)\left(\frac{1}{\eta_0}\frac{\mathrm{d}f^{[1]}}{\mathrm{d}r} + i\tilde{\eta}\left(\frac{1}{\eta_0^2} - k^2\right)\right)$$

at $r = \eta_0$.

Finally, the normal stress condition is given by

$$-p_1^{[1]} + \bar{\rho}p_1^{[2]} + \tau_{rr1}^{[1]} - \bar{\mu}\tau_{rr1}^{[2]} = \frac{1}{\mathrm{Ca}}\left(\frac{\eta_1}{\eta_0^2} + \frac{\partial^2\eta_1}{\partial z^2}\right),$$

which becomes, using the definitions for $\alpha^{[i]}$, $p_1^{[i]}$ and η_1,

$$-h^{[1]} + \bar{\rho}h^{[2]} + 2\frac{\mathrm{d}f^{[1]}}{\mathrm{d}r} - 2\bar{\mu}\Lambda\frac{\mathrm{d}f^{[2]}}{\mathrm{d}r} = \frac{\tilde{\eta}}{\mathrm{Ca}}\left(\frac{1}{\eta_0^2} - k^2\right).$$

Upon substitution of $h^{[i]}$, (3.2.26) and (3.2.39), into the above equation and using the kinematic condition, continuity of velocity and the tangential stress condition, we obtain

the normal stress condition in terms of $f^{[i]}$,

$$\frac{\mathrm{d}^3 f^{[2]}}{\mathrm{d}r^3} = \frac{1}{\bar{\mu}\Lambda}\frac{\mathrm{d}^3 f^{[1]}}{\mathrm{d}r^3} + \left(3\left(1-\frac{1}{\bar{\mu}\Lambda}\right)\left(\frac{1}{\eta_0^2}+k^2\right) + \frac{i\mathrm{Re}}{\bar{\mu}\Lambda}(1-\bar{\rho})\right)\frac{\mathrm{d}f^{[1]}}{\mathrm{d}r} + \tilde{\eta}\left(\frac{k^2}{\bar{\mu}\Lambda\mathrm{Ca}}\left(\frac{1}{\eta_0^2}-k^2\right) + i\left(\frac{3}{\eta_0}\left(1-\frac{1}{\bar{\mu}\Lambda}\right)\left(\frac{1}{\eta_0}-k^2\right) - \frac{i\mathrm{Re}}{\bar{\mu}\Lambda\eta_0}(1-\bar{\rho})\right)\right)$$

at $r = \eta_0$.

We are now in a position to determine a solution to this problem. The general solution to (3.2.27) is given by

$$f^{[1]}(r) = c_1 I_1(rk) + c_2 K_1(rk) + c_3 J_1(\sqrt{A}r) + c_4 K_1(-i\sqrt{A}r),$$

where

$$A = i\mathrm{Re} - k^2,$$

and is valid for $0 \leq r < \eta_0$. The general solution to (3.2.40) is given by

$$f^{[2]}(r) = d_1 I_1(rk) + d_2 K_1(rk) + d_3 J_1(\sqrt{B}r) + d_4 K_1(-i\sqrt{B}r),$$

where

$$B = \frac{i\mathrm{Re}\bar{\rho}}{\bar{\mu}\Lambda} - k^2,$$

and is valid for $\eta_0 < r < R_0$.

Using our previous work in section 2.1 to show that the two boundary conditions at $r = 0$ indicate $c_2 = c_4 = 0$, we have

$$f^{[1]}(r) = c_1 I_1(rk) + c_3 J_1(\sqrt{A}r).$$

Note that, as a general solution, this does not depend on any non-Newtonian parameter;

however, since the interfacial conditions are affected by the non-Newtonian nature of the outer fluid, it is possible that some non-Newtonian effects may be observed in the fluid near the interface.

We now have seven unknowns, $c_1, c_3, d_1, d_2, d_3, d_4$ and $\tilde{\eta}$, and seven remaining conditions to determine them. Rewriting these conditions in terms of the general solutions for $f^{[1]}$ and $f^{[2]}$ (see Appendix D) we are able to put them into the form $\boldsymbol{M} \cdot \boldsymbol{c} = \boldsymbol{b}$, where

$$\boldsymbol{c} = \begin{pmatrix} c_1 & c_3 & d_1 & d_2 & d_3 & d_4 & \tilde{\eta} \end{pmatrix}^T.$$

We may then use MATLAB to solve this system of equations and create plots which represent the flow.

Table 3.1: Standard Dimensional Parameter Values.

Parameter	Description	Value	Units
R_0	Radius	0.025	m
ω	Contractile frequency	$\pi/10$	rad/s
λ	Wavelength	0.06	m
$\mu^{[1]}$	Chyme zero shear viscosity	5	Pa·s
$\rho^{[1]}$	Chyme fluid density	1000	kg/m^3
$\mu^{[2]}$	Mucus zero shear viscosity	10	Pa·s
$\rho^{[2]}$	Mucus fluid density	1000	kg/m^3
λ_1	Mucus relaxation time	30	s
λ_2	Mucus retardation time	0.00195	s
σ	Interfacial tension	0.072	N/m

Table 3.2: Standard Nondimensional Parameter Values.

Parameter	Value
Re	0.039
k	$5\pi/6$
ε	0.01
η_0	0.995
Ca	0.5454
$\bar{\mu}$	2
$\bar{\rho}$	1
$\bar{\lambda}$	6.5×10^{-5}

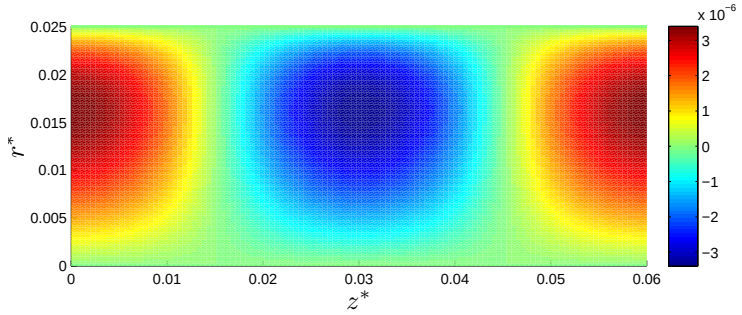

(a) $t = 0$ ($t^* = 0$ s)

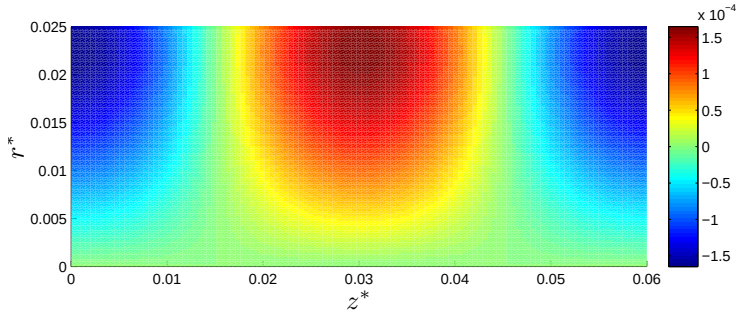

(b) $t = \pi/2$ ($t^* = 5$ s)

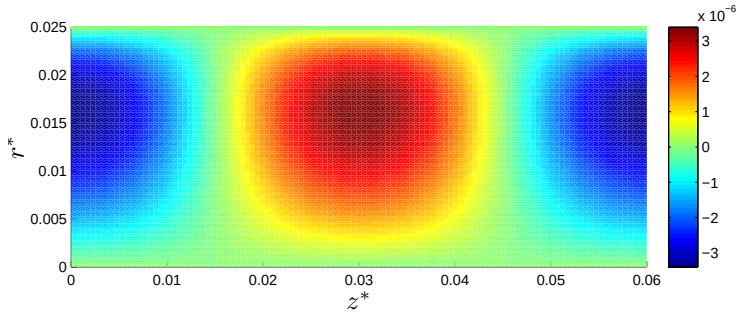

(c) $t = \pi$ ($t^* = 10$ s)

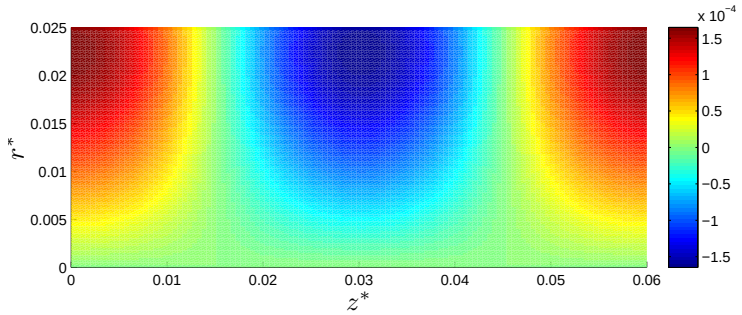

(d) $t = 3\pi/2$ ($t^* = 15$ s)

Figure 3.1: Colour plots of u_r^* (m/s) at O(ε) for the standard parameters, where r^* and z^* have units m. The colour scales differ between subplots in order to prevent detail being lost at the times with slower flow velocity.

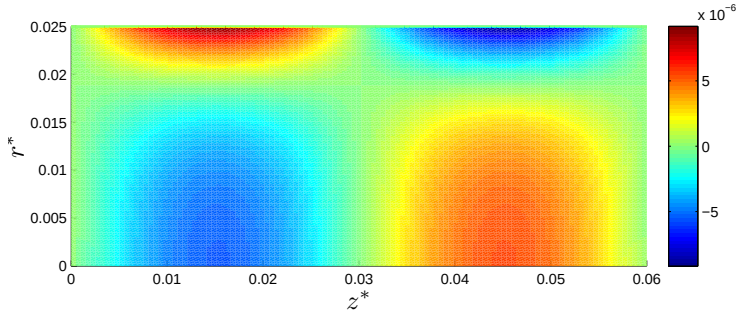

(a) $t = 0$ ($t^* = 0$ s)

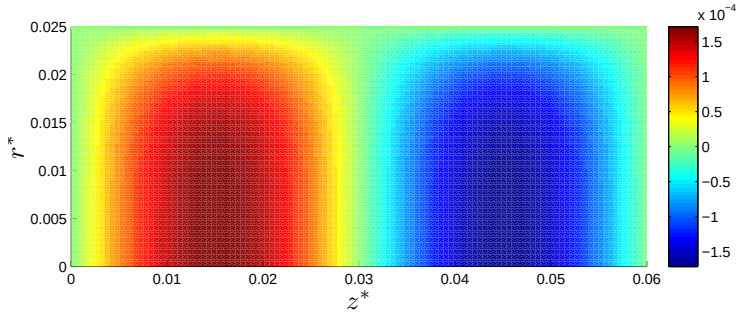

(b) $t = \pi/2$ ($t^* = 5$ s)

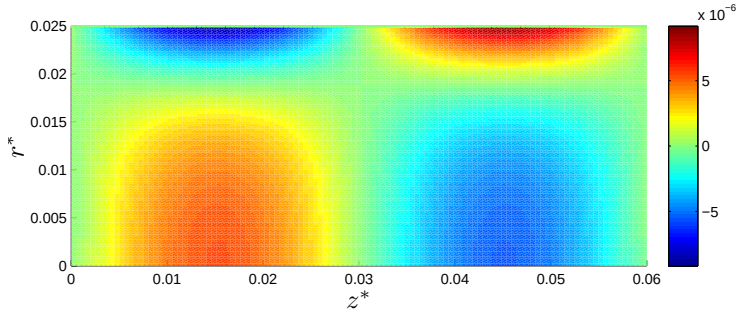

(c) $t = \pi$ ($t^* = 10$ s)

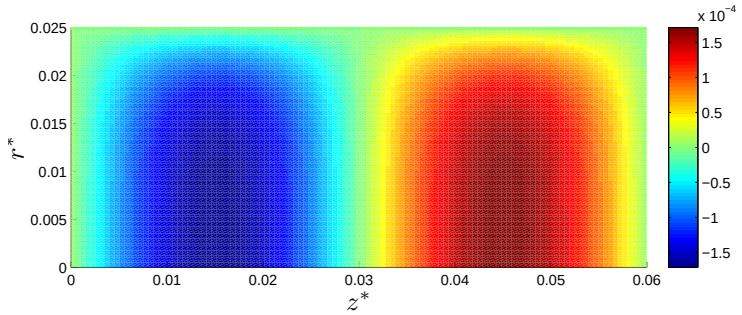

(d) $t = 3\pi/2$ ($t^* = 15$ s)

Figure 3.2: Colour plots of u_z^* (m/s) at O(ε) for the standard parameters, where r^* and z^* have units m. The colour scales differ between subplots in order to prevent detail being lost at the times with slower flow velocity.

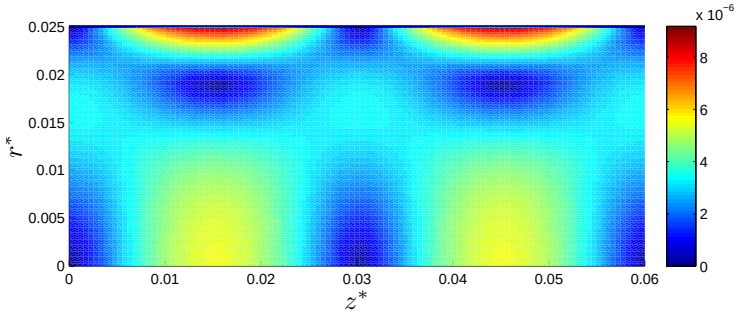

(a) $t = 0$ ($t^* = 0$ s)

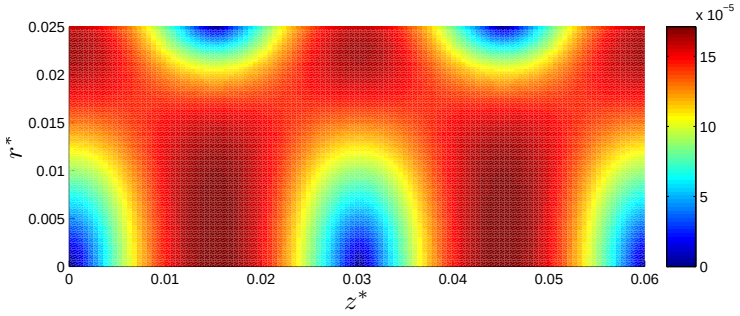

(b) $t = \pi/2$ ($t^* = 5$ s)

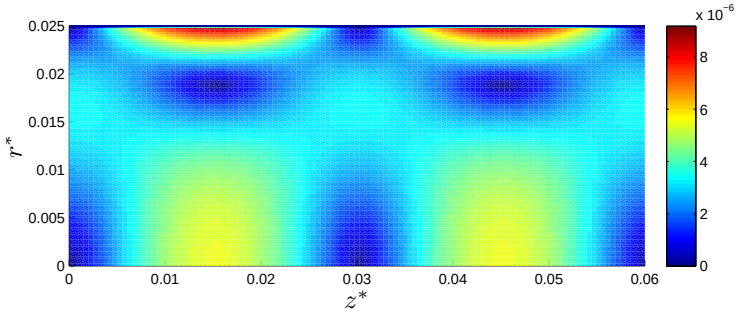

(c) $t = \pi$ ($t^* = 10$ s)

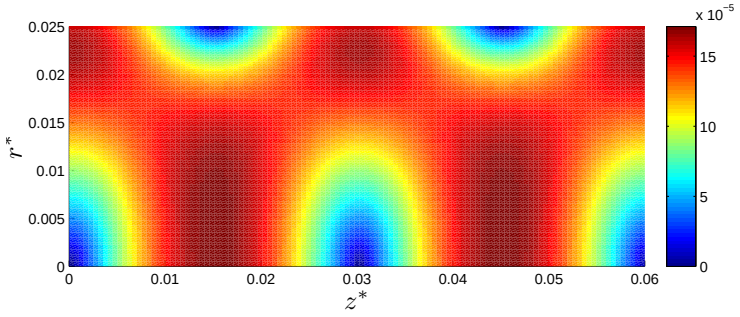

(d) $t = 3\pi/2$ ($t^* = 15$ s)

Figure 3.3: Magnitude of velocity (m/s) at O(ε) for the standard parameters, where r^* and z^* have units m. The colour scales differ between subplots in order to prevent detail being lost at the times with slower flow velocity.

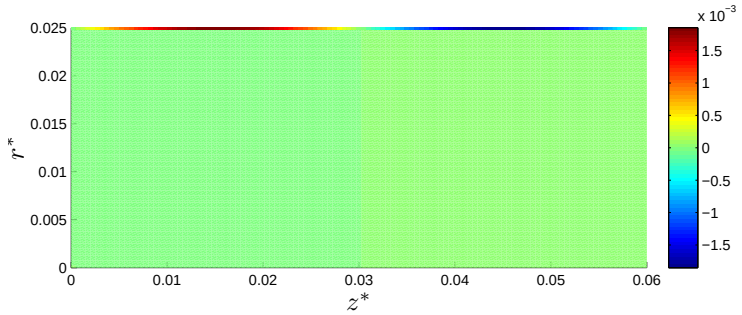

(a) $t = 0$ ($t^* = 0$ s)

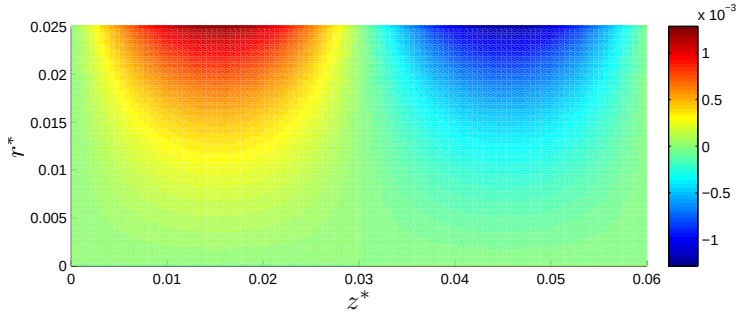

(b) $t = \pi/2$ ($t^* = 5$ s)

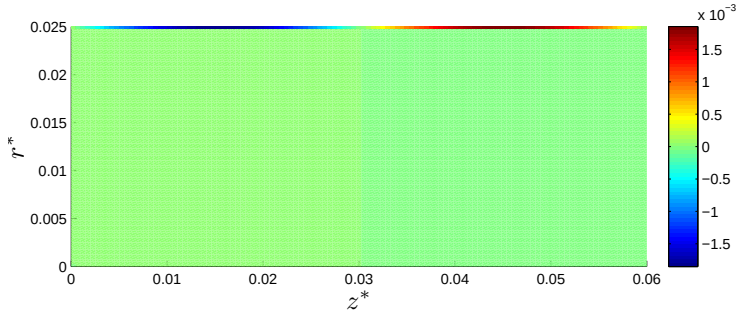

(c) $t = \pi$ ($t^* = 10$ s)

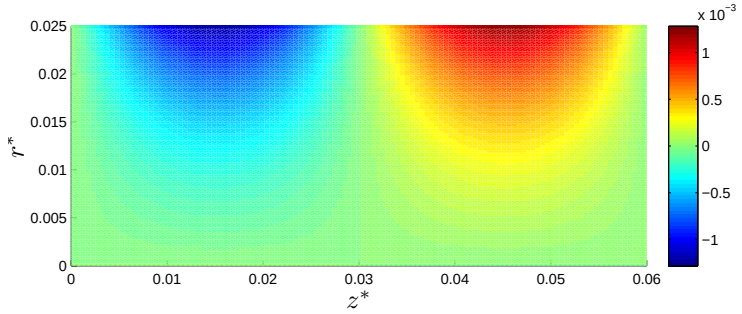

(d) $t = 3\pi/2$ ($t^* = 15$ s)

Figure 3.4: Vorticity of flow (s^{-1}) at $O(\varepsilon)$ for the standard parameters, where r^* and z^* have units m.

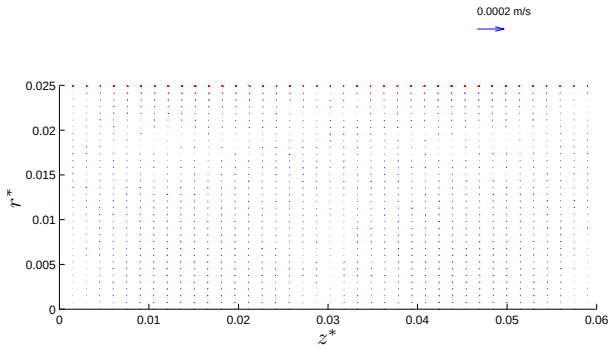

(a) $t = 0$ ($t^* = 0$ s)

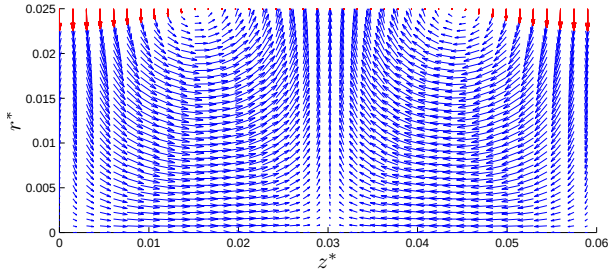

(b) $t = \pi/2$ ($t^* = 5$ s)

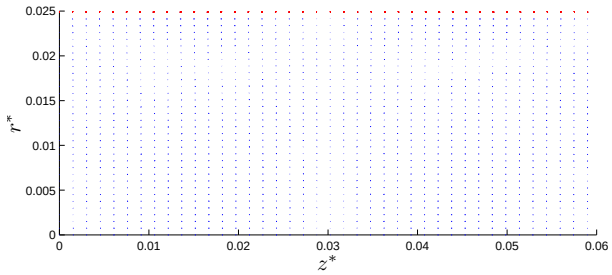

(c) $t = \pi$ ($t^* = 10$ s)

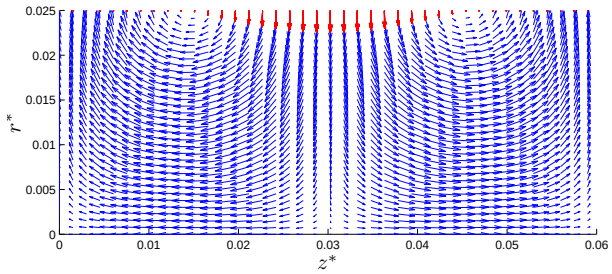

(d) $t = 3\pi/2$ ($t^* = 15$ s)

Figure 3.5: Velocity fields at O(ε) for the standard parameters at four time instants with blue representing chyme and red representing mucus, where r^* and z^* have units m.

So far in this chapter we have formulated the equations of motion and the boundary and interfacial conditions for the two layer flow of a Newtonian fluid and an Oldroyd B fluid. The viscoelastic Oldroyd B model was used to represent the thin layer of mucus lining the colonic epithelium. After formulating these equations and conditions we found solutions for the flow at O(ε). The only non-Newtonian parameters to appear in the general solution for the Oldroyd B fluid at O(ε) are $M^{[2]}$ and $\bar{\lambda}$ (through their effect on Λ), the scaled relaxation time and ratio between retardation and relaxation time respectively. In addition both the normal and tangential stress conditions involve Λ and we also have a normal stress condition appearing at O(1) which does not affect our flow fields but could be used as a pressure condition (which we have not considered in this thesis).

To view the effect on the flow of including a mucus layer we compare figures 2.2 - 2.6 to figures 3.1 - 3.5. There is little or no difference at $t = \pi/2$ and $t = 3\pi/2$, but small differences may be seen in the velocity magnitude and pattern at $t = 0$ and $t = \pi$ between the two models. This may be due to the elastic nature of mucus, with energy being released even when the wall is momentarily at rest. At these times both $|u_z^*|$ and the velocity magnitude have their maxima near the edge of the pipe with this model, whereas the maxima occur around the centre of the pipe with the previous one layer model. In addition u_r^* remains non-zero closer to the outer boundary in the two layer model. However, these differences in velocity occur only at $t = 0$ and $t = \pi$, where the flow is much slower than at other times; figures 2.6 and 3.5 put the differences in velocity magnitude into perspective. Thus there is little difference overall in the flow between the one and two layer models.

In the next section we shall investigate what influence the parameters specific to the two layer model have on the flow. We will do this by in turn fixing all except one parameter and allowing that one to take a range of values based on our understanding of the physical reality.

3.3 Variation of Mucus Specific Parameters

We now investigate the effects of varying the parameters specific to the two layer model. We consider only parameters specific to the mucus layer here since we will investigate the influence of other parameters in chapter 5.

The figures in this section look at plotting u_z^* for fixed values of z^* and u_r^* for fixed values of r^*; in these plots the velocity scale is 50 times the length scale. For u_z^* we look at (dimensional) $z^* = \lambda/12,\ \lambda/8,\ \lambda/4$, i.e. $z^* = 0.005,\ 0.0075,\ 0.015$ m. We only need to look at the first quarter of the wavelength since the two halves are anti-symmetric (about $z^* = \lambda/2$) and each half wavelength is symmetric about $z^* = \lambda/4$. For u_r^* we consider (nondimensional) $r = 0.1,\ 0.5,\ 0.9$, which corresponds to dimensional values of 0.0025, 0.0125 and 0.0225 m.

Figure 3.6(a) displays the u_z^* flow profile for the parameters from the previous section at $t = 0,\ \pi/2,\ \pi,\ 3\pi/2$, which corresponds to times of 0, 5, 10 and 15 s. At each time $|u_z^*|$ is greatest for $z^* = 0.015$ m and least for $z^* = 0.005$ m, as we expected based on figure 3.2. In the rest of this section we look at only $t = 0$ when considering the parameter influence on u_z^*, since flow at this time step contains regions of flow in both the positive and negative directions.

Similarly, figure 3.6(b) displays the u_r^* flow profile for the parameters from the previous section at $t = 0,\ \pi/2,\ \pi,\ 3\pi/2$. As we can see $|u_r^*|$ is greatest at $t = \pi/2$ and $t = 3\pi/2$ (again, as expected based on figure 3.1), thus we choose to consider u_r^* at $t = \pi/2$ for the rest of this section.

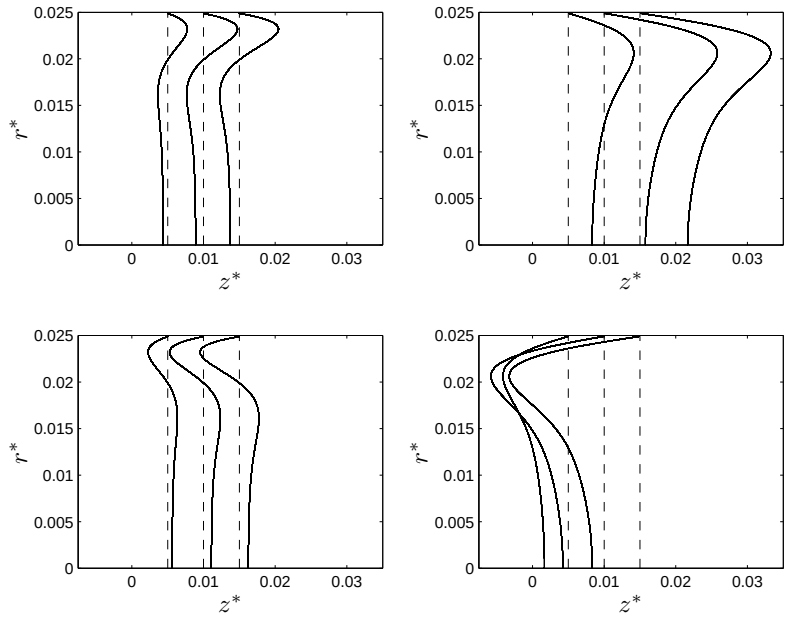

(a) u_z^* (m/s) for fixed values of z^* (m).

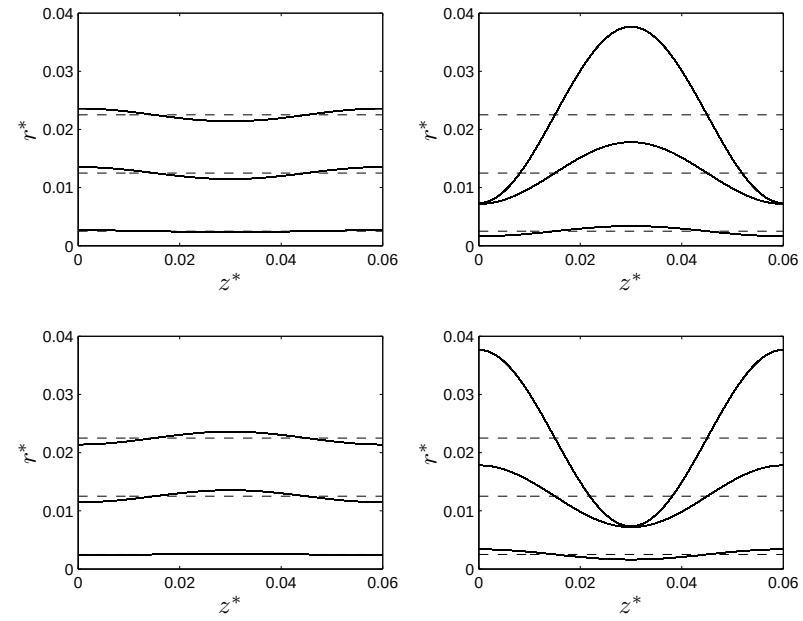

(b) u_r^* (m/s) for fixed values of r^* (m).

Figure 3.6: Flow profiles at $t = 0, \pi/2, \pi, 3\pi/2$ (l-r, t-b) for the standard parameters with velocity scale 50 times the length scale.

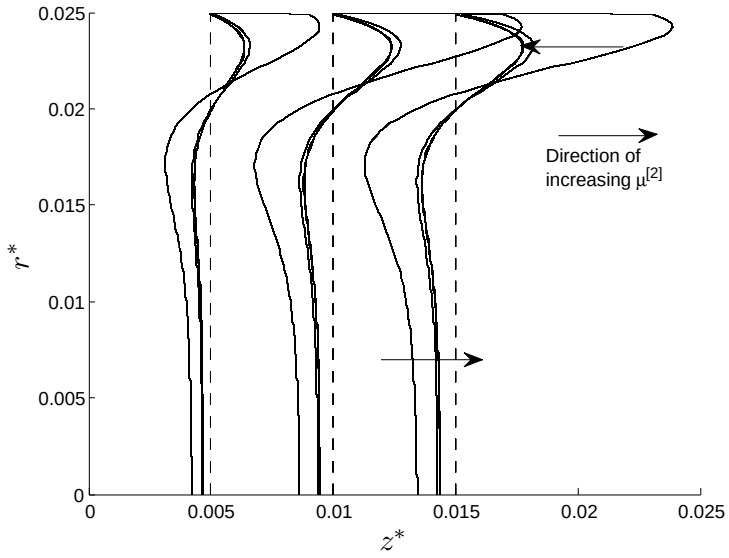

(a) u_z^* (m/s) for fixed values of z^* (m).

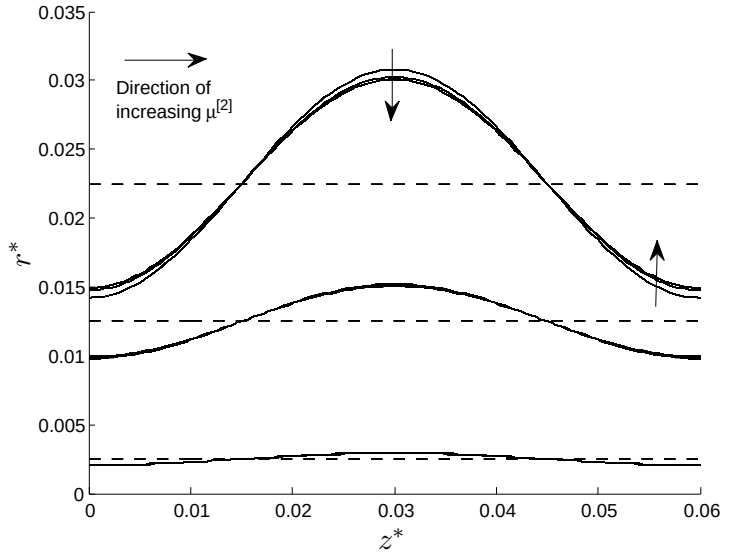

(b) u_r^* (m/s) for fixed values of r^* (m).

Figure 3.7: Flow profiles for varying $\mu^{[2]}$ (Pa·s) with velocity scale 50 times the length scale.

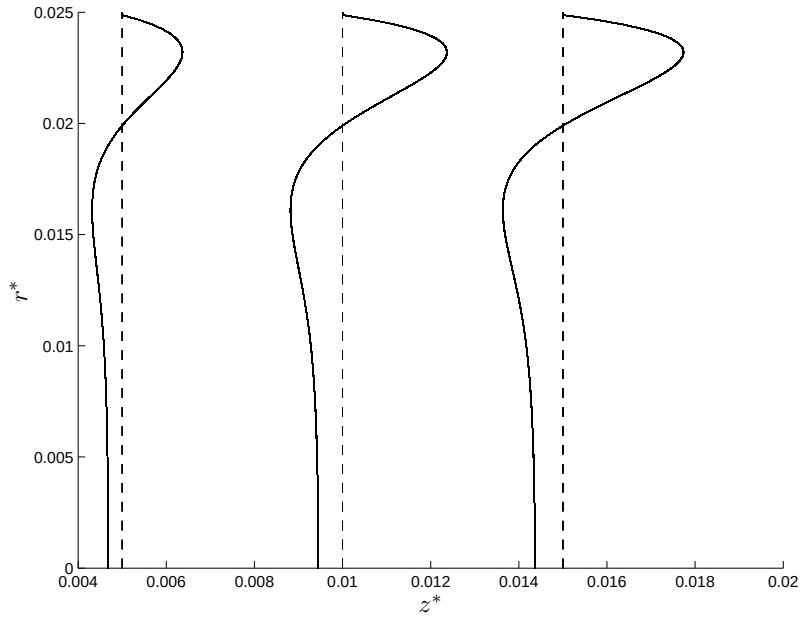

(a) u_z^* (m/s) for fixed values of z^* (m).

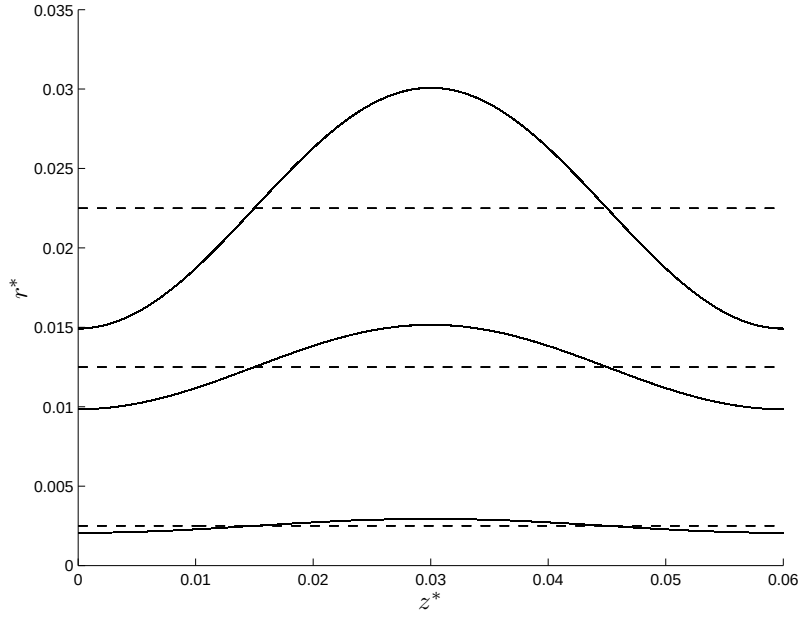

(b) u_r^* (m/s) for fixed values of r^* (m).

Figure 3.8: Flow profiles for varying λ_1 (s) with velocity scale 50 times the length scale.

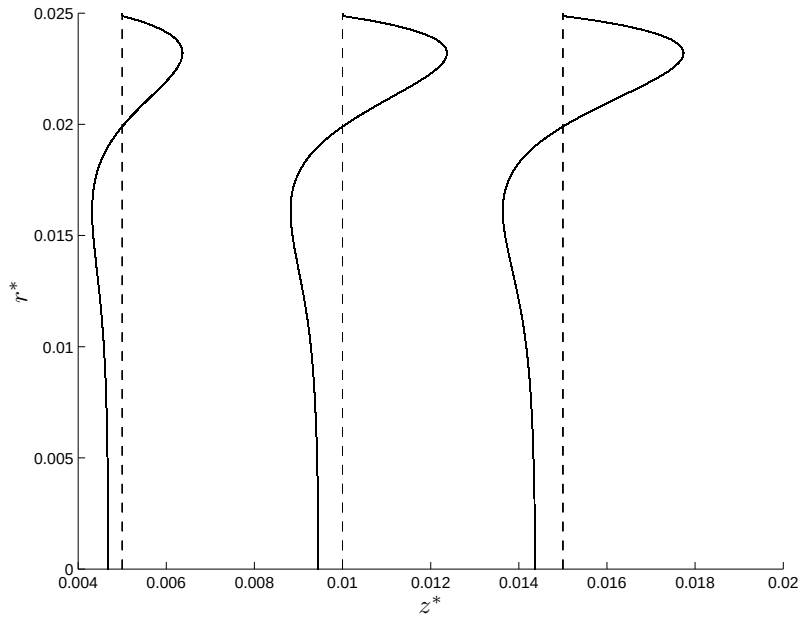

(a) u_z^* (m/s) for fixed values of z^* (m).

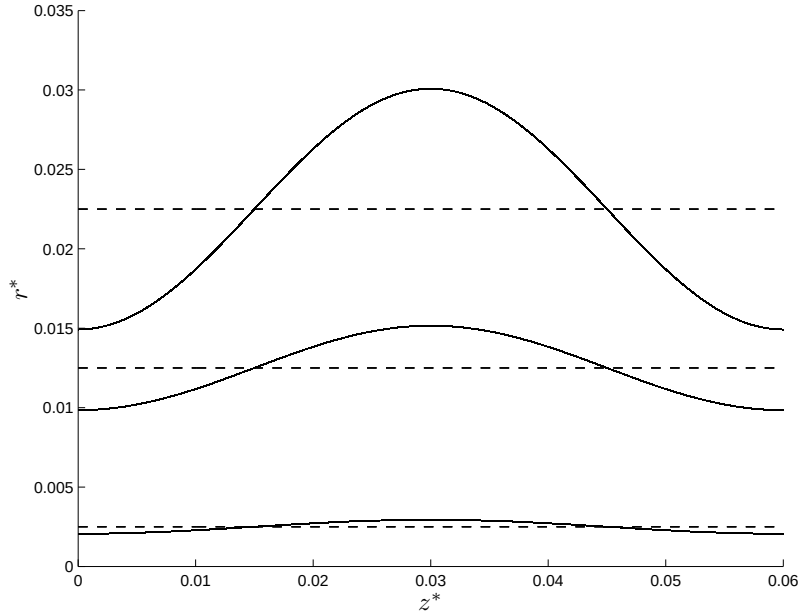

(b) u_r^* (m/s) for fixed values of r^* (m).

Figure 3.9: Flow profiles for varying $\rho^{[2]}$ (kg/m^3) with velocity scale 50 times the length scale.

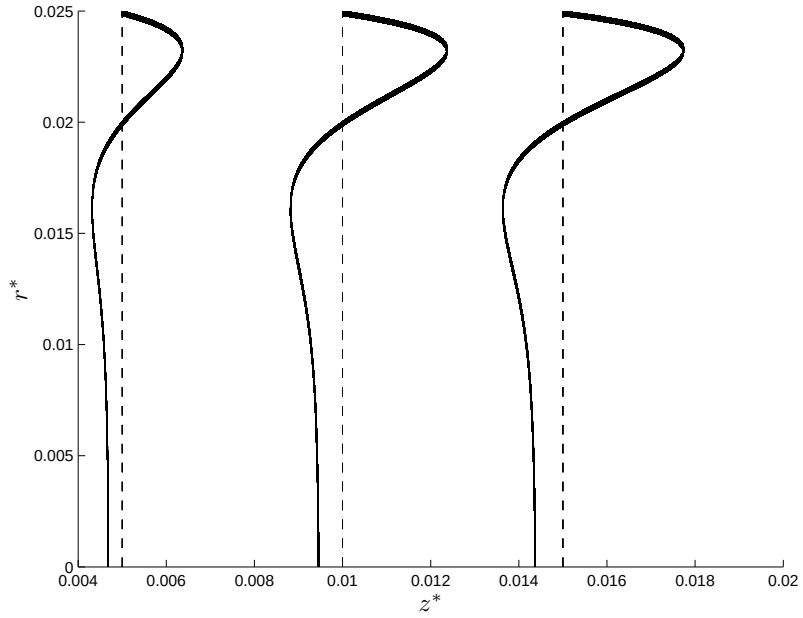

(a) u_z^* (m/s) for fixed values of z^* (m).

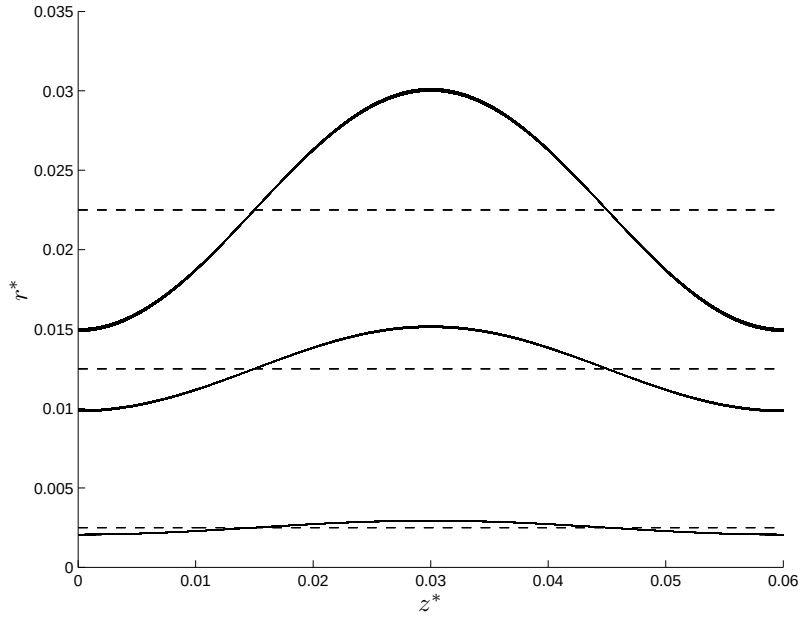

(b) u_r^* (m/s) for fixed values of r^* (m).

Figure 3.10: Flow profiles for varying η_0 with velocity scale 50 times the length scale.

Figure 3.7 displays the flow for the values $\mu^{[2]} = (0.01, 0.1, 1, 10, 100, 1000)$ Pa·s, this is equivalent to varying the ratio $\bar{\mu}$ between the viscosities of the two fluids (recall $\mu^{[1]} = 5$ Pa·s, $\bar{\mu} = \mu^{[2]}/\mu^{[1]}$). The flow appears to tend towards a limit which is reached when $\bar{\mu} \geq \mathrm{O}(1)$. Setting $\mu^{[2]} = 0.01$ Pa·s does have a relatively large effect on $|u_z^*|$, with the magnitude of flow significantly greater in the radial outer half than for the next value $\mu^{[2]} = 0.1$ Pa·s. However, the range of realistic physical values for mucus viscosity does not extend as low as 0.01 Pa·s; thus for the relevant range of mucus viscosities we see that altering the exact value has little effect on the flow velocities.

Figures 3.8 and 3.9 suggest that the value of the parameters λ_1 and $\rho^{[2]}$ has no effect on flow velocity for the ranges $\lambda_1 \in [0.1, 60]$ s and $\rho^{[2]} \in [800, 1300]$ kg/m^3. Similarly varying the value of η_0 in figure 3.10 between 0.992 and 1 (corresponding to mucus layer thicknesses of $200 - 0$ μm) has little effect on the overall flow viscosity.

In this chapter we have calculated the flow fields for the two layer flow of a Newtonian fluid and an Oldroyd B fluid. The viscoelastic Oldroyd B model was used to represent the thin layer of mucus lining the colonic epithelium. After formulating these equations and conditions we found solutions for the flow at $\mathrm{O}(\varepsilon)$. We found that the main difference between the one and two layer models is an increased fluid velocity at $t = 0,\ \pi$ in the two layer model; however the velocities at these times are much lower than at other times, thus the absolute effect on the flow is limited. Additionally we have shown that the mucus parameters have little effect on the flow velocity for the range of values we might expect them to take. Together these two results will lead us to use the one layer model when we investigate particle tracking in chapter 5. In the next chapter we consider one layer flow where chyme is represented using the Carreau rheological model.

Chapter 4

Modelling the Colon as a Pipe subject to Small Amplitude Wall Motion using a Carreau Rheological Model

In this chapter we create a model with the same geometrical features of that in chapter 2, i.e. an axisymmetric pipe with small amplitude wall contractions. In this case, however, we shall use a Carreau rheological model, rather than a Newtonian one, to represent colonic chyme.

As we have done previously we set the equation of the pipe boundary as

$$R^*(z^*,t^*) = \mathcal{R}\left(R_0\sqrt{1+2\varepsilon\left(\mathrm{e}^{i\left(\frac{2\pi}{\lambda}z^*-\omega t^*\right)}+\mathrm{e}^{-i\left(\frac{2\pi}{\lambda}z^*+\omega t^*\right)}\right)}\right). \tag{4.0.1}$$

4.1 The Carreau Equations

Recall that the constitutive equation for a Carreau fluid is given by (1.2.4),

$$\boldsymbol{\tau}^* = [(\mu_0 - \mu_\infty)(1 + (m\dot{\gamma}^*)^2)^{\frac{n-1}{2}} + \mu_\infty]\dot{\boldsymbol{\gamma}}^*,$$

where m is a constant parameter with dimension time and n is a dimensionless constant. The parameter m determines the shear rate at which the transition between Newtonian and power law behaviour occurs and n is the power law exponent and is a measure of the shear thinning nature of the fluid. The asymptotic values for viscosity are given by μ_0 and μ_∞, valid as $\dot{\gamma}^* \to 0$ and $\dot{\gamma}^* \to \infty$ respectively. This gives the Carreau model an advantage over the power law model, as the power law model breaks down at very high and very low shear rates; in particular under a small amplitude assumption the shear rates will be small.

The (dimensional) equations for a velocity field $\boldsymbol{u^*} = (u_r^*(r^*, z^*, t^*), 0, u_z^*(r^*, z^*, t^*))$ in axisymmetric cylindrical polar co-ordinates are given by

$$0 = \frac{1}{r^*}\frac{\partial}{\partial r^*}(r^* u_r^*) + \frac{\partial u_z^*}{\partial z^*} \tag{4.1.1}$$

$$\frac{\partial u_r^*}{\partial t^*} + u_r^*\frac{\partial u_r^*}{\partial r^*} + u_z^*\frac{\partial u_r^*}{\partial z^*} = \frac{1}{\rho}\left(-\frac{\partial p^*}{\partial r^*} + \frac{\tau_{rr}^*}{r^*} - \frac{\tau_{\theta\theta}^*}{r^*} + \frac{\partial \tau_{rr}^*}{\partial r^*} + \frac{\partial \tau_{rz}^*}{\partial z^*}\right) \tag{4.1.2}$$

$$\frac{\partial u_z^*}{\partial t^*} + u_r^*\frac{\partial u_z^*}{\partial r^*} + u_z^*\frac{\partial u_z^*}{\partial z^*} = \frac{1}{\rho}\left(-\frac{\partial p^*}{\partial z^*} + \frac{\tau_{rz}^*}{r^*} + \frac{\partial \tau_{rz}^*}{\partial r^*} + \frac{\partial \tau_{zz}^*}{\partial z^*}\right). \tag{4.1.3}$$

In addition, since the boundary conditions are independent of the type of fluid, we have

the conditions

$$\begin{aligned} u_r^*(R^*, z^*, t^*) &= \dot{R}^*(z^*, t^*) \\ u_z^*(R^*, z^*, t^*) &= 0 \\ u_r^*(0, z^*, t^*) &= 0 \\ \frac{\partial u_z^*}{\partial r^*}(0, z^*, t^*) &= 0. \end{aligned}$$

We must now find expressions for the components of the deviatoric stress tensor, $\boldsymbol{\tau}^*$. The shear rate tensor, $\dot{\boldsymbol{\gamma}}^*$, is given by the matrix

$$\dot{\boldsymbol{\gamma}}^* = \begin{pmatrix} 2\frac{\partial u_r^*}{\partial r^*} & 0 & \frac{\partial u_r^*}{\partial z^*} + \frac{\partial u_z^*}{\partial r^*} \\ 0 & 2\frac{u_r^*}{r^*} & 0 \\ \frac{\partial u_r^*}{\partial z^*} + \frac{\partial u_z^*}{\partial r^*} & 0 & 2\frac{\partial u_z^*}{\partial z^*} \end{pmatrix}$$

so that

$$\mathrm{tr}(\dot{\boldsymbol{\gamma}}^{*\boldsymbol{T}}\dot{\boldsymbol{\gamma}}^*) = 4\left(\frac{\partial u_r^*}{\partial r^*}\right)^2 + 2\left(\frac{\partial u_r^*}{\partial z^*} + \frac{\partial u_z^*}{\partial r^*}\right)^2 + 4\left(\frac{\partial u_z^*}{\partial z^*}\right)^2 + 4\left(\frac{u_r^*}{r^*}\right)^2$$

and

$$\dot{\gamma}^* = \sqrt{2\left(\frac{\partial u_r^*}{\partial r^*}\right)^2 + 2\left(\frac{\partial u_z^*}{\partial z^*}\right)^2 + \left(\frac{\partial u_z^*}{\partial r^*}\right)^2 + \left(\frac{\partial u_r^*}{\partial z^*}\right)^2 + 2\frac{\partial u_r^*}{\partial z^*}\frac{\partial u_z^*}{\partial r^*} + 2\left(\frac{u_r^*}{r^*}\right)^2}.$$

Therefore we find that the relevant components of shear stress are given by

$$\begin{aligned}
\tau^*_{rr} &= 2\frac{\partial u^*_r}{\partial r^*}[(\mu_0-\mu_\infty)(1+(m\dot\gamma^*)^2)^{\frac{n-1}{2}}+\mu_\infty] \\
\tau^*_{rz} &= \left(\frac{\partial u^*_r}{\partial z^*}+\frac{\partial u^*_z}{\partial r^*}\right)[(\mu_0-\mu_\infty)(1+(m\dot\gamma^*)^2)^{\frac{n-1}{2}}+\mu_\infty] \\
\tau^*_{\theta\theta} &= 2\frac{u^*_r}{r^*}[(\mu_0-\mu_\infty)(1+(m\dot\gamma^*)^2)^{\frac{n-1}{2}}+\mu_\infty] \\
\tau^*_{zz} &= 2\frac{\partial u^*_z}{\partial z^*}[(\mu_0-\mu_\infty)(1+(m\dot\gamma^*)^2)^{\frac{n-1}{2}}+\mu_\infty].
\end{aligned}$$

The relevant derivatives of these are given by

$$\frac{\partial \tau^*_{rr}}{\partial r^*} = 2\frac{\partial^2 u^*_r}{\partial r^{*2}}[(\mu_0-\mu_\infty)(1+(m\dot\gamma^*)^2)^{\frac{n-1}{2}}+\mu_\infty]+m^2(n-1)(\mu_0-\mu_\infty)$$
$$(1+(m\dot\gamma^*)^2)^{\frac{n-3}{2}}\frac{\partial u^*_r}{\partial r^*}\frac{\partial(\dot\gamma^{*2})}{\partial r^*}$$

$$\frac{\partial \tau^*_{rz}}{\partial z^*} = \left(\frac{\partial^2 u^*_r}{\partial z^{*2}}+\frac{\partial^2 u^*_z}{\partial r^*\partial z^*}\right)[(\mu_0-\mu_\infty)(1+(m\dot\gamma^*)^2)^{\frac{n-1}{2}}+\mu_\infty]+\frac{m^2(n-1)}{2}$$
$$(\mu_0-\mu_\infty)(1+(m\dot\gamma^*)^2)^{\frac{n-3}{2}}\left(\frac{\partial u^*_r}{\partial z^*}+\frac{\partial u^*_z}{\partial r^*}\right)\frac{\partial(\dot\gamma^{*2})}{\partial z^*}$$

$$\frac{\partial \tau^*_{rz}}{\partial r^*} = \left(\frac{\partial^2 u^*_r}{\partial z^*\partial r^*}+\frac{\partial^2 u^*_z}{\partial r^{*2}}\right)[(\mu_0-\mu_\infty)(1+(m\dot\gamma^*)^2)^{\frac{n-1}{2}}+\mu_\infty]+\frac{m^2(n-1)}{2}$$
$$(\mu_0-\mu_\infty)(1+(m\dot\gamma^*)^2)^{\frac{n-3}{2}}\left(\frac{\partial u^*_r}{\partial z^*}+\frac{\partial u^*_z}{\partial r^*}\right)\frac{\partial(\dot\gamma^{*2})}{\partial r^*}$$

$$\frac{\partial \tau^*_{zz}}{\partial z^*} = 2\frac{\partial^2 u^*_z}{\partial z^{*2}}[(\mu_0-\mu_\infty)(1+(m\dot\gamma^*)^2)^{\frac{n-1}{2}}+\mu_\infty]+m^2(n-1)(\mu_0-\mu_\infty)$$
$$(1+(m\dot\gamma^*)^2)^{\frac{n-3}{2}}\frac{\partial u^*_z}{\partial z^*}\frac{\partial(\dot\gamma^{*2})}{\partial z^*},$$

where

$$\frac{\partial(\dot{\gamma}^{*2})}{\partial r^*} = 4\frac{\partial u_r^*}{\partial r^*}\frac{\partial^2 u_r^*}{\partial r^{*2}} + 4\frac{\partial u_z^*}{\partial z^*}\frac{\partial^2 u_z^*}{\partial r^*\partial z^*} + 2\frac{\partial u_z^*}{\partial r^*}\frac{\partial^2 u_z^*}{\partial r^{*2}} + 2\frac{\partial u_r^*}{\partial z^*}\frac{\partial^2 u_r^*}{\partial r^*\partial z^*} + 2\frac{\partial u_r^*}{\partial z^*}\frac{\partial^2 u_z^*}{\partial r^{*2}} + 2\frac{\partial u_z^*}{\partial r^*}\frac{\partial^2 u_r^*}{\partial r^*\partial z^*} + 4\frac{u_r^*}{r^*}\left(\frac{1}{r^*}\frac{\partial u_r^*}{\partial r^*} - \frac{u_r^*}{r^{*2}}\right)$$

and

$$\frac{\partial(\dot{\gamma}^{*2})}{\partial z^*} = 4\frac{\partial u_r^*}{\partial r^*}\frac{\partial^2 u_r^*}{\partial z^*\partial r^*} + 4\frac{\partial u_z^*}{\partial z^*}\frac{\partial^2 u_z^*}{\partial z^{*2}} + 2\frac{\partial u_z^*}{\partial r^*}\frac{\partial^2 u_z^*}{\partial z^*\partial r^*} + 2\frac{\partial u_r^*}{\partial z^*}\frac{\partial^2 u_r^*}{\partial z^{*2}} + 2\frac{\partial u_r^*}{\partial z^*}\frac{\partial^2 u_z^*}{\partial z^*\partial r^*} + 2\frac{\partial u_z^*}{\partial r^*}\frac{\partial^2 u_r^*}{\partial z^{*2}} + 4\frac{u_r^*}{r^{*2}}\frac{\partial u_r^*}{\partial z^*}.$$

The continuity equation remains as (4.1.1), equation (4.1.2) now becomes

$$\rho\left(\frac{\partial u_r^*}{\partial t^*} + u_r^*\frac{\partial u_r^*}{\partial r^*} + u_z^*\frac{\partial u_r^*}{\partial z^*}\right) = -\frac{\partial p^*}{\partial r^*} + [(\mu_0 - \mu_\infty)(1 + (m\dot{\gamma}^*)^2)^{\frac{n-1}{2}} + \mu_\infty]$$
$$\left(\frac{2}{r^*}\frac{\partial u_r^*}{\partial r^*} - 2\frac{u_r^*}{r^{*2}} + 2\frac{\partial^2 u_r^*}{\partial r^{*2}} + \frac{\partial^2 u_r^*}{\partial z^{*2}} + \frac{\partial^2 u_z^*}{\partial r^*\partial z^*}\right) + m^2(n-1)(\mu_0 - \mu_\infty)$$
$$(1 + (m\dot{\gamma}^*)^2)^{\frac{n-3}{2}}\left(\frac{\partial u_r^*}{\partial r^*}\frac{\partial(\dot{\gamma}^{*2})}{\partial r^*} + \frac{1}{2}\left(\frac{\partial u_r^*}{\partial z^*} + \frac{\partial u_z^*}{\partial r^*}\right)\frac{\partial(\dot{\gamma}^{*2})}{\partial z^*}\right)$$

and equation (4.1.3) is given by

$$\rho\left(\frac{\partial u_z^*}{\partial t^*} + u_r^*\frac{\partial u_z^*}{\partial r^*} + u_z^*\frac{\partial u_z^*}{\partial z^*}\right) = -\frac{\partial p^*}{\partial z^*} + [(\mu_0 - \mu_\infty)(1 + (m\dot{\gamma}^*)^2)^{\frac{n-1}{2}} + \mu_\infty]$$
$$\left(\frac{1}{r^*}\left(\frac{\partial u_r^*}{\partial z^*} + \frac{\partial u_z^*}{\partial r^*}\right) + \frac{\partial^2 u_z^*}{\partial r^{*2}} + 2\frac{\partial^2 u_z^*}{\partial z^{*2}} + \frac{\partial^2 u_r^*}{\partial r^*\partial z^*}\right) + m^2(n-1)(\mu_0 - \mu_\infty)$$
$$(1 + (m\dot{\gamma}^*))^{\frac{n-3}{2}}\left(\frac{1}{2}\left(\frac{\partial u_r^*}{\partial z^*} + \frac{\partial u_z^*}{\partial r^*}\right)\frac{\partial(\dot{\gamma}^{*2})}{\partial r^*} + \frac{\partial u_z^*}{\partial z^*}\frac{\partial(\dot{\gamma}^{*2})}{\partial z^*}\right).$$

These equations may be simplified by noting that

$$\begin{aligned}\frac{\partial}{\partial r^*}(\nabla\cdot\boldsymbol{u^*}) &= \frac{\partial^2 u_r^*}{\partial r^{*2}} + \frac{1}{r^*}\frac{\partial u_r^*}{\partial r^*} - \frac{u_r^*}{r^{*2}} + \frac{\partial^2 u_z^*}{\partial r^*\partial z^*}\\ \frac{\partial}{\partial z^*}(\nabla\cdot\boldsymbol{u^*}) &= \frac{\partial^2 u_r^*}{\partial r^*\partial z^*} + \frac{1}{r^*}\frac{\partial u_r^*}{\partial z^*} + \frac{\partial^2 u_z^*}{\partial z^{*2}},\end{aligned}$$

but since our fluid is incompressible, $\nabla \cdot \boldsymbol{u}^* = 0$, therefore the two above expressions equal zero.

We must now nondimensionalise these equations, for this we use the scalings

$$\boldsymbol{u}^* = \omega R_0 \boldsymbol{u};\ \boldsymbol{x}^* = R_0 \boldsymbol{x};\ \text{and } t^* = \frac{1}{\omega} t,$$

additionally we scale pressure by

$$p^* = \frac{\rho(\omega R_0)^2}{\mathrm{Re}} p$$

where the Reynolds number is given by

$$\mathrm{Re} = \frac{\rho \omega R_0^2}{\mu_0}.$$

Tables 2.1 and 2.2 on page 46 display the standard parameter values that we use in this chapter. We introduce two dimensionless numbers, the first of these is a parameter, M, which we define as

$$M = m\omega$$

and the second is a parameter, μ_c, which we define as

$$\mu_c = \frac{\mu_\infty}{\mu_0}.$$

Since chyme is a shear thinning fluid we have $\mu_c < 1$. It is unclear what range of values m should take since it is a parameter specific to the Carreau model, which has not been fit to colonic rheological data. Fluids for which a Carreau-type model has been fit give a wide variation of values for m. For example, Escudier et al [18] fit a Carreau-Yasuda model to viscosity data from xanthan gum solutions and determined a value for the time

parameter of $\lambda_{CY} = 60.7$ s, whereas Wan Nik et al [69] fit a Carreau model to various bio-edible oils and found that their time parameter λ ranged from $0.132 - 1.61$ s. The Carreau model has also been used to describe blood flow, with a value of $\lambda = 3.313$ s given by Shibeshi and Collins [56] and in Appendix E we find a value of $m = 11309$ s for tomato soup.

The nondimensional equations of motion are given by

$$0 = \frac{1}{r}\frac{\partial}{\partial r}(ru_r) + \frac{\partial u_z}{\partial z};$$

$$\begin{aligned}\mathrm{Re}\left(\frac{\partial u_r}{\partial t} + u_r\frac{\partial u_r}{\partial r} + u_z\frac{\partial u_r}{\partial z}\right) = -\frac{\partial p}{\partial r} + [(1-\mu_c)(1+M^2\dot{\gamma}^2)^{\frac{n-1}{2}} + \mu_c] \\ \left(\frac{1}{r}\frac{\partial u_r}{\partial r} - \frac{u_r}{r^2} + \frac{\partial^2 u_r}{\partial r^2} + \frac{\partial^2 u_r}{\partial z^2}\right) + M^2(1-\mu_c)(n-1) \\ (1+M^2\dot{\gamma}^2)^{\frac{n-3}{2}}\left(\frac{\partial u_r}{\partial r}\frac{\partial(\dot{\gamma}^2)}{\partial r} + \frac{1}{2}\left(\frac{\partial u_r}{\partial z} + \frac{\partial u_z}{\partial r}\right)\frac{\partial(\dot{\gamma}^2)}{\partial z}\right);\end{aligned}$$

and

$$\begin{aligned}\mathrm{Re}\left(\frac{\partial u_z}{\partial t} + u_r\frac{\partial u_z}{\partial r} + u_z\frac{\partial u_z}{\partial z}\right) = -\frac{\partial p}{\partial z} + [(1-\mu_c)(1+M^2\dot{\gamma}^2)^{\frac{n-1}{2}} + \mu_c] \\ \left(\frac{1}{r}\frac{\partial u_z}{\partial r} + \frac{\partial^2 u_z}{\partial z^2} + \frac{\partial^2 u_z}{\partial r^2}\right) + M^2(1-\mu_c)(n-1) \\ (1+M^2\dot{\gamma}^2)^{\frac{n-3}{2}}\left(\frac{1}{2}\left(\frac{\partial u_r}{\partial z} + \frac{\partial u_z}{\partial r}\right)\frac{\partial(\dot{\gamma}^2)}{\partial r} + \frac{\partial u_z}{\partial z}\frac{\partial(\dot{\gamma}^2)}{\partial z}\right).\end{aligned} \tag{4.1.4}$$

The nondimensional boundary conditions are then given by

$$\begin{aligned} u_r(R,z,t) &= \dot{R}(z,t) \\ u_z(R,z,t) &= 0 \\ u_r(0,z,t) &= 0 \\ \frac{\partial u_z}{\partial r}(0,z,t) &= 0, \end{aligned}$$

where we recall

$$R(z,t) = \mathcal{R}\left(1 + \varepsilon\left(\mathrm{e}^{i(kz-t)} + \mathrm{e}^{-i(kz+t)}\right) - \frac{\varepsilon^2}{2}\left(\mathrm{e}^{2i(kz-t)} + \mathrm{e}^{-2i(kz+t)} + \mathrm{e}^{-2it}\right) + \mathrm{o}(\varepsilon^3)\right).$$

As in chapter 2 we expand the boundary and equation variables about $\varepsilon \ll 1$ so that

$$\begin{aligned} R(z,t) &= 1 + \varepsilon R_1(z,t) + \varepsilon^2 R_2(z,t) + \mathrm{o}(\varepsilon^3) \\ p(r,z,t) &= p_0 + \varepsilon p_1(r,z,t) + \varepsilon^2 p_2(r,z,t) + \mathrm{o}(\varepsilon^3) \\ u_r(r,z,t) &= \varepsilon u_{r1}(r,z,t) + \varepsilon^2 u_{r2}(r,z,t) + \mathrm{o}(\varepsilon^3) \\ u_z(r,z,t) &= \varepsilon u_{z1}(r,z,t) + \varepsilon^2 u_{z2}(r,z,t) + \mathrm{o}(\varepsilon^3), \end{aligned}$$

with the boundary conditions given by

$$\begin{aligned} \varepsilon u_{r1}(1,z,t) + \varepsilon^2\left(u_{r2}(1,z,t) + R_1(z,t)\frac{\partial u_{r1}}{\partial r}(1,z,t)\right) &= \varepsilon\dot{R}_1(z,t) + \varepsilon^2\dot{R}_2(z,t) \\ \varepsilon u_{z1}(1,z,t) + \varepsilon^2\left(u_{z2}(1,z,t) + R_1(z,t)\frac{\partial u_{z1}}{\partial r}(1,z,t)\right) &= 0 \\ \varepsilon u_{r1}(0,z,t) + \varepsilon^2 u_{r2}(0,z,t) &= 0 \\ \varepsilon\frac{\partial u_{z1}}{\partial r}(0,z,t) + \varepsilon^2\frac{\partial u_{z2}}{\partial r}(0,z,t) &= 0. \end{aligned}$$

For the rest of this chapter we make the assumption that $M = m\omega = \mathrm{O}(1/\sqrt{\varepsilon})$, in

doing so we may expand the terms involving $M^2\dot{\gamma}^2$ as follows

$$\left(1+M^2\dot{\gamma}^2\right)^{\alpha} \approx 1+\alpha M^2\dot{\gamma}^2+\frac{\alpha(\alpha-1)}{2}M^4\dot{\gamma}^4.$$

Note that $M^2\dot{\gamma}^2 = \mathrm{O}(\varepsilon)$.

The work of this section gives us the following problem at $\mathrm{O}(\varepsilon)$:

$$\begin{aligned}
0 &= \frac{1}{r}\frac{\partial}{\partial r}(ru_{r1})+\frac{\partial u_{z1}}{\partial z} \\
\mathrm{Re}\frac{\partial u_{r1}}{\partial t} &= -\frac{\partial p_1}{\partial r}+\frac{1}{r}\frac{\partial}{\partial r}\left(r\frac{\partial u_{r1}}{\partial r}\right)+\frac{\partial^2 u_{r1}}{\partial z^2}-\frac{u_{r1}}{r^2} \\
\mathrm{Re}\frac{\partial u_{z1}}{\partial t} &= -\frac{\partial p_1}{\partial z}+\frac{1}{r}\frac{\partial}{\partial r}\left(r\frac{\partial u_{z1}}{\partial r}\right)+\frac{\partial^2 u_{z1}}{\partial z^2}
\end{aligned}$$

subject to

$$\begin{aligned}
u_{r1}(1,z,t) &= \dot{R}_1(z,t) \\
u_{z1}(1,z,t) &= 0 \\
u_{r1}(0,z,t) &= 0 \\
\frac{\partial u_{z1}}{\partial r}(0,z,t) &= 0.
\end{aligned}$$

This is identical to the problem in section 2.1, thus the results of that section hold here. We now consider the flow at $\mathrm{O}(\varepsilon^2)$.

4.2 Shear Thinning Effects on the Flow of Chyme

We now consider the flow at $\mathrm{O}(\varepsilon^2)$ using the results from section 4.1. The $\mathrm{O}(\varepsilon^2)$ equations, letting $\hat{M} = \sqrt{\varepsilon}M = \mathrm{O}(1)$, are given by

$$0 = \frac{1}{r}\frac{\partial}{\partial r}(ru_{r2})+\frac{\partial u_{z2}}{\partial z} \tag{4.2.1}$$

$$\mathrm{Re}\left(\frac{\partial u_{r2}}{\partial t}+u_{r1}\frac{\partial u_{r1}}{\partial r}+u_{z1}\frac{\partial u_{r1}}{\partial z}\right)=-\frac{\partial p_2}{\partial r}+\frac{1}{r}\frac{\partial}{\partial r}\left(r\frac{\partial u_{r2}}{\partial r}\right)+\frac{\partial^2 u_{r2}}{\partial z^2}-\frac{u_{r2}}{r^2}$$
$$+(1-\mu_c)\frac{(n-1)}{2}\hat{M}^2\dot{\gamma}_1^2\left(\frac{1}{r}\frac{\partial}{\partial r}\left(r\frac{\partial u_{r1}}{\partial r}\right)+\frac{\partial^2 u_{r1}}{\partial z^2}-\frac{u_{r1}}{r^2}\right) \tag{4.2.2}$$

and

$$\mathrm{Re}\left(\frac{\partial u_{z2}}{\partial t}+u_{r1}\frac{\partial u_{z1}}{\partial r}+u_{z1}\frac{\partial u_{z1}}{\partial z}\right)=-\frac{\partial p_2}{\partial z}+\frac{1}{r}\frac{\partial}{\partial r}\left(r\frac{\partial u_{z2}}{\partial r}\right)+\frac{\partial^2 u_{z2}}{\partial z^2}$$
$$+(1-\mu_c)\frac{(n-1)}{2}\hat{M}^2\dot{\gamma}_1^2\left(\frac{1}{r}\frac{\partial}{\partial r}\left(r\frac{\partial u_{z1}}{\partial r}\right)+\frac{\partial^2 u_{z1}}{\partial z^2}\right), \tag{4.2.3}$$

where u_{r1}, u_{z1} and therefore $\dot{\gamma}_1$ are known from the previous section. The above equations differ from the ones at $\mathrm{O}(\varepsilon)$ in that they include both inertial and non-Newtonian effects.

As in the Newtonian case we have the following boundary conditions at $\mathrm{O}(\varepsilon^2)$

$$\begin{aligned}
u_{r2}(1,z,t) &= \dot{R}_2(z,t)-R_1(z,t)\frac{\partial u_{r1}}{\partial r}(1,z,t)\\
u_{z2}(1,z,t) &= -R_1(z,t)\frac{\partial u_{z1}}{\partial r}(1,z,t)\\
u_{r2}(0,z,t) &= 0\\
\frac{\partial u_{z2}}{\partial r}(0,z,t) &= 0.
\end{aligned}$$

Due to the extra terms involved, compared to the Newtonian model, we assume solutions of the form

$$u_{r2}(r,z,t)=\mathcal{R}\left(\alpha_1(r)\mathrm{e}^{2i(kz-t)}+\alpha_2(r)\mathrm{e}^{-2i(kz+t)}+\alpha_3(r)\mathrm{e}^{-2it}+\alpha_4(r)\mathrm{e}^{3i(kz-t)}\right.$$
$$\left.+\alpha_5(r)\mathrm{e}^{-3i(kz+t)}+\alpha_6(r)\mathrm{e}^{i(kz-3t)}+\alpha_7(r)\mathrm{e}^{-i(kz+3t)}\right)$$

$$u_{z2}(r,z,t)=\mathcal{R}\left(\beta_1(r)\mathrm{e}^{2i(kz-t)}+\beta_2(r)\mathrm{e}^{-2i(kz+t)}+\beta_3(r)\mathrm{e}^{-2it}+\beta_4(r)\mathrm{e}^{3i(kz-t)}\right.$$
$$\left.+\beta_5(r)\mathrm{e}^{-3i(kz+t)}+\beta_6(r)\mathrm{e}^{i(kz-3t)}+\beta_7(r)\mathrm{e}^{-i(kz+3t)}\right)$$

$$p_{z2}(r,z,t) = \mathcal{R}\left(\delta_1(r)\mathrm{e}^{2i(kz-t)} + \delta_2(r)\mathrm{e}^{-2i(kz+t)} + \delta_3(r)\mathrm{e}^{-2it} + \delta_4(r)\mathrm{e}^{3i(kz-t)} \right.$$
$$\left. + \delta_5(r)\mathrm{e}^{-3i(kz+t)} + \delta_6(r)\mathrm{e}^{i(kz-3t)} + \delta_7(r)\mathrm{e}^{-i(kz+3t)}\right).$$

In a similar manner to that in sections 2.1 and 2.2, we substitute these solutions into equations (4.2.1) - (4.2.3) and equating coefficients of the seven types of exponential we find $\alpha_1 = \alpha_2$, $\alpha_4 = \alpha_5$, $\alpha_6 = \alpha_7$, $\beta_1 = -\beta_2$, $\beta_4 = -\beta_5$, $\beta_6 = -\beta_7$, $\delta_1 = \delta_2$, $\delta_4 = \delta_5$ and $\delta_6 = \delta_7$. This leaves us with four sets of three equations.

The first set of equations

$$\frac{\mathrm{d}\alpha_1}{\mathrm{d}r} + \frac{\alpha_1}{r} + 2ik\beta_1 = 0 \tag{4.2.4}$$
$$\mathrm{Re}\left(-2i\alpha_1 + f\frac{\mathrm{d}f}{\mathrm{d}r} + ikfg\right) = -\frac{\mathrm{d}\delta_1}{\mathrm{d}r} + \frac{1}{r}\frac{\mathrm{d}\alpha_1}{\mathrm{d}r} - \frac{\alpha_1}{r^2} + \frac{\mathrm{d}^2\alpha_1}{\mathrm{d}r^2} - 4k^2\alpha_1 \tag{4.2.5}$$
$$\mathrm{Re}\left(-2i\beta_1 + f\frac{\mathrm{d}g}{\mathrm{d}r} + ikg^2\right) = -2ik\delta_1 + \frac{1}{r}\frac{\mathrm{d}\beta_1}{\mathrm{d}r} + \frac{\mathrm{d}^2\beta_1}{\mathrm{d}r^2} - 4k^2\beta_1 \tag{4.2.6}$$

are as in section 2.2.

The second set of equations are also as in section 2.2

$$\frac{\mathrm{d}\alpha_3}{\mathrm{d}r} + \frac{\alpha_3}{r} = 0$$
$$\mathrm{Re}\left(-2i\alpha_3 + 2f\frac{\mathrm{d}f}{\mathrm{d}r} - 2ikfg\right) = -\frac{\mathrm{d}\delta_3}{\mathrm{d}r} + \frac{1}{r}\frac{\mathrm{d}\alpha_3}{\mathrm{d}r} - \frac{\alpha_3}{r^2} + \frac{\mathrm{d}^2\alpha_3}{\mathrm{d}r^2}$$
$$-2i\mathrm{Re}\beta_3 = \frac{1}{r}\frac{\mathrm{d}\beta_3}{\mathrm{d}r} + \frac{\mathrm{d}^2\beta_3}{\mathrm{d}r^2}.$$

These have solutions

$$\alpha_3(r) = \frac{a}{r}$$
$$\beta_3(r) = b_1 J_0(r\sqrt{2i\mathrm{Re}}) + b_2 K_0(r\sqrt{2i\mathrm{Re}})$$
$$\delta_3(r) = c + \mathrm{Re}\left(2ia\ln r - 2\int_0^r f\frac{\mathrm{d}f}{\mathrm{d}r'}\,\mathrm{d}r' + 2ik\int_0^r fg\,\mathrm{d}r'\right),$$

where a, b_1, b_2 and c are constants to be determined.

In addition to those found in the Newtonian case we also have a third set of equations

$$\frac{\mathrm{d}\alpha_4}{\mathrm{d}r} + \frac{\alpha_4}{r} + 3ik\beta_4 = 0 \tag{4.2.7}$$

$$-3i\mathrm{Re}\alpha_4 = -\frac{\mathrm{d}\delta_4}{\mathrm{d}r} + \frac{1}{r}\frac{\mathrm{d}\alpha_4}{\mathrm{d}r} - \frac{\alpha_4}{r^2} + \frac{\mathrm{d}^2\alpha_4}{\mathrm{d}r^2} - 9k^2\alpha_4 + (1-\mu_c)\frac{(n-1)}{2}\hat{M}^2\left(2\left(\frac{\mathrm{d}f}{\mathrm{d}r}\right)^2 - 2k^2g^2 + \left(\frac{\mathrm{d}g}{\mathrm{d}r}\right)^2 - k^2f^2 + 2ikf\frac{\mathrm{d}g}{\mathrm{d}r} + 2\frac{f^2}{r^2}\right)\left(\frac{1}{r}\frac{\mathrm{d}f}{\mathrm{d}r} - \frac{f}{r^2} + \frac{\mathrm{d}^2f}{\mathrm{d}r^2} - fk^2\right) \tag{4.2.8}$$

$$-3i\mathrm{Re}\beta_4 = -3ik\delta_4 + \frac{1}{r}\frac{\mathrm{d}\beta_4}{\mathrm{d}r} + \frac{\mathrm{d}^2\beta_4}{\mathrm{d}r^2} - 9k^2\beta_4 + (1-\mu_c)\frac{(n-1)}{2}\hat{M}^2\left(2\left(\frac{\mathrm{d}f}{\mathrm{d}r}\right)^2 - 2k^2g^2 + \left(\frac{\mathrm{d}g}{\mathrm{d}r}\right)^2 - k^2f^2 + 2ikf\frac{\mathrm{d}g}{\mathrm{d}r} + 2\frac{f^2}{r^2}\right)\left(\frac{1}{r}\frac{\mathrm{d}g}{\mathrm{d}r} + \frac{\mathrm{d}^2g}{\mathrm{d}r^2} - k^2g\right) \tag{4.2.9}$$

and a fourth set

$$\frac{\mathrm{d}\alpha_6}{\mathrm{d}r} + \frac{\alpha_6}{r} + ik\beta_6 = 0 \tag{4.2.10}$$

$$-3i\mathrm{Re}\alpha_6 = -\frac{\mathrm{d}\delta_6}{\mathrm{d}r} + \frac{1}{r}\frac{\mathrm{d}\alpha_6}{\mathrm{d}r} - \frac{\alpha_6}{r^2} + \frac{\mathrm{d}^2\alpha_6}{\mathrm{d}r^2} - k^2\alpha_6 + (1-\mu_c)\frac{(n-1)}{2}\hat{M}^2\left(6\left(\frac{\mathrm{d}f}{\mathrm{d}r}\right)^2 - 6k^2g^2 - \left(\frac{\mathrm{d}g}{\mathrm{d}r}\right)^2 + k^2f^2 - 2ikf\frac{\mathrm{d}g}{\mathrm{d}r} + 6\frac{f^2}{r^2}\right)\left(\frac{1}{r}\frac{\mathrm{d}f}{\mathrm{d}r} - \frac{f}{r^2} + \frac{\mathrm{d}^2f}{\mathrm{d}r^2} - fk^2\right) \tag{4.2.11}$$

$$-3i\mathrm{Re}\beta_6 = -ik\delta_6 + \frac{1}{r}\frac{\mathrm{d}\beta_6}{\mathrm{d}r} + \frac{\mathrm{d}^2\beta_6}{\mathrm{d}r^2} - k^2\beta_6 + (1-\mu_c)\frac{(n-1)}{2}\hat{M}^2\left(2\left(\frac{\mathrm{d}f}{\mathrm{d}r}\right)^2 - 2k^2g^2 - 3\left(\frac{\mathrm{d}g}{\mathrm{d}r}\right)^2 + 3k^2f^2 - 6ikf\frac{\mathrm{d}g}{\mathrm{d}r} + 2\frac{f^2}{r^2}\right)\left(\frac{1}{r}\frac{\mathrm{d}g}{\mathrm{d}r} + \frac{\mathrm{d}^2g}{\mathrm{d}r^2} - k^2g\right). \tag{4.2.12}$$

As in section 2.2 rearranging equations (4.2.4) - (4.2.6) gives us expressions for β_1, δ_1

$$\beta_1(r) = \frac{i}{2k}\left(\frac{\mathrm{d}\alpha_1}{\mathrm{d}r} + \frac{\alpha_1}{r}\right)$$

$$\delta_1(r) = \frac{1}{4k^2}\frac{\mathrm{d}^3\alpha_1}{\mathrm{d}r^3} + \frac{1}{2rk^2}\frac{\mathrm{d}^2\alpha_1}{\mathrm{d}r^2} + \left(\frac{i\mathrm{Re}}{2k^2} - \frac{1}{4r^2k^2} - 1\right)\frac{\mathrm{d}\alpha_1}{\mathrm{d}r} + \left(\frac{1}{4r^3k^2} + \frac{i\mathrm{Re}}{2rk^2} - \frac{1}{r}\right)\alpha_1 + \frac{\mathrm{Re}}{2}\left(\frac{i}{k}f\frac{\mathrm{d}g}{\mathrm{d}r} - g^2\right)$$

and the ODE for α_1

$$\frac{1}{4k^2}\frac{\mathrm{d}^4\alpha_1}{\mathrm{d}r^4} + \frac{1}{2k^2r}\frac{\mathrm{d}^3\alpha_1}{\mathrm{d}r^3} + \left(\frac{i\mathrm{Re}}{2k^2} - \frac{3}{4k^2r^2} - 2\right)\frac{\mathrm{d}^2\alpha_1}{\mathrm{d}r^2} + \left(\frac{3}{4k^2r^3} + \frac{i\mathrm{Re}}{2k^2r} - \frac{2}{r}\right)\frac{\mathrm{d}\alpha_1}{\mathrm{d}r} + \left(4k^2 + \frac{2}{r^2} - i\mathrm{Re}\left(\frac{1}{2k^2r^2} + 2\right) - \frac{3}{4k^2r^4}\right)\alpha_1 + \mathrm{Re}\left(\frac{i}{2k}\left(f\frac{\mathrm{d}^2g}{\mathrm{d}r^2} + \frac{\mathrm{d}f}{\mathrm{d}r}\frac{\mathrm{d}g}{\mathrm{d}r}\right) - g\frac{\mathrm{d}g}{\mathrm{d}r} + f\frac{\mathrm{d}f}{\mathrm{d}r} + ikgf\right) = 0.$$

Rearranging (4.2.7) we find that

$$\beta_4(r) = \frac{i}{3k}\left(\frac{\mathrm{d}\alpha_4}{\mathrm{d}r} + \frac{\alpha_4}{r}\right)$$

substituting this into (4.2.9) we obtain an expression for δ_4,

$$\delta_4(r) = \frac{1}{9k^2}\frac{\mathrm{d}^3\alpha_4}{\mathrm{d}r^3} + \frac{2}{9rk^2}\frac{\mathrm{d}^2\alpha_4}{\mathrm{d}r^2} + \left(\frac{i\mathrm{Re}}{3k^2} - \frac{1}{9r^2k^2} - 1\right)\frac{\mathrm{d}\alpha_4}{\mathrm{d}r} + \left(\frac{1}{9r^3k^2} + \frac{i\mathrm{Re}}{3rk^2} - \frac{1}{r}\right)\alpha_4 - \frac{i}{6k}(1-\mu_c)(n-1)\hat{M}^2\left(2\left(\frac{\mathrm{d}f}{\mathrm{d}r}\right)^2 - 2k^2g^2 + \left(\frac{\mathrm{d}g}{\mathrm{d}r}\right)^2 - k^2f^2 + 2ikf\frac{\mathrm{d}g}{\mathrm{d}r} + 2\frac{f^2}{r^2}\right)\left(\frac{1}{r}\frac{\mathrm{d}g}{\mathrm{d}r} + \frac{\mathrm{d}^2g}{\mathrm{d}r^2} - k^2g\right)$$

Using this and (4.2.8) we obtain an ODE for α_4, given by

$$\begin{aligned}\frac{1}{9k^2}\frac{\mathrm{d}^4\alpha_4}{\mathrm{d}r^4}+\frac{2}{9k^2r}\frac{\mathrm{d}^3\alpha_4}{\mathrm{d}r^3}+\left(\frac{i\mathrm{Re}}{3k^2}-\frac{1}{9k^2r^2}-2\right)\frac{\mathrm{d}^2\alpha_4}{\mathrm{d}r^2}+\left(\frac{1}{3k^2r^3}+\frac{i\mathrm{Re}}{3k^2r}-\frac{2}{r}\right)\frac{\mathrm{d}\alpha_4}{\mathrm{d}r}\\ +\left(9k^2+\frac{2}{r^2}-i\mathrm{Re}\left(\frac{1}{3k^2r^2}+3\right)-\frac{1}{3k^2r^4}\right)\alpha_4-\frac{1}{2}(1-\mu_c)(n-1)\hat{M}^2\\ \left[\left(2\left(\frac{\mathrm{d}f}{\mathrm{d}r}\right)^2-2k^2g^2+\left(\frac{\mathrm{d}g}{\mathrm{d}r}\right)^2-k^2f^2+2ikf\frac{\mathrm{d}g}{\mathrm{d}r}+2\frac{f^2}{r^2}\right)\right.\\ \left(\frac{1}{r}\frac{\mathrm{d}f}{\mathrm{d}r}-\frac{f}{r^2}+\frac{\mathrm{d}^2f}{\mathrm{d}r^2}-fk^2+\frac{i}{3k}\left(\frac{1}{r}\frac{\mathrm{d}^2g}{\mathrm{d}r^2}-\frac{1}{r^2}\frac{\mathrm{d}g}{\mathrm{d}r}+\frac{\mathrm{d}^3g}{\mathrm{d}r^3}-k^2\frac{\mathrm{d}g}{\mathrm{d}r}\right)\right)\\ +\frac{i}{3k}\left(4\frac{\mathrm{d}f}{\mathrm{d}r}\frac{\mathrm{d}^2f}{\mathrm{d}r^2}-4k^2g\frac{\mathrm{d}g}{\mathrm{d}r}+2\frac{\mathrm{d}g}{\mathrm{d}r}\frac{\mathrm{d}^2g}{\mathrm{d}r^2}-2k^2f\frac{\mathrm{d}f}{\mathrm{d}r}+2ikf\frac{\mathrm{d}^2g}{\mathrm{d}r^2}+2ik\frac{\mathrm{d}f}{\mathrm{d}r}\frac{\mathrm{d}g}{\mathrm{d}r}\right.\\ \left.\left.+4\frac{f}{r^2}\frac{\mathrm{d}f}{\mathrm{d}r}-4\frac{f^2}{r^3}\right)\left(\frac{1}{r}\frac{\mathrm{d}g}{\mathrm{d}r}+\frac{\mathrm{d}^2g}{\mathrm{d}r^2}-k^2g\right)\right]=0.\end{aligned}$$

Rearranging (4.2.10) we find that

$$\beta_6(r)=\frac{i}{k}\left(\frac{\mathrm{d}\alpha_6}{\mathrm{d}r}+\frac{\alpha_6}{r}\right)$$

substituting this into (4.2.12) we obtain an expression for δ_6,

$$\begin{aligned}\delta_6(r)=\frac{1}{k^2}\frac{\mathrm{d}^3\alpha_6}{\mathrm{d}r^3}+\frac{2}{rk^2}\frac{\mathrm{d}^2\alpha_6}{\mathrm{d}r^2}+\left(\frac{3i\mathrm{Re}}{k^2}-\frac{1}{r^2k^2}-1\right)\frac{\mathrm{d}\alpha_6}{\mathrm{d}r}+\left(\frac{1}{r^3k^2}+\frac{3i\mathrm{Re}}{rk^2}-\frac{1}{r}\right)\alpha_6\\ -\frac{i}{2k}(1-\mu_c)(n-1)\hat{M}^2\left(2\left(\frac{\mathrm{d}f}{\mathrm{d}r}\right)^2-2k^2g^2-3\left(\frac{\mathrm{d}g}{\mathrm{d}r}\right)^2+3k^2f^2-6ikf\frac{\mathrm{d}g}{\mathrm{d}r}+2\frac{f^2}{r^2}\right)\\ \left(\frac{1}{r}\frac{\mathrm{d}g}{\mathrm{d}r}+\frac{\mathrm{d}^2g}{\mathrm{d}r^2}-k^2g\right)\end{aligned}$$

Using this and (4.2.11) we obtain an ODE for α_6, given by

$$\frac{1}{k^2}\frac{\mathrm{d}^4\alpha_6}{\mathrm{d}r^4}+\frac{2}{k^2r}\frac{\mathrm{d}^3\alpha_6}{\mathrm{d}r^3}+\left(\frac{3i\mathrm{Re}}{k^2}-\frac{3}{k^2r^2}-2\right)\frac{\mathrm{d}^2\alpha_6}{\mathrm{d}r^2}+\left(\frac{3}{k^2r^3}+\frac{3i\mathrm{Re}}{k^2r}-\frac{2}{r}\right)\frac{\mathrm{d}\alpha_6}{\mathrm{d}r}$$
$$+\left(k^2+\frac{2}{r^2}-3i\mathrm{Re}\left(\frac{1}{k^2r^2}+1\right)-\frac{3}{k^2r^4}\right)\alpha_6-(1-\mu_c)\frac{(n-1)}{2}\hat{M}^2$$
$$\left[\frac{i}{k}\left(4\frac{\mathrm{d}f}{\mathrm{d}r}\frac{\mathrm{d}^2f}{\mathrm{d}r^2}-4k^2g\frac{\mathrm{d}g}{\mathrm{d}r}-6\frac{\mathrm{d}g}{\mathrm{d}r}\frac{\mathrm{d}^2g}{\mathrm{d}r^2}+6k^2f\frac{\mathrm{d}f}{\mathrm{d}r}-6ikf\frac{\mathrm{d}^2g}{\mathrm{d}r^2}-6ik\frac{\mathrm{d}f}{\mathrm{d}r}\frac{\mathrm{d}g}{\mathrm{d}r}\right.\right.$$
$$\left.+4\frac{f}{r^2}\frac{\mathrm{d}f}{\mathrm{d}r}-4\frac{f^2}{r^3}\right)\left(\frac{1}{r}\frac{\mathrm{d}g}{\mathrm{d}r}+\frac{\mathrm{d}^2g}{\mathrm{d}r^2}-k^2g\right)+\frac{i}{k}\left(\frac{1}{r}\frac{\mathrm{d}^2g}{\mathrm{d}r^2}-\frac{1}{r^2}\frac{\mathrm{d}g}{\mathrm{d}r}+\frac{\mathrm{d}^3g}{\mathrm{d}r^3}-k^2\frac{\mathrm{d}g}{\mathrm{d}r}\right)$$
$$\left(2\left(\frac{\mathrm{d}f}{\mathrm{d}r}\right)^2-2k^2g^2-3\left(\frac{\mathrm{d}g}{\mathrm{d}r}\right)^2+3k^2f^2-6ikf\frac{\mathrm{d}g}{\mathrm{d}r}+2\frac{f^2}{r^2}\right)+\left(6\left(\frac{\mathrm{d}f}{\mathrm{d}r}\right)^2\right.$$
$$\left.\left.-6k^2g^2-\left(\frac{\mathrm{d}g}{\mathrm{d}r}\right)^2+k^2f^2-2ikf\frac{\mathrm{d}g}{\mathrm{d}r}+6\frac{f^2}{r^2}\right)\left(\frac{1}{r}\frac{\mathrm{d}f}{\mathrm{d}r}-\frac{f}{r^2}+\frac{\mathrm{d}^2f}{\mathrm{d}r^2}-fk^2\right)\right]=0.$$

We must now determine appropriate boundary conditions in terms of α_1, α_4 and α_6. We have

$$u_{r2}(r,z,t)=\mathcal{R}\left(\alpha_1(r)\left(\mathrm{e}^{2i(kz-t)}+\mathrm{e}^{-2i(kz+t)}\right)+\frac{a}{r}\mathrm{e}^{-2it}+\alpha_4(r)\left(\mathrm{e}^{3i(kz-t)}+\mathrm{e}^{-3i(kz+t)}\right)\right.$$
$$\left.+\alpha_6(r)\left(\mathrm{e}^{i(kz-3t)}+\mathrm{e}^{-i(kz+3t)}\right)\right)$$

$$u_{z2}(r,z,t)=\mathcal{R}\left(\beta_1(r)\left(\mathrm{e}^{2i(kz-t)}-\mathrm{e}^{-2i(kz+t)}\right)+\left(b_1J_0(r\sqrt{2i\mathrm{Re}})+b_2K_0(r\sqrt{2i\mathrm{Re}})\right)\mathrm{e}^{-2it}\right.$$
$$\left.+\beta_4(r)\left(\mathrm{e}^{3i(kz-t)}-\mathrm{e}^{-3i(kz+t)}\right)+\beta_6(r)\left(\mathrm{e}^{i(kz-3t)}-\mathrm{e}^{-i(kz+3t)}\right)\right)$$

and the boundary conditions

$$\begin{aligned}
u_{r2}(1,z,t) &= \dot{R}_2(z,t)-R_1(z,t)\frac{\partial u_{r1}}{\partial r}(1,z,t)\\
u_{z2}(1,z,t) &= -R_1(z,t)\frac{\partial u_{z1}}{\partial r}(1,z,t)\\
u_{r2}(0,z,t) &= 0\\
\frac{\partial u_{z2}}{\partial r}(0,z,t) &= 0.
\end{aligned}$$

We recall that

$$\begin{aligned} R_1(z,t) &= \mathcal{R}\left(\mathrm{e}^{i(kz-t)} + \mathrm{e}^{-i(kz+t)}\right) \\ R_2(z,t) &= \mathcal{R}\left(-\frac{1}{2}\left(\mathrm{e}^{2i(kz-t)} + \mathrm{e}^{-2i(kz+t)} + 2\mathrm{e}^{-2it}\right)\right) \\ u_{r1}(r,z,t) &= \mathcal{R}\left(f(r)\left(\mathrm{e}^{i(kz-t)} + \mathrm{e}^{-i(kz+t)}\right)\right) \\ u_{z1}(r,z,t) &= \mathcal{R}\left(g(r)\left(\mathrm{e}^{i(kz-t)} - \mathrm{e}^{-i(kz+t)}\right)\right), \end{aligned}$$

where f and g are as calculated in section 2.1.

We begin with the conditions on u_{r2}. Now $u_{r2}(0,z,t) = 0$ so we must set $a = 0$ (i.e. $\alpha_3(r) \equiv 0$) which leaves

$$\alpha_1(0)\left(\mathrm{e}^{2i(kz-t)} + \mathrm{e}^{-2i(kz+t)}\right) + \alpha_4(0)\left(\mathrm{e}^{3i(kz-t)} + \mathrm{e}^{-3i(kz+t)}\right) + \alpha_6(0)\left(\mathrm{e}^{i(kz-3t)} + \mathrm{e}^{-i(kz+3t)}\right) = 0,$$

from which we deduce $\alpha_1(0) = 0$, $\alpha_4(0) = 0$ and $\alpha_6(0) = 0$.

Considering the condition at the other boundary we note

$$\begin{aligned} R_1 \left.\frac{\partial u_{r1}}{\partial r}\right|_{r=1} &= \frac{\mathrm{d}f}{\mathrm{d}r}(1)\left(\mathrm{e}^{2i(kz-t)} + \mathrm{e}^{-2i(kz+t)} + 2\mathrm{e}^{-2it}\right) \\ &= i\left(\mathrm{e}^{2i(kz-t)} + \mathrm{e}^{-2i(kz+t)} + 2\mathrm{e}^{-2it}\right) \end{aligned}$$

and

$$\dot{R}_2 = i\left(\mathrm{e}^{2i(kz-t)} + \mathrm{e}^{-2i(kz+t)} + 2\mathrm{e}^{-2it}\right),$$

thus

$$\dot{R}_2 - R_1 \left.\frac{\partial u_{r1}}{\partial r}\right|_{r=1} = 0,$$

i.e. $u_{r2}(1,z,t) = 0$. This leaves us with $\alpha_1(1) = 0$, $\alpha_4(1) = 0$ and $\alpha_6(1) = 0$ and is consistent with $a = 0$.

Next we look at the conditions on u_{z2}. At $r = 0$, $\partial u_{z2}/\partial r = 0$, but

$$\frac{\partial u_{z2}}{\partial r} = \frac{\mathrm{d}\beta_1}{\mathrm{d}r}\left(\mathrm{e}^{2i(kz-t)} - \mathrm{e}^{-2i(kz+t)}\right) + \frac{\mathrm{d}\beta_4}{\mathrm{d}r}\left(\mathrm{e}^{3i(kz-t)} - \mathrm{e}^{-3i(kz+t)}\right) + \frac{\mathrm{d}\beta_6}{\mathrm{d}r}\left(\mathrm{e}^{i(kz-3t)} - \mathrm{e}^{-i(kz+3t)}\right) + \left(-b_1\sqrt{2i\mathrm{Re}}J_1(r\sqrt{2i\mathrm{Re}}) + ib_2\sqrt{2i\mathrm{Re}}K_1(-ir\sqrt{2i\mathrm{Re}})\right)\mathrm{e}^{-2it}$$

therefore we must consider the small argument expansions for Bessel functions [2, p360,375]. As $r \to 0$

$$\begin{aligned} J_1(r\sqrt{2i\mathrm{Re}}) &\sim \frac{\sqrt{2i\mathrm{Re}}}{2}r \\ K_1(-ir\sqrt{2i\mathrm{Re}}) &\sim \frac{i}{r\sqrt{2i\mathrm{Re}}}. \end{aligned}$$

This suggests that we must take $b_2 = 0$ and that $b_1 J_1(0) = 0$, leaving

$$\frac{\mathrm{d}\beta_1}{\mathrm{d}r}(0)\left(\mathrm{e}^{2i(kz-t)} - \mathrm{e}^{-2i(kz+t)}\right) + \frac{\mathrm{d}\beta_4}{\mathrm{d}r}(0)\left(\mathrm{e}^{3i(kz-t)} - \mathrm{e}^{-3i(kz+t)}\right) + \frac{\mathrm{d}\beta_6}{\mathrm{d}r}(0)\left(\mathrm{e}^{i(kz-3t)} - \mathrm{e}^{-i(kz+3t)}\right) = 0,$$

i.e. $\mathrm{d}\beta_1(0)/\mathrm{d}r = 0$, $\mathrm{d}\beta_4(0)/\mathrm{d}r = 0$ and $\mathrm{d}\beta_6(0)/\mathrm{d}r = 0$. Using the equations for β_i in terms of α_i we have the conditions

$$\begin{aligned} \frac{\mathrm{d}^2\alpha_1}{\mathrm{d}r^2} + \frac{1}{r}\frac{\mathrm{d}\alpha_1}{\mathrm{d}r} - \frac{\alpha_1}{r} &\to 0 \text{ as } r \to 0 \\ \frac{\mathrm{d}^2\alpha_4}{\mathrm{d}r^2} + \frac{1}{r}\frac{\mathrm{d}\alpha_4}{\mathrm{d}r} - \frac{\alpha_4}{r} &\to 0 \text{ as } r \to 0 \\ \frac{\mathrm{d}^2\alpha_6}{\mathrm{d}r^2} + \frac{1}{r}\frac{\mathrm{d}\alpha_6}{\mathrm{d}r} - \frac{\alpha_6}{r} &\to 0 \text{ as } r \to 0. \end{aligned}$$

As in chapter 2 considering the behaviour of these three expressions as $r \to 0$ leaves us

with

$$\begin{aligned}\frac{\mathrm{d}^2\alpha_1}{\mathrm{d}r^2}(0) &= 0\\ \frac{\mathrm{d}^2\alpha_4}{\mathrm{d}r^2}(0) &= 0\\ \frac{\mathrm{d}^2\alpha_6}{\mathrm{d}r^2}(0) &= 0.\end{aligned}$$

Finally we have

$$\begin{aligned}u_{z2}(1,z,t) &= -R_1(z,t)\frac{\partial u_{z1}}{\partial r}(1,z,t)\\ &= -\frac{\mathrm{d}g}{\mathrm{d}r}(1)\left(\mathrm{e}^{2i(kz-t)}-\mathrm{e}^{-2i(kz+t)}\right),\end{aligned}$$

but

$$\begin{aligned}\frac{\mathrm{d}g}{\mathrm{d}r}(1) &= \frac{i}{k}\left(\frac{\mathrm{d}^2f}{\mathrm{d}r^2}(1)+\frac{\mathrm{d}f}{\mathrm{d}r}(1)-f(1)\right)\\ &= \frac{i}{k}\frac{\mathrm{d}^2f}{\mathrm{d}r^2}(1)-\frac{2}{k},\end{aligned}$$

where f is known, therefore

$$\begin{aligned}\beta_1(1)\left(\mathrm{e}^{2i(kz-t)}-\mathrm{e}^{-2i(kz+t)}\right)-\left(b_1\sqrt{2i\mathrm{Re}}J_1(\sqrt{2i\mathrm{Re}})\right)\mathrm{e}^{-2it}+\beta_4(1)\left(\mathrm{e}^{3i(kz-t)}-\mathrm{e}^{-3i(kz+t)}\right)\\ +\beta_6(1)\left(\mathrm{e}^{i(kz-3t)}-\mathrm{e}^{-i(kz+3t)}\right)=\left(-\frac{i}{k}\frac{\mathrm{d}^2f}{\mathrm{d}r^2}(1)+\frac{2}{k}\right)\left(\mathrm{e}^{2i(kz-t)}-\mathrm{e}^{-2i(kz+t)}\right).\end{aligned}$$

Equating coefficients of the exponentials we have

$$\begin{aligned} b_1 &= 0 \\ \beta_1(1) &= -\frac{i}{k}\frac{\mathrm{d}^2 f}{\mathrm{d}r^2}(1) + \frac{2}{k} \\ \beta_4(1) &= 0 \\ \beta_6(1) &= 0. \end{aligned}$$

Using the equations for β_i in terms of α_i, together with the conditions $\alpha_i(0) = 0$ we have

$$\begin{aligned} \frac{\mathrm{d}\alpha_1}{\mathrm{d}r}(1) &= -2\frac{\mathrm{d}^2 f}{\mathrm{d}r^2}(1) - 4i \\ \frac{\mathrm{d}\alpha_4}{\mathrm{d}r}(1) &= 0 \\ \frac{\mathrm{d}\alpha_6}{\mathrm{d}r}(1) &= 0. \end{aligned}$$

In summary, the first set of boundary conditions are given by

$$\begin{aligned} \alpha_1(1) &= 0 \\ \alpha_1(0) &= 0 \\ \frac{\mathrm{d}\alpha_1}{\mathrm{d}r}(1) &= -2\frac{\mathrm{d}^2 f}{\mathrm{d}r^2}(1) - 4i \\ \frac{\mathrm{d}^2\alpha_1}{\mathrm{d}r^2}(0) &= 0, \end{aligned}$$

the second set by

$$\begin{aligned} \alpha_4(1) &= 0 \\ \alpha_4(0) &= 0 \\ \frac{\mathrm{d}\alpha_4}{\mathrm{d}r}(1) &= 0 \\ \frac{\mathrm{d}^2\alpha_4}{\mathrm{d}r^2}(0) &= 0, \end{aligned}$$

and the third set by

$$\begin{aligned} \alpha_6(1) &= 0 \\ \alpha_6(0) &= 0 \\ \frac{\mathrm{d}\alpha_6}{\mathrm{d}r}(1) &= 0 \\ \frac{\mathrm{d}^2\alpha_6}{\mathrm{d}r^2}(0) &= 0. \end{aligned}$$

We use MATLAB's bvp4c code to solve the three ODEs, using the standard parameters of chapter 2 and $\hat{M} = 1$. This leaves us able to investigate the influence of the two additional parameters n and $\mu_c = \mu_\infty/\mu_0$.

Figures 4.1 - 4.6 display colour plots of the velocities at $t = \pi/2$ for both $\varepsilon = 0.1$ and $\varepsilon = 0.5$ for different degrees of shear thinning behaviour. We consider $t = \pi/2$ since this time (together with $t = 3\pi/2$) is when the maximum values for velocity occur. In these six figures we look at Newtonian ($n = \mu_c = 1$), weakly shear thinning ($n = \mu_c = 0.9$), moderately shear thinning ($n = \mu_c = 0.5$) and strongly shear thinning ($n = \mu_c = 0.1$) parameters.

Figure 4.1 shows that the shear thinning parameters have little effect on the magnitude of u_r^* for $\varepsilon = 0.1$; although the area of flow at maximum velocity increases slightly as n and μ_c decrease. Increasing the value of ε to $\varepsilon = 0.5$, as displayed in figure 4.2, shows that

the maximum value of u_r^* is larger for strongly shear thinning parameters than the rest, but the most notable effect is on the regions of non-zero velocity. These regions appear to elongate as n and μ_c decrease; in doing so, the location of the maximum velocities moves from the wall of the colon toward the centre as the fluid becomes more shear thinning; this leads to u_r^* being a similar velocity at the wall for a strongly shear thinning fluid as a Newtonian one.

Figures 4.3 and 4.4 show that the outer edges of the main flow regions for u_z^* move closer to the the centre of the colon as the fluid becomes more shear thinning; i.e. the 'strip' of zero flow at the colon wall becomes wider. This effect is more pronounced for $\varepsilon = 0.5$, as is the increase in maximum velocity as the fluid becomes more shear thinning. Figure 4.4(d) ($n = \mu_c = 0, 1$, $\varepsilon = 0.5$) shows two regions of slow, relative to the maximum, velocity flow appearing between the colon wall and the main regions of flow. In addition we see that as n and μ_c decrease the maximum values of u_z^* no longer appear at the centre of the colon (i.e. along the z^*-axis).

Figures 4.5 and 4.6 show that the maximum magnitude of velocity increases as n and μ_c decrease. However, the distribution of flow also changes, therefore it may be beneficial to consider the spatial mean values for velocity magnitude as n and μ_c vary. In particular, figures 4.6(c) and 4.6(d) show an increase in regions with zero, or relatively low, velocity as the fluid becomes more shear thinning, especially near to the colon wall.

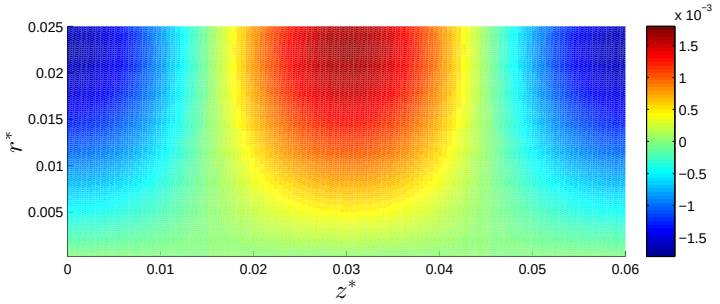

(a) Newtonian ($n = 1$, $\mu_c = 1$)

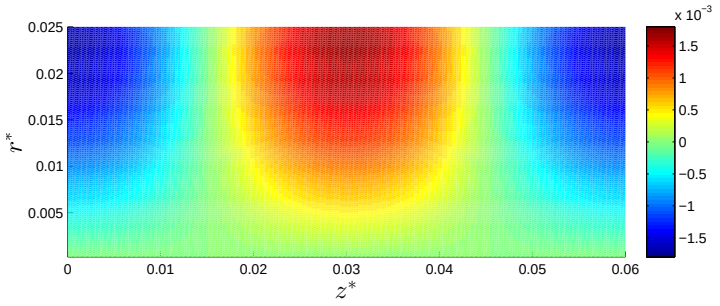

(b) $n = 0.9$, $\mu_c = 0.9$

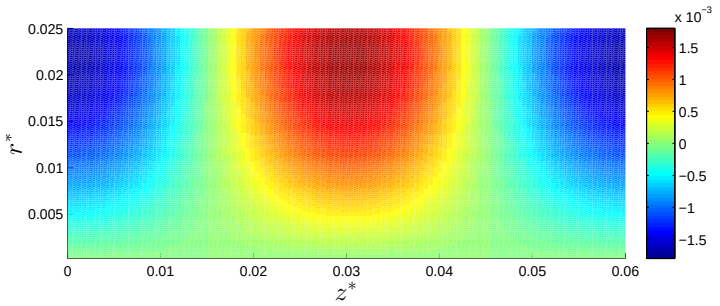

(c) $n = 0.5$, $\mu_c = 0.5$

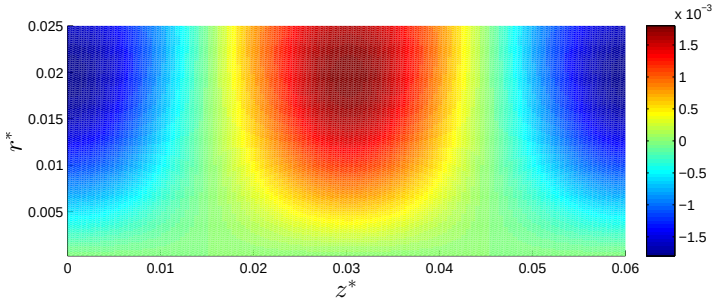

(d) $n = 0.1$, $\mu_c = 0.1$

Figure 4.1: Colour plots of u_r^* (m/s) up to $\mathrm{O}(\varepsilon^2)$ at $t = \pi/2$ for the standard parameters, with $\varepsilon = 0.1$, where r^* and z^* have units m.

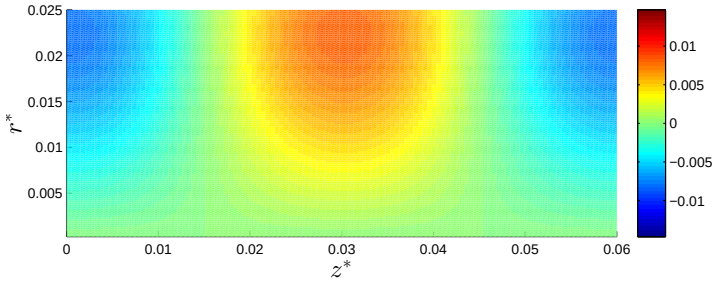

(a) Newtonian ($n = 1$, $\mu_c = 1$)

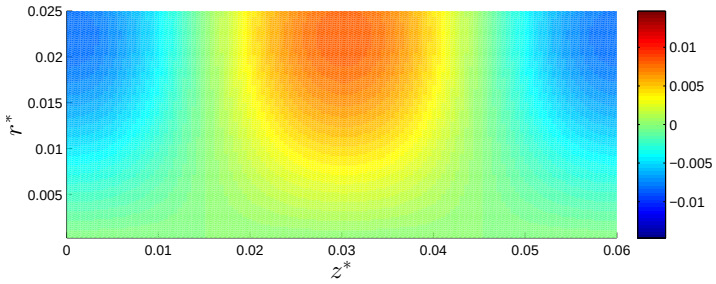

(b) $n = 0.9$, $\mu_c = 0.9$

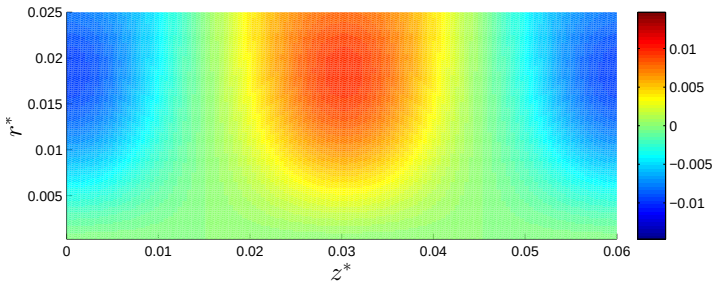

(c) $n = 0.5$, $\mu_c = 0.5$

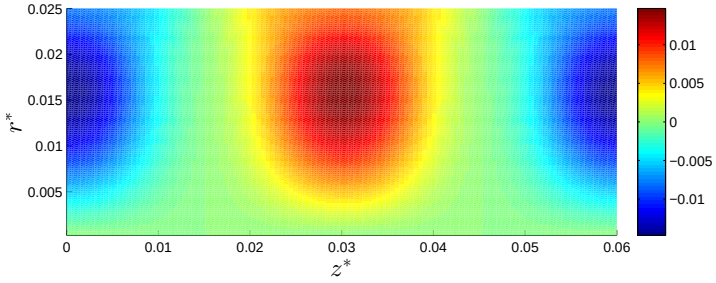

(d) $n = 0.1$, $\mu_c = 0.1$

Figure 4.2: Colour plots of u_r^* (m/s) up to $O(\varepsilon^2)$ at $t = \pi/2$ for the standard parameters, with $\varepsilon = 0.5$, where r^* and z^* have units m.

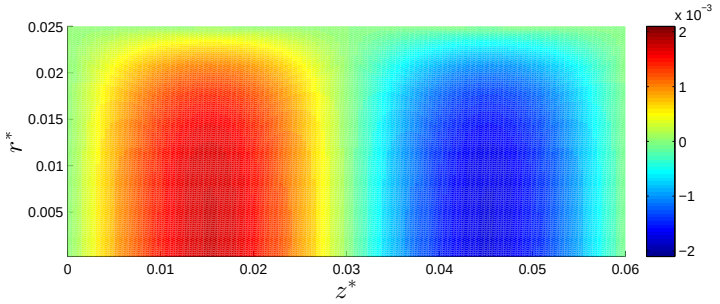

(a) Newtonian ($n = 1$, $\mu_c = 1$)

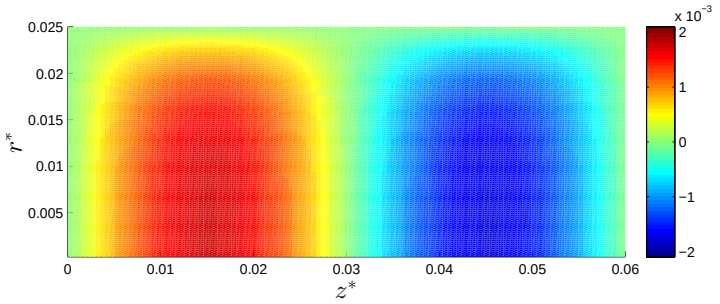

(b) $n = 0.9$, $\mu_c = 0.9$

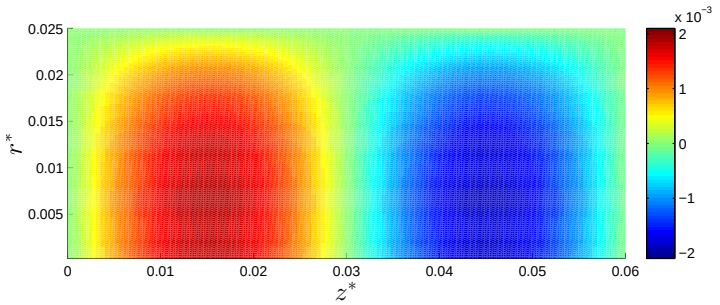

(c) $n = 0.5$, $\mu_c = 0.5$

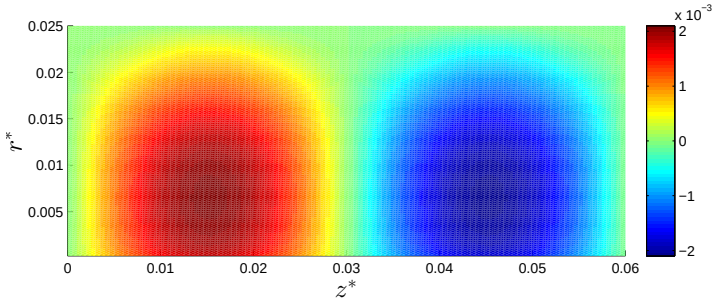

(d) $n = 0.1$, $\mu_c = 0.1$

Figure 4.3: Colour plots of u_z^* (m/s) up to $\mathrm{O}(\varepsilon^2)$ at $t = \pi/2$ for the standard parameters, with $\varepsilon = 0.1$, where r^* and z^* have units m.

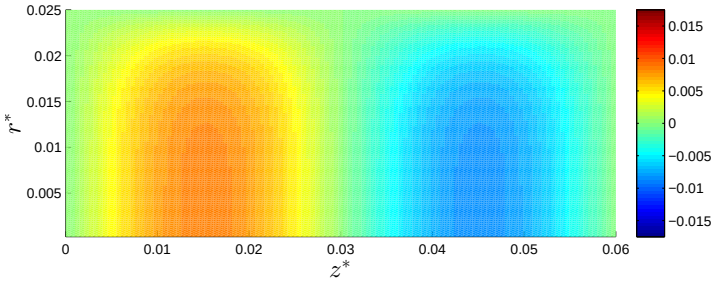

(a) Newtonian ($n = 1$, $\mu_c = 1$)

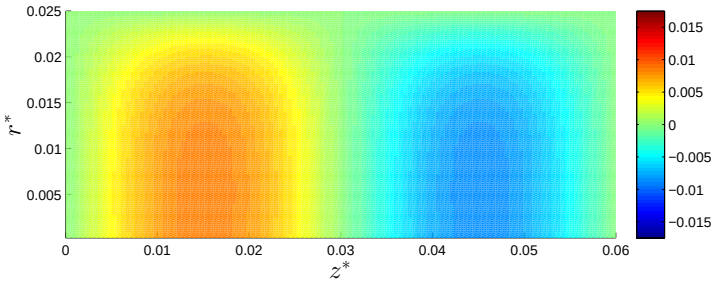

(b) $n = 0.9$, $\mu_c = 0.9$

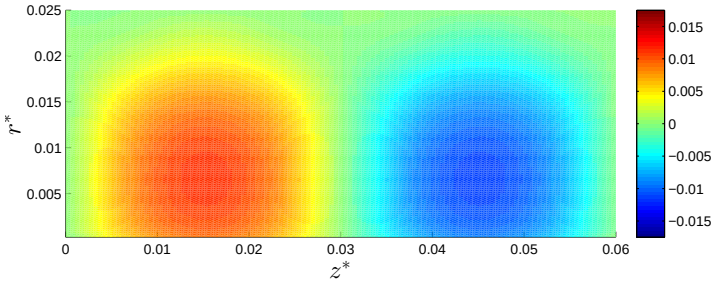

(c) $n = 0.5$, $\mu_c = 0.5$

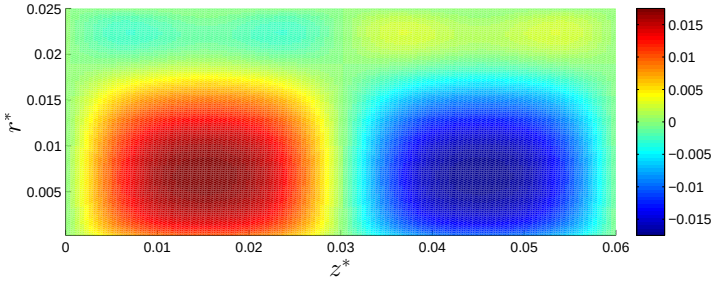

(d) $n = 0.1$, $\mu_c = 0.1$

Figure 4.4: Colour plots of u_z^* (m/s) up to $O(\varepsilon^2)$ at $t = \pi/2$ for the standard parameters, with $\varepsilon = 0.5$, where r^* and z^* have units m.

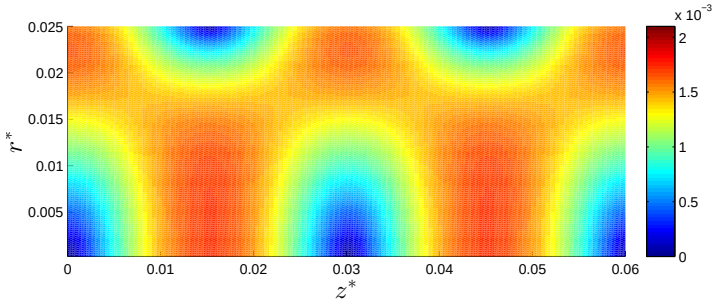

(a) Newtonian ($n = 1$, $\mu_c = 1$)

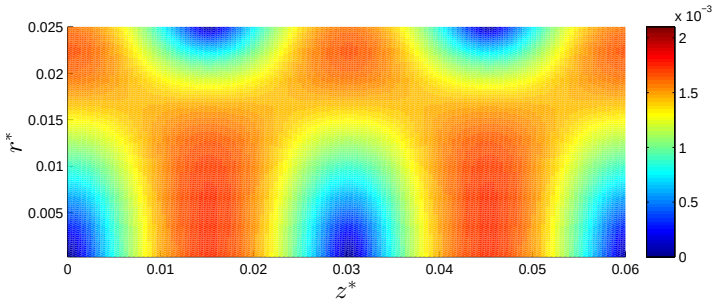

(b) $n = 0.9$, $\mu_c = 0.9$

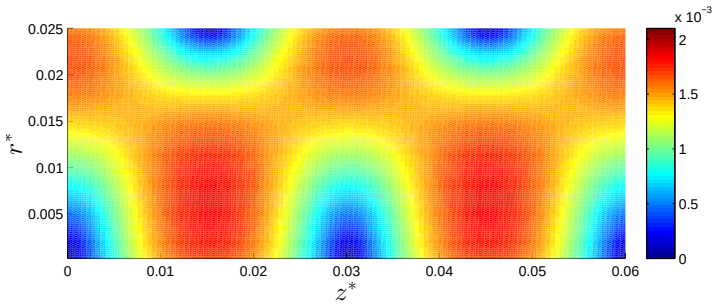

(c) $n = 0.5$, $\mu_c = 0.5$

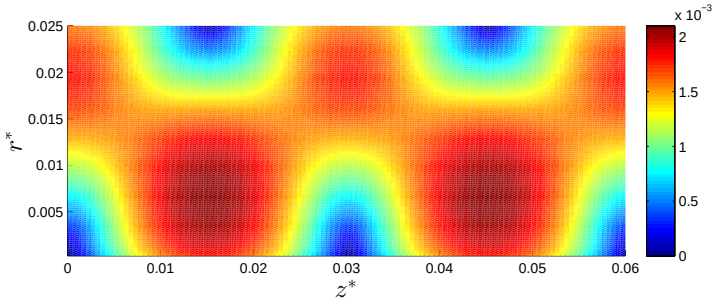

(d) $n = 0.1$, $\mu_c = 0.1$

Figure 4.5: Magnitude of velocity (m/s) up to $O(\varepsilon^2)$ at $t = \pi/2$ for the standard parameters, with $\varepsilon = 0.1$, where r^* and z^* have units m.

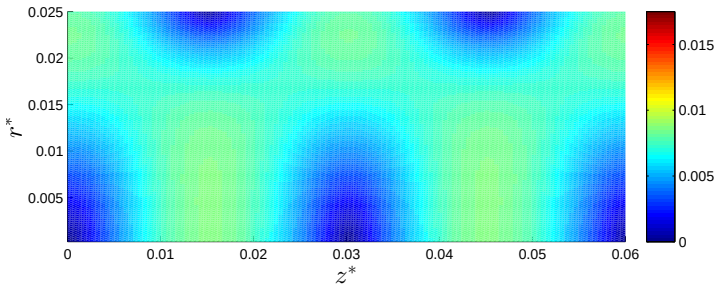

(a) Newtonian ($n = 1$, $\mu_c = 1$)

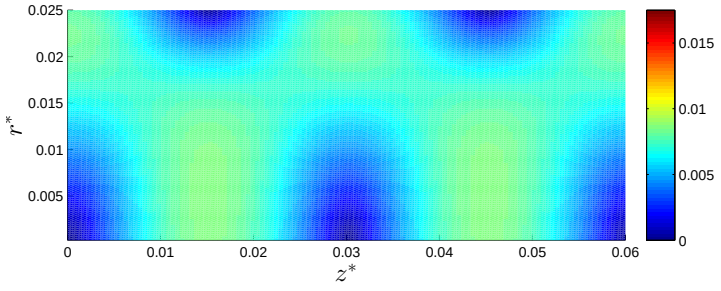

(b) $n = 0.9$, $\mu_c = 0.9$

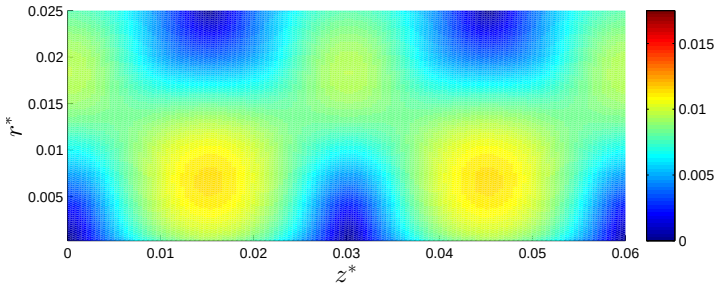

(c) $n = 0.5$, $\mu_c = 0.5$

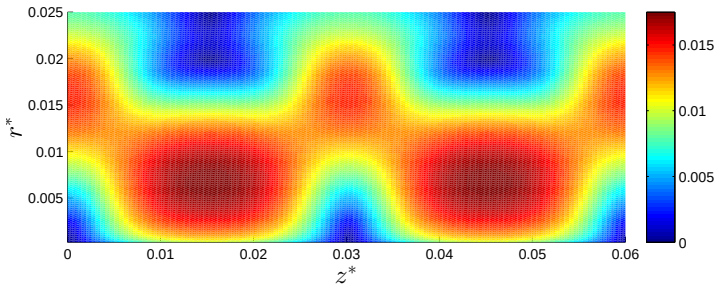

(d) $n = 0.1$, $\mu_c = 0.1$

Figure 4.6: Magnitude of velocity (m/s) up to $O(\varepsilon^2)$ at $t = \pi/2$ for the standard parameters, with $\varepsilon = 0.5$, where r^* and z^* have units m.

We now consider the spatial mean of $|\boldsymbol{u}^*| = \sqrt{u_r^{*2} + u_z^{*2}}$, given by

$$\langle |\boldsymbol{u}^*| \rangle_{r,z} = \frac{\int_0^{\lambda} \int_0^{R_0} |\boldsymbol{u}^*| \, r^* \, \mathrm{d}r^* \, \mathrm{d}z^*}{\int_0^{\lambda} \int_0^{R_0} r^* \, \mathrm{d}r^* \, \mathrm{d}z^*}.$$

We use a repeated mid-point rule to calculate the above integrals using MATLAB. Figure 4.7 shows the results of this when varying n for fixed values of μ_c. At $t = \pi/2$ it is clear that velocity magnitude increases as n and μ_c decrease. However, this is not the case at $t = 0$ and since $t = \pi/2$ is just one instant of time in the flow cycle we now consider the spatio-temporal mean of velocity magnitude,

$$\langle |\boldsymbol{u}^*| \rangle_{r,z,t} = \frac{\int_0^{2\pi} \int_0^{\lambda} \int_0^{R_0} |\boldsymbol{u}^*| \, r^* \, \mathrm{d}r^* \, \mathrm{d}z^* \, \mathrm{d}t}{\int_0^{2\pi} \int_0^{\lambda} \int_0^{R_0} r^* \, \mathrm{d}r^* \, \mathrm{d}z^* \, \mathrm{d}t}.$$

We note the result of the above calculation is not affected by leaving t as a nondimensional variable.

Plotting n against $\langle |\boldsymbol{u}^*| \rangle_{r,z,t}$ for fixed values of μ_c, we see that when $\varepsilon = 0.1$ (figure 4.8(a)) the mean velocity magnitude (over space and time) increases as n and μ_c increase, i.e. the velocity decreases as the fluid becomes more shear thinning. This is opposite to what happens with the spatial mean at $t = \pi/2$ as seen in figure 4.7(b); to get a clearer picture of what happens we consider how the spatial mean velocity varies with time. Figure 4.9 shows how the 'degree' of shear thinning behaviour of the fluid affects the way the spatial mean velocity varies with time. Figure 4.9(a) helps to explain the results in figure 4.8(a); although at the peaks where mean velocity is maximum the velocity is higher the more shear thinning the fluid is, the opposite occurs for lower velocities on the curve.

Figure 4.8(b) shows that we have the opposite relationship between n, μ_c and $\langle |\boldsymbol{u}^*| \rangle_{r,z,t}$ for $\varepsilon = 0.5$ compared with when $\varepsilon = 0.1$; i.e. mean velocity increases as n and μ_c decrease. Comparing the curves in the two plots of figure 4.9 shows us why we get different rela-

tionships between the shear thinning parameters and the spatio-temporal mean velocity magnitude for the two values of ε; we can see in figure 4.9(b) that the spatial mean velocity is highest when $\mu_c = 0.1$ for most of the contractile period when $\varepsilon = 0.5$, therefore we would expect $\langle|\boldsymbol{u}^*|\rangle_{r,z,t}$ to increase as the fluid becomes more shear thinning as figure 4.8(b) shows.

Figures 4.8 and 4.9 both suggest that the value of ε has a significant effect on the relationship between the shear thinning parameters and the magnitude of velocity. In order to investigate this we fix $n = 0.1$ and plot ε against $\langle|\boldsymbol{u}^*|\rangle_{r,z,t}$ for various values of fixed μ_c as in figure 4.10(a). We see that for larger values of ε in the range, mean velocity increases as the fluid becomes more shear thinning. Figure 4.10(b) enlarges the plot for the range of ε where the relationship between the value of the shear thinning parameters and mean velocity reverse. We see the same reversing in relationship between μ_c and $\langle|\boldsymbol{u}^*|\rangle_{r,z,t}$ for different values of n (figure 4.11); the lower the value of n, i.e. the more shear thinning the fluid, the lower the value for ε that leads to the type of relationship as in figure 4.8(b) (a decrease in n and μ_c leading to an increase in $\langle|\boldsymbol{u}^*|\rangle_{r,z,t}$).

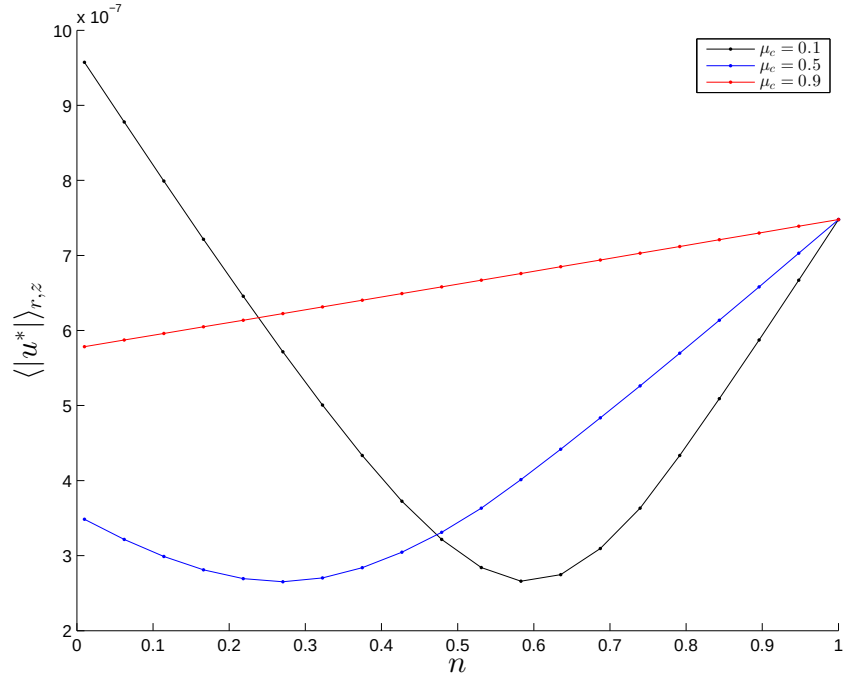

(a) $t = 0$

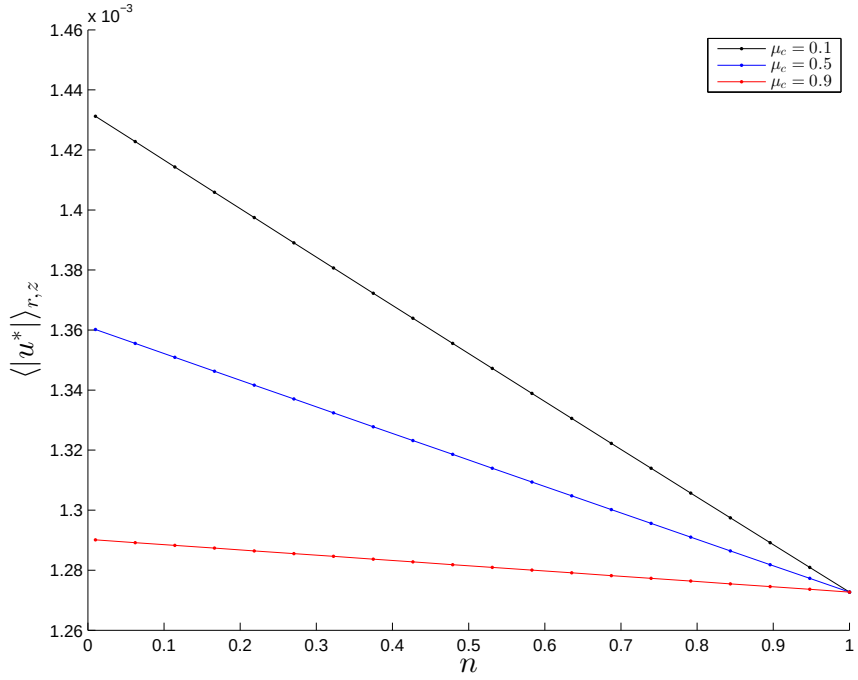

(b) $t = \pi/2$

Figure 4.7: Power law exponent n vs the spatial mean magnitude of flow, $\langle |\boldsymbol{u}^*| \rangle_{r,z}$, for $\varepsilon = 0.1$ and fixed values of viscosity ratio μ_c. We note that the plot for $t = \pi$ is identical to that of $t = 0$ and the plot for $t = 3\pi/2$ is identical to that of $t = \pi/2$ due to the symmetry of the flow.

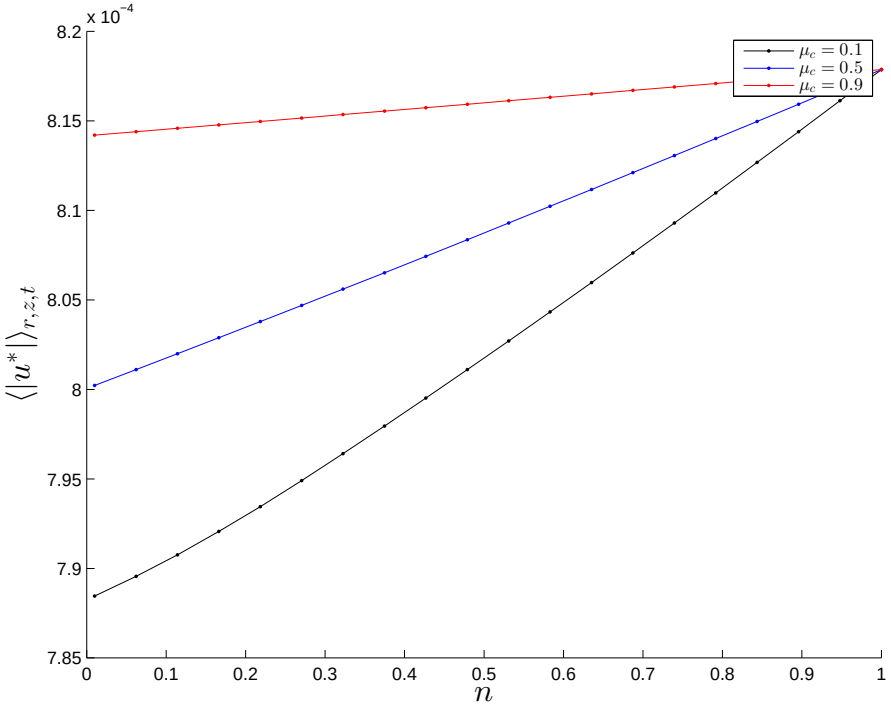

(a)

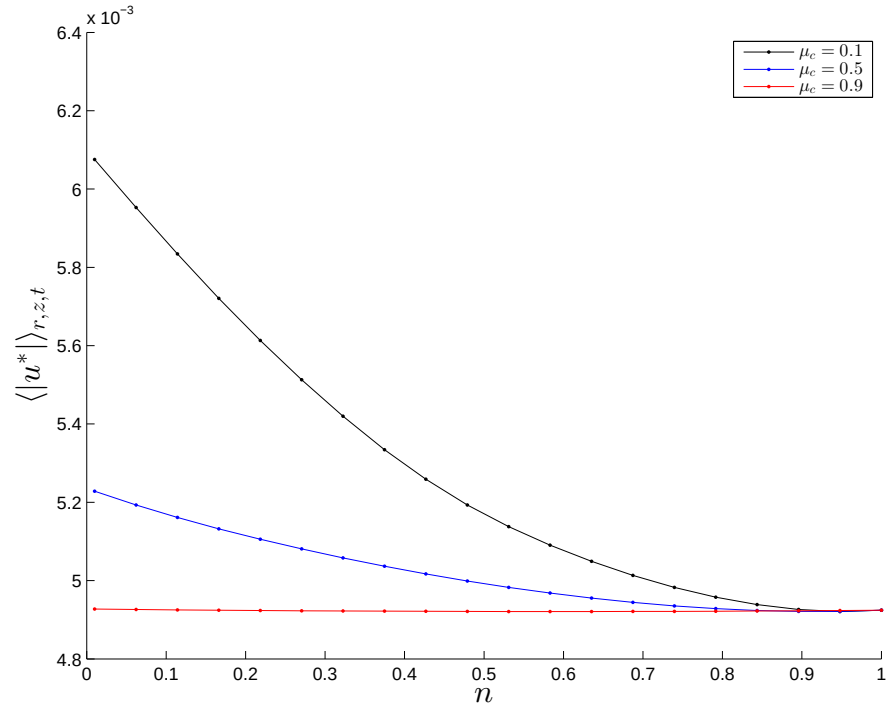

(b)

Figure 4.8: Power law exponent n vs the spatio-temporal mean $\langle|\boldsymbol{u}^*|\rangle_{r,z,t}$ for fixed values of viscosity ratio μ_c, with (a) $\varepsilon = 0.1$ and (b) $\varepsilon = 0.5$.

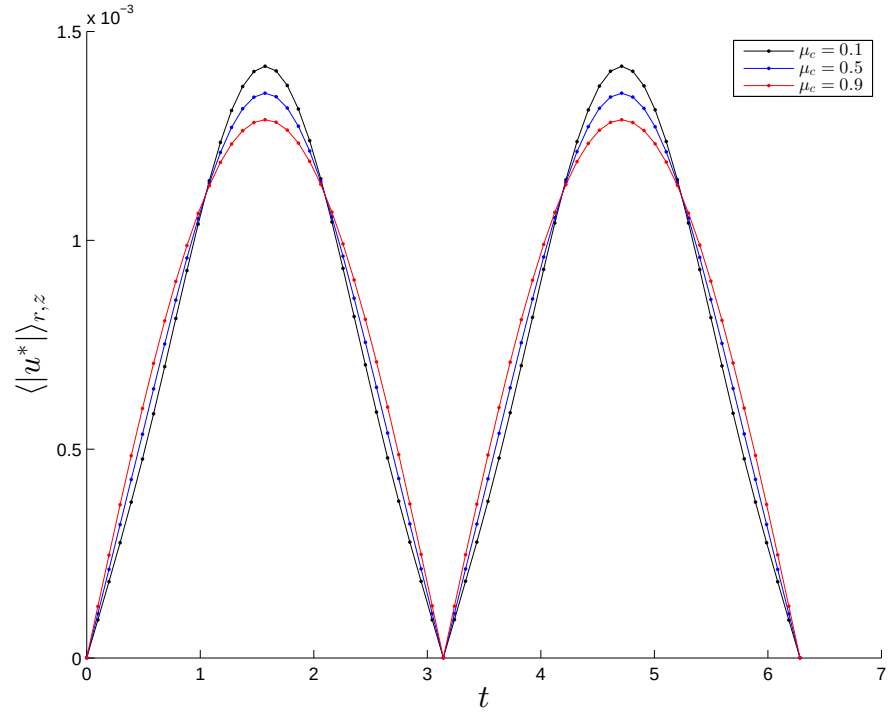

(a)

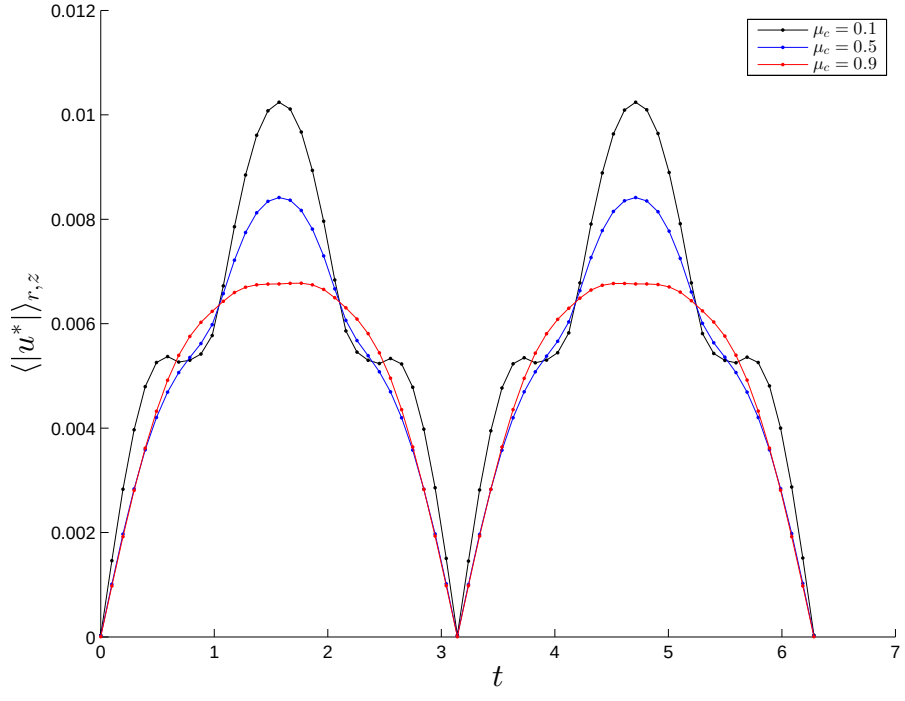

(b)

Figure 4.9: t vs $\langle|\boldsymbol{u}^*|\rangle_{r,z}$ for the power law exponent $n = 0.1$ and fixed values of viscosity ratio μ_c, with (a) $\varepsilon = 0.1$ and (b) $\varepsilon = 0.5$.

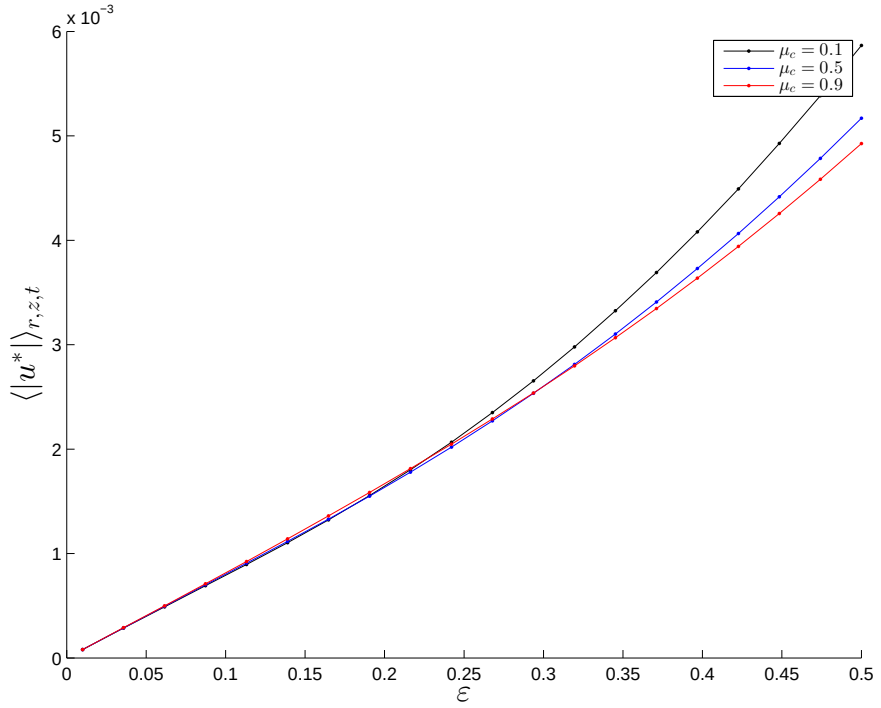

(a)

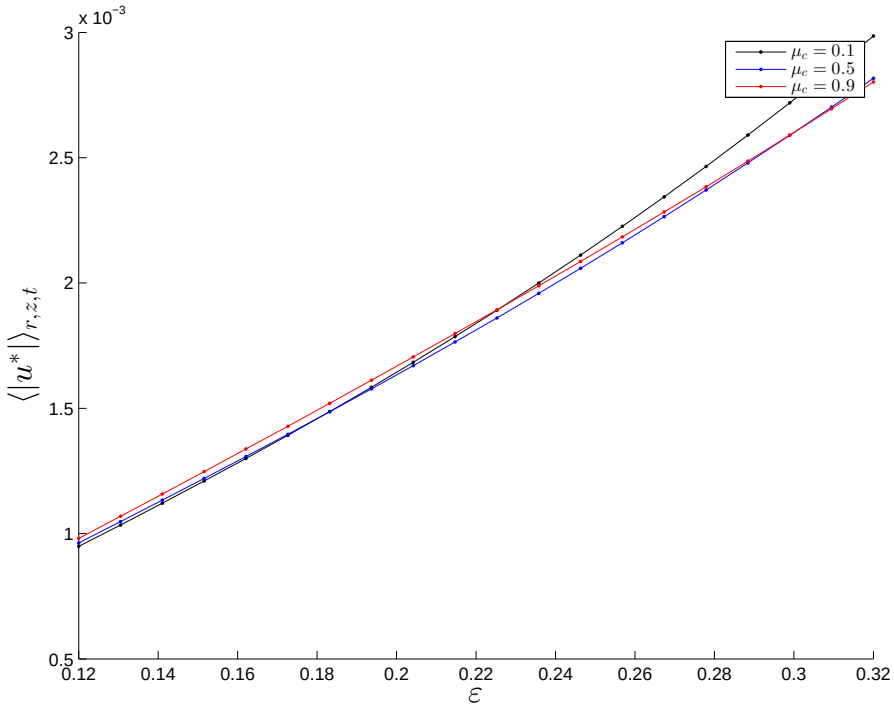

(b)

Figure 4.10: ε vs $\langle |\boldsymbol{u}^*| \rangle_{r,z,t}$ for the power law exponent $n = 0.1$ and fixed values of viscosity ratio μ_c. Figure (b) is an inset of figure (a).

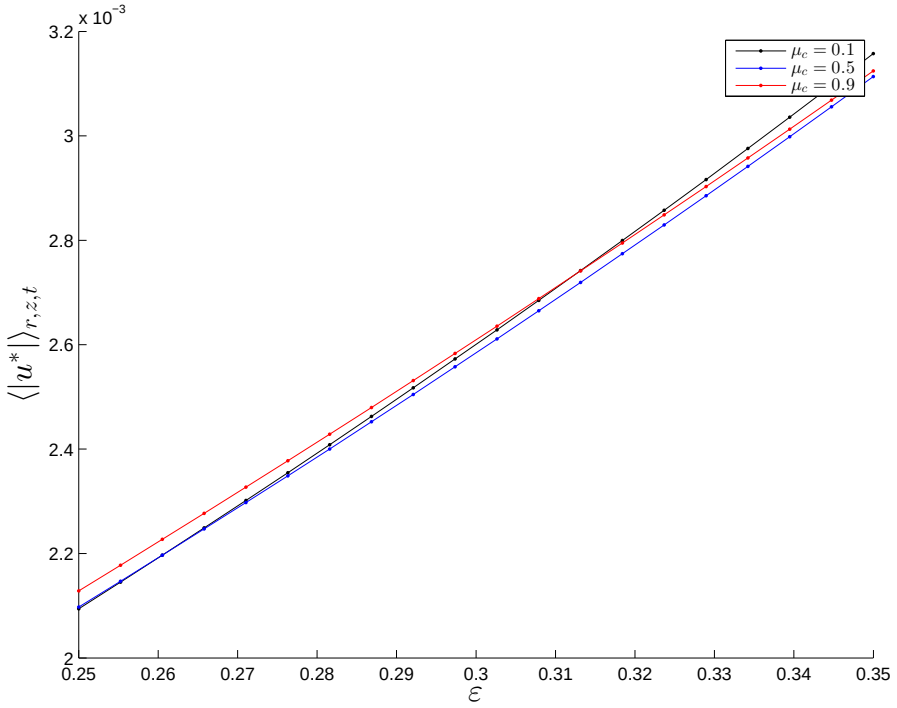

(a)

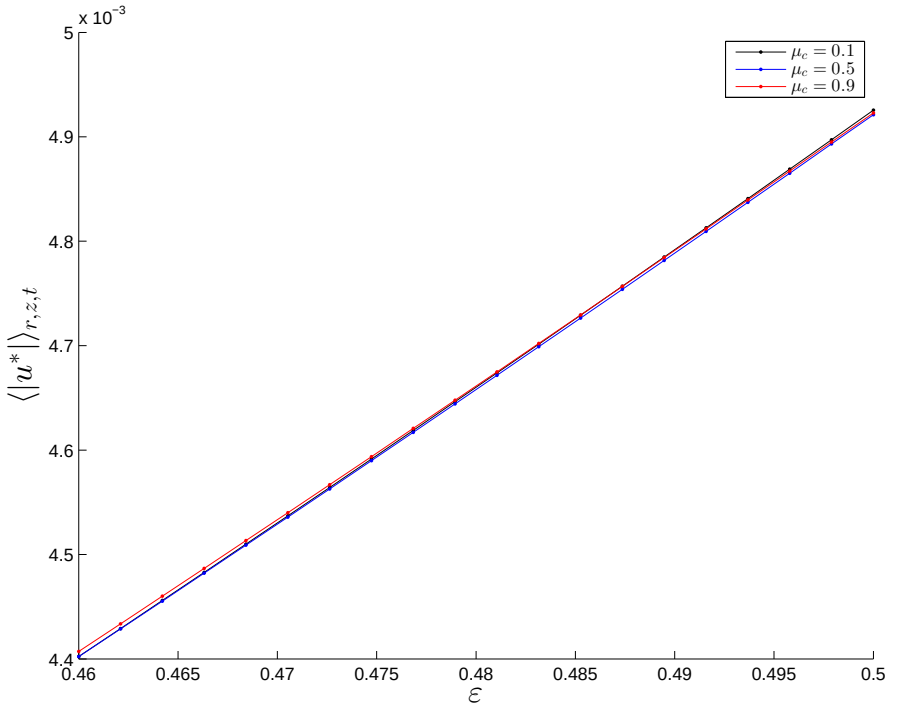

(b)

Figure 4.11: ε vs $\langle |\boldsymbol{u}^*| \rangle_{r,z,t}$ for fixed values of the viscosity ratio μ_c, with (a) $n = 0.5$ and (b) $n = 0.9$.

In this chapter we have calculated the flow fields of a Carreau fluid within a pipe of arbitrary radius and length driven by a small amplitude standing wave for the pipe wall. The Carreau fluid represents intestinal chyme, the pipe represents the ascending colon and the small amplitude standing wave represents the segmental contractions of the colon wall. Within our parameter regime we found the flow at $O(\varepsilon)$ is identical to that of a Newtonian fluid. At $O(\varepsilon^2)$, however, the flow is dependent on the Carreau shear thinning parameters. We found that the more shear thinning the fluid was, quantified by decreasing n and μ_c, the higher the maximum values of velocity; however, the relationship between the shear thinning parameters and mean velocity is less straightforward. Whether the spatio-temporal mean increases or decreases as μ_c decreases depends on the value of ε; in particular the critical range of ε where this relationship reverses depends on the power law exponent n. The lower the value of n, the lower the value $\varepsilon_c(n)$ for which the mean velocity increases as μ_c decreases when $\varepsilon \geq \varepsilon_c$.

In the next chapter we investigate particle transport within the ascending colon.

Chapter 5

Lagrangian Particle Tracking used as a Model for Drug Delivery

In this chapter we expand the work of chapter 2 to consider the transport of a particle once it enters the colon. We have chosen to use the one layer model for simplicity, due to the limited impact of mucus specific parameters on the bulk flow within our two layer model. For transportation of a particle it is the bulk flow which is important, thus the inclusion of only one layer is a suitable simplification. If we were instead concerned with the mechanisms of absorption or the chemical make up of a drug then consideration of the mucus layer and fluid interface would be more critical.

We consider a dosage form consisting of an outer vessel with several solid microspheres containing the drug to be delivered inside. These microspheres are released when the dosage reaches the colon via some mechanism such as the ones described in section 1.1. Figure 5.1 describes this process.

We estimate the size of the Péclet number, Pe, in order to determine the relative influence of advective and diffusive forces on transport. The diffusion coefficient for a

particle in a low Reynolds number fluid is given by the Stokes-Einstein equation

$$D = \frac{k_B T}{6\pi\mu r},$$

where $k_B \approx 1.38 \times 10^{-23}$ J/K is the Boltzmann constant; T is the absolute temperature of the fluid (~ 300 K at body temperature); μ is the viscosity of the fluid; and r is the radius of the microsphere. To find an approximate upper bound for D in our problem we take $k_B \approx 10^{-23}$ J/K and a microsphere radius of 1 μm, therefore

$$\begin{aligned} D &\approx \frac{10^{-23} \times 3 \times 10^2}{(3 \times 10)\pi \times 10^{-6}} \\ &\approx \mathrm{O}(10^{-16}\ \mathrm{m^2 s}). \end{aligned}$$

From this we have

$$\begin{aligned} \mathrm{Pe} &= \frac{\varepsilon\omega R_0^2}{D} \\ &\approx \mathrm{O}(10^{11}) \\ &\gg 1, \end{aligned}$$

thus advection dominates over diffusion and we consider advection as the mechanism of particle transport rather than diffusion or a combination of the two. In addition we do not consider dissolution of the microspheres, since we assume that the drug is not released until it reaches the mucosa.

We develop a MATLAB code for solving the relevant kinematic ODE and calculating the percentage of particles reaching the colon wall for absorption (given an even distribution at $t = 0$). We analyse these results and the effects of changing parameter values, including a mechanism for considering the length of diffusion of a given drug.

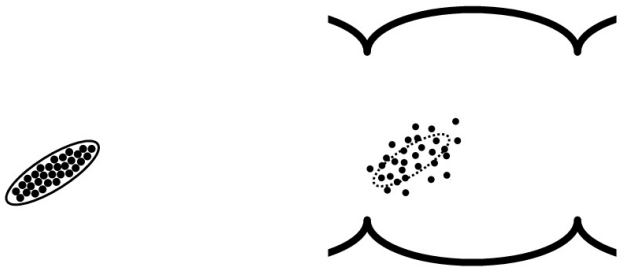

(a) Step 1: Intact dosage form.

(b) Step 2: Exterior of dosage form breaks down and begins to release microspheres.

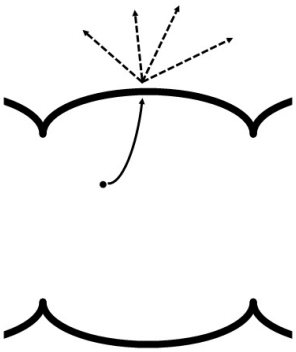

(c) Step 3: The microspheres are transported within the colon via advection, with the drug released into the bloodstream once the microsphere reaches the mucosa.

Figure 5.1: Stages of drug delivery in the colon.

5.1 Force Balance and Particle Tracking Method

We begin by considering the motion of a spherical particle through a given fluid, we may then use Stokes' Law for the frictional force acting on the particle. Thus using Newton's second law we have

$$m\frac{\mathrm{d}^2\boldsymbol{x}^*}{\mathrm{d}t^{*2}} = 6\pi\mu a\left(\boldsymbol{u}^*(\boldsymbol{x}^*) - \frac{\mathrm{d}\boldsymbol{x}^*}{\mathrm{d}t^*}\right), \tag{5.1.1}$$

where m is the mass of the particle; $\boldsymbol{x}^* = (r^*, z^*)$ gives the position of the particle; a is the radius of the particle; and $\boldsymbol{u}^*$ is the fluid velocity calculated (up to $\mathrm{O}(\varepsilon^2)$) in chapter 2. We also have the initial conditions

$$\begin{aligned} \boldsymbol{x}^*(0) &= \boldsymbol{x}_{\mathbf{0}}^* \\ \frac{\mathrm{d}\boldsymbol{x}^*}{\mathrm{d}t^*}(0) &= 0. \end{aligned}$$

Nondimensionalising equation (5.1.1) with $\boldsymbol{x}^* = R_0\boldsymbol{x}$, $\boldsymbol{u}^* = \omega R_0 \boldsymbol{u}^*$ and $t^* = t/\omega$ we have

$$\mathcal{M}\frac{\mathrm{d}^2\boldsymbol{x}}{\mathrm{d}t^2} = \boldsymbol{u}(\boldsymbol{x}) - \frac{\mathrm{d}\boldsymbol{x}}{\mathrm{d}t},$$

where

$$\begin{aligned} \mathcal{M} &= \frac{m\omega}{6\pi\mu a} \\ &= \frac{\frac{4}{3}\pi a^3 \rho_P \omega}{6\pi\mu a} \\ &= \frac{2a^2\rho_P\omega}{9\mu}, \end{aligned}$$

and ρ_P denotes the density of the particle. If we assume our particles have a radius of no more than 1 mm, i.e. $a = 10^{-3}$ m, and $\omega = \pi/10$ as in previous chapters, then taking $\rho_P \approx 2 \times 10^3$ kg/m^3 we have

$$\mathcal{M} \approx \frac{\frac{4\pi}{9} \times 10^{-4}}{\mu}.$$

Now, μ in this problem has been taken as 5 Pa·s and is unlikely to be smaller than $\mathrm{O}(10^{-1}\ \mathrm{Pa}\cdot\mathrm{s})$, thus $\mathcal{M} \ll 1$ and we use the equation

$$\frac{\mathrm{d}\boldsymbol{x}}{\mathrm{d}t} = \boldsymbol{u}(\boldsymbol{x}(t), t),$$

subject to $\boldsymbol{x}(0) = \boldsymbol{x_0}$, as our particle tracking ODE.

Recall that $\boldsymbol{u}$ is dependent on the functions f and α. Our results for α, determined using bvp4c, are valid only for $0.01 < r < 1$, to maintain numerical regularity, therefore we cannot calculate $\boldsymbol{u}$ outside this range. Once a particle reaches $r = 1$ it is considered to be 'captured' by the wall and no longer subject to the forces of the flow. Thus we set $\alpha = 0$ for both $r < 0.01$ and $r > 1$, and set $f = 0$ for $r > 1$.

We use an explicit Runge-Kutta (Dormand-Prince) formula implemented via MATLAB's ode45 algorithm to solve equation (5.1) subject to an initial condition on position. To begin with we run the code for $t \in [0, 2\pi]$, i.e. one cycle of the periodic contraction. We also set a maximum timestep with the ode45 code of $t = 0.02\pi$ (i.e. 1% of the cycle length) in order to minimise calculation errors.

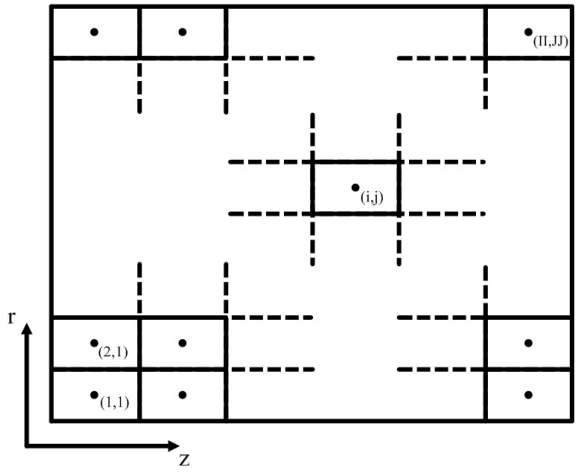

Figure 5.2: Grid of initial positions used for particle tracking with the indices $1 \leq i \leq II$ and $1 \leq j \leq JJ$.

To visualise these results we split the $r - z$ plane into a grid of equally sized rectangles and take the centre of each of these rectangles to be the initial position of one particle. Figures 5.3 and 5.4 show the results of this for various values of ε on a 10×10 grid for both full and half wavelengths. As we might expect, increasing the value of ε increases the distance that a particle travels.

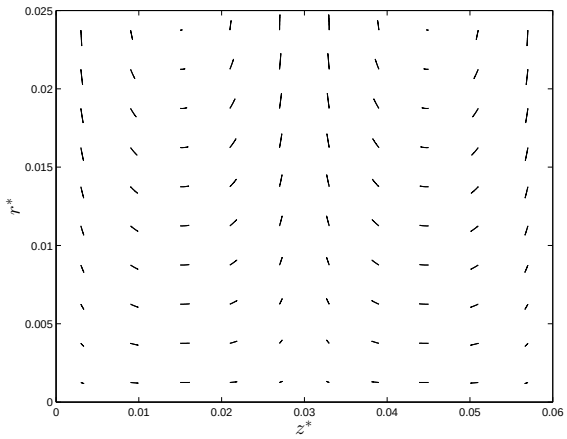

(a) $\varepsilon = 0.01$

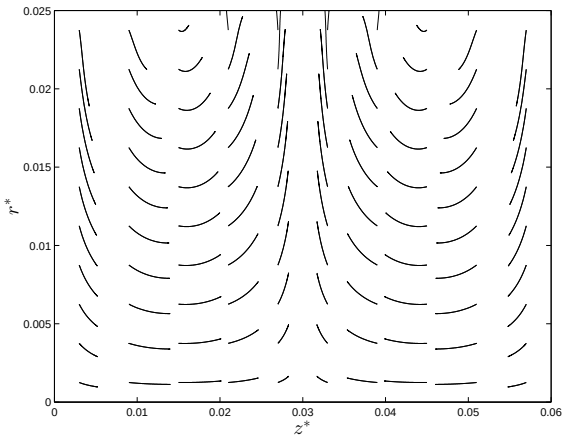

(b) $\varepsilon = 0.05$

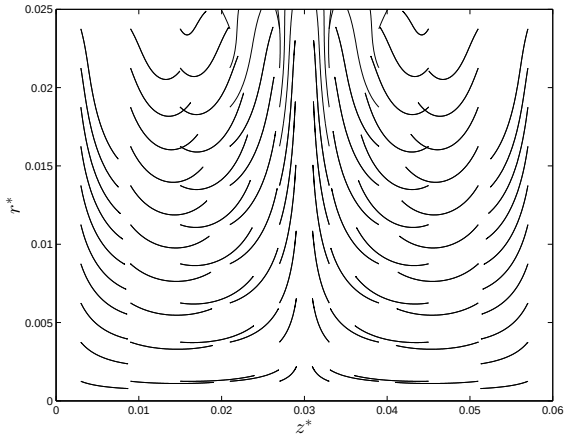

(c) $\varepsilon = 0.1$

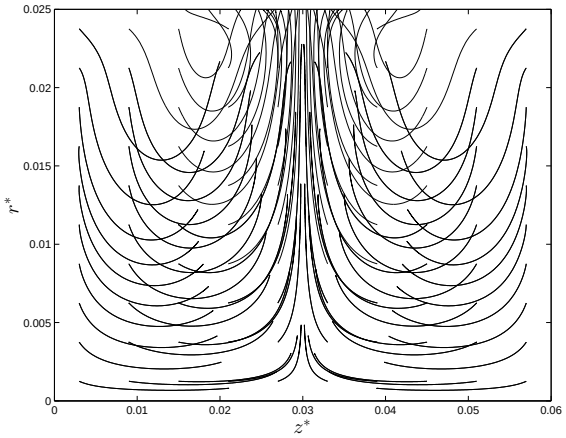

(d) $\varepsilon = 0.25$

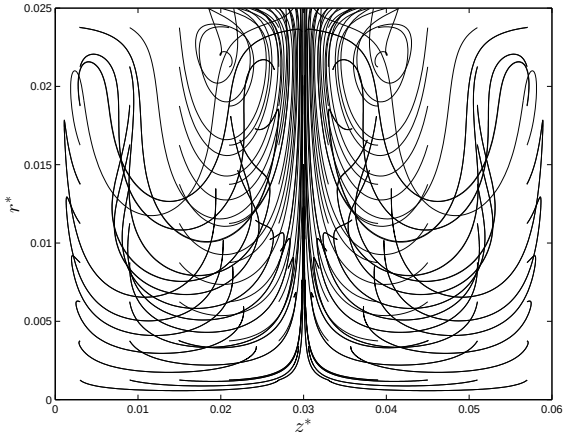

(e) $\varepsilon = 0.5$

Figure 5.3: Particle paths over one wavelength for a range of amplitudes.

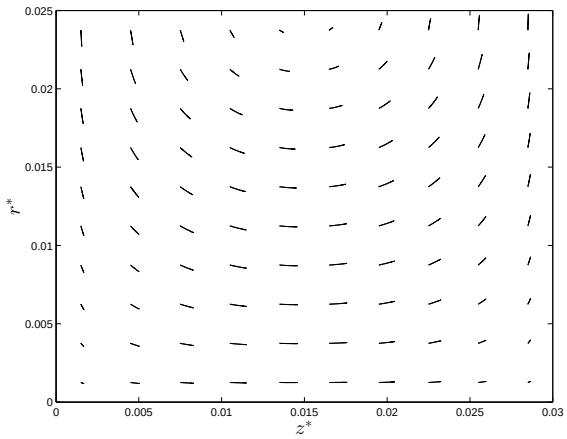

(a) $\varepsilon = 0.01$

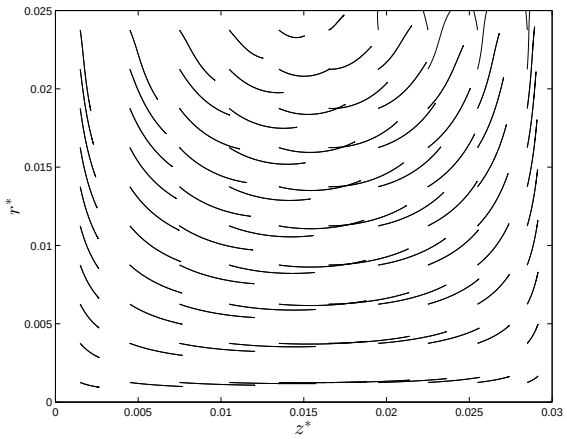

(b) $\varepsilon = 0.05$

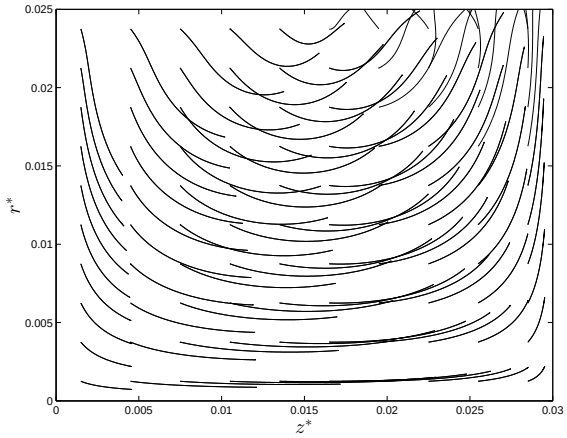

(c) $\varepsilon = 0.1$

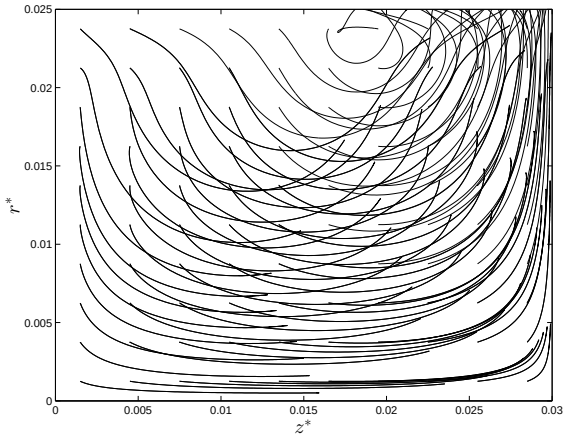

(d) $\varepsilon = 0.25$

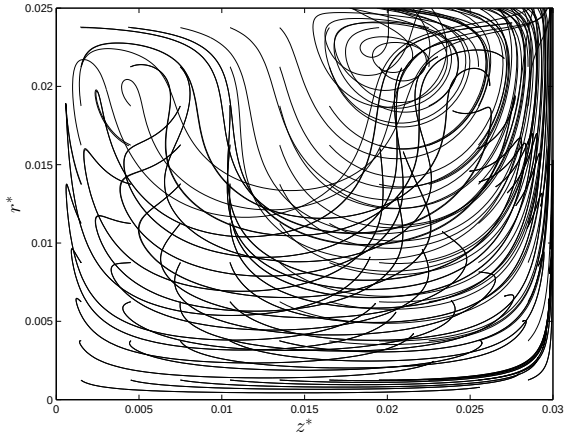

(e) $\varepsilon = 0.5$

Figure 5.4: Particle paths over half a wavelength for a range of amplitudes.

In order to analyse these results we need to calculate the proportion of particles which reach the wall. In addition we want to consider the effects of molecular diffusion on absorption, i.e. to mimic diffusion we specify a line where we consider a particle to be 'close enough' to the wall for drug absorption. To this end we introduce a parameter d, such that if $r \geq d$ at some point of the path the particle is considered to have reached the wall via diffusion. This allows us to create 'look up' tables with data which could be used for drugs with different diffusion coefficients and hence different characteristic length scales for diffusion.

Since we are dealing with a cylindrical geometry we need to consider volumes of the grid elements, rather than area of the $r-z$ plane, as the volume that an element of the plane represents increases as r does. The proportion of particles reaching $r = d$, $\phi(d)$, is then given by

$$\phi(d) = \frac{2\int\int_{\kappa(d)} r \, \mathrm{d}r \, \mathrm{d}z}{R_0^2 \lambda}, \tag{5.1.2}$$

where $\kappa(d)$ is the domain consisting of elements in the $r-z$ plane for which particles enter the region $r \geq d$. To calculate ϕ over half a wavelength instead we replace λ by $\lambda/2$. To determine (5.1.2) in MATLAB we first introduce a matrix M_{ij}, such that $M_{ij} = 1$ if there exists a point on the $(i,j)^{\text{th}}$ path such that $r \geq d$, otherwise $M_{ij} = 0$. This is done within the MATLAB function for f by switching the $(i,j)^{\text{th}}$ entry from 0 to 1 if $r \geq d$. The area of an annulus between $a < r < R$ is given by $\pi(R^2 - a^2)$, thus for each element such that $M_{ij} = 1$ we calculate the difference of the squares of the two r boundaries. We store these in a matrix V_{ij} (where $V_{ij} = 0$ if $M_{ij} = 0$), then the volume of particles reaching the wall is

$$\pi z \sum_{i,j} V_{ij},$$

where z is the width of one element. This allows us to find the proportion, ϕ, of particles

reaching the wall via

$$\begin{aligned}\phi &= \frac{\text{Volume of particles reaching the wall}}{\text{Total volume of cylinder}} \\ &= \frac{z\sum_{i,j} V_{ij}}{R_0^2\lambda}.\end{aligned}$$

Tables 5.1 and 5.2 display the results of this method over a full and half wavelength respectively using a 20×20 grid. Despite the symmetry of the flow the proportional results for a full wavelength are not identical to those of a half wavelength since the initial positions used in each case will be different. As we qualitatively observed using figures 5.3 and 5.4 increasing the value of ε, i.e. increasing the amplitude of the contraction relative to the colon radius, increases the proportion of particles which are absorbed. In addition, as we would expect, $\phi(d)$ increases as d decreases.

Table 5.1: Proportion of particles absorbed over one wavelength.

	ε				
d	0.01	0.05	0.1	0.25	0.5
1	0.029	0.129	0.257	0.548	0.667
0.99	0.039	0.129	0.261	0.548	0.667
0.98	0.049	0.153	0.273	0.548	0.667
0.97	0.098	0.202	0.322	0.571	0.676
0.95	0.125	0.219	0.343	0.581	0.676
0.9	0.216	0.305	0.416	0.613	0.781
0.85	0.302	0.385	0.496	0.658	0.805
0.8	0.383	0.454	0.559	0.696	0.821
0.7	0.530	0.586	0.661	0.780	0.855
0.5	0.755	0.791	0.828	0.894	0.931

Table 5.2: Proportion of particles absorbed over half a wavelength.

	ε				
d	0.01	0.05	0.1	0.25	0.5
1	0.029	0.124	0.261	0.545	0.688
0.99	0.039	0.137	0.261	0.549	0.688
0.98	0.044	0.149	0.270	0.554	0.688
0.97	0.098	0.206	0.328	0.573	0.698
0.95	0.125	0.223	0.345	0.575	0.708
0.9	0.216	0.313	0.423	0.613	0.781
0.85	0.302	0.393	0.489	0.654	0.826
0.8	0.383	0.464	0.552	0.694	0.843
0.7	0.530	0.593	0.662	0.774	0.871
0.5	0.757	0.789	0.829	0.892	0.928

5.2 The Effect of Parameters on Absorption

In this section we consider the influence our parameters have on the proportion of particles which are considered to have been absorbed. We consider our results over half a wavelength since the flow is symmetric, then the results will be more accurate than over a full wavelength due to smaller rectangles for the same size grid. We also choose to run our results for $\varepsilon = 0.1$, this keeps ε small but also makes the geometry slightly more realistic. We denote the proportion of particles absorbed over half a wavelength by the function ϕ, which is dependent on d and the parameter being varied. We run the codes for one cycle only since, due to the periodicity of flow, running the code for multiple cycles does not increase the value of ϕ. In addition, altering the period of the contraction does not affect the value of ϕ over a full cycle.

In order to decide what size of grid we should use we ran the code for the grid sizes shown in table 5.3. Convergence was achieved to within 10% relative error for a 20×20 grid compared to a 40×40 grid, thus we choose to use a 20×20 grid as a compromise between accuracy and running time of the code.

Table 5.3: Values of ϕ for different size grids.

	Number of subdivisions of each side of grid				
d	10	15	20	30	40
1	0.249	0.257	0.261	0.254	0.253
0.99	0.279	0.265	0.261	0.262	0.267
0.98	0.279	0.271	0.270	0.306	0.297
0.97	0.279	0.279	0.328	0.312	0.306
0.95	0.374	0.357	0.345	0.358	0.341
0.9	0.441	0.436	0.423	0.421	0.422
0.85	0.52	0.472	0.489	0.502	0.490
0.8	0.548	0.554	0.552	0.553	0.554
0.7	0.67	0.680	0.662	0.664	0.663
0.5	0.832	0.841	0.829	0.830	0.831

We recall that the dimensional parameters, together with our estimated values, are

given by

$$R_0 = 0.025 \text{ m};\ \lambda = 0.06 \text{ m};\ \omega = \frac{\pi}{10} \text{ rad/s};\ \mu_0 = 5 \text{ Pa} \cdot \text{s};\ \text{and } \rho = 1000 \text{ kg/m}^3.$$

From these we have the nondimensional parameters

$$\text{Re} = \frac{\rho \omega R_0^2}{\mu_0};\ k = \frac{2\pi R_0}{\lambda};\ \text{and } \varepsilon = \frac{\varepsilon^*}{R_0}.$$

The ratio between inertial and viscous effects is given by εRe; k represents the ratio between colonic radius and contractile wavelength; and ε gives us the amplitude of the contractions as a proportion of radius. Since both r and z are scaled with respect to the same parameter (i.e. R_0) and we are investigating proportions over one contraction, it is possible to consider the effects of parameters by looking only at the nondimensional groupings.

The dimensional parameters above yield base values for the nondimensional parameters of

$$\begin{aligned} \text{Re} &= 0.0125\pi \approx 0.039 \\ k &= \frac{5\pi}{6} \approx 2.62. \end{aligned}$$

In order to select a reasonable range of values to investigate for Re and k we first consider realistic ranges for the dimensional parameters. We shall consider a range for ε separately, as this is of particular interest to pharmacologists.

We have already mentioned that the diameter of the colon varies from 8.5 cm at the caecum to 2.5 cm at the sigmoid colon [70]. Thus we take a range for R_0 of $0.015 - 0.04$ m, corresponding to diameters of $3 - 8$ cm.

There does not appear to be any information pertaining to the length of individual

haustra in the literature, but we do know that the ascending colon is approximately 12 cm in length [1] and we use this as a guide. The length of one haustrum is taken to be represented by half the wavelength of a contraction. For example if there were four segments to the ascending colon then each would be approximately 3 cm in length, giving a wavelength of $\lambda = 6$ cm. We choose a range of haustrum length of $2 - 5$ cm, giving a range for λ of $0.04 - 0.1$ m.

The angular frequency ω is given by $\omega = 2\pi/P$, where P is the period of the contractile wave. In section 1.3.2 we reported ranges of contractile frequency of the circular muscle as $2.5 - 3$ per minute [43], $1 - 6$ per minute [71] and 6.3 ± 0.6 per minute [22]. In addition Bassotti et al. [6] found a range of frequencies of $2 - 8$ per minute, with 3 per minute the most common (hence our choice of $P = 20$ s as a base value earlier). Thus we take a range for P of $7.5 - 30$ s, i.e. a range for ω of $\pi/15 - 4\pi/15$ rad/s, corresponding to $2 - 8$ cycles per minute.

Data on the viscosity of the chyme in various intestinal regions may be found in section 1.3.1. The viscosity of rat small intestinal content, measured at a shear rate of 50 s^{-1} was found to be 1.877 Pa·s or 1.868 Pa·s depending on diet [34]. However our rheological models require the zero shear viscosity, so measurements taken at a lower shear rate are desirable. At a shear rate of 1 s^{-1} the viscosities of chicken small intestinal and caecal contents have been measured as 3.8 Pa·s and 82 Pa·s respectively [64] and the viscosity of pig caecal content as 3.7 Pa·s [65]. From this data we choose a range for μ_0 of $1 - 80$ Pa·s.

Finally, the fluid density of chyme has not been extensively measured. One value found for chyme is given by Takahashi et al. [64] as 1030 kg/m^3 for the caecal content of chickens. The density of water at room temperature is approximately 1000 kg/m^3, close to the value of Takahashi et al. Therefore, since we lack information on mucus and chyme densities, we take a range of values for ρ of $800 - 1300$ kg/m^3.

Using these ranges we have

$$\mathrm{Re}_{max} \approx 1.74;\ \mathrm{Re}_{min} \approx 0.000471;\ k_{max} = 2\pi \text{ and } k_{min} = \frac{3\pi}{10},$$

we therefore choose the ranges $0.0004 \leq \mathrm{Re} \leq 1.75$ and $3\pi/10 \leq k \leq 2\pi$. Tables 5.4 and 5.5 display the results for these ranges.

Table 5.4: Values of ϕ for a range of values for Re with $k = 5\pi/6$.

	Re				
d	0.0004	0.4378	0.8752	1.3126	1.75
1	0.261	0.261	0.261	0.261	0.261
0.99	0.261	0.261	0.261	0.261	0.261
0.98	0.270	0.270	0.270	0.270	0.280
0.97	0.328	0.328	0.329	0.329	0.329
0.95	0.345	0.342	0.342	0.342	0.342
0.9	0.423	0.423	0.423	0.423	0.423
0.85	0.489	0.489	0.489	0.489	0.489
0.8	0.552	0.552	0.552	0.552	0.552
0.7	0.662	0.662	0.662	0.662	0.662
0.5	0.829	0.831	0.831	0.831	0.831

Table 5.5: Values of ϕ for a range of values for k with $\mathrm{Re} = 0.039$.

	k				
d	0.3π	0.725π	1.15π	1.575π	2π
1	0.260	0.257	0.252	0.253	0.249
0.99	0.264	0.261	0.260	0.260	0.257
0.98	0.272	0.279	0.271	0.269	0.261
0.97	0.324	0.326	0.327	0.316	0.295
0.95	0.352	0.345	0.339	0.323	0.308
0.9	0.427	0.423	0.411	0.392	0.381
0.85	0.504	0.492	0.473	0.452	0.434
0.8	0.566	0.554	0.539	0.517	0.492
0.7	0.675	0.665	0.647	0.621	0.599
0.5	0.843	0.834	0.815	0.793	0.780

As we can see from table 5.4, with the exception of four values for d, altering the value of Re within this range has no effect on the proportion of particles absorbed. For the four

values of d where this is not the case (0.98, 0.97, 0.95 and 0.5) the differences in the value of ϕ as Re is varied are limited; therefore it is reasonable to conclude that the exact value of Re, within this range, is not important in calculating the proportion of particles which are absorbed.

Table 5.5 displays the results of our parameter variation for k and in doing so shows no simple relation between k and ϕ. In order to investigate further we consider how the mean velocity changes with k, we look at the nondimensional velocity since this depends only on k, Re and ε.

The spatio-temporal mean of a variable u in cylindrical co-ordinates is given by

$$\langle u \rangle_{r,z,t} = \frac{\int_0^{2\pi} \int_0^{\pi/k} \int_0^1 u \; r \; \mathrm{d}r \; \mathrm{d}z \; \mathrm{d}t}{\int_0^{2\pi} \int_0^{\pi/k} \int_0^1 r \; \mathrm{d}r \; \mathrm{d}z \; \mathrm{d}t}.$$

In order to calculate this to find $\langle |\boldsymbol{u}| \rangle_{r,z,t}$, where $|\boldsymbol{u}| = \sqrt{u_r^2 + u_z^2}$, we use a repeated mid-point rule to work out the spatial mean $\langle u \rangle_{r,z}(t)$ and then a left rectangle rule to determine the mean over time.

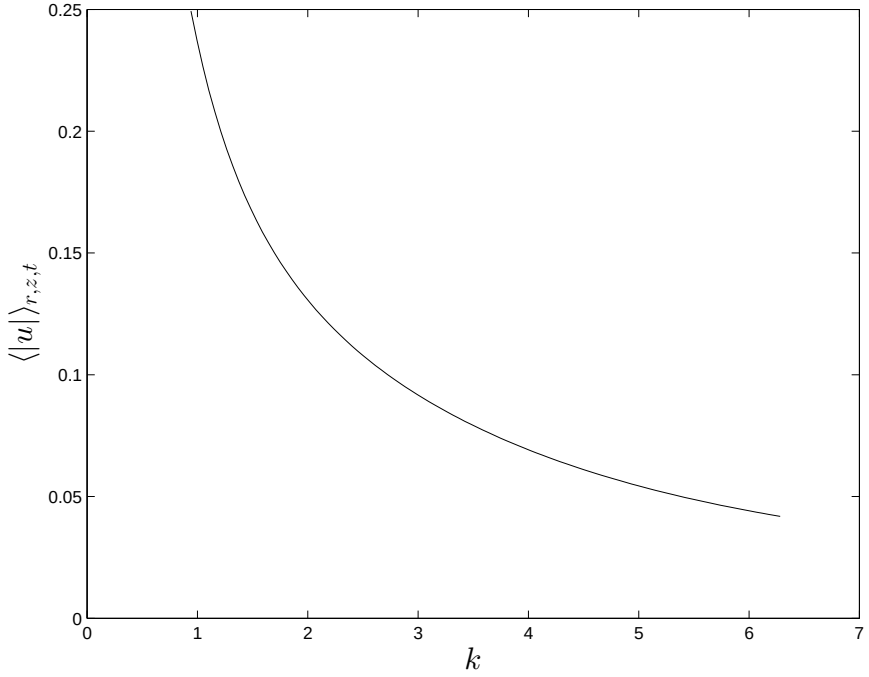

(a) k vs $\langle |\boldsymbol{u}| \rangle_{r,z,t}$

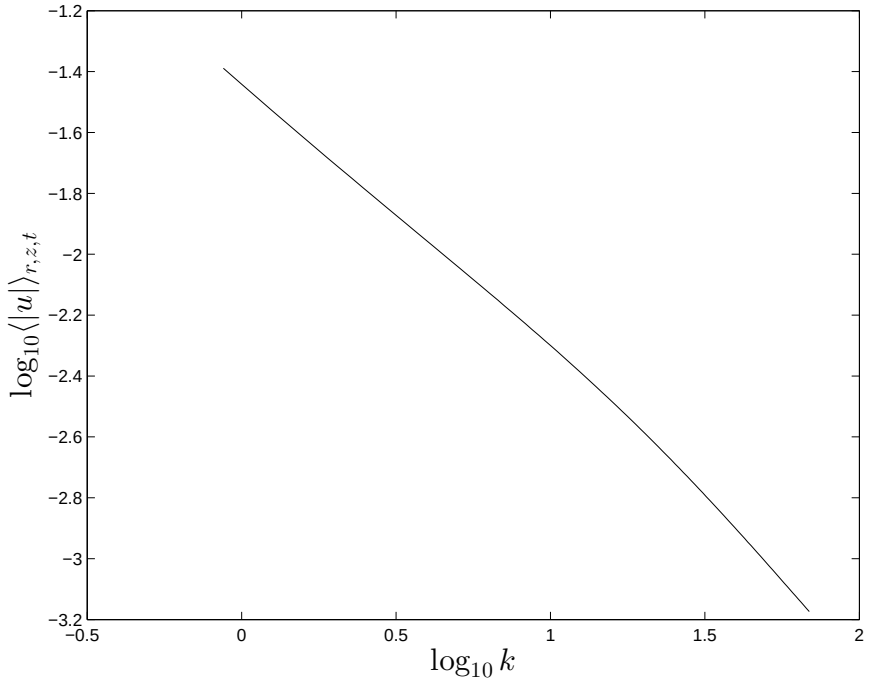

(b) $\log_{10} k$ vs $\log_{10}\langle |\boldsymbol{u}| \rangle_{r,z,t}$

Figure 5.5: Relationships between k and mean velocity (a) linear scale; and (b) logarithmic scale.

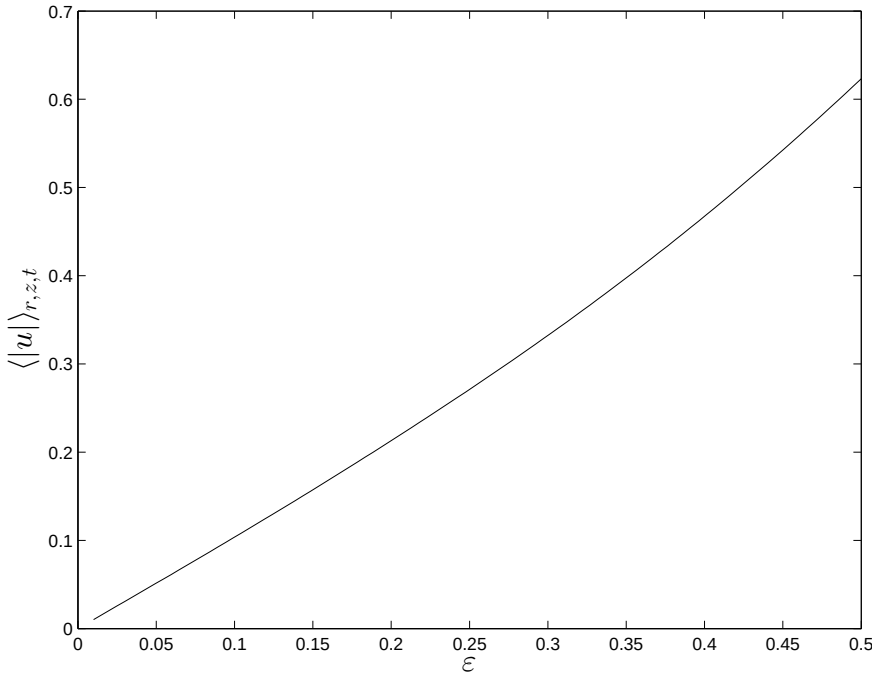

(a) ε vs $\langle |\boldsymbol{u}| \rangle_{r,z,t}$

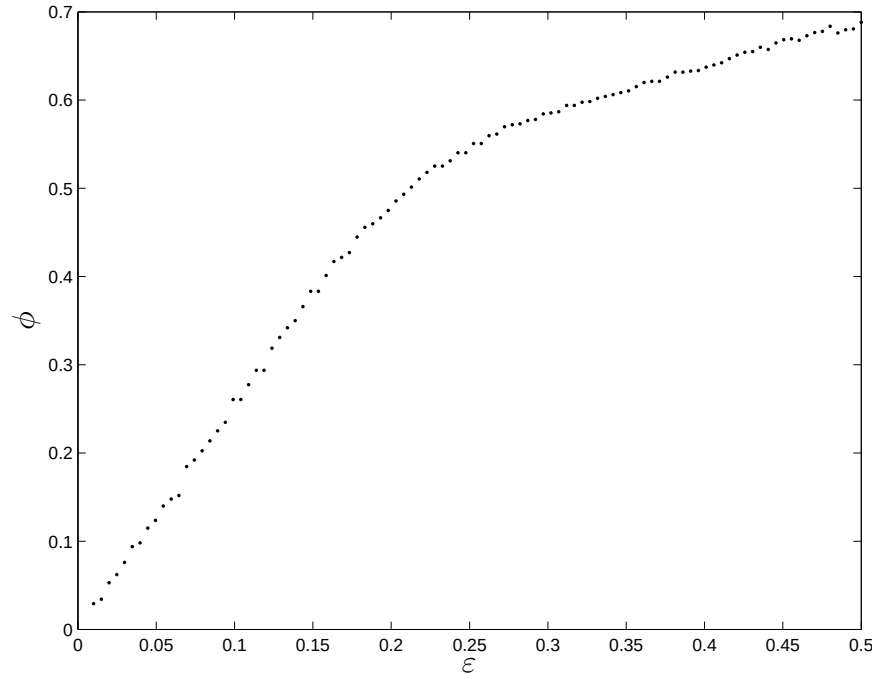

(b) ε vs ϕ

Figure 5.6: Graphs displaying the relationships between (a) ε and mean velocity; and (b) ε and $\phi(1)$, where $\phi(1)$ is the proportion of particles (by volume) which are captured by the wall over the course of one contractile cycle.

Figure 5.5 displays the relationship between k and the mean velocity $\langle|\boldsymbol{u}|\rangle_{r,z,t}$. This figure shows that the relationship between k and velocity is relatively simple, with mean velocity decreasing as the radius of the pipe increases relative to the wavelength. This suggests that differences in mean velocity are not responsible for the non-monotonic changes that we see in the value of ϕ as k is increased. Ultimately however the range of ϕ for each value of d is small; for example, running the MATLAB code for $d = 1$ for 100 equally spaced values of k for the same range of k as in table 5.5 we find $\phi_{max} = 0.260$ and $\phi_{min} = 0.249$. This is the difference between 24.9% and 26% of a drug dosage being absorbed, which in practical terms is negligible.

We have already considered ε in tables 5.1 and 5.2. These results are of particular interest to pharmacologists for a number of reasons. Physically the contractile amplitude differs between individual haustra and changes at a given haustrum in separate contractile cycles. In addition we can see that ε is the parameter which has the largest, and only significant, effect on particle absorption. Figure 5.6 displays the relationships between ε, $\langle|\boldsymbol{u}|\rangle_{r,z,t}$ and $\phi(1)$. The relationship between amplitude and velocity is linear, whereas the relationship between ε and ϕ is linear for $\varepsilon \lesssim 0.25$, after which the rate of increase of ϕ slows down with respect to ε but is still monotonically increasing.

We also consider the dimensional variable ω; this is because ω also has an effect on the length of time we allow for a particle to reach the colon wall. As we noted earlier in this section due to the periodicity of the flow, running the code for multiple cycles does not increase the value of ϕ. This is not physically realistic and in practice other contractile activity will affect the proportion of particles which are captured by the wall. In addition altering the contractile frequency and running the code for the length of one cycle does not affect the value of ϕ. Instead we consider fixing the dimensional, rather than nondimensional, time for which we run the code. We choose to run the code for $t \in [0, 20\omega]$ which is equivalent to $t^* \in [0, 20]$ s, i.e. the length of one cycle when using the

standard parameter value $\omega = \pi/10$ rad/s.

Over the range for ω of $\pi/15 - 4\pi/15$ rad/s running the code for $t^* \in [0, 20]$ s yielded the same results as running for $t \in [0, 2\pi]$. However running the code for 20 s as opposed to one cycle does have a significant effect when considering low frequencies of contractile activity.

Table 5.6: Values of ϕ after 20 seconds for a range of values for ω with Re $= \omega/8$ and $k = 5\pi/6$.

	ω (rad/s)					
d	$\pi/1800$	$\pi/900$	$\pi/450$	$\pi/30$	$2\pi/45$	$\pi/18$
1	0	0	0	0.193	0.245	0.261
0.99	0	0	0	0.206	0.261	0.261
0.98	0	0	0	0.206	0.266	0.270
0.97	0.098	0.098	0.098	0.266	0.314	0.328
0.95	0.098	0.098	0.098	0.282	0.342	0.345
0.9	0.19	0.19	0.19	0.36	0.412	0.423
0.85	0.278	0.278	0.278	0.444	0.486	0.489
0.8	0.36	0.36	0.36	0.516	0.546	0.552
0.7	0.51	0.51	0.51	0.629	0.660	0.662
0.5	0.75	0.75	0.75	0.813	0.829	0.829

Table 5.6 displays the results for ϕ after 20 s, where the period of contraction ranges from 1 hour to 36 s. As we can see the lowest frequencies (corresponding to contractile periods of 15 minutes to 1 hour) result in no particles being captured by the wall in the first 20 s of the cycle, which seems physically realistic; 75% of particles would, however, enter the radial outer half of the colon in this time period. As we reach frequencies of $\pi/30$ rad/s (i.e. 1 contraction per minute) we begin to see values for ϕ converging towards our earlier results for $\varepsilon = 0.1$, Re $= 0.039$ and $k = 5\pi/6$; in fact the results are identical for $\omega = \pi/18$ rad/s, i.e. a contractile period of 36 s. Therefore our earlier results may be considered robust over a 20 s time period, provided the period of contraction is no longer than about 45 s. However, since over one full cycle the proportion of particles absorbed is independent of the contractile frequency, in practice this only means that it would take

longer for the same volume of drug to be absorbed in a patient with low frequency colonic contractions.

In this chapter we investigated the method of Lagrangian particle tracking as a model for drug delivery. We used a force balance and estimates for the relevant parameters to determine the kinematic ODE to be solved. We set up a spatial grid in the $r - z$ plane to visualise the results and used this to calculate an estimate for the proportion of particles which would be absorbed. In doing this we also set up a mechanism to allow length of diffusion to be taken into account, by letting the function $\phi(d)$ represent the proportion of particles which enter the region $r \geq d$. We then considered the effects of the parameters ε (contractile amplitude), Re (viscous versus inertial forces), k (aspect ratio) and ω (contractile frequency) on the value of ϕ.

We found that ε has the largest effect on particle absorption, with ϕ increasing as ε increases. Varying both Re and ω has very little effect within our parameter regime, with the value of ω having no effect if ϕ is considered over a whole contractile cycle. We found that altering the aspect ratio, k, does have an effect on the value of ϕ, however the relationship between the two parameters is not simple enough to draw any conclusions. In practical terms the difference in the value of ϕ for different values of k in our parameter range is negligible.

Altering the number of contractile cycles does not increase the value of ϕ in our problem whereas in reality the cumulative proportion of particles absorbed would increase in further cycles. This is due to the influence of other contractile activity as well as changes in amplitude between contractile cycles in the physical situation. Thus our values for $\phi(d)$ in this chapter may be considered a lower bound for the proportion of particles entering the region $r \geq d$.

Chapter 6

Conclusions and Further Work

In this thesis we have presented three models of the ascending colon undergoing segmental contractions and have used one of these to begin to model site-specific drug delivery. The three models are:

- a one layer model of flow of a Newtonian fluid;
- a two layer model consisting of an inner Newtonian fluid and an outer Oldroyd B fluid; and
- a one layer model of flow of a Carreau fluid.

The motivation for this arose from current pharmacological interest in oral drug delivery to the colon; the ascending colon is the region where most mixing and absorption occurs. A mathematical model is desirable to help with the understanding of dosage form behaviour within the colonic environment. In particular, a mathematical model has advantages over a physical one due to its versatility in changing conditions via parameter variation.

We began by constructing one and two layer fluid models of the flow within the ascending colon under segmental contractions, using both Newtonian and more rheologically relevant fluid models. In doing this we studied the appropriate literature in order to understand the geometry and motility of the colon, the fluid rheology and any important

considerations relating to drug delivery. It was necessary to also consider the small intestine, in particular the ileum, due to a lack of colonic data in some cases, e.g. chyme viscosity; the rheological similarity between the terminal small intestine and the proximal colon make this a reasonable region to study. Some parameters are more constrained by the data than others, for example textbook values are given for the radius R_0 but no information was found on the viscosity of colonic mucus or of human chyme. Here we have had to use data either from other regions of the human body or from animal studies. After presenting our fluid models we then used the one layer model to model drug delivery via the method of Lagrangian particle tracking.

Throughout this thesis we have made various assumptions and simplifications, which may be split into those relating to geometry and those relating to flow. We have chosen to model the contractions of the colonic smooth muscle using a standing wave of small amplitude. The standing wave mimics the mixing effects of segmental contractions on the fluid flow, with no overall fluid transport. Taking the amplitude of this wave to be $\mathrm{O}(\varepsilon)$, where $\varepsilon \ll 1$, allows us to employ perturbation techniques to describe the flow, thus simplifying the problem. We also assumed that flow is induced purely by the motion of the boundary, i.e. there is no underlying pressure gradient and that this wall motion is axisymmetric, due to the nature of muscular contractions; thus it makes sense to assume that the flow is also axisymmetric. In order to simplify the problem we considered the fluid to be homogeneously distributed and the contractions driving the flow to be continuous.

We began by constructing the first model; a one layer model where chyme was represented by a Newtonian fluid. We found that at each time step, flow in the axial direction is antisymmetric, whilst radial flow is symmetric, about $z^* = \lambda/2$, where λ is the wavelength of the wall contraction; velocity magnitude is also symmetric about $z^* = \lambda/2$. In this sense flow in the negative and positive directions could be considered to 'balance' out over one wavelength at each time step. In addition to the symmetries at each time

step, the flow displayed antisymmetry in time over one cycle for u_r^* and u_z^*. We found no obvious differences in the flow between the results for $O(\varepsilon)$ and up to $O(\varepsilon^2)$ for $\varepsilon = 0.01$, which suggests there would be no advantage in going to higher order.

It is well established that both chyme and mucus display non-Newtonian behaviour. In particular, chyme displays shear thinning behaviour and mucus displays viscoelastic behaviour. In our second model, the two layer model, we have left chyme as a Newtonian fluid, but included a thin layer of mucus, represented by the viscoelastic Oldroyd B model. In this two layer model the only non-Newtonian parameters involved at $O(\varepsilon)$ are $M^{[2]} = \lambda_1\omega$ and $\lambda = \lambda_2/\lambda_1$, both of which relate to timescales. These appear in the normal and tangential interfacial conditions as well as the general solution for the Oldroyd B layer and do affect the flow at $O(\varepsilon)$. We found that there was little or no difference in the flow at $t = \pi/2$ and $t = 3\pi/2$ between the one and two layer models. For $t = 0$ and $t = \pi$ there were some small differences in the velocities, with the velocity being greater in the two layer model. However, since the velocities at $t = 0$ and $t = \pi$ are still much lower than those at other times we conclude that adding a mucus layer in the way we did has little impact on the overall flow.

We investigated the influence of the mucus specific parameters on the two layer flow by considering the flow velocities; we found that within a range of realistic values for these parameters the exact value of each parameter is not important to the flow profiles. For this reason, together with the similarities in bulk flow behaviour between the one and two layer models, and for simplicity, we chose to use the one layer model when considering drug delivery.

We could investigate the influence of parameters further by examining their effects on the mucus layer, rather than just the bulk flow. However, the flow within the mucus layer may not be relevant as to whether a dosage form is delivered to the layer in the first place. Instead the effects on the mucus layer could be considered as part of more in

depth work investigating the transfer of a drug through mucus to the epithelium. Cu and Saltzman [11] and Khanvilkar et al. [26] review models of molecular diffusion and drug transfer through mucus.

One problem that we have identified with our small amplitude approach in the two layer model is the use of ε as our small parameter. Note that the value of ε describes the amplitude as a fraction of the pipe radius, however our mucus layer thickness is much smaller than this value, i.e. $1 - \eta_0 \ll \varepsilon$. To fix this problem in future work we could consider returning to a one layer model but employing a slip condition at the boundary to represent the thin mucus layer. This approach could be coupled with both small amplitude and numerical methods. Another potential area to explore occurs at our fluid interface. Our calculations have assumed that mucus and chyme are immiscible, however this is not the case. Relaxing this assumption would be a potential area to investigate.

In order to investigate the effects of the shear thinning behaviour of chyme we returned to a one layer model. In our third model chyme was represented by a Carreau fluid model. A Carreau fluid is an example of a generalised Newtonian fluid and may be either shear thinning (as in the case of chyme) or shear thickening. We assumed that $M = m\omega = \mathrm{O}(1/\sqrt{\varepsilon})$, where ω is the radial frequency of the colonic contractions and m is the time parameter of the Carreau model, relating to when the transition between Newtonian and power law flow occurs. Within our parameter regime we found the flow at $\mathrm{O}(\varepsilon)$ is identical to that of a Newtonian fluid. At $\mathrm{O}(\varepsilon^2)$, however, the flow is dependent on the shear thinning parameters n and μ_c; n is the power law exponent and μ_c is the ratio between the infinite and the zero shear viscosities. The lower the two of these values (where $0 < n,\ \mu_c < 1$) the more shear thinning the fluid.

We found that the more shear thinning the fluid was, the higher the maximum values of velocity; however, the relationship between the shear thinning parameters and mean velocity is less straightforward. Whether the spatio-temporal mean increases or decreases

as μ_c decreases depends on the value of ε; in particular the critical range of ε where this relationship reverses depends on the power law exponent n. The lower the value of n, the lower the value $\varepsilon_c(n)$ for which the mean velocity increases as μ_c decreases when $\varepsilon \geq \varepsilon_c$.

For the purpose of investigating site-specific drug delivery within the ascending colon we assumed a dosage delivery system consisting of microparticles. In this situation drug transport would be dominated by advective, rather than diffusive, forces. Thus we employed the technique of Lagrangian particle tracking to quantify and analyse drug delivery, using the velocity fields from the Newtonian one layer model. We assumed an even distribution of particles throughout the $r - z$ plane over half a wavelength and set up a function $\phi(d)$, whose value represents the proportion of particles (by volume) which enter the region $r \geq d$ in the course of one contractile cycle. Due to the periodicity of the flow, we found that running the code for multiple cycles did not increase the value of ϕ. In practice continued contractile activity may affect the proportion of particles which are captured by the wall to some degree. In addition altering the contractile frequency and running the code for the length of one cycle did not affect the value of ϕ.

One limitation of our colonic model is the small amplitude assumption. We know that small amplitude contractions are not a physically precise model, however this does not preclude the use of small amplitude expansions to gain insight into the physics. Since this method allows us to quantify the error in our solutions it is also possible to increase ε until we reach the value which gives us a maximum acceptable error; our model was expanded up to $\mathrm{O}(\varepsilon^2)$, therefore any error in our solution is of order ε^3. When considering particle tracking we allowed the value of ε to be increased as high as $\varepsilon = 0.5$, which had a significant effect on our results. For example, when $\varepsilon = 0.01$, the proportion of particles which are captured by the wall is approximately 3%, whereas this jumps to approximately 69% when $\varepsilon = 0.5$ (see table 5.2). Varying the other nondimensional parameters, Re and k, for a realistic range of values for this problem had little effect on the proportion of

particles absorbed, with values for $\phi(1)$ ranging between approximately 0.249 and 0.261 for $\varepsilon = 0.1$. We could expand this work further by using the velocity fields calculated from the one layer Carreau model; this would allow us to investigate the effects of the shear thinning parameters on drug delivery.

One way to relax the need for a small amplitude assumption in modelling colonic contractile activity would be to employ techniques such as the finite element method. This would not be a simple problem, due to the use of a Eulerian description for flow but a Lagrangian one for the moving boundary. Therefore more involved techniques such as an arbitrary Lagrangian-Eulerian (ALE) description (see, for example, [24]) would have to be explored. However, this would also allow us to compare our results for larger values of ε to determine the validity of our approach for these larger values. As it stands, we may confidently use our results for, say, $\varepsilon = 0.1$ as a lower bound for values of ϕ.

The work in this thesis could be expanded further by considering the interaction between different types of contractile activity and the effects that this has on both flow and mixing, giving more insight into the time frames involved in drug absorption.

Previously fluid flow within the GI tract has been considered from a transit perspective, that is contractions have been modelled as peristaltic travelling waves, mostly under a long wavelength assumption, rather than specifically considering the effects of segmental contractions on flow. The mathematics developed in this thesis could be applied to other systems involving non propulsive contractions and fluid mixing; in particular systems where such contractions are small in amplitude and the geometry has an aspect ratio of O(1). For example, with some modifications to the geometry, the work in this thesis could be applied to fluid mixing within the stomach.

The work in this thesis has shown that the colon is an extremely effective fluid mixing system, for example with an amplitude half the length of the radius, 68% of drug particles are captured by the colonic wall over just one contractile cycle; a more realistic

amplitude may be a quarter the length of the radius, in which case approximately 55% of drug particles are captured. In addition the results obtained in chapter 5 show that the proportion of particles considered to be absorbed by the colonic epithelium is robust to changes in parameter values, with the exception of amplitude. This is very positive in terms of drug delivery, as it means individual differences in variables such as chyme viscosity may be discounted; conditions which affect the amplitude of contractions would need more careful consideration.

Appendix A

Cylindrical Polar Co-ordinates

Here we show our conversion into cylindrical polar co-ordinates of the equations of motion for an incompressible fluid in the absence of external body forces:

$$\nabla \cdot \boldsymbol{u} = 0 \tag{A.1}$$

$$\frac{\mathrm{D}\boldsymbol{u}}{\mathrm{D}t} = \frac{1}{\rho}\left(-\nabla p + \nabla \cdot \boldsymbol{\tau}\right), \tag{A.2}$$

where

$$\frac{\mathrm{D}\boldsymbol{u}}{\mathrm{D}t} = \frac{\partial \boldsymbol{u}}{\partial t} + \left(\boldsymbol{u} \cdot \nabla\right)\boldsymbol{u}.$$

In cartesian co-ordinates we considered the velocity field $\boldsymbol{u} = u\hat{\boldsymbol{x}} + v\hat{\boldsymbol{y}} + w\hat{\boldsymbol{z}}$. With cylindrical polar co-ordinates we wish to instead consider $\boldsymbol{u} = u_r\hat{\boldsymbol{r}} + u_\theta\hat{\boldsymbol{\theta}} + u_z\hat{\boldsymbol{z}}$, where u_r, u_θ, u_z are functions of r, θ, z and t,

$$\begin{pmatrix} r \\ \theta \\ z \end{pmatrix} = \begin{pmatrix} \sqrt{x^2 + y^2} \\ \tan^{-1}\left(\frac{y}{x}\right) \\ z \end{pmatrix}$$

and

$$\begin{pmatrix} \hat{\boldsymbol{r}} \\ \hat{\boldsymbol{\theta}} \\ \hat{\boldsymbol{z}} \end{pmatrix} = \begin{pmatrix} \cos\theta & \sin\theta & 0 \\ -\sin\theta & \cos\theta & 0 \\ 0 & 0 & 1 \end{pmatrix} \begin{pmatrix} \hat{\boldsymbol{x}} \\ \hat{\boldsymbol{y}} \\ \hat{\boldsymbol{z}} \end{pmatrix}.$$

We first consider the time derivative of $\boldsymbol{u}$. The expression for this is slightly more complicated than it is for cartesian co-ordinates since both unit vectors $\hat{\boldsymbol{r}}$ and $\hat{\boldsymbol{\theta}}$ change with time. We have

$$\frac{\partial \hat{\boldsymbol{r}}}{\partial t} = \frac{\partial \theta}{\partial t}\hat{\boldsymbol{\theta}}, \quad \frac{\partial \hat{\boldsymbol{\theta}}}{\partial t} = -\frac{\partial \theta}{\partial t}\hat{\boldsymbol{r}}, \quad \text{and} \quad \frac{\partial \hat{\boldsymbol{z}}}{\partial t} = 0,$$

which, after application of the product rule, gives us

$$\frac{\partial \boldsymbol{u}}{\partial t} = \left(\frac{\partial u_r}{\partial t} - \frac{u_\theta^2}{r}\right)\hat{\boldsymbol{r}} + \left(\frac{\partial u_\theta}{\partial t} + \frac{u_r u_\theta}{r}\right)\hat{\boldsymbol{\theta}} + \frac{\partial u_z}{\partial t}\hat{\boldsymbol{z}}. \tag{A.3}$$

The following two expressions are taken from Acheson [3, p352],

$$\nabla\phi = \frac{\partial \phi}{\partial r}\hat{\boldsymbol{r}} + \frac{1}{r}\frac{\partial \phi}{\partial \theta}\hat{\boldsymbol{\theta}} + \frac{\partial \phi}{\partial z}\hat{\boldsymbol{z}} \tag{A.4}$$

$$\boldsymbol{u}\cdot\nabla = u_r\frac{\partial}{\partial r} + \frac{u_\theta}{r}\frac{\partial}{\partial \theta} + u_z\frac{\partial}{\partial z} \tag{A.5}$$

and we are left only to consider the divergence of the matrix $\boldsymbol{\tau}$. Given that

$$\nabla\cdot\boldsymbol{u} = \frac{1}{r}\frac{\partial}{\partial r}(ru_r) + \frac{1}{r}\frac{\partial u_\theta}{\partial \theta} + \frac{\partial u_z}{\partial z} \tag{A.6}$$

in cylindrical polar co-ordinates [3, p352], we find that

$$\nabla\cdot\boldsymbol{\tau} = \frac{1}{r}\begin{pmatrix} \tau_{rr} - \tau_{\theta\theta} + r\frac{\partial \tau_{rr}}{\partial r} + \frac{\partial \tau_{\theta r}}{\partial \theta} + r\frac{\partial \tau_{zr}}{\partial z} \\ 2\tau_{r\theta} + r\frac{\partial \tau_{r\theta}}{\partial r} + \frac{\partial \tau_{\theta\theta}}{\partial \theta} + r\frac{\partial \tau_{z\theta}}{\partial z} \\ \tau_{rz} + r\frac{\partial \tau_{rz}}{\partial r} + \frac{\partial \tau_{\theta z}}{\partial \theta} + r\frac{\partial \tau_{zz}}{\partial z} \end{pmatrix}. \tag{A.7}$$

Setting equation (A.6) equal to zero gives us the continuity equation in cylindrical polar co-ordinates. Using equations (A.3) - (A.7) we can now write out the cylindrical components of (A.1) and (A.2) to give us the four equations of motion:

$$0 = \frac{1}{r}\frac{\partial}{\partial r}(ru_r) + \frac{1}{r}\frac{\partial u_\theta}{\partial \theta} + \frac{\partial u_z}{\partial z} \tag{A.8}$$

$$\frac{\mathrm{D}u_r}{\mathrm{D}t} - \frac{u_\theta^2}{r} = \frac{1}{\rho}\left(-\frac{\partial p}{\partial r} + \frac{1}{r}\left(\tau_{rr} - \tau_{\theta\theta} + r\frac{\partial \tau_{rr}}{\partial r} + \frac{\partial \tau_{\theta r}}{\partial \theta} + r\frac{\partial \tau_{zr}}{\partial z}\right)\right) \tag{A.9}$$

$$\frac{\mathrm{D}u_\theta}{\mathrm{D}t} + \frac{u_r u_\theta}{r} = \frac{1}{\rho r}\left(-\frac{\partial p}{\partial \theta} + 2\tau_{r\theta} + r\frac{\partial \tau_{r\theta}}{\partial r} + \frac{\partial \tau_{\theta\theta}}{\partial \theta} + r\frac{\partial \tau_{z\theta}}{\partial z}\right) \tag{A.10}$$

$$\frac{\mathrm{D}u_z}{\mathrm{D}t} = \frac{1}{\rho}\left(-\frac{\partial p}{\partial z} + \frac{1}{r}\left(\tau_{rz} + r\frac{\partial \tau_{rz}}{\partial r} + \frac{\partial \tau_{\theta z}}{\partial \theta} + r\frac{\partial \tau_{zz}}{\partial z}\right)\right) \tag{A.11}$$

where

$$\frac{\mathrm{D}}{\mathrm{D}t} = \frac{\partial}{\partial t} + u_r\frac{\partial}{\partial r} + \frac{u_\theta}{r}\frac{\partial}{\partial \theta} + u_z\frac{\partial}{\partial z}.$$

We also need to know the components of the rate of deformation tensor, $\boldsymbol{D}$, in cylindrical polar co-ordinates. These are given by [3, p353]:

$$D_{rr} = \frac{\partial u_r}{\partial r}, \quad D_{\theta\theta} = \frac{1}{r}\frac{\partial u_\theta}{\partial \theta} + \frac{u_r}{r}, \quad D_{zz} = \frac{\partial u_z}{\partial z},$$

$$D_{\theta z} = \frac{1}{2}\left(\frac{1}{r}\frac{\partial u_z}{\partial \theta} + \frac{\partial u_\theta}{\partial z}\right), \quad D_{zr} = \frac{1}{2}\left(\frac{\partial u_r}{\partial z} + \frac{\partial u_z}{\partial r}\right),$$

$$\text{and} \quad D_{r\theta} = \frac{1}{2}\left(r\frac{\partial}{\partial r}\left(\frac{u_\theta}{r}\right) + \frac{1}{r}\frac{\partial u_r}{\partial \theta}\right).$$

Appendix B

Derivation of the Components of the Oldroyd B Constitutive Equation

The constitutive equation for an Oldroyd B fluid is given by

$$\boldsymbol{\tau} + \lambda_1 \boldsymbol{\tau}^{\nabla} = \mu(\dot{\boldsymbol{\gamma}} + \lambda_2 \dot{\boldsymbol{\gamma}}^{\nabla}),$$

where $\boldsymbol{A}^{\nabla}$ is the upper convected derivative of $\boldsymbol{A}$, given by

$$\begin{aligned} \boldsymbol{A}^{\nabla} &= \frac{D\boldsymbol{A}}{Dt} - (\nabla \boldsymbol{u})^T \cdot \boldsymbol{A} - \boldsymbol{A} \cdot (\nabla \boldsymbol{u}) \\ &= \frac{\partial \boldsymbol{A}}{\partial t} + (\boldsymbol{u} \cdot \nabla)\boldsymbol{A} - (\nabla \boldsymbol{u})^T \cdot \boldsymbol{A} - \boldsymbol{A} \cdot (\nabla \boldsymbol{u}). \end{aligned}$$

In an axisymmetric cylindrical geometry we have

$$\nabla \boldsymbol{u} = \begin{pmatrix} \frac{\partial u_r}{\partial r} & 0 & \frac{\partial u_r}{\partial z} \\ 0 & \frac{u_r}{r} & 0 \\ \frac{\partial u_z}{\partial r} & 0 & \frac{\partial u_z}{\partial z} \end{pmatrix},$$

thus the shear rate is given by

$$\begin{aligned}\dot{\boldsymbol{\gamma}} &= \nabla\boldsymbol{u} + (\nabla\boldsymbol{u})^T \\ &= \begin{pmatrix} 2\frac{\partial u_r}{\partial r} & 0 & \frac{\partial u_r}{\partial z} + \frac{\partial u_z}{\partial r} \\ 0 & 2\frac{u_r}{r} & 0 \\ \frac{\partial u_r}{\partial z} + \frac{\partial u_z}{\partial r} & 0 & 2\frac{\partial u_z}{\partial z} \end{pmatrix}.\end{aligned}$$

This allows us to find the components of $(\nabla\boldsymbol{u})^T \cdot \dot{\boldsymbol{\gamma}} + \dot{\boldsymbol{\gamma}} \cdot (\nabla\boldsymbol{u})$:

$$\begin{aligned} rr &: 4\left(\frac{\partial u_r}{\partial r}\right)^2 + 2\frac{\partial u_z}{\partial r}\left(\frac{\partial u_r}{\partial z} + \frac{\partial u_z}{\partial r}\right) \\ rz &: 2\left(\frac{\partial u_r}{\partial r}\frac{\partial u_r}{\partial z} + \frac{\partial u_z}{\partial r}\frac{\partial u_z}{\partial z}\right) + \left(\frac{\partial u_r}{\partial z} + \frac{\partial u_z}{\partial r}\right)\left(\frac{\partial u_r}{\partial r} + \frac{\partial u_z}{\partial z}\right) \\ \theta\theta &: 4\left(\frac{u_r}{r}\right)^2 \\ zz &: 4\left(\frac{\partial u_z}{\partial z}\right)^2 + 2\frac{\partial u_r}{\partial z}\left(\frac{\partial u_r}{\partial z} + \frac{\partial u_z}{\partial r}\right), \end{aligned}$$

all others are zero. In addition we have the non-zero components of $(\boldsymbol{u} \cdot \nabla)\,\dot{\boldsymbol{\gamma}}$:

$$\begin{aligned} rr &: 2\left(u_r\frac{\partial^2 u_r}{\partial r^2} + u_z\frac{\partial^2 u_r}{\partial r\partial z}\right) \\ rz &: u_r\left(\frac{\partial^2 u_r}{\partial r\partial z} + \frac{\partial^2 u_z}{\partial r^2}\right) + u_z\left(\frac{\partial^2 u_z}{\partial r\partial z} + \frac{\partial^2 u_r}{\partial z^2}\right) \\ \theta\theta &: 2\left(u_r\frac{\partial}{\partial r}\left(\frac{u_r}{r}\right) + u_z\frac{\partial}{\partial z}\left(\frac{u_r}{r}\right)\right) \\ zz &: 2\left(u_r\frac{\partial^2 u_z}{\partial r\partial z} + u_z\frac{\partial^2 u_z}{\partial z^2}\right) \end{aligned}$$

and

$$\frac{\partial\dot{\boldsymbol{\gamma}}}{\partial t} = \begin{pmatrix} 2\frac{\partial^2 u_r}{\partial t\partial r} & 0 & \frac{\partial^2 u_r}{\partial t\partial z} + \frac{\partial^2 u_z}{\partial t\partial r} \\ 0 & \frac{2}{r}\frac{\partial u_r}{\partial t} & 0 \\ \frac{\partial^2 u_r}{\partial t\partial z} + \frac{\partial^2 u_z}{\partial t\partial r} & 0 & 2\frac{\partial^2 u_z}{\partial t\partial z} \end{pmatrix}.$$

Together these tell us that $\tau_{\theta r} = \tau_{\theta z} = 0$ and considering the left hand side of the constitutive relation we have the following components of $(\nabla \boldsymbol{u})^T \cdot \boldsymbol{\tau} + \boldsymbol{\tau} \cdot (\nabla \boldsymbol{u})$:

$$\begin{aligned} rr &: 2\left(\tau_{rr}\frac{\partial u_r}{\partial r} + \tau_{rz}\frac{\partial u_z}{\partial r}\right) \\ rz &: \tau_{rr}\frac{\partial u_r}{\partial z} + \tau_{zz}\frac{\partial u_z}{\partial r} + \tau_{rz}\left(\frac{\partial u_r}{\partial r} + \frac{\partial u_z}{\partial z}\right) \\ \theta\theta &: 2\tau_{\theta\theta}\frac{u_r}{r} \\ zz &: 2\left(\tau_{zz}\frac{\partial u_z}{\partial z} + \tau_{rz}\frac{\partial u_r}{\partial z}\right). \end{aligned}$$

Using this information we find four equations for the components of shear stress in terms of the fluid velocities,

$$\tau_{rr} + \lambda_1\left(\frac{\partial \tau_{rr}}{\partial t} + u_r\frac{\partial \tau_{rr}}{\partial r} + u_z\frac{\partial \tau_{rr}}{\partial z} - 2\tau_{rr}\frac{\partial u_r}{\partial r} - 2\tau_{rz}\frac{\partial u_z}{\partial r}\right) = 2\mu\left(\frac{\partial u_r}{\partial r} + \lambda_2\left(\frac{\partial^2 u_r}{\partial t \partial r} + u_r\frac{\partial^2 u_r}{\partial r^2} + u_z\frac{\partial^2 u_r}{\partial z \partial r} - 2\left(\frac{\partial u_r}{\partial r}\right)^2 - \frac{\partial u_z}{\partial r}\left(\frac{\partial u_r}{\partial z} + \frac{\partial u_z}{\partial r}\right)\right)\right);$$

$$\tau_{rz} + \lambda_1\left(\frac{\partial \tau_{rz}}{\partial t} + u_r\frac{\partial \tau_{rz}}{\partial r} + u_z\frac{\partial \tau_{rz}}{\partial z} - \tau_{rr}\frac{\partial u_r}{\partial z} - \tau_{zz}\frac{\partial u_z}{\partial r} - \tau_{rz}\left(\frac{\partial u_r}{\partial r} + \frac{\partial u_z}{\partial z}\right)\right) = \mu\left(\frac{\partial u_r}{\partial z} + \frac{\partial u_z}{\partial r} + \lambda_2\left(\frac{\partial^2 u_r}{\partial t \partial z} + \frac{\partial^2 u_z}{\partial t \partial r} + u_r\left(\frac{\partial^2 u_r}{\partial r \partial z} + \frac{\partial^2 u_z}{\partial r^2}\right) + u_z\left(\frac{\partial^2 u_z}{\partial z \partial r} + \frac{\partial^2 u_r}{\partial z^2}\right) - 2\left(\frac{\partial u_r}{\partial r}\frac{\partial u_r}{\partial z} + \frac{\partial u_z}{\partial r}\frac{\partial u_z}{\partial z}\right) - \left(\frac{\partial u_r}{\partial z} + \frac{\partial u_z}{\partial r}\right)\left(\frac{\partial u_r}{\partial r} + \frac{\partial u_z}{\partial z}\right)\right)\right);$$

$$\tau_{\theta\theta} + \lambda_1\left(\frac{\partial \tau_{\theta\theta}}{\partial t} + u_r\frac{\partial \tau_{\theta\theta}}{\partial r} + u_z\frac{\partial \tau_{\theta\theta}}{\partial z} - 2\tau_{\theta\theta}\frac{u_r}{r}\right) = 2\frac{\mu}{r}\left(u_r + \lambda_2\left(\frac{\partial u_r}{\partial t} + u_r\frac{\partial u_r}{\partial r} + u_z\frac{\partial u_r}{\partial z} - 3\frac{u_r^2}{r}\right)\right);$$

and finally

$$\tau_{zz} + \lambda_1 \left(\frac{\partial \tau_{zz}}{\partial t} + u_r \frac{\partial \tau_{zz}}{\partial r} + u_z \frac{\partial \tau_{zz}}{\partial z} - 2\tau_{zz} \frac{\partial u_z}{\partial z} - 2\tau_{rz} \frac{\partial u_r}{\partial z} \right) = 2\mu \left(\frac{\partial u_z}{\partial z} + \lambda_2 \left(\frac{\partial^2 u_z}{\partial t \partial z} + u_r \frac{\partial^2 u_z}{\partial r \partial z} + u_z \frac{\partial^2 u_z}{\partial z^2} - 2 \left(\frac{\partial u_z}{\partial z} \right)^2 - \frac{\partial u_r}{\partial z} \left(\frac{\partial u_r}{\partial z} + \frac{\partial u_z}{\partial r} \right) \right) \right).$$

Appendix C

Interfacial Conditions Between Two Fluids

We denote the interface between the two fluids under consideration by the equation

$$F(x_1, x_2, x_3, t) = 0,$$

so that, for example, in cartesian co-ordinates this may be expressed as

$$F(x, y, z, t) = z - \eta(x, y, t) = 0, \text{ or } z = \eta(x, y, t).$$

In this section we let p_1, μ_1 and $\boldsymbol{t_1}$ represent the pressure, dynamic viscosity and stress vector for the first fluid respectively and similarly for p_2, μ_2 and $\boldsymbol{t_2}$ with the second fluid.

For both viscous and inviscid liquids we have the kinematic condition which states that any particles at the interface must remain at the interface [3, p65]. Therefore we must have

$$\frac{\mathrm{D}F}{\mathrm{D}t} = \frac{\partial F}{\partial t} + (\boldsymbol{u} \cdot \nabla)F = 0, \text{ on } F = 0. \tag{C.1}$$

For viscous fluids we must also have continuity of velocity, so that $\boldsymbol{u_1} = \boldsymbol{u_2}$ on $F = 0$.

We have the normal stress condition for a viscous liquid, which tells us that the normal

component of stress at the free surface is balanced by the surface tension; this relates the change in pressure across the interface to the interfacial tension and the curvature of the given interface. The curvature, κ, is given by

$$\kappa = \nabla \cdot \hat{\boldsymbol{n}}, \tag{C.2}$$

where $\hat{\boldsymbol{n}}$ is the unit normal to the interface, and the coefficient of surface/interfacial tension is denoted by σ. The stress vector, $\boldsymbol{t}$, is given in terms of the stress tensor, $\boldsymbol{\sigma}$, by

$$t_i = \sigma_{ij} n_j.$$

For a Newtonian fluid,

$$\boldsymbol{\sigma} = -p\boldsymbol{I} + \mu\dot{\boldsymbol{\gamma}},$$

which allows us to write [3, p209]

$$\boldsymbol{t} = -p\boldsymbol{n} + \mu[2(\boldsymbol{n} \cdot \nabla)\boldsymbol{u} + \boldsymbol{n} \times (\nabla \times \boldsymbol{u})], \tag{C.3}$$

where $\boldsymbol{n}$ is a unit vector normal to the interface. If we take $\boldsymbol{n}$ to be the unit normal pointing out of fluid one, then the normal stress condition becomes

$$(\boldsymbol{t_1} - \boldsymbol{t_2}) \cdot \boldsymbol{n} = -\sigma\kappa, \text{ on } F = 0. \tag{C.4}$$

We also require that the tangential components of stress are continuous across the interface, i.e.

$$\boldsymbol{t_1} \cdot \boldsymbol{l} = \boldsymbol{t_2} \cdot \boldsymbol{l}, \text{ on } F = 0, \tag{C.5}$$

where $\boldsymbol{l}$ is a vector tangential to the interface.

Appendix D

Boundary and Interfacial Conditions for Two Layer Flow in terms of General Solutions

We consider the boundary and interfacial conditions used to determine the constants in the general solutions to the problem of two layer flow, with an inner Carreau layer and an outer Oldroyd B layer.

Rewriting our conditions in terms of the general solutions of $f^{[1]}$ and $f^{[2]}$ allows us to form a system of equations of the form $\boldsymbol{M} \cdot \boldsymbol{x} = \boldsymbol{b}$.

The two remaining boundary conditions are given by

$$\begin{aligned} f^{[2]}(1) &= -i \\ \frac{\mathrm{d}f^{[2]}}{\mathrm{d}r}(1) &= i, \end{aligned}$$

which may then be written as

$$d_1 I_1(k) + d_2 K_1(k) + d_3 J_1(\sqrt{B}) + d_4 K_1(-i\sqrt{B}) = -i$$

and

$$d_1\left(kI_0(k)-I_1(k)\right)+d_2\left(-kK_0(k)-K_1(k)\right)+d_3\left(\sqrt{B}J_0(\sqrt{B})\right.$$
$$\left.-J_1(\sqrt{B})\right)+d_4\left(i\sqrt{B}K_0(-i\sqrt{B})-K_1(-i\sqrt{B})\right)=i.$$

Recall that continuity of velocity is given by the two equations

$$\begin{aligned} f^{[1]}(\eta_0) &= f^{[2]}(\eta_0) \\ \frac{\mathrm{d}f^{[1]}}{\mathrm{d}r}(\eta_0) &= \frac{\mathrm{d}f^{[2]}}{\mathrm{d}r}(\eta_0), \end{aligned}$$

which we then write as

$$c_1I_1(\eta_0k)+c_3J_1(\sqrt{A}\eta_0)-d_1I_1(\eta_0k)-d_2K_1(\eta_0k)-d_3J_1(\sqrt{B}\eta_0)$$
$$-d_4K_1(-i\sqrt{B}\eta_0)=0$$

and

$$c_1\left(kI_0(\eta_0k)-\frac{I_1(\eta_0k)}{\eta_0}\right)+c_3\left(\sqrt{A}J_0(\sqrt{A}\eta_0)-\frac{J_1(\sqrt{A}\eta_0)}{\eta_0}\right)+d_1\left(-kI_0(\eta_0k)+\frac{I_1(\eta_0k)}{\eta_0}\right)$$
$$+d_2\left(kK_0(\eta_0k)+\frac{K_1(\eta_0k)}{\eta_0}\right)+d_3\left(-\sqrt{B}J_0(\sqrt{B}\eta_0)+\frac{J_1(\sqrt{B}\eta_0)}{\eta_0}\right)$$
$$+d_4\left(-i\sqrt{B}K_0(-i\sqrt{B}\eta_0)+\frac{K_1(-i\sqrt{B}\eta_0)}{\eta_0}\right)=0.$$

The kinematic condition is given by

$$f^{[i]}(\eta_0)=-i\tilde{\eta}$$

and we write this in terms of the inner fluid as

$$c_1 I_1(\eta_0 k) + c_3 J_1(\sqrt{A}\eta_0) + i\tilde{\eta} = 0.$$

Recall that the tangential stress condition at $r = \eta_0$ is given by

$$\frac{\mathrm{d}^2 f^{[2]}}{\mathrm{d}r^2} = \frac{1}{\bar{\mu}\Lambda}\frac{\mathrm{d}^2 f^{[1]}}{\mathrm{d}r^2} + \left(\frac{1}{\bar{\mu}\Lambda} - 1\right)\left(\frac{1}{\eta_0}\frac{\mathrm{d}f^{[1]}}{\mathrm{d}r} + i\tilde{\eta}\left(\frac{1}{\eta_0^2} - k^2\right)\right),$$

which may be written in terms of the general solutions as

$$\begin{aligned} c_1\left(-\frac{k^2 I_1(\eta_0 k)}{\bar{\mu}\Lambda} - \frac{I_1(\eta_0 k)}{\bar{\mu}\Lambda\eta_0^2} + \frac{kI_0(\eta_0 k)}{\eta_0} - \frac{I_1(\eta_0 k)}{\eta_0^2}\right) + c_3\left(\frac{AJ_1(\sqrt{A}\eta_0)}{\bar{\mu}\Lambda} - \frac{J_1(\sqrt{A}\eta_0)}{\bar{\mu}\Lambda\eta_0^2}\right. \\ \left. + \frac{\sqrt{A}J_0(\sqrt{A}\eta_0)}{\eta_0} - \frac{J_1(\sqrt{A}\eta_0)}{\eta_0^2}\right) + d_1\left(k^2 I_1(\eta_0 k) + \frac{2I_1(\eta_0 k)}{\eta_0^2} - \frac{kI_0(\eta_0 k)}{\eta_0}\right) \\ + d_2\left(k^2 K_1(\eta_0 k) + \frac{2K_1(\eta_0 k)}{\eta_0^2} + \frac{kK_0(\eta_0 k)}{\eta_0}\right) + d_3\left(-BJ_1(\sqrt{B}\eta_0) + \frac{2J_1(\sqrt{B}\eta_0)}{\eta_0^2}\right. \\ \left. - \frac{\sqrt{B}J_0(\sqrt{B}\eta_0)}{\eta_0}\right) + d_4\left(-BK_1(-i\sqrt{B}\eta_0) + \frac{2K_1(-i\sqrt{B}\eta_0)}{\eta_0^2} - \frac{i\sqrt{B}K_0(-i\sqrt{B}\eta_0)}{\eta_0}\right) \\ + \tilde{\eta}\left(i\left(\frac{1}{\eta_0} - k^2\right)\right) = 0. \end{aligned}$$

The normal stress condition at $r = \eta_0$ is given by

$$\begin{aligned} \frac{\mathrm{d}^3 f^{[2]}}{\mathrm{d}r^3} = \frac{1}{\bar{\mu}\Lambda}\frac{\mathrm{d}^3 f^{[1]}}{\mathrm{d}r^3} + \left(3\left(1 - \frac{1}{\bar{\mu}\Lambda}\right)\left(\frac{1}{\eta_0^2} + k^2\right) + \frac{i\mathrm{Re}}{\bar{\mu}\Lambda}(1 - \bar{\rho})\right)\frac{\mathrm{d}f^{[1]}}{\mathrm{d}r} + \tilde{\eta}\left(\frac{k^2}{\bar{\mu}\Lambda\mathrm{Ca}}\right. \\ \left.\left(\frac{1}{\eta_0^2} - k^2\right) + i\left(\frac{3}{\eta_0}\left(1 - \frac{1}{\bar{\mu}\Lambda}\right)\left(\frac{1}{\eta_0} - k^2\right) - \frac{i\mathrm{Re}}{\bar{\mu}\Lambda\eta_0}(1 - \bar{\rho})\right)\right), \end{aligned}$$

which may then be written as

$$c_1\left(\frac{1}{\bar{\mu}\Lambda}\left(-k^3I_0(\eta_0k)+\frac{2k^2I_1(\eta_0k)}{\eta_0}-\frac{3kI_0(\eta_0k)}{\eta_0^2}+\frac{6I_1(\eta_0k)}{\eta_0^3}\right)+\left(3\left(1-\frac{1}{\bar{\mu}\Lambda}\right)\left(\frac{1}{\eta_0}+k^2\right)\right.\right.$$
$$\left.\left.+\frac{i\mathrm{Re}}{\bar{\mu}\Lambda}(1-\bar{\rho})\right)\left(-kI_0(\eta_0k)+\frac{I_1(\eta_0k)}{\eta_0}\right)\right)+c_3\left(\frac{1}{\bar{\mu}\Lambda}\left(\sqrt{A}^3J_0(\sqrt{A}\eta_0)-\frac{2AJ_1(\sqrt{A}\eta_0)}{\eta_0}\right.\right.$$
$$\left.-\frac{3\sqrt{A}J_0(\sqrt{A}\eta_0)}{\eta_0^2}+\frac{6J_1(\sqrt{A}\eta_0)}{\eta_0^3}\right)+\left(3\left(1-\frac{1}{\bar{\mu}\Lambda}\right)\left(\frac{1}{\eta_0}+k^2\right)+\frac{i\mathrm{Re}}{\bar{\mu}\Lambda}(1-\bar{\rho})\right)$$
$$\left.\left.\left(-\sqrt{A}J_0(\sqrt{A}\eta_0)+\frac{J_1(\sqrt{A}\eta_0)}{\eta_0}\right)\right)+d_1\left(k^3I_0(\eta_0k)-\frac{2k^2I_1(\eta_0k)}{\eta_0}+\frac{3kI_0(\eta_0k)}{\eta_0^2}-\frac{6I_1(\eta_0k)}{\eta_0^3}\right)\right.$$
$$+d_2\left(-k^3K_0(\eta_0k)-\frac{2k^2K_1(\eta_0k)}{\eta_0}-\frac{3kK_0(\eta_0k)}{\eta_0^2}-\frac{6K_1(\eta_0k)}{\eta_0^3}\right)$$
$$+d_3\left(-\sqrt{B}^3J_0(\sqrt{B}\eta_0)+\frac{2BJ_1(\sqrt{B}\eta_0)}{\eta_0}+\frac{3\sqrt{B}J_0(\sqrt{B}\eta_0)}{\eta_0^2}-\frac{6J_1(\sqrt{B}\eta_0)}{\eta_0^3}\right)$$
$$+d_4\left(-i\sqrt{B}^3K_0(-i\sqrt{B}\eta_0)+\frac{2BK_1(-i\sqrt{B}\eta_0)}{\eta_0}+\frac{3i\sqrt{B}K_0(-i\sqrt{B}\eta_0)}{\eta_0^2}-\frac{6K_1(-i\sqrt{B}\eta_0)}{\eta_0^3}\right)$$
$$\left.+\tilde{\eta}\left(\frac{k^2}{\bar{\mu}\Lambda\mathrm{Ca}}\left(\frac{1}{\eta_0^2}-k^2\right)+i\left(\frac{3}{\eta_0}\left(1-\frac{1}{\bar{\mu}\Lambda}\right)\left(\frac{1}{\eta_0^2}-k^2\right)-\frac{i\mathrm{Re}}{\bar{\mu}\Lambda\eta_0}(1-\bar{\rho})\right)\right)=0.\right.$$

Appendix E

Determining Model Parameters from Rheological Data

In this appendix we detail the methods used to fit rheological model parameters to fluid viscosity data. We took a logarithmic scale plot of $\dot{\gamma}$ versus μ for a tomato soup solution from Medauden [42] and imported this into MATLAB. We then used the MATLAB function ginput to collect co-ordinates for data points on the shear rate-viscosity curve and used linear transformations to extract the original data points, shown in table E.1.

We began by fitting all 28 data points from table E.1 to a Carreau model of the form

$$\mu(\dot{\gamma}) = (\mu_0 - \mu_\infty)\left(1 + (m\dot{\gamma})^2\right)^{\frac{n-1}{2}} + \mu_\infty.$$

Table E.1: Data points taken from [42].

	$\dot{\gamma}$ (s^{-1})	μ (Pa $\cdot$ s)
1	0.0000152628	9313.247052
2	0.0000170077	9871.474375
3	0.0000229823	9871.474375
4	0.0000301244	10130.19902
5	0.0000455141	8236.265485
6	0.0000548208	8130.408368
7	0.0000806157	7283.825798
8	0.000120163	5922.047822
9	0.00017492	5659.903006
10	0.000262499	4398.032425
11	0.001012252	1522.594546
12	0.169617112	11.09031343
13	0.790495171	2.983452317
14	2.365265132	1.278620235
15	6.057353845	0.623654155
16	12.32505579	0.401728446
17	21.90442239	0.294510731
18	35.65157679	0.213133485
19	58.6182579	0.166690217
20	79.21011922	0.157263962
21	115.6956881	0.142723137
22	173.0362967	0.120631485
23	252.739847	0.10064889
24	379.282524	0.078209305
25	602.8735601	0.068719288
26	907.7879797	0.054093623
27	1462.595177	0.040433522
28	2661.647757	0.029642178

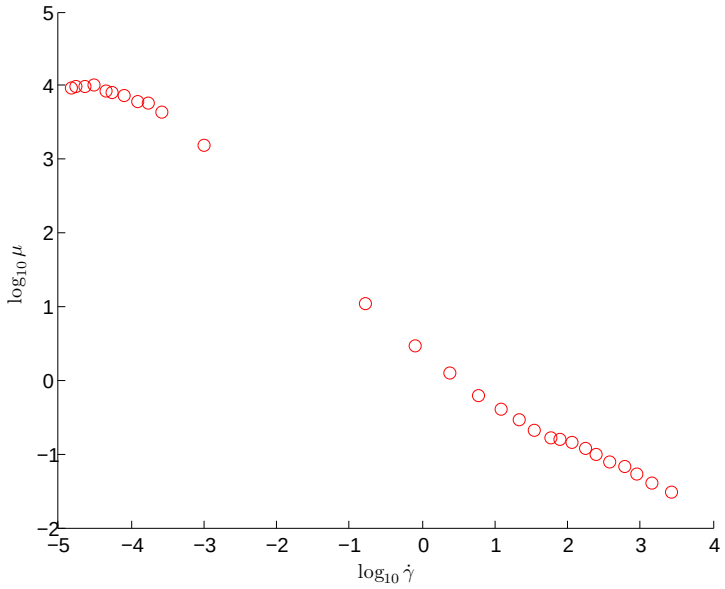

Figure E.1: $\log_{10}\dot{\gamma}$ vs $\log_{10}\mu$ for data points taken from table E.1 [42].

First we set up the residual function

$$\mathrm{Res}(\mu_0, \mu_\infty, m, n) = \sum_{i=1}^{28} |\log_{10}(\mu(\dot{\gamma}_i; \mu_0, \mu_\infty, m, n)) - \log_{10}(\mu_i)|^2,$$

where $\mu(\dot{\gamma}_i; \mu_0, \mu_\infty, m, n)$ is the Carreau model evaluated at the i^{th} value of $\dot{\gamma}$ and μ_i is the corresponding viscosity data value. We then used MATLAB's optimisation function fminsearch, which implements a simplex search algorithm, to perform a least squares approximation by finding the parameter values which minimise Res. We provided an initial estimate of $(\mu_0, \mu_\infty, m, n) = (8000, 0.1, 10000, 0.2)$ which led to the results, displayed in figure E.2,

$$\mu_0 = 9806;\ \mu_\infty = 0.0471;\ m = 11309;\ n = 0.1438;\ \text{and Res} = 0.2242.$$

The data cannot reasonably be fit to the exponential or De Kee models over such a

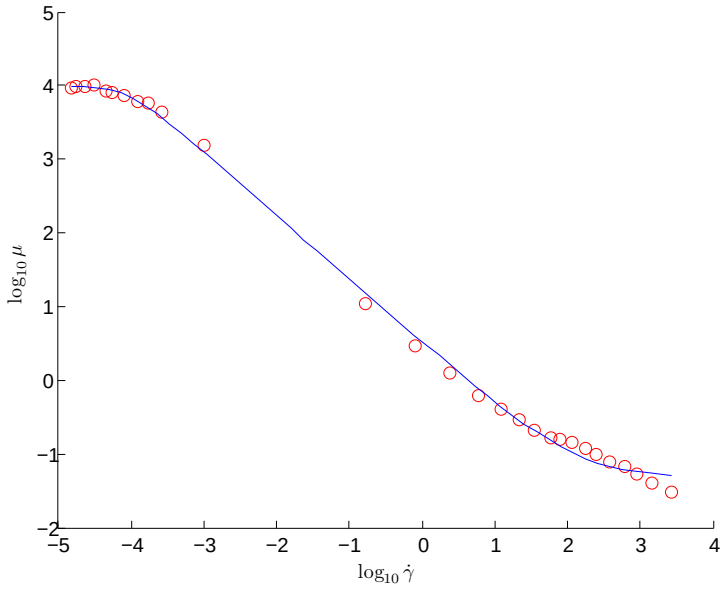

Figure E.2: Logarithmic flow curve of the Carreau model fit to rheological data from table E.1 [42].

large range of shear rates, instead we restrict the data to a smaller range of shear rate. There is a large jump in data values between points 11 and 12, the shear rates in our problem are of O(0.01) which falls into this gap in data. Since shear rates are likely to be larger, rather than smaller, than this we take the 5 data points $12-16$ and fit these to a De Kee model in a similar way to that previously outlined.

Recall for a De Kee model we have [10, p40]

$$\mu(\dot{\gamma}) = \mu_1 \mathrm{e}^{-t_1\dot{\gamma}} + \mu_2 \mathrm{e}^{-0.1t_1\dot{\gamma}} + \mu_\infty,$$

taking an initial estimate of $(\mu_1, \mu_2, \mu_\infty, t_1) = (3.2, 1, 0, 1)$ we obtain the results, displayed in figure E.3,

$$\mu_1 = 15.75;\ \mu_2 = 2.025;\ \mu_\infty = 0.3708;\ t_1 = 3.417;\ \text{and Res} = 6.8 \times 10^{-6}.$$

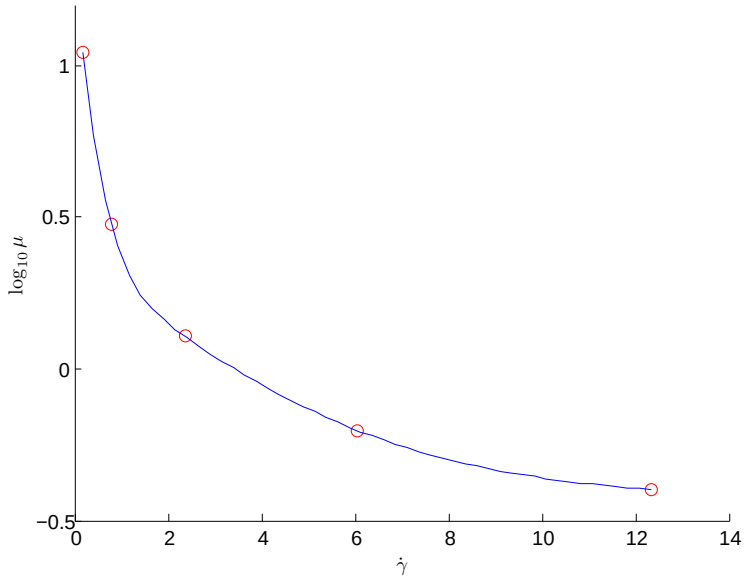

Figure E.3: Semi-log flow curve of the De Kee model fit to a subset of data from E.1 [42].

These results illustrate the possibilities with fitting rheological models to viscosity data. In order to draw more specific conclusions in relation to the colon we would ideally have a larger number of data points, with a higher resolution of shear rate. It would also be interesting to consider the rheology of a more realistic type of fluid to mimic actual human digesta.

If we calculate the equations of motion for a De Kee fluid and follow the asymptotic methods used in the main body of this thesis with the parameter values above, we find that the flow in a pipe with small amplitude standing wave boundary contractions is identical to that of a Newtonian fluid.

List of References

[1] P. Abrahams. *The Atlas of the Human Body*. Amber Books Ltd, London, 2009.

[2] M. Abramowitz and I.A. Stegun, editors. *Handbook of Mathematical Functions*. Dover Publications, Inc., New York, 1965.

[3] D.J. Acheson. *Elementary Fluid Dynamics*. Oxford University Press, Oxford, 1990.

[4] P.A. Bampton, P.G. Dinning, M.L. Kennedy, D.Z. Lubowski, and I.J. Cook. Prolonged multi-point recording of colonic manometry in the unprepared human colon: Providing insight into potentially relevant pressure wave parameters. *The American Journal of Gastroenterology*, 96(6):1838–1848, 2001.

[5] H.A. Barnes, J.F. Hutton, and K. Walters. *An Introduction to Rheology*. Elsevier Science Publishers B.V., Amsterdam, 1989.

[6] G. Bassotti, G. Bucaneve, M.A. Pelli, and A. Morelli. Contractile frequency patterns of the human colon. *Neurogastroenterology and Motility*, 2(1):73–78, 1990.

[7] G. Bassotti, M. Clementi, E. Antonelli, M.A. Pelli, and M. Tonini. Low amplitude propagated contractile waves: a relevant propulsive mechanism of human colon. *Digestive and Liver Disease*, 33:36–40, 2001.

[8] G. Bassotti, G. Iantorno, S. Fiorella, L. Bustos-Fernandez, and C.R. Bilder. Colonic motility in man: Features in normal subjects and in patients with chronic idiopathic constipation. *The American Journal of Gastroenterology*, 94(7):1760–1770, 1999.

[9] R.B. Bird, R.C. Armstrong, and O. Hassager. *Dynamics of Polymeric Liquids Volume 1: Fluid Dynamics*. Wiley-Interscience, New York, 2nd edition, 1987.

[10] P.J. Carreau, D.C.R. De Kee, and R.P. Chhabra. *Rheology of Polymeric Systems, Principles and Applications*. Hanser, Munich, 1997.

[11] Y. Cu and W.M. Saltzman. Mathematical modeling of molecular diffusion through mucus. *Advanced Drug Delivery Reviews*, 61(2):101–114, 2009.

[12] J.R.N. Curt and R. Pringle. Viscosity of gastric mucus in duodenal ulceration. *Gut*, 10:931–934, 1969.

[13] C.L. Dikeman and Jr G.C. Fahey. Viscosity as related to dietary fiber: A review. *Critical Reviews in Food Science and Nutrition*, 46:649–663, 2006.

[14] S. Dillard, S. Krishnan, and H.S. Udaykumar. Mechanics of flow and mixing at antroduodenal junction. *World Journal of Gastroenterology*, 13(9):1365–1371, 2007.

[15] D. Doraiswamy. The origins of rheology: A short historical excursion. *Rheological Bulletin*, 71:1–9, 2002.

[16] M.A. Eastwood. The physiological effect of dietary fiber: An update. *Annual Review of Nutrition*, 12:19–35, 1992.

[17] K. Edsman and H. Hägerström. Pharmaceutical applications of mucoadhesion for the non-oral routes. *Journal of Pharmacy and Pharmacology*, 57(1):3–22, 2005.

[18] M.P. Escudier, I.W. Gouldson, A.S Pereira, F.T. Pinho, and R.J. Poole. On the reproducibility of the rheology of shear-thinning liquids. *Journal of non-Newtonian Fluid Mechanics*, 97:99–124, 2001.

[19] J.B. Frøkjær, S.D. Andersen, A.M. Drewes, and H. Gregersen. Ultrasound-determined geometric and biomechanical properties of the human duodenum. *Digestive Diseases and Sciences*, 51:1662–1669, 2006.

[20] J.B. Frøkjær, D. Liao, A. Bergmann, B.P. McMahon, E. Steffensen, A.M. Drewes, and H. Gregersen. Three-dimensional biomechanical properties of the human rectum evaluated with magnetic resonance imaging. *Neurogastroenterology and Motility*, 17:531–540, 2005.

[21] J.B. Frøkjær, D. Liao, E. Steffensen, C. Dimcevski, A. Bergmann, A.M. Drewes, and H. Gregersen. Geometric and mechanosensory properties of the sigmoid colon evaluated with magnetic resonance imaging. *Neurogastroenterology and Motility*, 19:253–262, 2007.

[22] R.C. Gill, K.R. Cote, K.L. Bowes, and Y.J. Kingma. Human colonic smooth muscle: electrical and contractile activity in vitro. *Gut*, 27:293–299, 1986.

[23] J.A. Henry, G. O'Sullivan, and A.S. Pandit. Using computed tomography scans to develop an ex-vivo gastric model. *World Journal of Gastroenterology*, 13(9):1372–1377, 2007.

[24] T.J.R. Hughes, W.K. Liu, and T.K. Zimmermann. Lagrangian-Eulerian finite element formulation for incompressible viscous flows. *Computer Methods in Applied Mechanics and Engineering*, 29:329–349, 1981.

[25] F.M. Kelvin and R. Gardiner. *Clinical Imaging of the Colon and Rectum.* Raven Press, New York, 1987.

[26] K. Khanvilkar, M.D. Donovan, and D.R. Flanagan. Drug transfer through mucus. *Advanced Drug Delivery Reviews*, 48:173–193, 2001.

[27] Y.S.R. Krishnaiah, S. Satyanarayana, Y.V. Rama Prasad, and S. Narasimha Roa. Evaluation of guar gum as a compression coat for drug targeting to colon. *International Journal of Pharmaceutics*, 171:137–146, 1998.

[28] S.K. Lai, Y. Wang, D. Wirtz, and J. Hanes. Micro- and macrorheology of mucus. *Advanced Drug Delivery Reviews*, 61:86–100, 2009.

[29] E. Lauga. Propulsion in a viscoelastic fluid. *Physics of Fluids*, 19:083104.1–13, 2007.

[30] J.T. Lee, C.A. Bailey, and A.L. Cartwright. Guar meal germ and hull fractions differently affect growth performance and intestinal viscosity of broiler chickens. *Poultry Science*, 82:1589–1595, 2003.

[31] D. Liao, J.B. Frøkjær, J. Yang, J. Zhao, A.M. Drewes, O.H. Gilja, and H. Gregersen. Three-dimensional surface model analysis in the gastrointestinal tract. *World Journal of Gastroenterology*, 12(18):2870–2875, 2006.

[32] D. Liao, H. Gregersen, T. Hausken, O.H. Gilja, M. Mundt, and G. Kassab. Analysis of surface geometry of the human stomach using real-time 3-d ultrasonography in vivo. *Neurogastroenterology and Motility*, 16:315–324, 2004.

[33] D. Liao, J. Zhao, Y. Fan, and H. Gregersen. Two-layered quasi-3d finite element model of the oesophagus. *Medical Engineering and Physics*, 26:535–543, 2004.

[34] E.K. Lund, J.M. Gee, J.C. Brown, P.J. Wood, and I.T. Johnson. Effect of oat gum on the physical properties of the gastrointestinal contents and on the uptake of d-galactose and cholesterol by rat small intestine in vitro. *British Journal of Nutrition*, 62:91–101, 1989.

[35] E.O. Macagno and J. Christensen. Fluid mechanics of the duodenum. *Annual Review of Fluid Mechanics*, 12:139–158, 1980.

[36] G.T. Macfarlane, S. Macfarlane, and G.R. Gibson. Validation of a three-stage compound continuous culture system for investigating the effect of retention time on the ecology and metabolism of bacteria in the human colon. *Microbial Ecology*, 35:180–187, 1998.

[37] K. Matsuo, H. Ota, T. Akamatsu, A. Sugiyama, and T. Katsuyama. Histochemistry of the surface mucous gel layer of the human colon. *Gut*, 40:782–789, 1997.

[38] E.L. McConnell, H.M. Fadda, and A.W. Basit. Gut instincts: Explorations in intestinal physiology and drug delivery. *International Journal of Pharmaceutics*, 364:213–226, 2008.

[39] D.E. McDonald, D.W. Pethick, B.P. Mullan, and D.J. Hampson. Increasing viscosity of the intestinal contents alters small intestinal structure and intestinal growth, and stimulates proliferation of enterotoxigenic *Escherichia coli* in newly-weaned pigs. *British Journal of Nutrition*, 86:487–498, 2001.

[40] S. McGinty, S. McKee, and R. McDermott. Analytic solutions of Newtonian and non-Newtonian pipe flows subject to a general time-dependent gradient. *Journal of Non-Newtonian Fluid Mechanics*, 162:54–79, 2009.

[41] B.P. McMahon, K.D. Oddie, K.W. Moloney, and H. Gregersen. Computation of flow through the oesophagogastric junction. *World Journal of Gastroenterology*, 13(9):1360–1364, 2007.

[42] K. Mehauden. *Evaluation of the Thermal and Mixing Performance of an Agitated Vessel for Processing of Complex Liquid Foodstuffs*. PhD thesis, Chemical Engineering, University of Birmingham, 2008.

[43] J.J. Misiewicz. Colonic motility (symposium on colonic motility). *Gut*, 16:311–314, 1975.

[44] J.C. Misra and S.K. Pandey. Peristaltic flow of a multilayered power-law fluid through a cylindrical tube. *International Journal of Engineering Science*, 39:387–402, 2001.

[45] F.A. Morrison. *Understanding Rheology*. Rheology Series. Oxford University Press, 2001.

[46] J.G. Oldroyd. On the formulation of rheological equations of state. *Proceedings of the Royal Society of London. Series A, Mathematical and Physical Sciences*, 200(1063):523–541, 1950.

[47] C. Olsson and S. Holmgren. The control of gut motility. *Comparative Biochemistry and Physiology - Part A: Molecular and Integrative Physiology*, 128(3):479–501, 2001.

[48] A. Pal, J.G. Brasseur, and B. Abrahamsson. A stomach road or "magenstrasse" for gastric emptying. *Journal of Biomechanics*, 40:1202–1210, 2007.

[49] J.F. Pinto. Site specific drug delivery systems within the gastro-intestinal tract: From the mouth to the colon. *International Journal of Pharmaceutics*, 395:44–52, 2010.

[50] R.D. Pullan, G.A.O. Thomas, M. Rhodes, R.G. Newcombe, G.T. Williams, A. Allen, and J. Rhodes. Thickness of adherent mucus gel on colonic mucosa in humans and its relevance to colitis. *Gut*, 35:353–359, 1994.

[51] M.S. Quraishi, N.S. Jones, and J. Mason. The rheology of nasal mucus: a review. *Clinical Otorhinolaryngology*, 23:403–413, 1998.

[52] A.R. Roa and M. Mishra. Peristaltic transport of a power-law fluid in a porous tube. *Journal of Non-Newtonian Fluid Mechanics*, 121:163–174, 2004.

[53] F.G. Roberts, H.A. Smith, A.G. Low, P.R. Ellis, E.R. Morris, and I.E. Sambrook. Influence of guar gum flour of different molecular weights on viscosity of jejunal digesta in the pig. *Proceedings of the Nutrition Society*, 49:53A, 1990.

[54] A. Rubenstein and B. Tirosh. Mucus gel thickness and turnover in the gastrointestinal tract of the rat: response to cholinergic stimulus and implication for mucoadhesion. *Pharmaceutical Research*, 11(6):794–799, 1994.

[55] C. Schiller, C.P. Fröhlich, T. Giessmann, W. Siegmund, H. Mönnikes, N. Hosten, and W. Weitschies. Intestinal fluid volumes and transit of dosage forms as assessed by magnetic resonance imaging. *Alimentary Pharmacological Therapy*, 22:971–979, 2005.

[56] S.S. Shibeshi and W.E. Collins. The rheology of blood flow in a branched arterial system. *Applied Rheology*, 15(6):398–405, 2005.

[57] V.R. Sinha and R. Kumria. Polysaccharides in colon-specific drug delivery. *International Journal of Pharmaceutics*, 224:19–38, 2001.

[58] V.R. Sinha and R. Kumria. Microbially triggered drug delivery to the colon. *European Journal of Pharmaceutical Sciences*, 18:3–18, 2003.

[59] J.D. Smart. The basics and underlying mechanisms of mucoadhesion. *Advanced Drug Delivery Reviews*, 57:1556–1568, 2005.

[60] D.J. Smith, E.A. Gaffney, and J.R. Blake. A viscoelastic traction layer model of muco-ciliary transport. *Bulletin of Mathematical Biology*, 69:289–327, 2007.

[61] P. Spratt, C. Nicolella, and D.L. Pyle. An engineering model of the human colon. *Trans IChemE, Part C, Food and Bioproducts Processing*, 83(C2):147–157, 2005.

[62] V. Strugala, P.W. Dettmar, and J.P. Pearson. Thickness and continuity of the adherent colonic mucus barrier in active and quiescent ulcerative colitis and crohn's disease. *International Journal of Clinical Practice*, 62(5):762–769, 2008.

[63] A. Swidsinski, B.C. Sydora, Y. Doerffel, V. Loening-Baucke, M. Vaneechoutte, M. Lupicki, J. Scholze, H. Lochs, and L.A. Dieleman. Viscosity gradient within the mucus layer determines the mucosal barrier function and the spatial organization of the intestinal microbiota. *Inflammatory Bowel Diseases*, 13(8):963–970, 2007.

[64] T. Takahashi, M. Goto, and T. Sakata. Viscoelastic properties of the small intestinal and caecal contents of the chicken. *British Journal of Nutrition*, 91:867–872, 2004.

[65] T. Takahashi and T. Sakata. Large particles increase viscosity and yield stress of pig cecal contents without changing basic viscoelastic properties. *The Journal of Nutrition*, 132:1026–1030, 2002.

[66] T. Takahashi and T. Sakata. Viscous properties of pig cecal contents and the contribution of solid particles to viscosity. *Nutrition*, 20:377–382, 2004.

[67] D. Tripathi, S.K. Pandey, and S. Das. Peristaltic transport of a generalised Burgers' fluid: Application to the movement of chyme in small intestine. *Acta Astronautica*, 2011.

[68] F.J.O. Varum, E.L. McConnell, J.J.S. Sousa, F. Veiga, and A. Basit. Mucoadhesion and the gastrointestinal tract. *Critical Reviews in Therapeutic Drug Carrier Systems*, 25(3):207–258, 2008.

[69] W.B. Wan Nik, F.N. Ani, H.H. Masjuki, and S.G. Eng Giap. Rheology of bio-edible oils according to several rheological models and its potential as hydraulic fluid. *Industrial Crops and Products*, 22:249–255, 2005.

[70] N. Washington, C. Washington, and C.G. Wilson. *Physiological Pharmaceutics: Barriers to Drug Absorption*, chapter 7: Drug Delivery to the Large Intestine and Rectum. Taylor and Francis, London, 2nd edition, 2001.

[71] N.W. Weisbrodt. *Gastrointestinal Physiology*, chapter 6: Motility of the Large Intestine. Mosby, London, 6th edition, 2001.

[72] C.G. Wilson. The transit of dosage forms through the colon. *International Journal of Pharmaceutics*, 395:17–25, 2010.

[73] H.F. Woollard, J. Billingham, O.E. Jensen, and G. Lian. A multi-scale model for solute transport in a wavy-walled channel. *Journal of Engineering Mathematics*, 64:25–48, 2009.

[74] W. Yang, T.C. Fung, K.S. Chian, and C.K. Chong. Instability of the two-layered thick-walled esophageal model under the external pressure and circular outer boundary condition. *Journal of Biomechanics*, 40:481–490, 2007.

[75] W. Yang, T.C. Fung, K.S. Chian, and C.K. Chong. Three-dimensional finite element model of the two-layered oesophagus, including the effects of residual strains and buckling of mucosa. *Proc IMechE [H] Journal of Engineering in Medicine*, 221:417–426, 2007.

[76] R. Yassi, L.K. Cheng, S. Al-Ali, N.P. Smith, A.J. Pullan, and J.A. Windsor. An anatomically based mathematical model of the gastroesophageal junction. *Proceedings of the 26th Annual International Conference of the IEEE EMBS*, pages 635–638, 2004.